UNCLASSIFIED

AD NUMBER
AD470095
NEW LIMITATION CHANGE
TO Approved for public release, distribution unlimited
FROM Distribution authorized to U.S. Gov't. agencies and their contractors; Administrative/Operational Use; SEP 1965. Other requests shall be referred to Air Force Weapons Laboratory, Research and Technology Division, Kirtland AFB, NM.
AUTHORITY
afwl ltr, 29 apr 1985

THIS PAGE IS UNCLASSIFIED

AD 470095

AUTHORITY: AFWL ltr, 29 Apr 85

THIS REPORT HAS BEEN DELIMITED
AND CLEARED FOR PUBLIC RELEASE
UNDER DOD DIRECTIVE 5200.20 AND
NO RESTRICTIONS ARE IMPOSED UPON
ITS USE AND DISCLOSURE.

DISTRIBUTION STATEMENT A

APPROVED FOR PUBLIC RELEASE;
DISTRIBUTION UNLIMITED.

SECURITY MARKING

The classified or limited status of this report applies to each page, unless otherwise marked.
Separate page printouts MUST be marked accordingly.

THIS DOCUMENT CONTAINS INFORMATION AFFECTING THE NATIONAL DEFENSE OF THE UNITED STATES WITHIN THE MEANING OF THE ESPIONAGE LAWS, TITLE 18, U.S.C., SECTIONS 793 AND 794. THE TRANSMISSION OR THE REVELATION OF ITS CONTENTS IN ANY MANNER TO AN UNAUTHORIZED PERSON IS PROHIBITED BY LAW.

NOTICE: When government or other drawings, specifications or other data are used for any purpose other than in connection with a definitely related government procurement operation, the U. S. Government thereby incurs no responsibility, nor any obligation whatsoever; and the fact that the Government may have formulated, furnished, or in any way supplied the said drawings, specifications, or other data is not to be regarded by implication or otherwise as in any manner licensing the holder or any other person or corporation, or conveying any rights or permission to manufacture, use or sell any patented invention that may in any way be related thereto.

CATALOGED BY: DDC
AS AD No. 470095

AFWL-TR-65-39

AFWL-TR
65-39

ELECTROMAGNETIC FIELD DISTORTIONS AND CURRENTS IN AND NEAR BURIED CABLES AND BUNKERS

Arthur L. Whitson and Edward F. Vance

Stanford Research Institute
Menlo Park, California
Contract AF 29(601)-5904

DDC
SEP 23 1965
TISIA B

TECHNICAL REPORT NO. AFWL-TR-65-39

September 1965

AIR FORCE WEAPONS LABORATORY
Research and Technology Division
Air Force Systems Command
Kirtland Air Force Base
New Mexico

AFWL-TR-65-39

Research and Technology Division
AIR FORCE WEAPONS LABORATORY
Air Force Systems Command
Kirtland Air Force Base
New Mexico

When U. S. Government drawings, specifications, or other data are used for any purpose other than a definitely related Government procurement operation, the Government thereby incurs no responsibility nor any obligation whatsoever, and the fact that the Government may have formulated, furnished, or in any way supplied the said drawings, specifications, or other data, is not to be regarded by implication or otherwise, as in any manner licensing the holder or any other person or corporation, or conveying any rights or permission to manufacture, use, or sell any patented invention that may in any way be related thereto.

This report is made available for study with the understanding that proprietary interests in and relating thereto will not be impaired. In case of apparent conflict or any other questions between the Government's rights and those of others, notify the Judge Advocate, Air Force Systems Command, Andrews Air Force Base, Washington, D. C. 20331.

Qualified users may obtain copies of this report from DDC.

Distribution is limited because of the technology discussed in the report.

AFWL-TR-65-39

ELECTROMAGNETIC FIELD DISTORTIONS AND CURRENTS IN AND NEAR BURIED CABLES AND BUNKERS

Arthur L. Whitson and Edward F. Vance

Stanford Research Institute
Menlo Park, California
Contract AF 29(601)-5904

TECHNICAL REPORT NO. AFWL-TR-65-39

FOREWORD

This report, submitted 5 August 1965, covers research conducted during the period 18 March 1963 through 28 February 1965 by Stanford Research Institute, Menlo Park, California, under Air Force Contract No. AF 29(601)-5904, Project 5710, Program Element 7.60.06.01.5, and Stanford Research Institute's Project 4427. Lt William R. Graham and Lt Donald R. Marston, WLRP, were the Air Force's program monitors. This effort was partially funded by the Laboratory Director's Funds.

The authors would like to acknowledge the assistance of others who have contributed to the success of this program. Great credit is due L. E. Orsak, who designed the CW transmitter and all of the receiving systems used in the measurement program. The measurements in the field were carried out by A. W. Fuller, J A. Martin, C. W. Shell, and C. M. Code. A. R. Bemis of USAEL also assisted in the measurement program. Mr. Martin and H. W. Parker also assisted in the data analysis and evaluation. The authors are also grateful to Drs. J. E. Nanevicz and W. E. Blair for the many fruitful discussions of the technical aspects of the program.

The authors acknowledge the considerable assistance given this research program by the entire Electromagnetic Pulse group at AFWL.

This report has been reviewed and is approved.

Donald R. Marston

DONALD R. MARSTON
1Lt USAF
Project Officer

Clyde C. Reynolds

CLYDE C. REYNOLDS
Lt Colonel USAF
Chief, Physics Branch

William H. Stephens

WILLIAM H. STEPHENS
Colonel USAF
Chief, Research Division

ABSTRACT

The first purpose of this report is to establish the electromagnetic properties of a land area containing numerous buried wires, cables, and other subterranean structures by measuring the deviations produced by these structures in the electric and magnetic fields from an electric monopole antenna of known characteristics. The second purpose of this report is to determine the currents induced in the buried conductors and to establish a practical method of predicting these currents for conductors near the surface of the earth. The portable system utilized in the experimental work is designed to perform the necessary field mapping (both CW and impulse) in the 0.5- to 510-kc frequency range. This system is described and evaluated. Field mapping accuracy is demonstrated to be 5 percent for magnitude, 5 degrees for phase relative to local vertical electric field, and 1 degree for the spatial orientation of the fields. A cable current theory based on a transmission line model is developed for isolated or widely separated cables. This theory and Wait's wave impedance theory for currents induced in closely spaced cables are experimentally confirmed by measurements of currents induced in conductors on or near the surface of the earth. For pulse field and current calculations, the transfer functions from the transmitter to the receiving location are obtained using a computer program for Fourier transforms.

This page intentionally left blank.

CONTENTS

I INTRODUCTION 1
A. Purpose 1
B. Approach 2

II ELECTRIC AND MAGNETIC FIELDS ABOUT A MONOPOLE ANTENNA 7
A. General 7
B. Vertical Electric and Azimuthal Magnetic Fields 9
C. Radial Electric Field 10
D. Calculation of Antenna Effective Height, h_e 11
E. Field Equations 13
F. Calculation of Antenna Capacitance, C_a 13
G. Polarization of the Radiation Electric Field Components 14

III CABLE CURRENT THEORY 21
A. General 21
B. Equations for Transmission Line 23
C. Wire Current from Wait's Theory 25
D. Impedence and Admittance of the Conductor 27
E. Summary 33

IV INSTRUMENTATION 35
A. General 35
B. CW Transmitter 35
C. CW Receivers 40
1. General 40
2. Magnetic (Loop) Antenna Receiver 40
3. Electric (Plate) Antenna Receiver 43
4. Cable-Current Receiver 43
D. Pulse Transmitter 44
E. Pulse Receivers 46

V SYSTEM OPERATION AND CALIBRATION 49
A. General 49
B. CW Transmitting System 49
C. Voltmeters 51
D. CW Receiving Systems 52
1. Operating Procedure 52
2. Electric Field Sensor (Plate) 58
3. Magnetic Field Sensor (Loop) 59
4. Current Sensors 60
E. CW System Performance 63

VI WIRE-CURRENT MEASUREMENTS ON THE SURFACE 67
A. General 67
B. Radial Insulated Wire with Ends Floating 68
C. 100-Foot-Diameter Loop 78
D. Summary 81

VII WIRE CURRENTS MEASUREMENTS BELOW THE SURFACE 83
A. General 83
B. Bare 10-Gauge Copper Wire (Cable Z) 83
C. Insulated Cable (Cable N) 87
D. Conducting Sheath Cable (Cable L) 98
E. Lead Sheath Cable (Cable A) 101
F. Pie-Shaped Loop 111
G. 100-Foot Diameter Loop 118
H. 100-Foot Diameter Loop with Guard Ring 120
I. Aluminum Sheath Arcs (Cables T_1 and T_2) 125
J. Summary 127

VIII FIELD MEASUREMENTS NEAR CABLES AND BUNKERS 135
A. General 135
B. Bare 10-Gauge Copper Wire (Cable Z) 136
C. Conducting Sheath Cable (Cable L) 145
D. Pie-Shaped Loop 147
E. Bunkers 5.601 and 519.03 160
F. Summary 176

IX PULSE MEASUREMENTS 179
A. General 179
B. Data Processing 180
C. Currents in Buried Radial Cables 190
D. Currents in Pie-Shaped Loop 198
E. Electric and Magnetic Fields 198
F. Comments on Pulse Measurements 205

X SUMMARY AND CONCLUSIONS 211

APPENDIX A SOLUTION TO THE CABLE-CURRENT EQUATION 215

APPENDIX B EQUIPMENT SCHEMATICS 227

APPENDIX C TABULATED CW DATA 249

APPENDIX D FOURIER TRANSFORM 265

REFERENCES 271

ILLUSTRATIONS

Fig. 1	Location of Transmitter for Evaluation Tests	3
Fig. 2	Cable and Bunker Test Area	5
Fig. 3	Transmitter and Antenna System	8
Fig. 4	Polarization Ellipse for E Field ($\alpha = -3\pi/4$)	15
Fig. 5	Polarization Ellipse as Function of kr	17
Fig. 6	Transmission Line Model of Radial Conductor	22
Fig. 7	Round Conductor Immersed in Conducting Soil	28
Fig. 8	Idealized Conductor Configurations for Estimating Line Parameters	32
Fig. 9	CW Transmitter Block Diagram	36
Fig. 10	CW Transmitter Loading Coil	38
Fig. 11	Transmitting Antenna Base	39
Fig. 12	CW Receiver Block Diagram	41
Fig. 13	Pulse Transmitter	45
Fig. 14	Pulse Receiver Block Diagram	47
Fig. 15	CW Receiving System	53
Fig. 16	E- and H-Field Measurement Setup	54
Fig. 17	E- and H-Field Sensor-Receiver Orientations	55
Fig. 18	Response of Current Sensors to Transmitter Fields	62
Fig. 19	System Performance E Field	64
Fig. 20	System Performance H Field	65

Fig. 21 Measured Magnitude of Current Induced in 10-Gauge Insulated Wire 69

Fig. 22 Measured Phase of Current Induced in 10-Gauge Insulated Wire 70

Fig. 23 Polar Plot of Current Measured at Center of Wire as Wire Length is Varied (f = 62 kc) 72

Fig. 24 Induced Current Measured at 62 kc for Resonant Length and 2500-Foot Length 73

Fig. 25 Computed Magnitude of Current Induced in 10-Gauge Insulated Wire 74

Fig. 26 Computed Phase of Current Induced in 10-Gauge Insulated Wire 75

Fig. 27 Polar Plot of Current in 10-Gauge Insulated Wire at 510 kc 77

Fig. 28 Measured Magnitude of Current in 100-Foot-Diameter Loop . . 79

Fig. 29 Measured Magnitude of Current in Bare 10-Gauge Copper Wire 84

Fig. 30 Measured Phase of Current in Bare 10-Gauge Copper Wire 85

Fig. 31 Characteristic Impedance and Propagation Factor for Buried, Bare 10-Gauge Copper Wire 86

Fig. 32 Computed Magnitude of Current in Bare 10-Gauge Copper Wire 88

Fig. 33 Computed Phase (Relative to Antenna Voltage) of Current in Bare 10-Gauge Copper Wire 89

Fig. 34 Computed Phase of Current in Bare 10-Gauge Copper Wire 90

Fig. 35 Measured Magnitude of Current in Insulated Cable 91

Fig. 36 Measured Phase of Current in Insulated Cable 93

Fig. 37 Characteristic Impedance and Propagation Factor for Insulated Cable 94

Fig. 38 Computed Magnitude of Current in Insulated Cable 95

Fig. 39 Computed Phase of Current in Insulated Cable 96

Fig. 40 Measured Magnitude of Current in Conducting Sheath Cable . . 99

Fig. 41 Measured Phase of Current in Conducting Sheath Cable 100

Fig. 42 Measured Magnitude of Current in Lead Sheath Cable 102

Fig. 43 Measured Phase of Current in Lead Sheath Cable 103

Fig. 44 Characteristic Impedance and Propagation Factor for Lead Sheath Cable 104

Fig. 45 Computed Magnitude of Lead Sheath Current Using Transmission Line Theory 105

Fig. 46 Computed Phase of Lead Sheath Current Using Transmission Line Theory 106

Fig. 47 Computed Magnitude of Current in Lead Sheath or Conducting Sheath Cable Using Wait's Theory and Transmission Line Theory 109

Fig. 48 Measured Magnitude of Shield Current in Pie-Shaped Loop . . 113

Fig. 49 Measured Phase of Shield Current in Pie-Shaped Loop 114

Fig. 50 Measured Magnitude of Core-Wire Current in Pie-Shaped Loop 115

Fig. 51 Measured Phase of Core-Wire Current in Pie-Shaped Loop . . 116

Fig. 52 Measured Magnitude of Current in 100-Foot-Diameter Loop . . 119

Fig. 53 Measured Phase of Current in 100-Foot-Diameter Loop 120

Fig. 54 Measured Magnitude of Current in 100-Foot-Diameter Loop with Guard Ring (Total Current) 121

Fig. 55 Measured Magnitude of Current in 100-Foot-Diameter Loop with Guard Ring (12-Gauge Wire Only) 122

Fig. 56 Measured Magnitude of Current in 100-Foot-Diameter Loop with Guard Ring (4/0-Gauge Wire Only) 123

Fig. 57 Measured Phase of Current in 100-Foot-Diameter Loop with Guard Ring (Total Current) 125

Fig. 58 Measured Phase of Current in 100-Foot-Diameter Loop with Guard Ring (12-Gauge Wire Only) 126

Fig. 59 Measured Phase of Current in 100-Foot-Diameter Loop with Guard Ring (4/0-Gauge Wire Only) 127

Fig. 60 Measured Magnitude of Current in Arc 500 Feet from Transmitter 128

Fig. 61 Measured Phase of Current in Arc 500 Feet from Transmitter 129

Fig. 62 Measured Magnitude of Current in Arc 2000 Feet from Transmitter 130

Fig. 63 Measured Phase of Current in Arc 2000 Feet from Transmitter 131

Fig. 64 H_ϕ Magnitude Near 10-Gauge Copper Wire at 1760 Feet 137

Fig. 65 H_ϕ Phase Near 10-Gauge Copper Wire at 1760 Feet 138

Fig. 66 H_θ Null Magnitude Near 10-Gauge Copper Wire at 1760 Feet . . 139

Fig. 67 H_r Null Magnitude Near 10-Gauge Copper Wire at 1760 Feet . . 140

Fig. 68 H Tilt and H Yaw Near 10-Gauge Copper Wire at 1760 Feet . . 142

Fig. 69 H Tilt and H Yaw Near 10-Gauge Copper Wire at 1760 Feet . . 143

Fig. 70 H_ϕ and H_I Magnitudes 10 Feet from 10-Gauge Copper Wire . . . 144

Fig. 71 H_ϕ Magnitude Near Conducting Sheath Cable at 2030 Feet 146

Fig. 72 H_ϕ Phase Near Conducting Sheath Cable at 2030 Feet 147

Fig. 73 H_θ Null Magnitude Near Conducting Sheath Cable at 2030 Feet 148

Fig. 74 H_r Null Magnitude Near Conducting Sheath Cable at 2030 Feet 149

Fig. 75 H Tilt and H Yaw Near Conducting Sheath Cable at 2030 Feet 150

Fig. 76 H Tilt and H Yaw Near Conducting Sheath Cable at 2030 Feet 151

Fig. 77 H_ϕ and H_I Magnitudes 10-Feet from Conducting Sheath Cable 152

Fig. 78 H_ϕ Magnitude in Pie-Shaped Loop 154

Fig. 79 H_θ Null and H_r Null Magnitude in Pie-Shaped Loop 155

Fig. 80 H Tilt in Pie-Shaped Loop 156

Fig. 81 E_θ Magnitude in Pie-Shaped Loop 158

Fig. 82 E_r Null and E_ϕ Null Magnitude in Pie-Shaped Loop 159

Fig. 83 E Pitch in Pie-Shaped Loop 160

Fig. 84 Bunker 5.601 Plan View 161

Fig. 85 Bunker 519.03 Plan View 162

Fig. 86 H_ϕ Magnitude Near Bunkers 164

Fig. 87 H Tilt Near Bunker 5.601 165

Fig. 88 H Yaw Near Bunker 5.601 166

Fig. 89 H Tilt and H Yaw Near Bunker 519.03 168

Fig. 90 E_θ Magnitude Near Bunkers 169

Fig. 91 E_r Null Magnitude Near Bunkers 171

Fig. 92 E Pitch and E Tilt Near Bunker 5.601 172

Fig. 93 E Pitch Near Bunker 519.03 173

Fig. 94 E Tilt Near Bunker 519.03 175

Fig. 95 Pulse Recordings with Calibrations 181

Fig. 96 Fourier Transform Processing Error 183

Fig. 97 Transmitted Pulse Time Waveform and Frequency Spectrum .. 185

Fig. 98 Comparison of 100-kc and 500-kc Processed Time Waveforms 187

Fig. 99 Comparison of 100-kc and 500-kc Processed Frequency Spectrums 188

Fig. 100 Pulse Wire Current at 1000 Feet in Bare 10-Gauge Copper Wire 191

Fig. 101 Pulse Wire Current at 1750 Feet in Bare 10-Gauge Copper Wire 192

Fig. 102 Pulse Wire Current at 3000 Feet in Bare 10-Gauge Copper Wire 193

Fig. 103 Pulse Current at 1050 Feet in Conducting Sheath Cable 195

Fig. 104 Pulse Current at 2050 Feet in Conducting Sheath Cable 196

Fig. 105 Pulse Current at 3050 Feet in Conducting Sheath Cable 197

Fig. 106 Pulse Sheath Current in Outer Arc of Pie-Shaped Loop (Bunker 523.08) 199

Fig. 107 Pulse Core Current in Outer Arc of Pie-Shaped Loop (Bunker 523.08) 200

Fig. 108 E_θ at 1600 Feet 202

Fig. 109 H_ϕ at 1600 Feet 203

Fig. 110 Predicted E_θ and H_ϕ at 1600 Feet 204

Fig. 111 E_θ Over Bunker 519.03 206

Fig. 112 H_ϕ Over Bunker 519.03 207

Fig. 113 E_θ Over Bare 10-Gauge Copper Wire at 1740 Feet 208

Fig. 114 H_ϕ Over Bare 10-Gauge Copper Wire at 1740 Feet 209

Fig. B-1 Switchable Frequency Oscillator Schematic 230

Fig. B-2 CW Transmitter Power Amplifier Schematic 231

Fig. B-3 Matching Transformers and Antenna Current Monitor Schematic 232

Fig. B-4 Antenna Voltage Monitor Schematic 233

Fig. B-5 CW Transmitter Power Supply Schematic 234

Fig. B-6 Plate Matching Network Schematic 235

Fig. B-7 Loop Matching Network Schematic 236

Fig. B-8 Mo-Permalloy Current Sensor Schematic 237

Fig. B-9 Ferrite Current Sensor Schematic 238

Fig. B-10 Wide-Band Preamplifier Schematic 239

Fig. B-11 Switchable Frequency Receiver Schematic 240

Fig. B-12 Phase Reference Receiver Schematic 241

Fig. B-13 Quadrature Signal Generator Schematic 242

Fig. B-14 Calibration Oscillator Schematic 243

Fig. B-15 Pulse Transmitter Schematic 244

Fig. B-16 Plate Matching Unit (Pulse) Schematic 245

Fig. B-17 Plate Amplifier (Pulse) Schematic 246

Fig. B-18 Loop Receiver (Pulse) Schematic 247

Fig. B-19 Current Receiver (Pulse) Schematic 248

TABLES

Table I CW Transmitter Parameters 51

Table II Sensor Parameters 58

Table III Properties of Bare Cables 105

Table IV Pulse Systems Inverse Frequency Response 184

Table C-1 Induced Current in 10-Gauge Insulated Wire 252

Table C-2 Induced Current at 62 kc in Resonant-Length 10-Gauge Insulated Wire 253

Table C-3 Induced Current in 100-Foot-Diameter Loop 254

Table C-4 Induced Current in Bare 10-Gauge Copper Wire (Cable Z) 255

Table C-5 Induced Current in Insulated Cable N 256

Table C-6 Induced Current in Conducting Sheath Cable L 257

Table C-7 Induced Current in Lead Sheath Cable A 258

Table C-8 Induced Shield Current in Pie-Shaped Loop 259

Table C-9 Induced Core Current in Pie-Shaped Loop 260

Table C-10 Induced Current in 12-Gauge 100-Foot-Diameter Loop 261

Table C-11 Induced Current in Guarded 100-Foot-Diameter Loops 262

Table C-12 Induced Current in Arc of Aluminum Sheath Cable 263

This page intentionally left blank.

I
INTRODUCTION

A. Purpose

Accurate measurement of electromagnetic fields may be used to deduce some characteristics of the source of the fields if the electromagnetic properties of the region of space containing the source and the field measurement site are known. Conversely, if the characteristics of the source of the electromagnetic fields are known, accurate measurements of the electromagnetic fields may be used to deduce some of the characteristics of the region of space about the source. In a practical experiment in which unknown source characteristics are to be determined by measuring fields about the source, it is necessary to establish, either experimentally or by construction, the characteristics of the region. One purpose of the research described in this report was to establish the electromagnetic properties of a land area containing numerous buried wires, cables, and other structures and subterranean geological properties by measuring the electric and magnetic fields produced at points in the area by an electric monopole antenna of known characteristics. A second purpose of this research program was to determine the currents induced in the buried conductors and to establish a practical method of analysis applicable to buried conductors near the surface of the ground.

For radiated electromagnetic fields in free space, the electric and magnetic components are assumed to be orthogonal and related in magnitude by the free-space impedance. The presence of the earth, which may not be homogeneous, can alter the field structure. Thus, to make measurements that can lead to an understanding of the cause for a particular electromagnetic field structure, all possible field parameters should be independently measured. For electromagnetic waves these parameters are the magnitude and phase of all components of the electric and magnetic fields. Electric fields must be

measured with electric field sensors and magnetic fields must be measured with magnetic field sensors. For this research effort, measurements were to be made over an area to determine if inhomogenities, both known and unknown below the earth's surface, could cause the electromagnetic fields in the vicinity of a vertical radiator to differ appreciably from the fields computed assuming a homogeneous earth.

B. Approach

The frequency range of interest was limited to 0.5 to 510 kc. To generate the electromagnetic field in this frequency range an easily transportable low-power switchable frequency transmitter operating at a continuous frequency of 0.5, 1, 2, 5, 10, 20.6, 62, 100, 200, 450, or 510 kc was constructed to drive a 100-foot tower. Special narrow-band battery-powered receivers and electromagnetic field sensors were constructed to measure individual wave component magnitude and phase and component spatial orientation. For example, the major magnetic field near the transmitter is predicted to be azimuthal and counterclockwise about the radiating antenna. (See Sec. II). The magnetic field receiving system was designed to determine the magnitude and phase of this magnetic field and its orientation in space. The equipment, described in Sec. IV and Appendix B, was designed so that electromagnetic fields could be mapped out to about 2 km.

Field distortions that may exist due to earth inhomogenities are not expected to be large. Thus, very precise measurements are desirable. Design goals were signal magnitude accuracy to better than 5 percent (0.4 db), phase accuracy to 5 degrees, and field orientation accuracy to 1 degree. These goals were essentially attained by careful equipment design and considerable testing of the entire system. This testing took place in an area (shown in Fig. 1) that was free of known man-made structures. The ground conductivity in the testing area was measured to a depth of 2000 feet. Fifty-two measurement locations about the transmitter tower were surveyed and marked. Measurements were made at these locations about the transmitter to develop operating procedures and an understanding of the measurements systems. This procedure required some 1700 individual measurements and is described

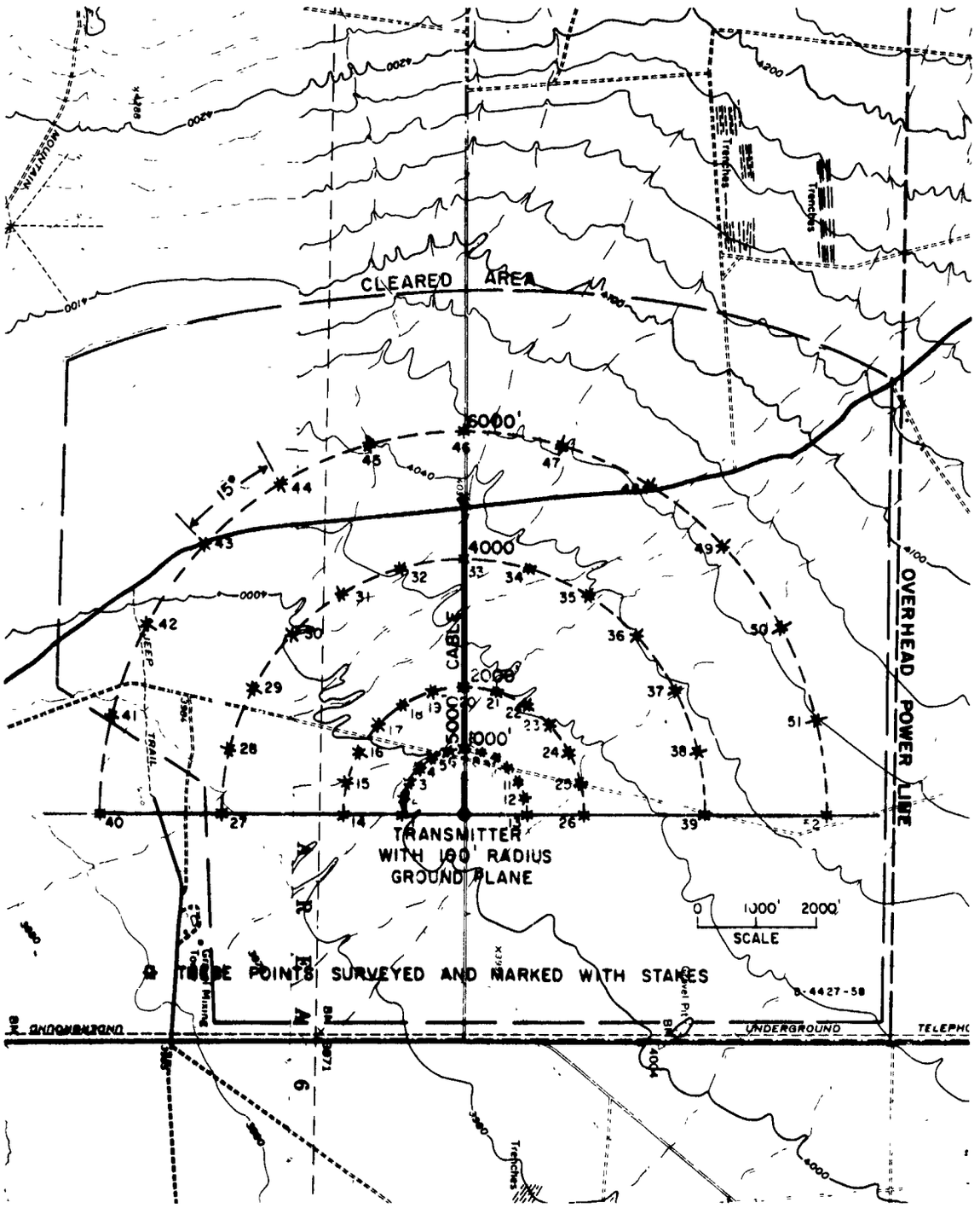

FIG. 1 LOCATION OF TRANSMITTER FOR EVALUATION TESTS

in Sec. V. Simple man-made structures were installed in the area shown in Fig. 1, to determine effects and system performance in the vicinity of such structures under relatively controlled conditions. These structures were simple radial and azimuthal cables and circular loops on the surface. Equipment to measure the currents in such structures was designed and evaluated. The results of these measurements (presented in Sec. VI) formed the experimental test of the analytical expression for induced cable currents.

Upon completion of the evaluation tests, the entire system was moved to the area shown in Fig. 2. This area contained many buried cables and bunkers. Cables were located on one side of the transmitter and no cables were located on the opposite side of the transmitter. As was done for the test area, ground conductivity was measured to a depth of 2000 feet. Electric and magnetic field measurements above the surface and cable current measurements below the surface were made at the locations shown in Fig. 2. Sections VII and VIII present the results of these measurements.

Upon completion of the CW measurements outlined above, the system was modified to transmit and record a transient pulse at selected locations. The transmitted pulse spectrum was peaked at about 12 kc. The pulse system gave continuous spectrum data that was compared with the CW data obtained at fixed frequencies, and gave directly the pulse waveforms that were received on the various cables for an impinging transmitted pulse. Section IX presents the pulse data.

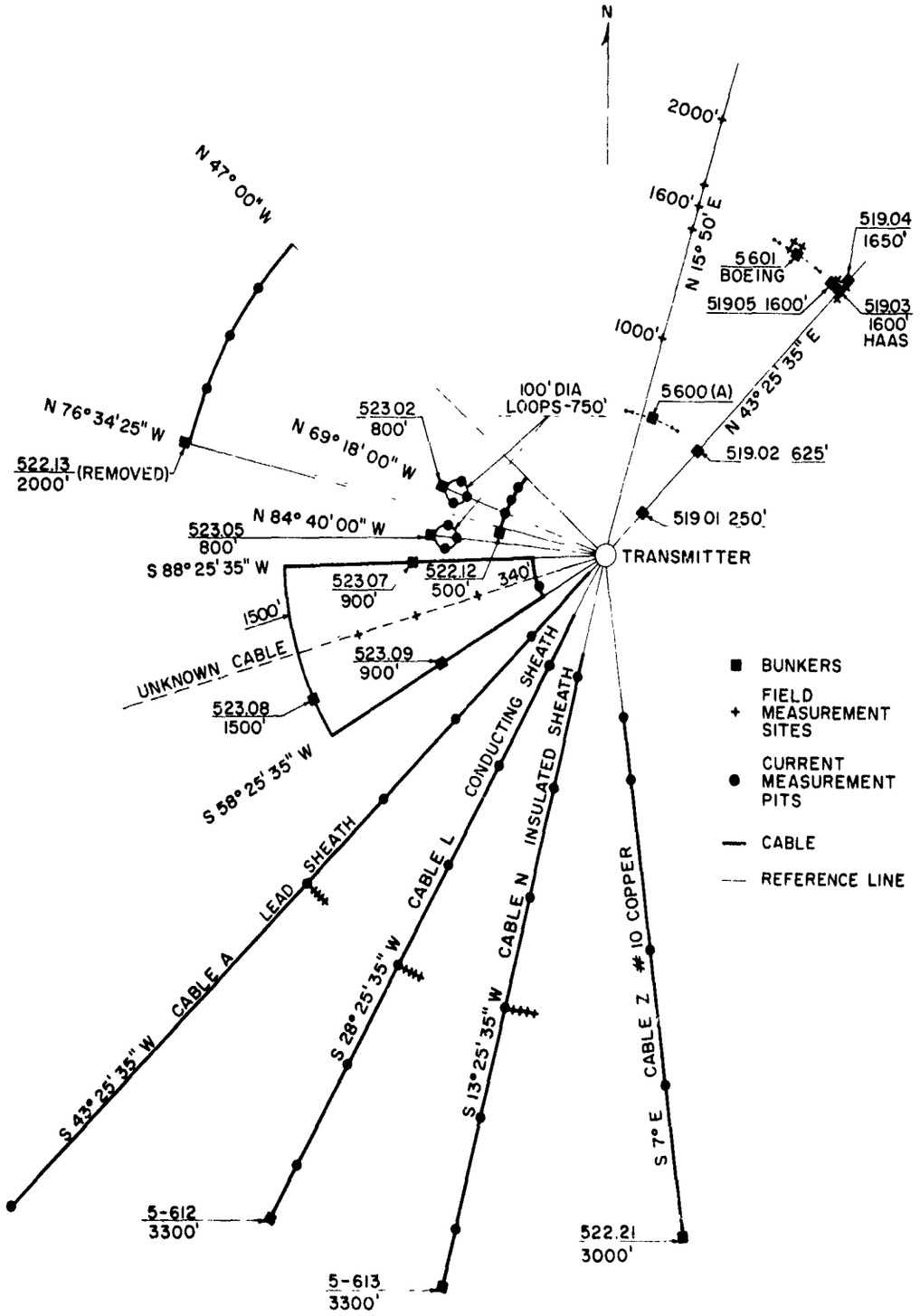

FIG. 2 CABLE AND BUNKER TEST AREA

This page intentionally left blank.

II

ELECTRIC AND MAGNETIC FIELDS ABOUT A MONOPOLE ANTENNA

A. General

The monopole antenna described in this section is a 100-foot-high tower installed over relatively dry earth (with soil conductivity between 4×10^{-3} and 2×10^{-2} mhos/m).[1,2*] This antenna (shown in Fig. 3) is provided with a ground screen consisting of ninteen ground radials of 10-gauge copper wire extending to a radius of 100 feet from the antenna base. At the 100-foot radius, the ground radials are connected to 6-foot copper-clad ground rods driven into the soil.

It is desired to determine the electric and magnetic fields produced at the air/earth interface by such an antenna at various distances from the antenna. For this purpose, the antenna may be considered a point source of radiation with little error, since, in the range of interest, the antenna height is usually less than 10 percent of the horizontal distance to the point where the fields are to be determined. Throughout the range of frequencies of interest, assuming the relative dielectric constant of the soil to be 10,

$$\frac{\sigma}{\omega\epsilon} \approx \frac{4 \times 10^{-3}}{\frac{20\pi}{36\pi} \times 10^{-9} f} = \frac{7.2 \times 10^{6}}{f} \gg 1$$

so that for the purpose of calculating the principal components (i.e., vertical electric and azimuthal magnetic) of the fields, the ground may be treated as a good conductor. To determine the magnitude of the radial electric field, however, it will be necessary to take into account the finite conductivity of the soil. Finally, because the 100-foot transmitting antenna is electrically short

*References are listed at the end of the report.

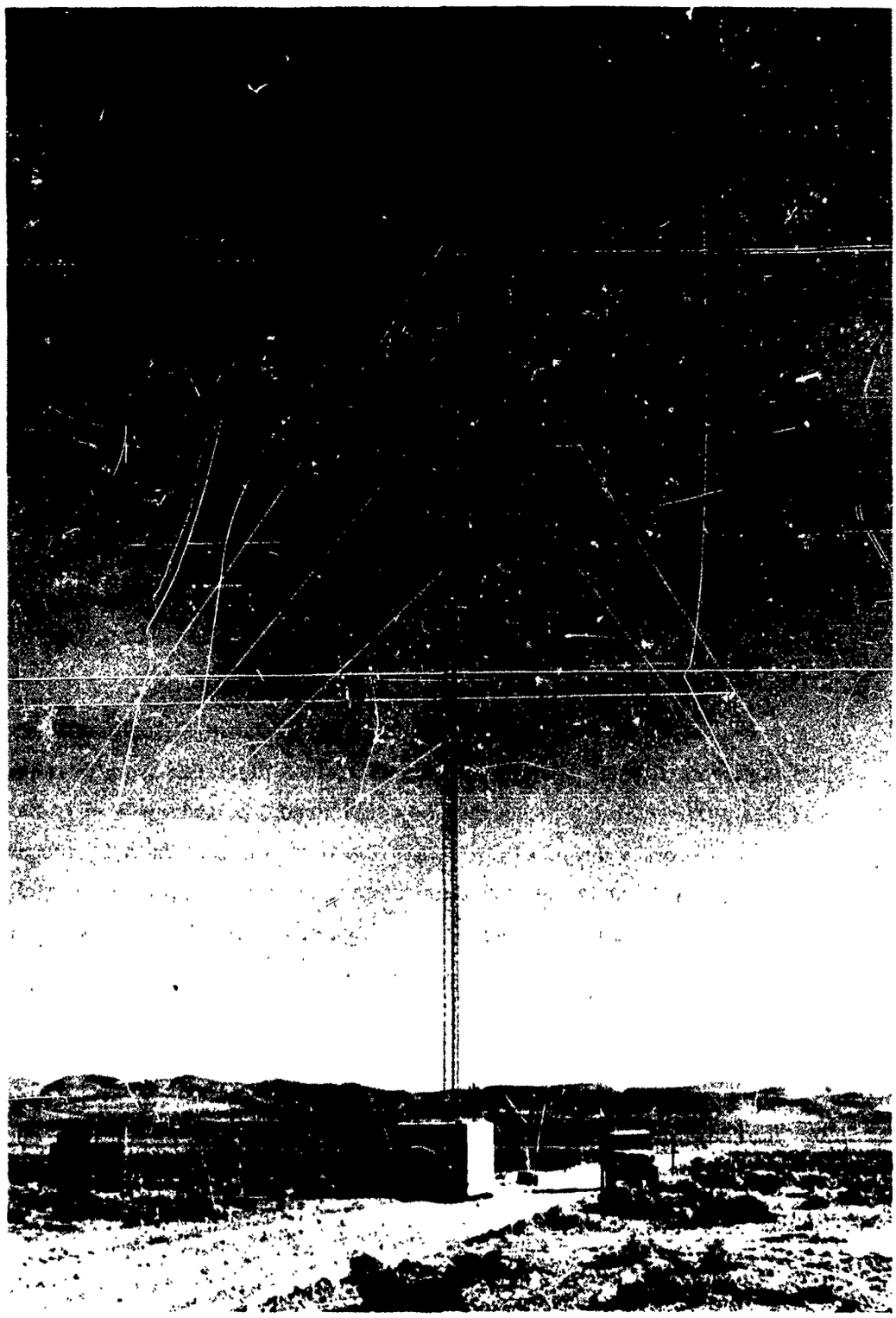

D-4427-166

FIG. 3 TRANSMITTER AND ANTENNA SYSTEM

throughout the frequency range (at 510 kc, the antenna is only 0.052-wavelength high), well known formulas for the fields about short dipoles will be applicable.

B. Vertical Electric and Azimuthal Magnetic Fields*

The vertical electric field, E_θ, and the azimuthal magnetic field, H_ϕ, at a distance r from an electrically short monopole in phasor form, are[3]

$$E_\theta = \frac{I_0 h_e}{2\pi}\left[\frac{j\omega\mu_0}{r} + \frac{1}{j\omega\epsilon_0 r^3} + \frac{\eta_0}{r^2}\right] e^{-jkr} \sin\theta \qquad (1)$$

$$H_\phi = \frac{I_0 h_e}{2\pi}\left[\frac{jk}{r} + \frac{1}{r^2}\right] e^{-jkr} \sin\theta \qquad (2)$$

where

I_0 = Base current in amperes (with the factor $e^{j\omega t}$ omitted)

h_e = Effective height of monopole in meters

ω = $2\pi f$, the signal radian frequency

μ_0 = $4\pi \times 10^{-7}$, the permeability of free space

ϵ_0 = $(36\pi \times 10^9)^{-1}$, the permittivity of free space

k = $\omega\sqrt{\mu_0 \epsilon_0}$, the phase constant

η_0 = $\sqrt{\mu_0/\epsilon_0}$, the intrinsic impedance of free space

j = $\sqrt{-1}$

and r, θ, and ϕ are the spherical coordinates with the origin at the antenna base, and the axis of the antenna is the $\theta = 0$ line.

*Unrationalized MKS units are used throughout this report.

Since the input impedance of the antenna is almost entirely capacitive reactance, the input current can be replaced by

$$I_0 \approx j\omega C_a V_a$$

where C_a is the antenna input capacitance (exclusive of the stray capacitance of the base of the antenna), and V_a is the antenna driving voltage.

In relation to the voltage applied to the antenna terminals, therefore, the field strengths at a distance r from the transmitter are

$$\frac{E_\theta}{V_a} = \frac{h_e C_a}{2\pi}\left\{\left[-\frac{\omega^2\mu_0}{r} + \frac{1}{\epsilon_0 r^3}\right] + j\frac{\omega\eta_0}{r^2}\right\} e^{-jkr} \tag{3}$$

$$\frac{H_\phi}{V_a} = \frac{h_e C_a}{2\pi}\left\{\frac{-k\omega}{r} + j\frac{\omega}{r^2}\right\} e^{-jkr} \tag{4}$$

at the air/earth interface ($\theta = \pi/2$) when $r \gg h_e$.

C. Radial Electric Field

The radial electric field strength at the surface of a ground of finite conductivity can be computed from the radial earth current and the surface impedance per unit radial length of the earth. The radial current is directly related to the azimuthal magnetic field by

$$I_r = -2\pi r H_\phi$$

and the impedance per unit length in the radial direction is readily obtainable from the theory of the surface impedance of skin effect:

$$Z_r = \frac{1 + j}{2\pi r \sigma \delta}$$

where σ is the soil conductivity and δ is the skin depth defined by

$$\delta = \frac{1}{\sqrt{\pi f \mu \sigma}} \quad ;$$

The radial electric-field strength at the interface is thus

$$E_r = I_r Z_r$$

$$= - \frac{(1 + j)}{\sigma \delta} H_\phi$$

or

$$\frac{E_r}{V_a} = - (1 + j) \left(\frac{\pi f \mu_0}{\sigma} \right)^{1/2} \frac{H_\phi}{V_a} \quad . \tag{5}$$

Thus, the radial electric field lags the azimuthal magnetic field by 135 degrees in phase and differs in magnitude by a factor involving the square root of the frequency.

D. Calculation of Antenna Effective Height, h_e

The electric field components E_θ, E_r, and H_ϕ derived in Secs. II-B and II-C are those measured near the ground at a distance r from an electrically short transmitting antenna. If the antenna internal resistance and radiation resistance are neglected, the transmitting antenna moment is specified by applied voltage, V_a, effective height, h_e, and input capacitance, C_a.

The effective height for the monopole is defined[4] as follows:

$$h_e = \frac{1}{I_0}\int_0^h I(z)\,dz \tag{6}$$

where I_0 is the current at the base, $I(z)$ is current distribution along the antenna, and h is the antenna length. It is assumed in the model that the earth can be approximated to be a perfect conductor for the purpose of using a perfect image and hence using an antenna current distribution symmetrical about the ground $(z = 0)$. This is a reasonable assumption for frequencies of concern here.

The current distribution of a monopole of length h and effective radius a_e has been thoroughly investigated by Hallén, King, and Harrison; and the analysis is discussed by Kraus.[5] For an electrically short antenna, the current distribution is the following:

$$I(z) = I_0 \frac{\sin k\,(h - |z|)}{kh \cos kh} . \tag{7}$$

Substituting Eq. (7) into Eq. (6) and integrating gives the following expression for effective height:

$$h_e = \frac{h(1 - \cos kh)}{(kh)^2 \cos kh} . \tag{8}$$

For the case of the electrically short antenna, $kh \ll 1$, therefore Eq. (8) can be expanded to give the following approximation:

$$h_e \approx \frac{h}{2}\left[1 + \frac{5}{12}(kh)^2\right] , \quad kh \ll 1 . \tag{9}$$

At zero frequency, $h_e = h/2$, which is the effective height of a very short monopole.

E. Field Equations

Equation (8) can be combined with Eqs. (3), (4), and (5) to give the field components around a short vertical monopole in the 0.5-to-510-kc frequency range. These components are

$$\frac{E_\theta}{V_a} = \frac{C_a}{2\pi\epsilon_o r^3}\left[\frac{h(1 - \cos kh)}{(kh)^2 \cos kh}\right]\left[1 + jkr - (kr)^2\right] \tag{10}$$

$$\frac{H_\phi}{V_a} = \frac{j\omega C_a}{2\pi r^2}\left[\frac{h(1 - \cos kh)}{(kh)^2 \cos kh}\right]\left[1 + jkr\right] \tag{11}$$

for $r \gg h$, and

$$\frac{E_r}{V_a} = -(1 + j)\left(\frac{\pi f \mu_0}{\sigma}\right)^{1/2} \frac{H_\phi}{V_a} \tag{12}$$

for $r \gg h$, and $r \gg \delta$.

F. Calculation of Antenna Capacitance, C_a.

The antenna input capacitance of the electrically short monopole has been thoroughly investigated and is discussed by Schelkunoff.[6] For a cylindrical antenna the capacitance is given as

$$C_a = \frac{2\pi\epsilon h}{\ln(h/a_e) - 1} \tag{13}$$

where a_e is the cylindrical antenna radius or the equivalent radius of an antenna whose cross section is noncircular. The antenna cross section used in this case is an equilateral triangle. According to Lo,[7] the radius of an equivalent cylindrical antenna is

$$a_e = 0.4214 s \tag{14}$$

where s is the length of one side of the triangular cross section.

G. Polarization of the Radiation Electric Field Components

The total electric field at any point of observation around the electrically short vertical transmitting antenna is described by the two space orthogonal electric field components E_θ and E_r. The received electrical signal at any specific distance from the transmitting antenna is the spacial vector sum of these two field components. The instantaneous values of E_θ and E_r, using standard phasor notation are given as follows:

$$e_\theta(t) = |E_\theta| \cos \omega t \tag{15a}$$

$$e_r(t) = |E_r| \cos(\omega t + \alpha) \tag{15b}$$

where α is the time phase difference of $e_r(t)$ with respect to $e_\theta(t)$. Equation (15) generally describes an electric field phasor that is elliptically polarized in the E_θ, E_r plane. The general spatial configuration for this ellipse, shown in Fig. 4, is simply described by the following expression:[8]

$$\tan 2\tau = \frac{2\rho \cos \alpha}{1 - \rho^2} \tag{16}$$

where $\rho = |E_r|/|E_\theta|$, normally a number $< 10^{-2}$ for the case here, and τ is the space "tilt" angle of the ellipse and is the spatial angle between E_θ and the major axis, and also between E_r and the minor axis. Equation (16) is obtained by rotating the E_θ, E_r coordinates into E_1, E_2, which are the major and minor ellipse axes respectively (see Fig. 4). Since both E_1, E_2 and E_r, E_θ are pairs of orthogonal coordinates, the amount of rotation is given by the space angle of rotation, τ. The rotating phasor, e(t), whose tip describes the ellipse, is calculated from Eq. (15). An arbitrary orientation e(t), at a space angle ξ, can be written as follows:

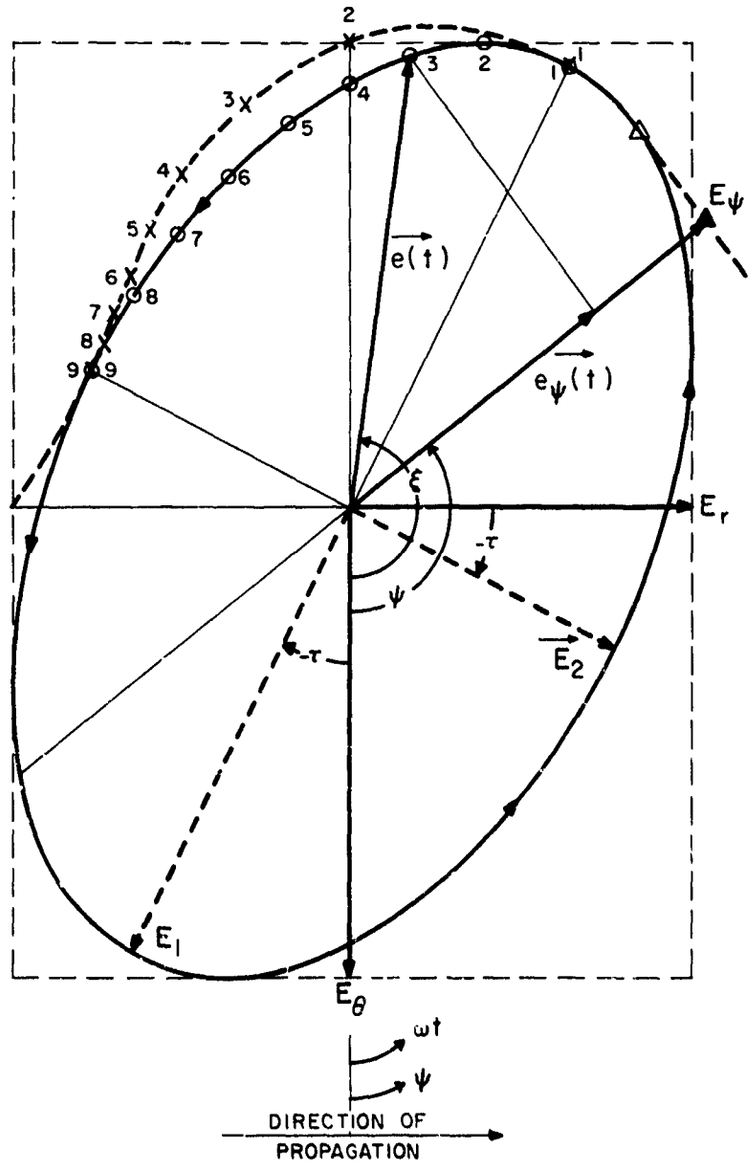

FIG. 4 POLARIZATION ELLIPSE FOR E FIELD ($\tau = -3\pi/4$)

$$\xi = \tan^{-1}(e_r/e_\theta) = \tan^{-1}\left[\rho(\cos\alpha - \sin\alpha \tan\omega t)\right] \tag{17}$$

so that the angular velocity, of e(t) is:

$$\frac{d\xi}{dt} = -\frac{\omega\rho\sin\alpha}{\cos^2\omega t + \rho^2\cos^2(\omega t + \alpha)} . \tag{18}$$

The angular velocity of e(t) is not generally constant. (It is constant only for circular polarization, $\rho = 1$ and $\alpha = \pi/2$.)

Examination of the electric fields defined by Eqs. (10) and (12) shows that the time angle, α , varies from $-\pi/4$ (near zone) to $-3\pi/4$ (far zone), as shown in Fig. 5(a). As indicated in Eq. (16), the polarization ellipse tilt angle, τ , tilts backward for $\alpha > -\pi/2$, is vertical for $\alpha = -\pi/2$, and tilts forward for $\alpha < -\pi/2$ [shown in Fig. 5(b)] . This implies that the field minimum (null) occurs at a forward angle above the horizontal in the near zone, and below the horizontal in the far zone. For negative α , which includes all situations considered here, Eq. (18) shows that the ellipses are always "backward" polarized – that is, they appear to be "rolling" toward the transmitter. For positive α , the ellipses are "forward" polarized and appear to be rolling away from the transmitter. In all cases, the ellipse must fit inside a rectangle bounded by $\pm|E_\theta|$ and $\pm|E_r|$ (shown in Fig. 4).

The projection of e(t) on any axis at the space angle ψ shown in Fig. 4 is

$$e_\psi(t) = e_\theta(t)\cos\psi + e_r(t)\sin\psi . \tag{19}$$

Equation (19) can be shown to be

$$e_\psi = |E_\psi|\cos(\omega t + \zeta) \tag{20a}$$

where

$$|E_\psi| = |E_\theta|\left(\cos^2\psi + \rho\cos\alpha\sin 2\psi + \rho^2\sin^2\psi\right)^{1/2} \tag{20b}$$

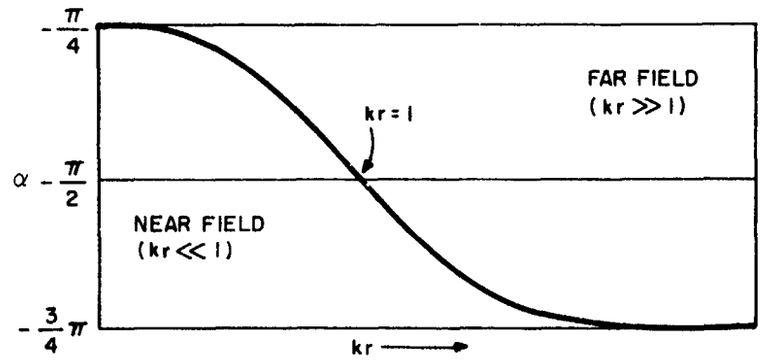

(a) SKETCH OF α FROM NEAR FIELD TO FAR FIELD AS A FUNCTION OF (kr)

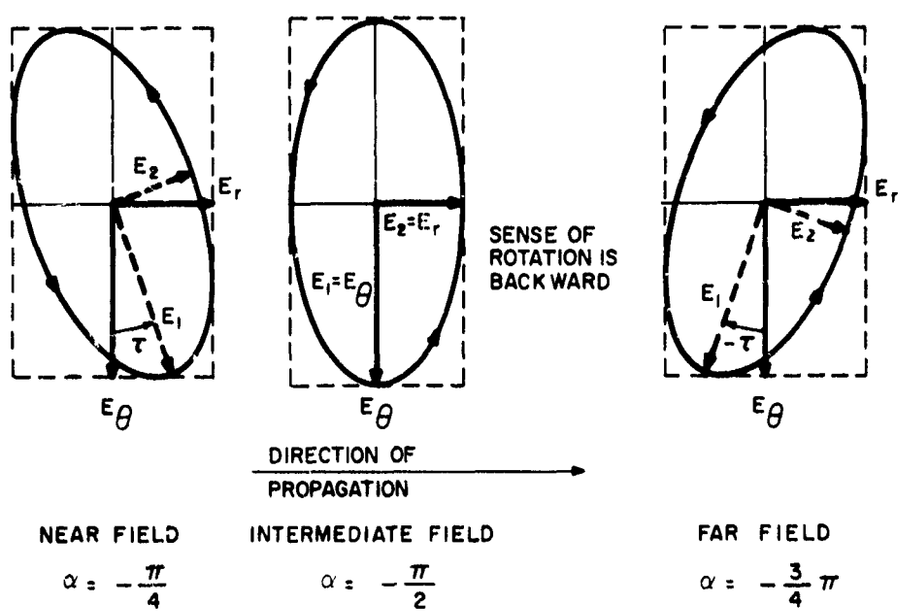

(b) SKETCH OF POLARIZATION ELLIPSES FOR α

FIG. 5 POLARIZATION ELLIPSE AS FUNCTION OF kr

$$\zeta = \tan^{-1}\left(\frac{\rho \sin\alpha \sin\psi}{\cos\psi + \rho\cos\alpha \sin\psi}\right) . \tag{20c}$$

The instantaneous field in the ψ direction, e_ψ, is always a cosinusoidal function of frequency ω and of amplitude $|E_\psi|$ and phase, ζ, both of which are determined by the axis angle, ψ, the original signals E_θ, E_r, and their time phase relation, α.

If the sensor is oriented with its maximum sensitivity in the ψ direction, the peak magnitude and phase of this sensor signal are determined by the tangent to the ellipse which is perpendicular to ψ axis (see Fig. 4). Phase is determined by the point of tangency at the point (Δ) on the ellipse, and magnitude is determined by the intersection ($\blacktriangle$) of the tangent and the ψ axis. Thus, it is seen that the sensor does not always measure the magnitude and phase in the direction of the ψ axis. The sensor does measure the magnitude and phase of $\epsilon(t)$ in the direction of the sensor when the ψ axis is aligned with either the major axis (peak field measurement), and $\psi = \psi_{max} = \psi_1 = \tau$, or with the minor axis (minimum or null field measurement), and $\psi = \psi_{min} = \psi_1 = \pi/2 + \tau$.

In addition, from Eq. (20) it can be seen that for $\psi = \psi_o = 0$, corresponding to vertical sensor orientation, then $|E_{\psi=o}| = |E_\theta|$ and $\zeta_{\psi=o} = 0$. Similarly, for $\psi = \psi_r = \pi/2$, corresponding horizontal antenna orientation, then $|E_{\psi=\pi/2}| = |E_r|$ and $\zeta_{\psi=\pi/2} = \alpha$. Thus, the sensor oriented vertically or horizontally measures exactly E_θ or E_r, respectively, with the proper phase.*

Substituting $\psi_1 = \tau$ into Eq. (20b) gives the E_1 and its time phase with respect to E_θ to be:

$$|E_1| = |E_\theta| \left(\cos^2 \tau + \rho \cos\alpha \sin 2\tau + \rho^2 \sin^2\tau\right)^{1/2} \tag{21a}$$

*This assumes that the sensor response to a signal oriented in the sensor null is identically equal to zero.

$$\zeta_1 = \tan^{-1}\left(\frac{\rho \sin \alpha \sin \tau}{\cos \tau + \rho \cos \alpha \sin \tau}\right). \tag{21b}$$

Substituting $\psi_2 = \pi/2 + \tau$ into Eq. (20b) gives E_2 and its time phase with with respect to E_θ to be:

$$|E_2| = |E_r|\left(\cos^2\tau - \frac{1}{\rho}\cos\alpha \sin 2\tau + \frac{1}{\rho^2}\sin^2\tau\right)^{1/2} \tag{22a}$$

$$\zeta_2 = \tan^{-1}\left(\frac{\rho \sin \alpha \cos \tau}{-\sin \tau + \rho \cos\alpha \cos\tau}\right). \tag{22b}$$

From Eq. (20c), the rate of change of ζ with respect to ψ is

$$\frac{d\zeta}{d\psi} = \frac{\rho \sin \alpha}{\cos^2\psi + \rho \cos\alpha \sin 2\psi + \rho^2 \sin^2\psi} = \left|\frac{E_\theta}{E_\psi}\right|^2 \rho \sin\alpha \tag{23}$$

For $\rho \ll 1$ (the case of interest here) the angle τ is small so that ψ_{max} is near $\psi \approx 0$ and ψ_{min} is near $\psi \approx \pi/2$. Thus

$$\left.\frac{d\zeta}{d\psi}\right|_{\psi \approx \psi_{min}} \approx 1/\rho \sin\alpha \tag{24a}$$

and

$$\left.\frac{d\zeta}{d\psi}\right|_{\psi \approx \psi_{max}} \approx \rho \sin\alpha \quad . \tag{24b}$$

Equation (24) shows that the rate of change of ζ with respect to ψ near ψ_2 gives a relatively rapid change in ζ, whereas a slight change in ψ near ψ_1 gives a relatively slow change in ζ.

The dependence of the magnitude and phase of the sensor field E_ψ is shown in pictorial form in Fig. 4 as ψ is varied from π to $3\pi/2$. The circles (o) correspond to a phase point, ζ, on the ellipse for a particular position of e(t). The corresponding cross (x), with the same number, gives the sensor orientation angle ψ for observing this ζ. It is immediately apparent that the phase is changing most rapidly near the field minimum, since the (x) are more closely spaced for the relatively evenly spaced (o), and that the phase is changing most slowly near the field maximum, since the (x) are more widely spaced for the relatively evenly spaced (o).

It has been shown that for fields that contain more than one spatial component that only certain parameters of this resulting field can be measured. The field described by E_θ and E_r, where $|E_\theta| \gg |E_r|$, is elliptically polarized in θ-r plane. Measurements of E_θ (both magnitude and phase) can be made by orientation of the sensor in the vertical (θ) direction. Orientation of the sensor for minimum output defines the ellipse axis orientation which defines the spatial orientation of the resultant field. The magnitude in this null is not $|E_r|$ but is approximately $|E_r|$. Phase in the null is very sensitive to sensor orientation and is consequently very inaccurate. These parameters (major field magnitude and phase, total field spatial orientation, and limited minor field magnitude are the only measureable parameters that can be made on any electromagnetic field composed of two components where one component is very much larger than the other. For two fields within one order of magnitude of each other, generally, by proper sensor orientation, both fields can be defined.

III
CABLE CURRENT THEORY

A. General

As indicated in Sec. II, a short vertical monopole driven against an infinite, conducting ground plane will produce an azimuthal magnetic field H_ϕ and a vertical electric field E_θ at the surface of the ground plane. If the ground plane is an imperfect conductor such as the surface of the earth, a radial component of electric field will also be produced in the ground as a result of ground currents and ground impedance. Any radially directed conductor in or near the ground will therefore have a current induced in it by the radial electric field. The manner in which the conductor is coupled to the radial electric field in the ground determines the induced current, which is of primary interest in this section.

A conductor lying in or near the ground may be visualized as a two-conductor transmission line with the ground serving as the return conductor. The line will have an impedance per unit length and an admittance per unit length, the same as any other transmission line, and from these a propagation factor and a characteristic impedance can be determined. In the presence of a radial electric field in the ground, the line is driven by a distributed generator. An appropriate transmission line model for the radial conductor under the influence of a radial electric field is shown in Fig. 6. The series impedance Z of the line element is due to the resistance and reactance of the conductor and the ground return, and the admittance Y of the line element is due to the capacitive susceptance between the conductor and ground and to the admittance of the ground itself. The distributed generator voltage per unit length E is the radial electric field strength (or, in the event the wire is not parallel to the radial field strength vector, the component of the radial field along the wire.)

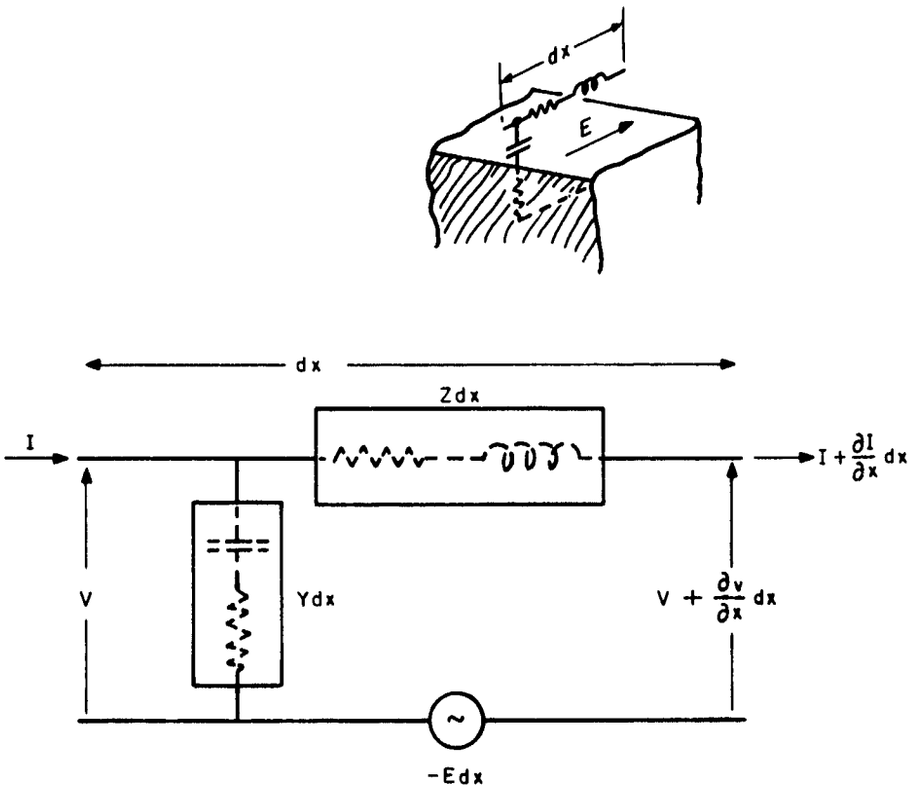

FIG. 6 TRANSMISSION LINE MODEL OF RADIAL CONDUCTOR

This model of the radial conductor is appropriate if the presence of the conductor does not appreciably alter the radial electric field strength in the ground except in the immediate vicinity of the conductor.

At each point along the conductor, a current increment is injected through the admittance Y by the radial electric field. This current combines (with proper regard for phase) with current arriving from farther up the line and propagates down the line in accordance with the propagation characteristics of the conductor/ground transmission line. Because the characteristics of the conductor/ground transmission line are determined in part by the properties of the ground, a wavelength on the line is shorter than a free-space wavelength and the line attenuation may be fairly high. Hence, current on the line does not

propagate with the same phase as the radial electric field (which propagates in accordance with free-space conditions), and an interference between the radial field and the line current occurs. This interference is sometimes complicated by the fact that the line current is attenuated as it propagates, so that currents induced far away (several wavelengths) from a point of interest are so greatly attenuated that they do not appreciably affect the current at the point.

At the ends of the conductor, the current wave is reflected in the same manner as on a conventional transmission line. Hence standing waves are set up on the line. If the line is electrically long, however, the line attenuation may be such that the reflected wave is attenuated to an insignificant value before it has propagated very far from the reflecting end. In this case, the standing wave exists only near the end of the conductor. Far from the end, the standing wave appearance of the current distribution is actually the result of interference between the conductor current propagating down the line and the current injected along the line by the radial electric field.

B. Equations for Transmission Line

To compute the current induced in a conductor under the influence of a radial electric field, the model of the transmission line element shown in Fig. 6 will be solved. From the figure, the rate of change of the line voltage is

$$\frac{dV}{dx} = -IZ - E \tag{25}$$

and the rate of change of the line current is

$$\frac{dI}{dx} = -VY \ . \tag{26}$$

Differentiating Eq. (26) and substituting for dV/dx in Eq. (25), we obtain the differential equation for the line currents:

$$\frac{d^2I}{dx^2} - ZYI = YE \ . \tag{27}$$

The solution of this equation when E is the radial electric field of a vertical monopole antenna is derived in Appendix A, and is:

$$I(x) = K_1 e^{\gamma x} + K_2 e^{-\gamma x} + F(x) \tag{28}$$

where

$$F(x) = -A \left\{ \cosh \gamma(x + a) \log (x + a) + \frac{e^{\gamma(x + a)}}{2} \sum_{n=1}^{\infty} \frac{\left[-(jk + \gamma)(x + a)\right]^n}{n \cdot n!} \right.$$

$$\left. + \frac{e^{-\gamma(x + a)}}{2} \sum_{n=1}^{\infty} \frac{\left[-(jk - \gamma)(x + a)\right]^n}{n \cdot n!} \right\} \tag{29}$$

and

$$A = Y(1 - j)\sqrt{\frac{\pi f \mu}{\sigma}}\, \omega \frac{hC_a V_a}{4\pi}$$

a = Radial distance to the end of the conductor nearest the transmitter

x = Distance along the wire measured from the near end ($x + a = r$, the radial distance from the transmitter)

C_a, V_a = Capacitance and driving voltage of the transmitting antenna

γ^2 = ZY, the propagation factor for the line squared.

For a particular conductor, the constants K_1 and K_2 are evaluated from considerations of the line terminations. If the ends of the conductor are open-circuited, the current is zero at the ends and the constants can be evaluated directly from Eq. (28). In the more general case, where the conductor is not open-circuited at the ends, the constants can be evaluated from:

$$\frac{V(0)}{I(0)} = -Z_1 \qquad \frac{V(d)}{I(d)} = Z_2 . \tag{30}$$

where Z_1 and Z_2 are the terminating impedances at the near end $(x = 0)$ and at the far end $(x = d)$, respectively. From Eqs. (26) and (28),

$$V(x) = -\frac{1}{Y}\frac{dI}{dx} = -Z_o\left[K_1 e^{\gamma x} - K_2 e^{-\gamma x} + F_v(x)\right] \tag{31}$$

where

$$Z_o = \gamma/Y = \sqrt{Z/Y}$$

$$F_v(x) = \frac{1}{Z_0 Y}\frac{dF(x)}{dx} = \frac{1}{\gamma}\frac{dF(x)}{dx}\,. \tag{32}$$

$F_v(x)$ and the constants K_1 and K_2 are derived in Appendix A.

From Eqs. (28) and (31), therefore, the current in the conductor and the potential of the conductor relative to local undisturbed ground potential can be computed for arbitrary terminations, provided the impedance per unit length and the admittance per unit length can be determined for the conductor.

The above analysis is based on the assumption that the conductor is long compared to a skin depth in the soil and that there are no other conductors close enough to affect the ambient radial electric field in the ground (i.e., there are no other conductors within a few skin depths of the conductor under consideration). If the conductors are close enough together that mutual coupling effects become significant, the transmission line analysis becomes very complex, and other approaches to the cable current problem are desirable.

C. Wire Current from Wait's Theory[9]

Wait has analyzed the problem of determining the current induced in closely spaced antenna ground radials on a wave impedance basis, rather than on the transmission line basis used above. Wait's analysis of the currents induced in radial cables is based on the division of the antenna ground current between the wave impedance η of the soil and the wave impedance Z_q of the

ground radial system. Hence, of the total current I_t at radius r from the antenna, a portion I is carried by the ground radials and the remainder is carried by the soil. The wire current is thus

$$I = \frac{\eta}{\eta + Z_q} I_t \tag{33}$$

where

$$I_t = -2\pi r H_\phi \tag{34}$$

$$\eta = \sqrt{\frac{j\omega\mu}{j\omega\epsilon + \sigma}} \approx \sqrt{\frac{j\omega\mu}{\sigma}} = \frac{(1 + j)}{\sigma\delta} . \tag{35}$$

For a parallel-wire grid, the wave impedance for normal incidence with the E-vector parallel to the grid wires is

$$Z_q = \frac{j\omega\mu b}{2\pi} \log \frac{b}{2\pi r_o} \tag{36}$$

where r_o is the wire radius and b is the wire spacing (b should be less than the skin depth in the soil). For a ground screen of N radial wires uniformly spaced about the base of the antenna, Wait lets

$$b = \frac{2\pi r}{N}$$

so that

$$Z_q = \frac{j\omega\mu r}{N} \log \frac{r}{N r_o} . \tag{37}$$

Using H_ϕ from Eq. (4) we can write, for the total current in all N wires,

$$I = -\omega h_e C_a V_a \left\{ \frac{j}{r} - k \right\} e^{-jkr} \left[\frac{1}{1 + (1 + j)\frac{r}{N\delta} \log \frac{r}{Nr_o}} \right] \tag{38}$$

where it is assumed that $h_e \ll \lambda$, $h_e \ll r$, and $\delta > \frac{2\pi r}{N}$.

D. Impedance and Admittance of the Conductor

The conductors of interest in this report are round wires or cables which may be either insulated from the ground or in direct contact with the soil. The impedance and admittance per unit length of round wires with coaxial cylindrical return conductors are available from elementary texts on electromagnetic theory. When the return conductor is the rather poorly conducting soil, the impedance and admittance per unit length must take into account the resistance and the reactance of the return conductor. The problem of computing the impedance and admittance of the ground return is also a skin effect problem in cylindrical coordinates. The impedance per unit length of a tubular conductor [10] of inside radius r_1 and outside radius r_2 is

$$Z_T = \frac{1 - j}{2\pi r_1 \sigma\delta} \left[\frac{J_o(X_1)H_1^{(1)}(X_2) - J_1(X_2)H_o^{(1)}(X_1)}{J_1(X_1)H_1^{(1)}(X_2) - J_1(X_2)H_1^{(1)}(X_1)} \right]$$

where $X_1 = (1 - j)r_1/\delta$ and $X_2 = (1 - j)r_2/\delta$, when the driving field is on the inside of the tube. If the outer radius r_2 is allowed to approach infinity, the impedance approaches

$$Z_s = \frac{1 - j}{2\, r_1 \sigma\delta} \left\{ \frac{H_o^{(1)}\left[(1 - j)\frac{r_1}{\delta}\right]}{H_1^{(1)}\left[(1 - j)\frac{r_1}{\delta}\right]} \right\} \tag{39}$$

since

$$\lim_{X_2 \to \infty} \frac{H_1^{(1)}(X_2)}{J_1(X_2)} = 0 \ .$$

Thus, the contribution of the ground to the impedance of a round conductor immersed in a conducting soil of infinite extent (see Fig. 7) is obtained.

The admittance per unit length of the soil is most readily obtained from the propagation factor for the soil and the impedance. Thus,

$$Y_s = \frac{\gamma_s^2}{Z_s} \tag{40}$$

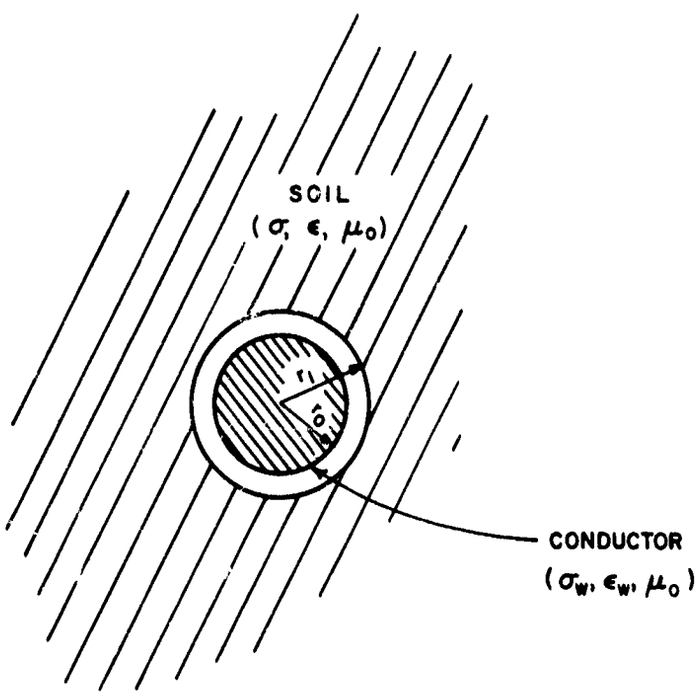

FIG. 7 ROUND CONDUCTOR IMMERSED IN CONDUCTING SOIL.

where

$$\gamma_s^2 = j\omega\mu(\sigma + j\omega\epsilon) \approx j\omega\mu\sigma .$$

The internal impedance per unit length of a round wire of radius r_o is[11]

$$Z_w = \frac{1 - j}{2\pi r_o \sigma_w \delta_w} \left\{ \frac{J_o\left[(1 - j)\frac{r_o}{\delta_w}\right]}{J_1\left[(1 - j)\frac{r_o}{\delta_w}\right]} \right\} \tag{41}$$

where σ_w and δ_w are the conductivity and skin depth for the metal of the wire.

The dielectric gap between the conductor and the soil contributes to the external inductance of the conductor and the capacitive admittance. The external inductive reactance is:

$$X_e = \frac{\omega\mu}{2\pi} \log \frac{r_1}{r_o} \tag{42}$$

and the capacitive susceptance is

$$B_e = \frac{2\pi\omega\epsilon}{\log\left(\frac{r_1}{r_o}\right)} . \tag{43}$$

The inductive reactance is in series with the internal impedance of the wire and the impedance of the ground return. The capacitive susceptance is in series with the admittance of the soil.

The series impedance per unit length of the conductor and its return is thus

$$Z = Z_s + Z_w + jX_e$$

$$= \frac{1 - j}{2\pi} \left\{ \frac{H_o^{(1)}\left[(1 - j)\frac{r_1}{\delta}\right]}{r_1 \sigma \delta H_1^{(1)}\left[(1 - j)\frac{r_1}{\delta}\right]} + \frac{J_o\left[(1 - j)\frac{r_o}{\delta_w}\right]}{r_o \sigma_w \delta_w J_1\left[(1 - j)\frac{r_o}{\delta_w}\right]} \right\}$$

$$+ \frac{j\omega\mu}{2\pi} \log \frac{r_1}{r_o} \tag{44}$$

and the shunt admittance per unit length of the conductor is:

$$Y = \frac{jY_s B_e}{Y_s + jB_e} \tag{45}$$

where Y_s and B_e are defined by Eqs. (40) and (43). Often, if the conductor is bare, the susceptance B_e is large compared to Y_s so that $Y \approx Y_s$, and if the conductor is insulated, the ground admittance is large compared to B_e so that $Y \approx jB_e$. The former approximation may be poor at very low frequencies (particularly if the wire is oxidized or polarized), and the latter approximation may be poor at very high frequencies where the capacitive susceptance becomes large.

The conductor impedance and admittance derived above apply strictly only to a conductor immersed in a conducting soil of infinite extent. Because the soil nearest the conductor contributes the most to the impedance and admittance, however, these impedances and admittances should be approximately correct for any conductor submerged several conductor diameters below the surface of the ground. Under this condition, the conductor is sufficiently covered with soil that the capacitive admittance of the insulation, the internal impedance of the conductor, and the external inductance of the conductor are essentially the same as for a conductor buried at an infinite depth. The admittance of the soil is also affected only slightly, because this admittance is

limited primarily by the soil in the immediate vicinity of the conductor. The only significant difference between the properties of the conductor buried at a finite depth and the conductor buried at infinite depth, therefore, is in the internal impedance of the soil. For the conductor buried at a finite depth, the internal impedance of the soil will be somewhat larger than that determined by Eq. (39), because the internal impedance of the soil is also determined to a large extent by the soil nearest the conductor. However, the error incurred by using Eq. (39) for a conductor buried several conductor diameters deep is probably no greater than the error incurred as a result of uncertainties in the soil properties and in uniformity. For the buried conductors of interest in this report, therefore, these values should be satisfactory, since all of these conductors are buried at least 10 conductor diameters deep.

If the conductor is at the air/earth interface or above ground, approximations such as those suggested by the primed quantities in Fig. 8 may be used to estimate the impedance and admittance per unit length. If the axis of the conductor is in the surface, the upper half of the conductor can be neglected, as illustrated in Fig. 8(a). All impedances except the external inductance are then approximately doubled and the admittances are approximately halved. For conductors with small external inductance (i.e., bare conductors or conductors with thin insulation), therefore, the propagation factor is essentially unchanged, but the characteristic impedance is approximately twice that for a conductor immersed in an infinite medium.

For a conductor above ground, as shown in Fig. 8(b), the impedance of the wire, the external inductive reactance, and the capacitive susceptance of the air space can be computed from conventional formulas. An approximation to the impedance of the ground return may be obtained by computing Z_s for the configuration shown in Fig. 8(c). If $r_1 \gg r_o$, the ground admittance Y_s will be negligible compared to the capacitive susceptance of the air space.

In addition, Sunde has derived approximate expressions for the impedance and admittance of an insulated wire at the air/earth interface or in the ground. These expressions are, however, transcendental functions of the complex propagation factor. Sunde gives[12]

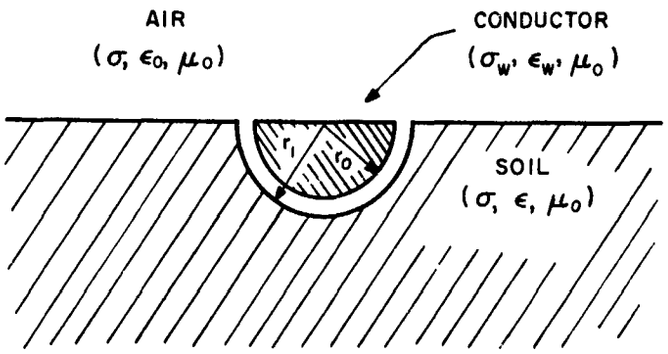

$Z' \approx 2Z$ [SEE EQ. (44)]

$Y' \approx Y/2$ [SEE EQ. (45)]

$\gamma' \approx \gamma$

$Z_0' \approx 2Z_0$

(a)

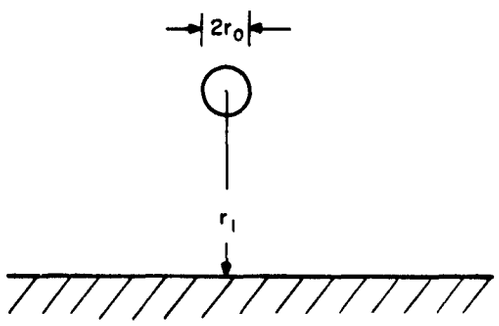

$$X_e = \frac{\omega\mu}{2\pi} \cosh^{-1}\frac{r_1}{r_0}$$

$$B_e = \frac{2\pi\omega\epsilon}{\cosh^{-1}\frac{r_1}{r_0}}$$

$Z_w' \approx Z_w$ [SEE EQ. (41)]

(b)

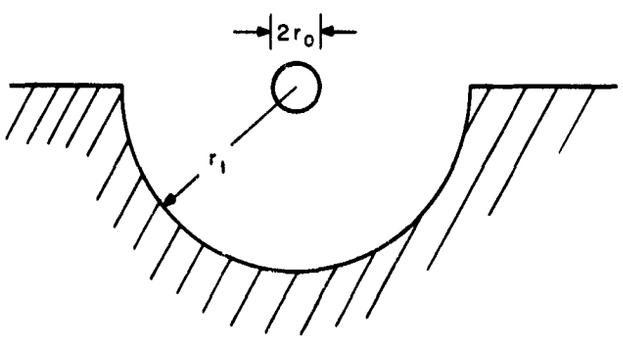

$Z_s' \approx 2Z_s$ [SEE EQ. (39)]

$Y_s' \approx \frac{1}{2}Y_s$ [SEE EQ. (40)]

(c)

FIG. 8 IDEALIZED CONDUCTOR CONFIGURATIONS FOR ESTIMATING LINE PARAMETERS

$$Y(\gamma) = \left[Y_i^{-1} + \frac{1}{\pi(\sigma + j\omega\epsilon)} \log \frac{1.12}{\gamma r_1} \right]^{-1} \tag{46}$$

$$Z(\gamma) = Z_w + \frac{j\omega\mu}{2\pi} \log \frac{1.85}{r_1(\gamma_s^2 + \gamma^2)^{1/2}} \tag{47}$$

where $Y_i = jB_e$ is the insulation admittance and $\gamma^2 = Z(\gamma)Y(\gamma)$.

Because of the transcendental form of these expressions, it is virtually impossible to solve for γ explicitly. Since Z and Y vary only as the logarithm of γ, however, it should be adequate tc make a prudent guess at the value of γ and to use this value to calculate Y and Z from Sunde's expressions above. An appropriate choice for γ might be

$$\gamma \approx \gamma_o = jk$$

since γ_o would be the propagation factor if the ground were a perfect conductor (assuming the dielectric constant of the insulation is 1). By using this value for γ and noting that $\sigma \gg \omega\epsilon$, Eqs. (46) and (47) can be written

$$Y = \left[\frac{1}{\pi r_1} \log \frac{1.12}{kr_1} + j\left(B_e - \frac{1}{2\sigma}\right) \right]^{-1} \tag{48}$$

$$Z = R_i + \frac{\omega\mu}{8} + j\omega\left[L_i + \frac{\mu}{2\pi} \log \frac{1.85}{r_1\sqrt{\omega\mu\sigma}} \right] \tag{49}$$

where

$$R_i + j\omega L_i = Z_w ,$$

E. Summary

Two theoretical models have been established for computing the current induced in a conductor in or near the ground by an electric field directed along

the conductor. The first, which will be called the transmission line model, is applicable to isolated conductors or to conductors that are sufficiently far from neighboring conductors that the neighboring conductors do not appreciably affect the electric field strength in the vicinity of the conductor of interest. In the transmission line model, a conductor lying in or near the ground is visualized as a two-conductor transmission line with the ground serving as the return conductor. The line will have an impedance per unit length and an admittance per unit length that are determined from the electrical properties of the conductor, its insulation, and the soil. From these, a propagation factor and a characteristic impedance can be determined. When a radial electric field is established in the ground, the field may be visualized as a distributed generator driving the line along its entire length. Formulas for computing the impedance per unit length and the admittance per unit length were developed for both bare and insulated conductors.

The second theoretical model, which will be called the "wave impedance" model, is applicable to groups of conductors that are closely spaced so that mutual coupling effects are significant. The wave impedance model was developed by Wait to study the currents flowing in antenna ground radials. In essence, the wave impedance model consists of the intrinsic impedance of the soil shunted by the wave impedance of the grid of conductors. The current induced in the grid/soil complex by an electromagnetic wave propagating into the soil is divided between the soil impedance and the impedance of the grid of conductors. The wave impedance of the grid of conductors is determined by the conductor size and spacing. The wave impedance theory is applicable to conductors that are spaced less than two or three skin-depths (in the soil) apart and tightly coupled to the soil.

IV
INSTRUMENTATION

A. General

The source of CW signals for the electromagnetic mapping is a low-power switchable-frequency transmitter operating at fixed frequencies of 0.5, 1, 2, 5, 10, 20.6, 62, 100, 200, 450, and 510 kc. The transmitter drives a tuned, electrically short, vertical antenna. The radiated signal power is sufficient for the desired measurements to be carried out within a radius of approximately 2 km. The mapping is accomplished by using transportable receivers that have the capability of performing electric and magnetic field measurements and measurement of currents flowing in cables.

B. CW Transmitter

A block diagram of the CW transmitter is shown in Fig. 9. Schematics are shown in Appendix B.

The switchable-frequency LC oscillator provides low-level signals on each of the eleven frequencies used. A different set of tuning elements selected by a front-panel switch is used for each frequency.

The wide-band power amplifier covers the frequency range 0.5 to 510 kc. The output of the power amplifier is operated Class B push-pull and provides an output of 50 volts peak-to-peak into 10 ohms (30 watts). This output is matched to the resonated vertical antenna by means of five matching transformers, one of which is selected for each frequency. These are high-quality transformers that have negligible insertion power loss. The output lead of the matching transformer is connected to the tuning coil and the ground lead is connected to an antenna current monitor. This current monitor measures the total current through the series tuning coil and the antenna. (This current is not used as an accurate measurement of antenna current because it also includes

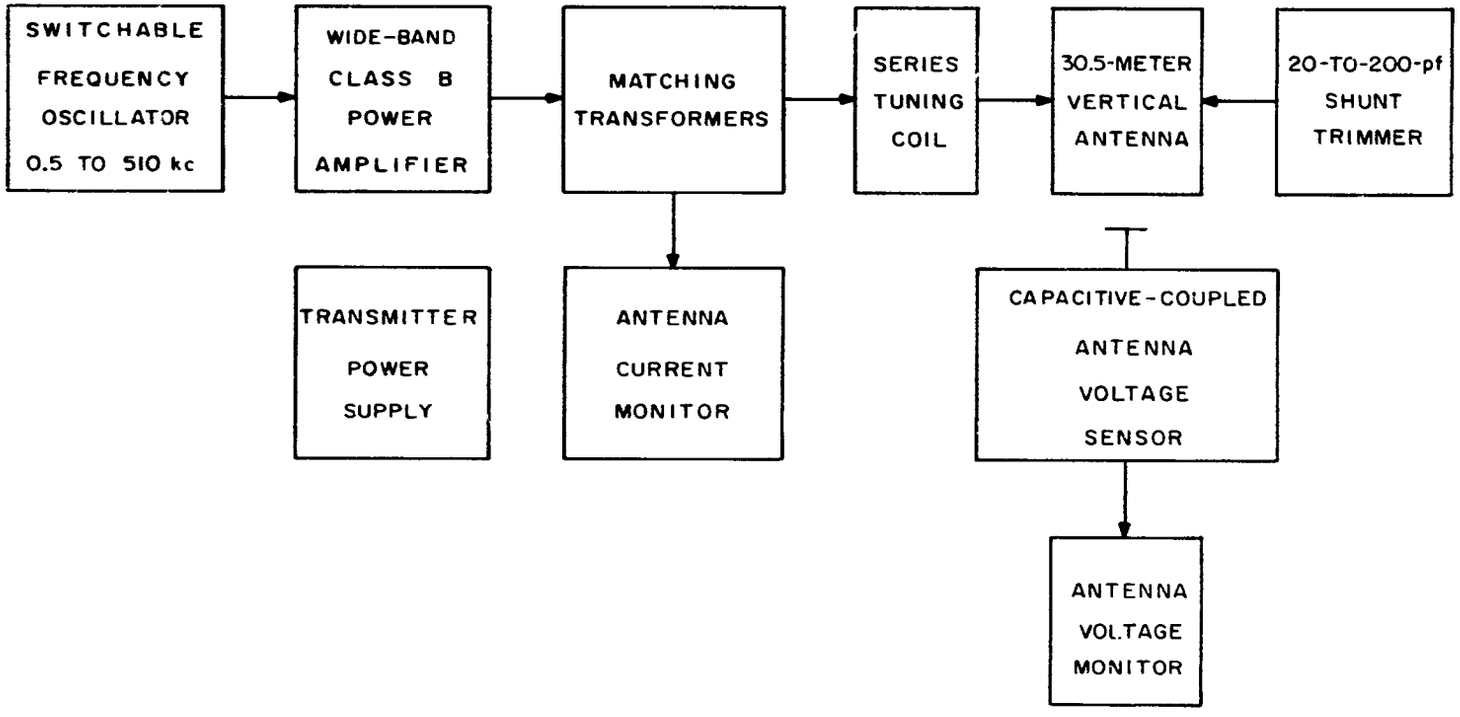

FIG. 9 CW TRANSMITTER BLOCK DIAGRAM

current in the stray capacitance of the tuning coil and antenna base structure.) The voltage appearing on the transformer output lead is relatively low, being the antenna voltage divided by the antenna-circuit quality factor (Q).

The series-tuning coil for resonating the antenna is a high-Q, high-voltage coil that must withstand voltage equal to that applied to the antenna. Different coils are used at each frequency with inductances ranging from approximately 200 henrys at 500 cps to 0.2 henry at 510 kc. The coils have Q's ranging from about 75 to 250. Each coil is wound on a 7.5-cm-diameter phenolic tube that is approximately 30 cm long. The windings are multilayer solenoidal windings with insulation between windings. The windings are vacuum-potted with a semi-flexible epoxy resin potting compound to provide good high-voltage performance. A ferrite core in the form of a single E is used for all frequencies and has a center post that accommodates the phenolic tube upon which the coils are wound. The E-core configuration provides a large air gap in the magnetic path, thus allowing a relatively large amount of reactive power to be handled by a small core without saturation (the energy is stored in the air gap instead of in the core). Figure 10 shows the E-core, a loading coil, and the antenna feed tube in their high-voltage protective housing.

The radiating antenna is a triangular-cross-section tower 30.5 meters in height. The triangle cross section is 0.52m on a side. This tower is supported by three high-voltage insulators mounted on a support base atop the transmitter van. A ground plane consisting of 19 radials is supported 8 feet above the ground out to a radius of 30 meters and is then terminated in the ground using 6-foot ground stakes.

A cylindrical tube approximately 7.5 cm in diameter extends through a hole in roof of the van into the tuning coil housing to connect the antenna to the coil. Each coil provides approximately the proper inductance for tuning the antenna; however, a vernier tuning control is provided by a vacuum capacitor mounted next to the antenna on the roof of the van. The tuning capacitor, base insulators, and antenna feed are shown in Fig. 11. The tuning capacitor has a tuning range of 20 to 200 $\mu\mu$f and a voltage rating of 100 kv. A drive mechanism extending through the roof of the van provides convenient operator control.

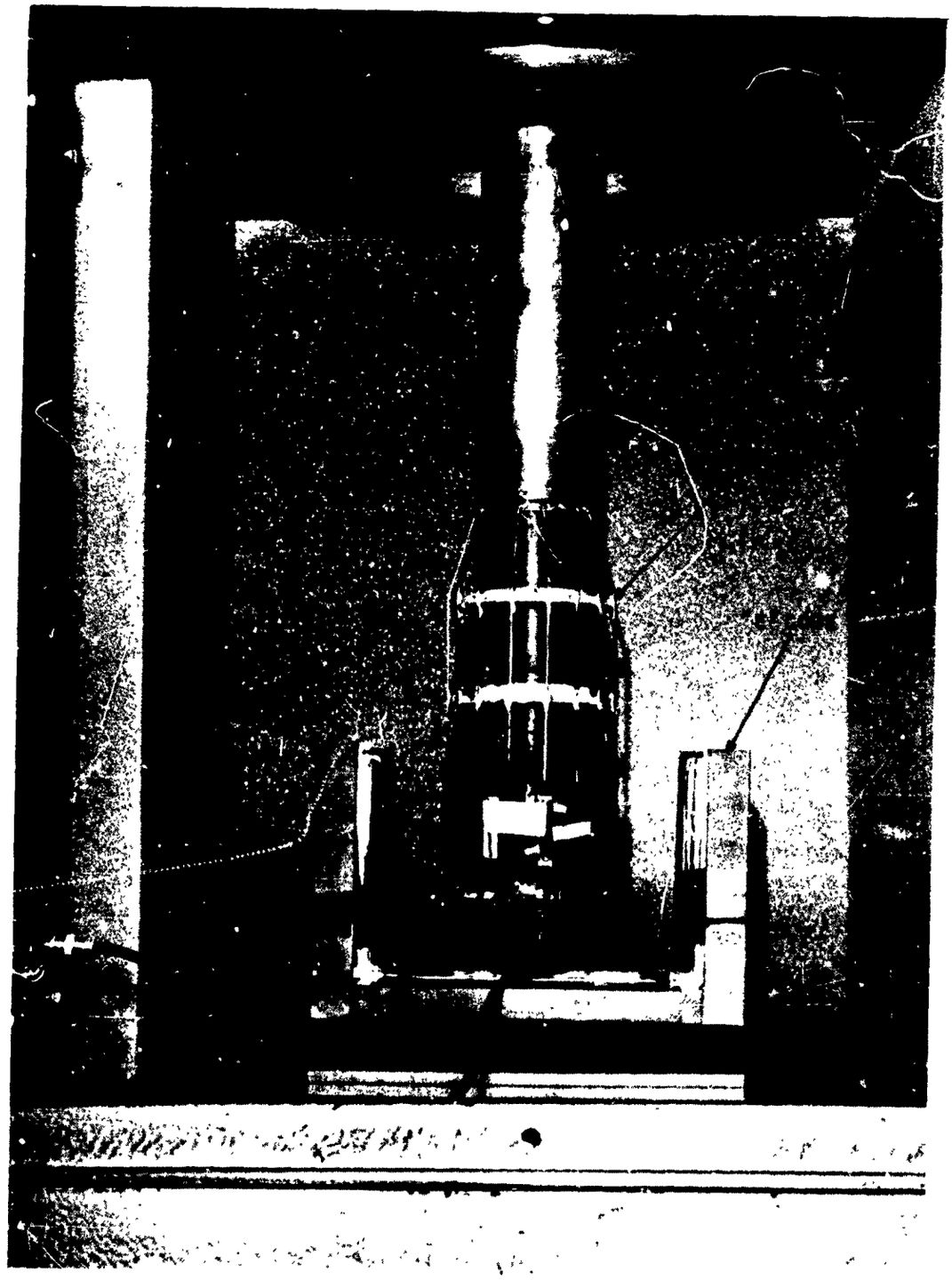

D-4427-165

FIG. 10 CW TRANSMITTER LOADING COIL

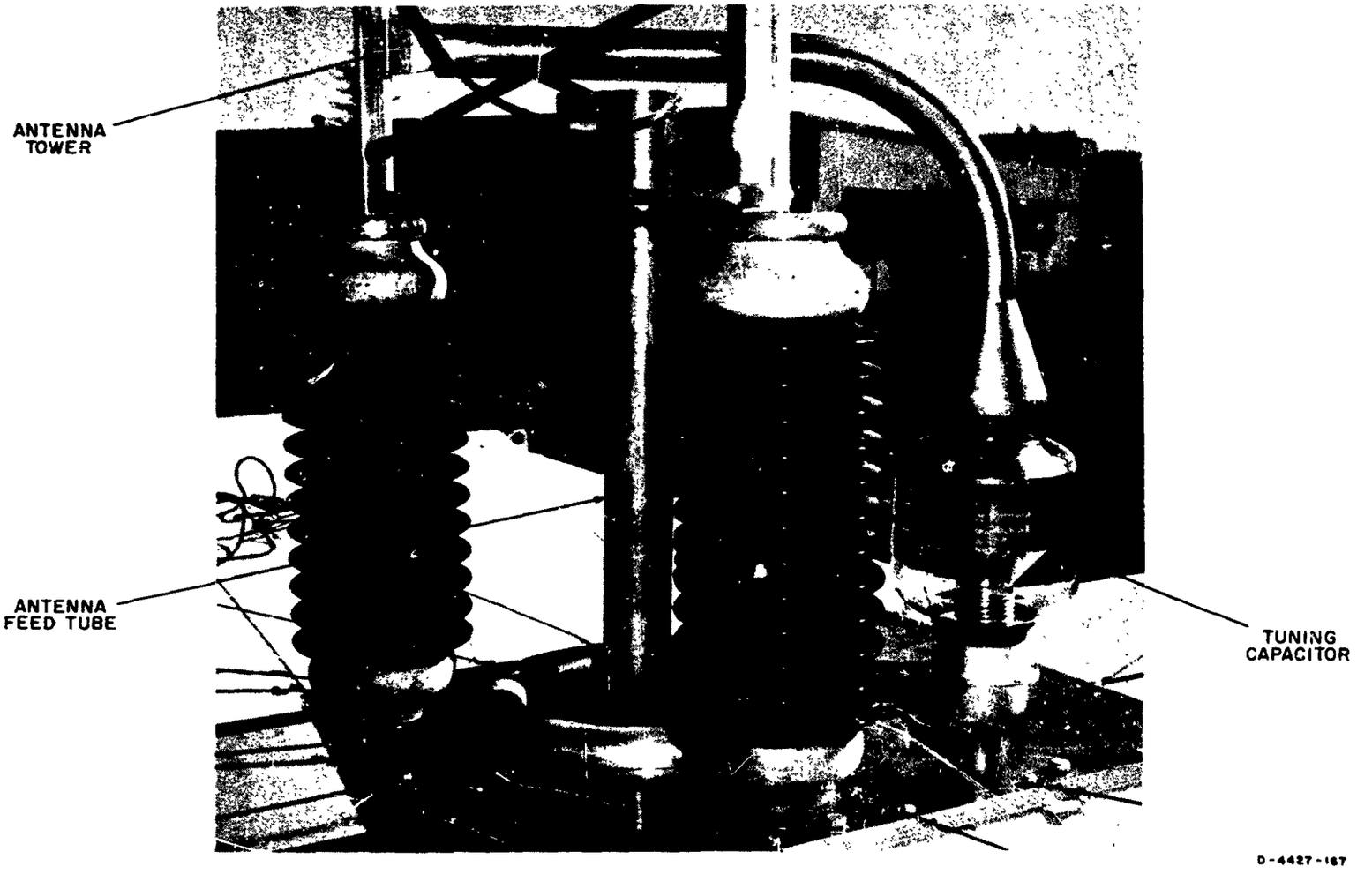

FIG. 11 TRANSMITTING ANTENNA BASE

In order to monitor the antenna voltage, a capacitive probe is mounted adjacent to the antenna base on the van roof. The probe consists of a flat plate mounted on insulators and connected to a monitor inside the van via a coax cable. The antenna voltage monitor consists of voltage range switches, amplifier for providing an output for an external meter, and an amplitude detector that operates a panel meter. The antenna voltage monitor is calibrated at voltages sufficiently low to allow a voltmeter to be connected directly to the transmitting antenna.

A low-voltage power regulator provides dc power to all circuits associated with the transmitter. The input to the regulator is standard 117 vac, 60 cps, provided from a portable supply.

C. CW Receivers

1. General

The receivers used to measure the fields produced by the transmitter are transportable units that operate on self-contained batteries. Although the electronic units of the receivers are easily hand-carried, two men are required to carry the antennas and supporting bases, and the antennas are normally transported by a small truck.

A block diagram of a typical CW receiver is shown in Fig. 12. Schematics are shown in Appendix B. This typical receiver is that used for all continuous-wave signals.

2. Magnetic (Loop) Antenna Receiver

The loop antenna consists of a single turn of thick-wall (2-in-diameter) aluminum tubing in a square shape approximately 1.5m on a side. The loop is mounted on a swivel and gimbal that allows the antenna to be oriented to the desired direction. The area of the loop antenna was determined to give adequate sensitivity and the conductor cross section was chosen to give good low-frequency performance. Threshold sensitivity varies from 10^{-8} amp/meter at 0.5 kc to 3×10^{-10} amp/meter at 510 kc. To obtain this sensitivity, the antenna is tuned

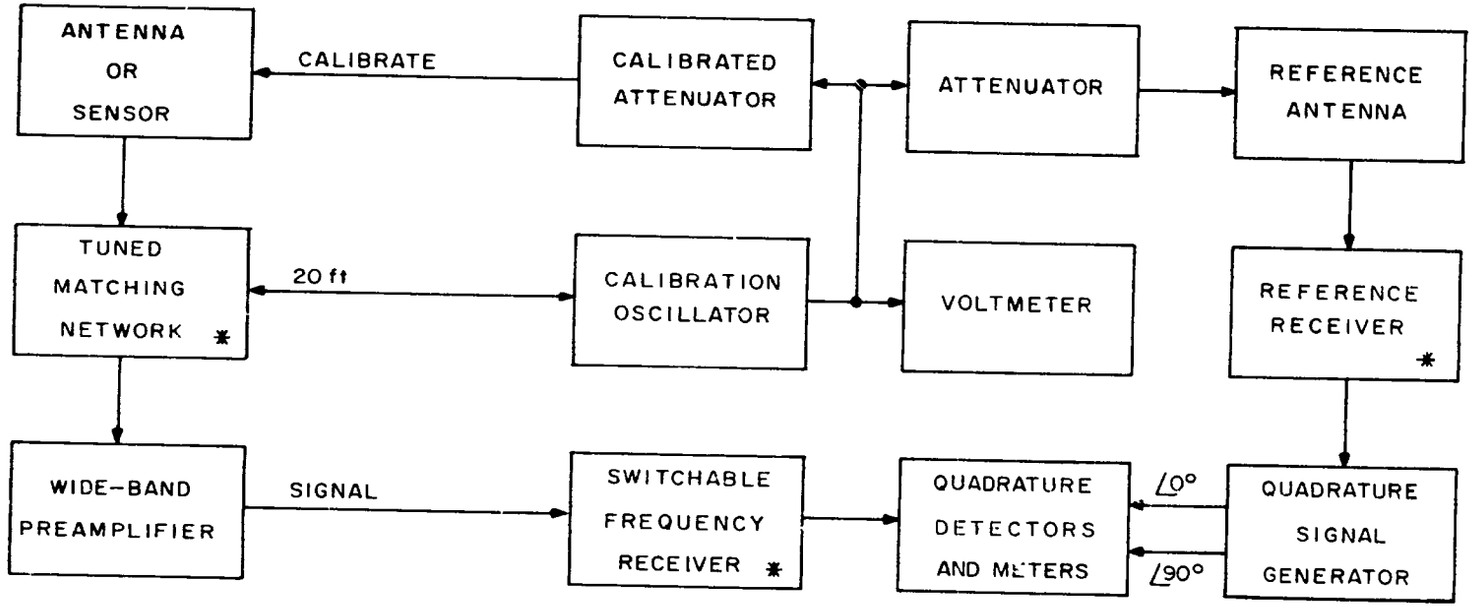

* CONTAIN GAIN (ATTENUATOR) SWITCHES

FIG. 12 CW RECEIVER BLOCK DIAGRAM

and matched to a low-noise wide-band preamplifier.* The output of the preamplifier is applied to the receiver that provides additional selectivity and amplification. The output of this receiver is detected with respect to two phase-quadrature synchronous reference signals. The outputs of the two detectors appear on meters. Proper combination of these two output readings provides magnitude and phase of the incoming signal, the magnitude being determined by:

$$\left(M_1^2 + M_2^2\right)^{1/2} \tag{50}$$

where M_1 and M_2 are the two output meter readings. Phase is with respect to the reference signal and is determined by:

$$\tan^{-1} \frac{M_2}{M_1} . \tag{51}$$

The phase reference is the local vertical electric field. A short vertical whip antenna approximately 2 meters tall is used as a reference antenna. The reference antenna is connected to a low-noise preamplifier and tuned amplifer that is switch-tuned to the desired frequency. The output of the tuned amplifier is applied to a quadrature signal generator. The output of the quadrature signal generator has two components that have been clipped to constant amplitude level and whose phase difference is 90 degrees.

The phase and amplitude response of the receiving system is calibrated by applying appropriately attenuated signals to the receiving and reference antennas from a common calibration oscillator. The grounds for the calibration and receiving systems were connected only at each end of the 20-foot cables (see Fig. 12). The calibration injection points at the sensor and at the reference receiver were permanently connected through ungrounded connectors.

---

*To reduce the antenna sensitivity to electric fields, the primary of a matching transformer is balanced with center tap grounded and has an electrostatic shield between primary and secondary.

3. Electric (Plate) Antenna Receiver

Except for the sensing antenna and matching network, this receiver is identical to the loop antenna receiver described in Sec. IV-C-2.

The electric antenna consists of two parallel plates 1.5 m on a side and separated by 20 cm. The mesh plates are supported by phenolic insulators. The antenna is mounted on a swivel and gimbal identical to the loop antenna mount that allows the antenna to be oriented to the desired direction.

The size and spacing of the antenna plates were determined to provide adequate sensitivity. Threshold sensitivity varies from 0.1 μv/m at 0.5 kc to 0.004 μv/m at 510 kc. As in the loop receiver, the antenna is tuned and matched with a balanced shielded transformer to a low-noise wide-band preamplifier.

4. Cable-Current Receiver

Except for the sensing antenna and matching network, this receiver is identical to the loop antenna receiver described in Sec. IV-C-2. The sensor for the cable current receiver is a toroidal core that is bisected to enable the core to be placed around a conductor. A molybdenum-permalloy-powder toroid having a relative permeability of 125 and nominal dimensions of 4.0 inch outside diameter, 2.25 inch inside diameter, and 0.625 inch thickness was used for the core. A single-layer winding consisting of 260 turns of 22-gauge enameled copper wire was wound on the core, and the winding and core were cast in an epoxy resin and fitted with a hinge and latch. The exterior surface of the casting was copper plated to reduce electrostatic coupling between the wire and the winding. (A gap was left in the copper plating so that it did not act as a shorted turn.)

The full 260 turns are paralleled with a fixed capacitance to resonate at 0.5 kc. At all higher frequencies, only a fraction of the turns is used.* Above 20.6 kc, the pickup could be used without tuning. (Above about 40 kc, the core losses reduce the Q of the windings sufficiently to make resonating of little value.) A more sensitive ferrite-cored pickup device was built to operate at the higher frequencies. The high-frequency ferrite-cored pickup was tuned

*The pickups were later modified so that the full 260 turns were used at frequencies from 0.5 to 20.6 kc (see Sec. VII).

with fixed capacitors at 62, 100, 200, 450, and 510 kc. On both sensors, the tuning capacitors and an attenuator were contained in a chassis attached to the pickup device.

D. Pulse Transmitter

The high-voltage pulse generator for the pulse transmitter consisted of two capacitor banks that were charged in parallel from a dc high-voltage supply and connected in series to discharge through a highly damped oscillatory circuit containing the transmitting antenna (tuning capacitor removed). Except for the dc high-voltage supply, the entire pulse transmitter was mounted atop the CW transmitter van. The pulse transmitter is pictured in Fig. 13. The pulse transmitter schematic is shown in Appendix B. Two 120-kv capacitor banks are charged in parallel from a 120-kv dc power supply through the 125-kv, 20-megohm resistors. A spark gap (lower gap), which consists of two 4-1/2-inch-diameter aluminum spheres, is adjusted to fire at about 100 kv. When the lower gap fires, the charged capacitor banks are connected in series through the spark channel, so that the voltage across the upper spark gap is suddenly increased to approximately 200 kv, and the upper gap fires, allowing the capacitors to discharge through the circuit containing the transmitting antenna and a pulse-shaping load impedance (inductance and resistance).

The time constant of the capacitor banks and the dc charging resistors is much greater than the time constant of the capacitor bank and load impedance, so that the pulse shape is determined by the damped oscillation of the capacitors with the load inductance and the load resistor. When both gaps are conducting, the effective capacitance shunting the load is the series combination of the capacitor banks in parallel with the antenna capacitance. This capacitance and the load inductance resonate at about 12 kc. A damping resistor is mounted between the upper gap and the transmitting antenna to reduce antenna ringing. The pulse repetition rate is determined by the sparking voltage of the lower gap and the time required for the capacitor banks to charge. Repetition rates of 1 or 2 pulses per second were normally used.

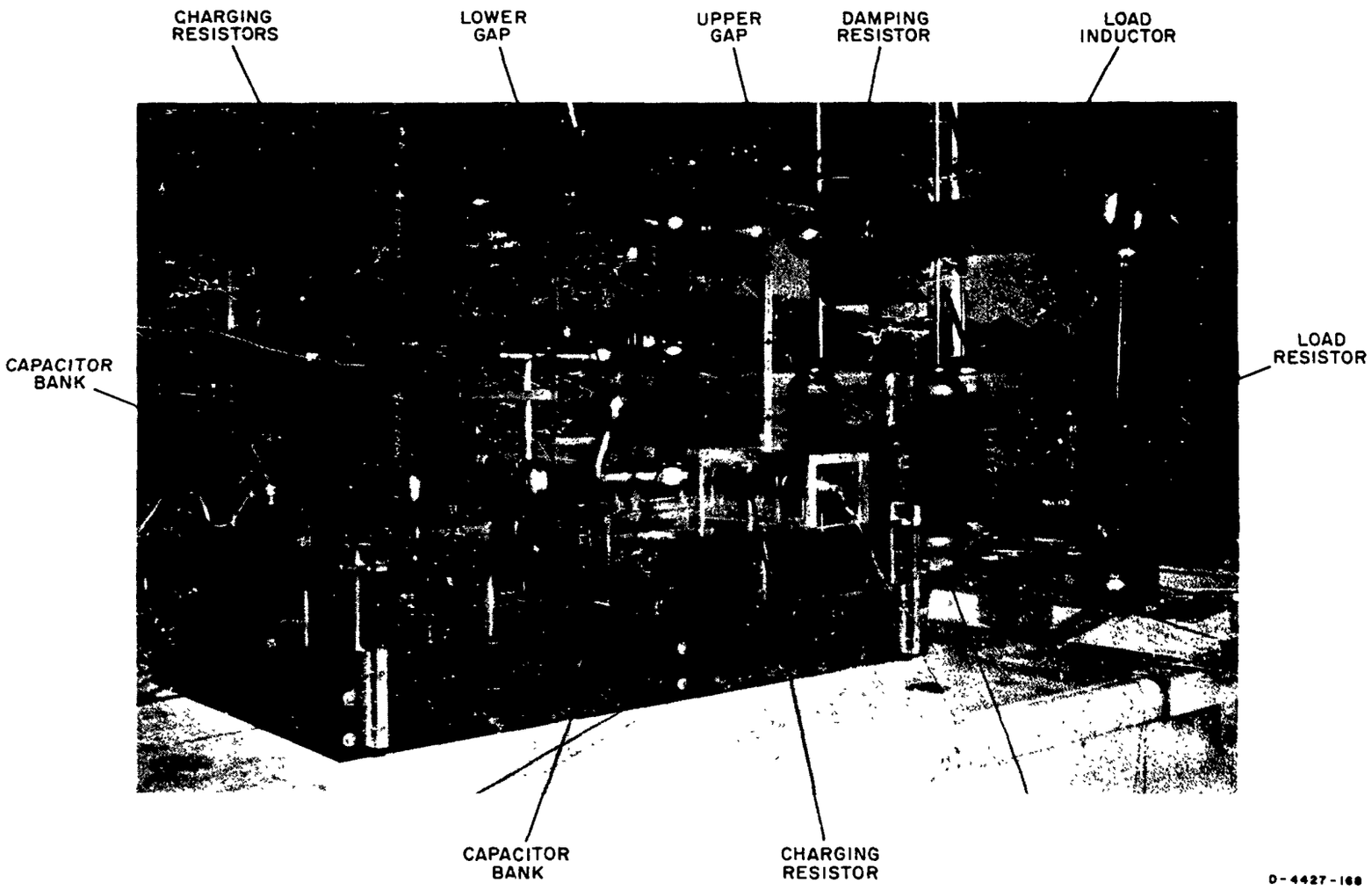

FIG. 13 PULSE TRANSMITTER

E. Pulse Receivers

A typical pulse receiver is shown in Fig. 14. Three similar pulse receivers were used. Schematics are shown in Appendix B. The magnetic and electric receivers use the CW loop and plate sensors. The cable-current-pulse receiver includes a new wide-band current sensor. Matching networks appropriate for the loop antenna, plate antenna, or the cable-current sensor match these sensors to a wide-band preamplifier. The output of the preamplifier is further amplified and then observed on an oscilloscope. Two bandwidths are available -- 100 and 500 kc. The oscilloscope trace is photographed by opening the camera shutter and single-triggering the oscilloscope. Calibration is provided by a signal-generator and attenuator to current-inject a signal directly into the plate sensor through a small capacitor, into the loop sensor through a resistor, and into the current sensor through a single turn through the sensor.

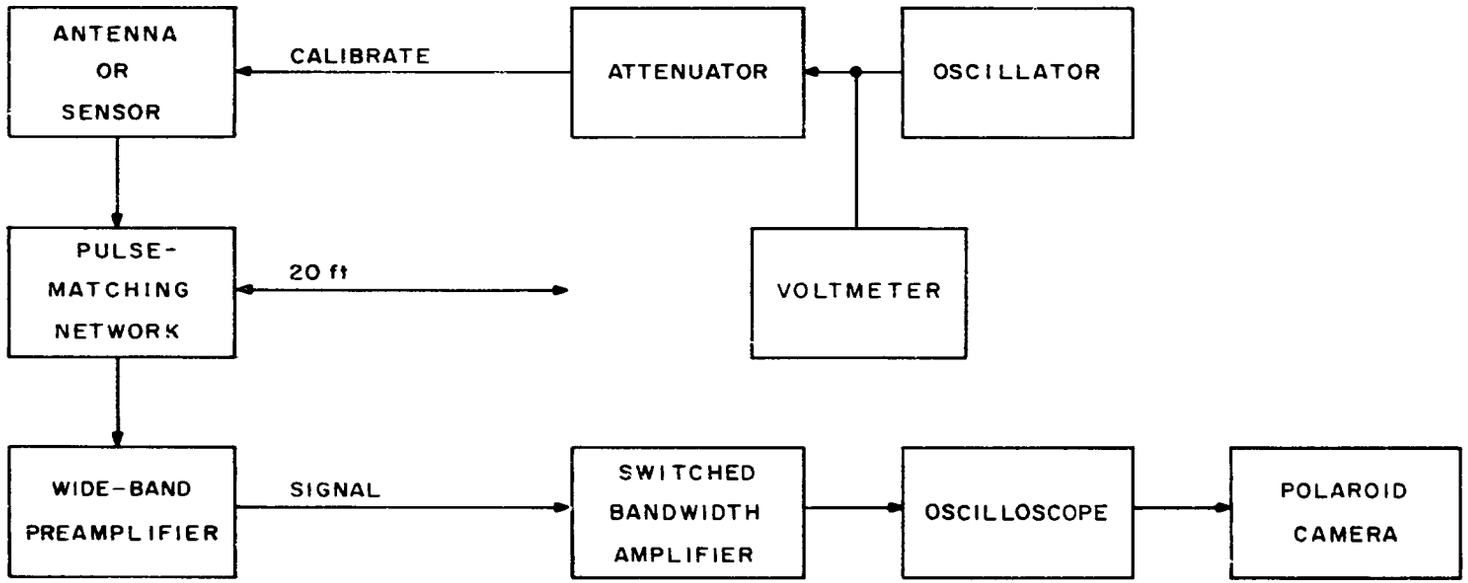

FIG. 14 PULSE RECEIVER BLOCK DIAGRAM

This page intentionally left blank.

V

SYSTEM OPERATION AND CALIBRATION

A. General

Signal measurements were made using manual recording of data with redundancy and overall calibration of the system for each measurement. This procedure removed the effect of equipment variations from the data, thus allowing relatively simple instruments to be used. Parameters not calibrated with each measurement, such as antenna characteristics, calibration heights, and meters were repeatedly calibrated to ensure that their characteristics were known.

B. CW Transmitting System

The equations developed in Sec. II completely describe the electro-magnetic fields around the transmitter as functions of V_a (antenna volts), C_a (antenna capacitance), h_e (antenna effective height), and known physical constants. The antenna effective height [see Eq. (9)] for a 102-foot tower (100-foot mast on 2-foot insulators) is one half the physical length or 15.55 meters except for small increases above 100 kc.

Antenna capacitance C_a from Eqs. (13) and (14) for the 31.1m triangular tower 0.52m on a side is 438 $\mu\mu$f. Measurements to confirm the antenna capacitance were made. However, such measurements are not clearly defined for the transmitting antenna feed tube (see Fig. 11) contributes to both the antenna capacitance and the base capacitance. Measurements using a capacitance voltage divider method* were made to determine the following:

*Calculations of capacitance from these measurements are no better than ± 1% due to meter reading accuracy.

(1) Total capacitance with tuning capacitor near minimum--509 $\mu\mu$f

(2) Capacitance with tuning capacitor removed--486 $\mu\mu$f

(3) Feed tube capacitance--43 $\mu\mu$f. This capacitance is the difference between the capacitance (2) and the capacitance after removing the feed tube.

(3) Tower capacitance--426 $\mu\mu$f. This capacitance is the change in capacitance when the tower is removed from the three insulators, leaving the insulator capacitance as 12.5 $\mu\mu$f.

(4) Insulator capacitance measured 4.2 $\mu\mu$f for each insulator or 12.6 $\mu\mu$f for all three insulators.

The measurements indicate that the active antenna capacitance is about 426 $\mu\mu$f with a base capacitance of about 80 $\mu\mu$f, with the trimmer on minimum. Calculated (438 $\mu\mu$f) and measured capacitance are in fair agreement. Measured capacitance of 426 $\mu\mu$f was used as the antenna capacitance.

The voltage, V_a on the transmitting antenna was monitored using a capacitance probe (insulated plate) near the base of the transmitting antenna and a capacitance voltage divider to give a voltmeter indication of the antenna voltage. The voltmeter was an HP 400D VTVM. The probe was calibrated by applying 300 volts rms to the antenna and adjusting the voltage divider (see Fig. B-4 Appendix B) to give 0.03 volts rms on the HP 400D. Thus, the voltage recorded times 10^4 equals the antenna voltage. This calibration was verified at each frequency and was repeated every two weeks during operation.

During operation of the CW transmitter, the frequency is monitored to insure a constant frequency to within 0.1%. Transmitter tuning is monitored by oscilloscope display of the power amplifier output. Correct tuning occurs when this voltage is at a minimum and is symmetrical in wave shape. The relative antenna current and voltage were normally adjusted to the values shown in Table I.

Table I

CW TRANSMITTER PARAMETERS

Frequency (kc)	Tuning Capacitance (turns)	Tuning Voltage Peak-Peak (v)	Antenna Current (%)	Antenna Voltage (kv)
0.508	26	48	62	19.0
1.005	12	48	71	17.0
1.997	11	34	94	16.0
5.011	12	34	96	10.0
10.008	10	28	87	7.00
20.586	11	22	100	5.00
62.105	14	22	67	3.00
100.212	15	46	46	1.60
200.480	15	20	62	2.00
450.286	13	20	26	1.20
509.989	10	20	15	1.00

C. Voltmeters

All measurements of fields were normalized to transmitter antenna voltage. Antenna voltage was monitored with an HP 400D, with a standard accuracy of 2%. The receiving system claibration used HP 403A battery-operated voltmeters. These voltmeters were always used at one of six voltages so that it was possible to use the HP 400D as a standard and scribe the HP 403A scale to agree with the HP 400D. Thus, for measurements normalized to the transmitter antenna voltage, the meter calibrations were accurate to the reading capability of the operator. All voltmeters showed frequency variations that varied over a ±2% range but did not vary between instruments by more than a total range of 1%. Since all data were normalized to the transmitter voltage, this variation resulted in a 1% inaccuracy that was not calibrated out of the data.

The effects of temperature on the HP 403A meters over the normal operating range of 30° F to 150° F could not be noticed within the normal meter

reading accuracy. The same was true for the HP 400D which was always operated in an air conditioned environment.

D. CW Receiving System

1. Operating Procedure

Three field measurements were made with one basic receiving system. To aid in easy transport, the common receiving system was mounted on a ground plane on a little red wagon as shown in Fig. 15. The receiving system was connected to a sensor (and matching network) with two twenty-foot coax cables (one for calibration and one for sensor output). For E- and H-field measurements, the base of the sensor mount was aligned on a radial line through the transmitter by sighting on the transmitting antenna. The base was then leveled to better than one degree using a bubble level. Figure 16 pictures the system setup for E_θ and H_ϕ. Orientations for all six field component directions are shown in Fig. 17. For magnetic field measurements (and for the cable current measurements) the receiving system is placed so that the 20-foot cables are perpendicular to the radial and vertical E fields, so that minimum currents will be induced in the cables. For electric field measurements, the receiving system and operator had to be placed beyond 15 feet from the antenna in the antenna null to avoid distorting the antenna field pattern. This criterion was most critical when measuring E_r and E_ϕ. For H_ϕ and E_θ (major field components) the sensors were mechanically set to the positions shown in Fig. 17. For all other field component directions the sensors were nulled on the major field components using a 20-foot wooden-pole drive shaft to adjust the sensor position. In a null, the sensor output was very sensitive to sensor position (see Sec. II-G). Normally, three readings were obtained for each null so that the nimimum could be found* These three readings were normally within one or two degrees of sensor orientation.

Each sensor has a calibration terminal through which a known calibration signal was injected directly onto the sensor so that the entire receiving

*The quadrature outputs being both phase- and amplitude-sensitive only crudely indicate when a minimum magnitude is obtained.

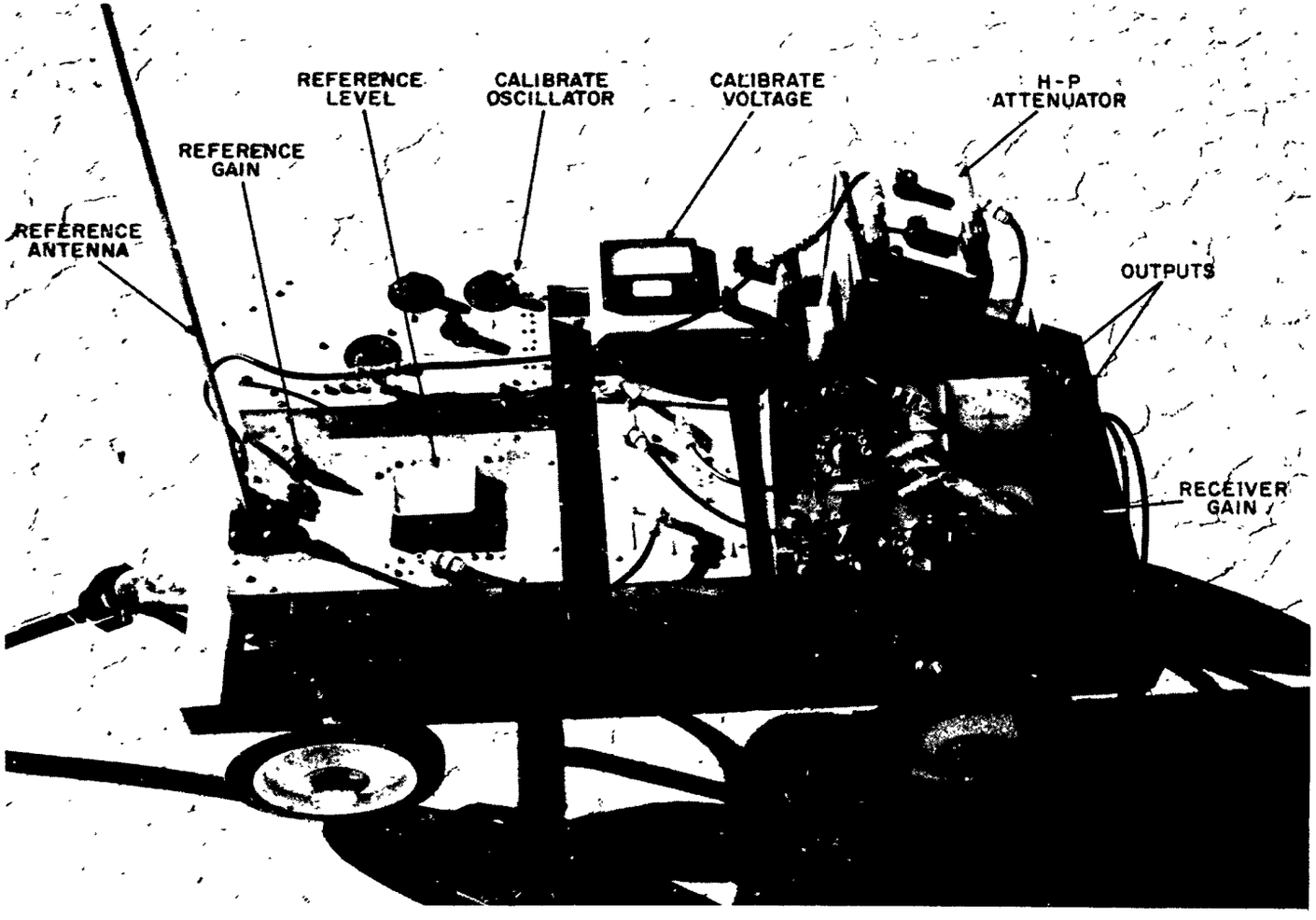

D-4427-169

FIG. 15 CW RECEIVING SYSTEM

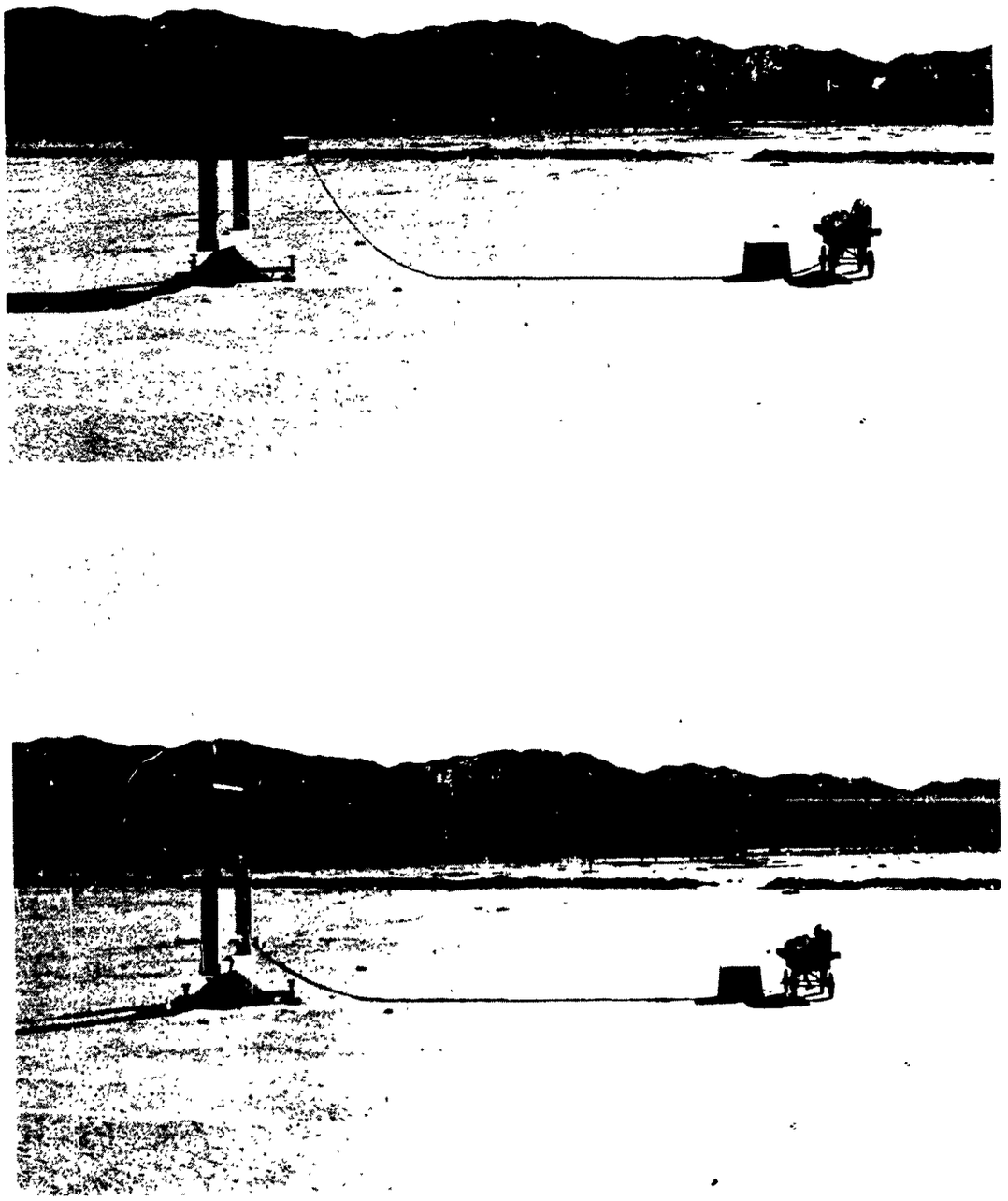

D-4427-170

FIG. 16 E- AND H-FIELD MEASUREMENT SETUP

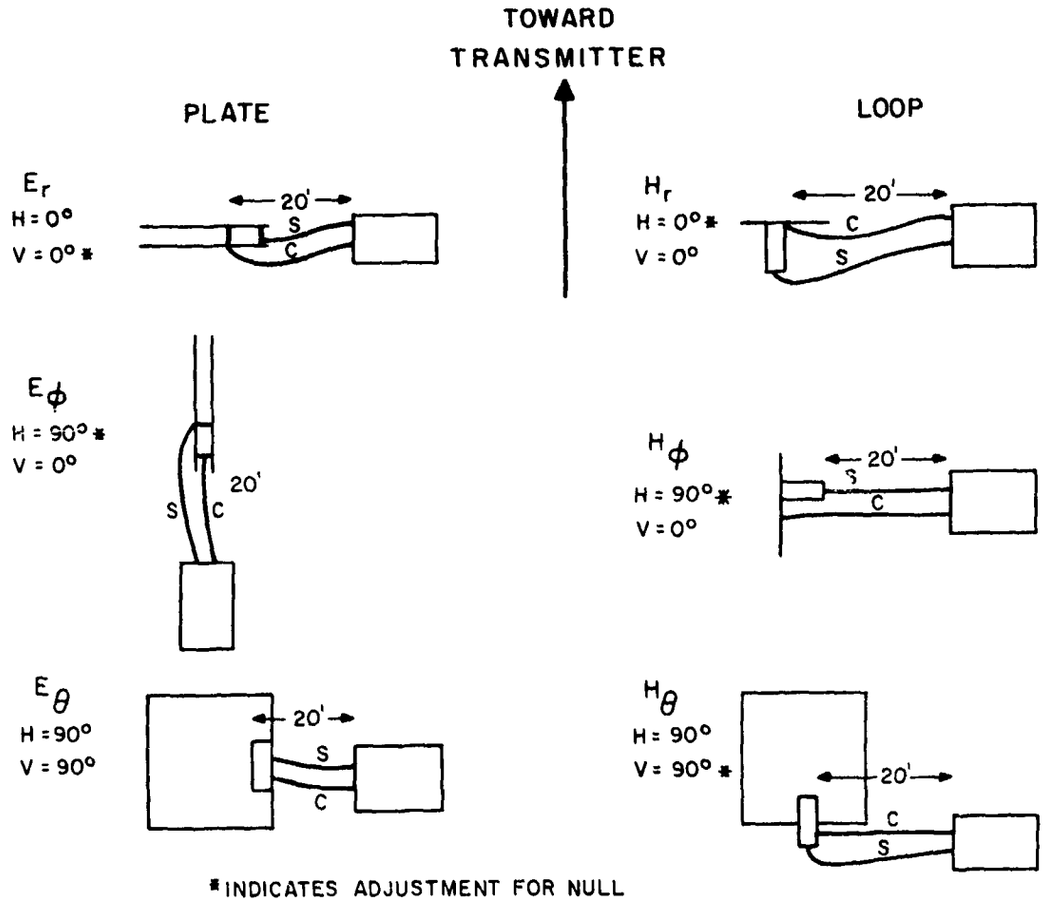

FIG. 17 E- AND H-FIELD SENSOR-RECEIVER ORIENTATIONS

system circuitry could be calibrated for each measurement. For each data point, in addition to the housekeeping functions (time, date, location, operator, equipment serial numbers, sensor, and sensor orientation), recordings were made of transmitter voltage, transmitter frequency, sensor gain setting, receiver gain setting, reference gain setting, reference signal level, and the two output signal levels (M_1 and M_2). A calibrate signal was injected* and ad-

*The calibration oscillator was off during signal measurements.

justed in frequency to give a zero beat (with the transmitted signal) in the reference receiver. The zero beat was within a few cycles per second at the highest frequency (510 kc) and to within one or two cycles per minute at the lowest frequency (500 cps). To insure a maximum phase error less than 5 degrees, the calibrate signal frequency had to be within 0.1%** (or better) of the transmitted frequency. With the transmitter off, the HP attenuator was then adjusted to give outputs near those recorded when measuring signal. Voltage into the HP attenuator, HP attenuator setting, reference signal level, and the two output signal levels was recorded along with the outputs when the HP attenuator was at a maximum (110 db). This last measurement was used as an indication of the stray coupling from the calibrate signal source into the receiving system and indicated calibration validity. This recording procedure gave an accurate measure of receiving system gain and included redundancy in the form of gain settings to check the operator and the calibration.†

The recorded data was computer processed to give signal amplitude:

$$|S| = \frac{V_{cal}}{RK} \frac{A_{sig}}{A_{cal}} \frac{10^3}{V_a} \tag{52}$$

where

$|S|$ = Amplitude in 10^{-6}units/10^3 antenna volts

V_{cal} = Calibration voltage in 10^{-6} volts

$20 \log R$ = HP attenuator setting

K = Sensor calibration constant

**Receiver predetection filter has a Q of 50.
†Each component of the receiving system was periodically checked to verify that system gain was known and essentially stable for each gain setting.

A_{sig} = Signal amplitude using Eq. (50)

A_{cal} = Calibrate amplitude using Eq. (50)

V_a = Transmitter antenna voltage,

and signal phase:

$$\text{phase } S = \text{Phase } A_{sig} - \text{phase } A_{cal} \tag{53}$$

where phase is determined using Eq. (51).

In addition, the computer indicated when the gain measured during calibration was incompatible (± 50%) with known system gains from gain settings, and the value of the calibration pickup in percent of full-scale output. Whenever the computer indicated a gain error in the system, that data was not used unless a reasonable recording error could be demonstrated. The calibration pickup normally was below 1 or 2 percent of full-scale output; exceptions generally being with system gain at maximum (small signal levels).

2. Electric Field Sensor (Plate)

The electric field sensor was a parallel-plate antenna whose effective height or area and capacitive reactance were measured. The sensor was tuned with a Q of about 5 at each frequency (the frequencies are listed in Table II), so that neither short-circuit nor open-circuit assumptions are valid for determining the sensor sensitivity. The sensor capacitance was determined by substitution of a high-quality capacitor in place of the sensor. The substitution capacitor was selected to give a tuned frequency within 0.1% of the values in Table II. For this measurement the sensor matching network was non-terminated (high Q). The capacitor was made of two series capacitors (368.1 and 368.1 $\mu\mu$f) giving an antenna capacitance of 184 $\mu\mu$f. These capacitors were used as a dummy antenna for other measurements described below.

The effective height of the electric field sensor was measured by comparison with a plate antenna of known area. A one-square-meter section

Table II

SENSOR PARAMETERS

Plate				Loop		
Tuned Frequency (kc)	Common Mode Rejection (db)	Calibrate Ratio	Calibrate Constant (K_p)	Tuned Frequency (kc)	Calibrate Constant (K_L)	Current Pickup Calibrate Constant (K_I)
0.495	67.9	193	30.5	0.505	7100	600
0.993	75	193	30.5	0.996	7100	600
1.995	59.8	184	20.1	1.997	7100	600
4.980	56.5	193	30.5	4.989	7100	600
10.022	68	197.5	31.2	9.989	7100	600
20.555	58.1	207	32.7	20.601	7100	600
62.026	75.3	197.5	31.2	61.973	7100	426
100.017	73.7	200	31.6	100.194	7100	426
200.227	62.9	212	33.5	200.749	7100	426
451.380	67.2	224	35.4	449.919	7100	426
510.281	66.3	224	35.4	508.770	7100	426

of a large ground plane was isolated from ground with a 5-mil gap.* The short-circuit current was measured to determine the vertical electric field E_θ impinging on this one-square-meter area. For such an antenna,

$$I_{\text{short circuit}} = 2\pi f \epsilon_o A_p |E_\theta| \tag{54}$$

where

f = Signal frequency

*The 5 mil-gap insures that the maximum error in area is less than 0.1%.

$$\epsilon_o = 8.854 \times 10^{-12} \text{ farads/meter}$$

$$A_p = \text{Area in square meters.}$$

By measuring the vertical electric field E_θ at the same time and location with the system parallel-plate field sensor, the effective height of the electric field sensor was found to be 0.158 meters.

The calibration signal for the electric field receiving system was injected through a nominal 2- $\mu\mu$f capacitor onto the sensor. The capacitance used to determine the sensor capacitance was used as a dummy sensor to measure the ratio of the injected calibration signal to the sensor signal. This ratio is shown in Table II along with the value of K_p for Eq. (52) and the common mode rejection in db.* The variation with frequency occurs since a new matching network with its associated stray capacitances is switched in at each frequency.

3. Magnetic Field Sensor (Loop)

The magnetic field sensor is a single-turn square loop made of 2-inch-diameter aluminum pipe. The center-to-center distance on the loop is 58 inches for a loop area of 2.17 square meters. The loop reactance was measured to be 3.92 microhenries. The loop-antenna calibration signal is injected through 10.19 kilohms (measured on a bridge), providing a current source for the calibration signal.

Thus

$$I_{calibrate} = \frac{V_{cal}}{R}$$

*Common mode rejection was maximized prior to the above measurements by balancing the system stray capacitance from the sensor leads to ground at each frequency.

and

$$I_{signal} = \frac{A_L \eta_o}{Lc} |H|$$

where

V_{cal} = Calibration voltage

R = Calibration resistance = 10.19 kilohms

A_L = Loop area = 2.17 square meters

η_o = 120π

L = Loop inductance = 3.92 mecrohenries

c = Velocity of light

$|H|$ = Magnetic field strength--amps/m

For a $I_{calibrate}$ equal to I_{signal},

$$\frac{V_{cal}}{H} = \frac{AR\eta_o}{Lc} = 7100 = K_L \text{ in Eq. (52)} \tag{55}$$

K_L is only as accurate as knowledge of the effective area and inductance. The inductance is probably known to no better than ±3%. Since the loop is made of 2-inch-diameter pipe, its acutal effective area may differ from that assumed. However, attempts tc accurately determine loop area using large-wire antenna theory indicated that the effective area does not vary greatly from the assumed pipe-center-to-pipe-center area.

Common-mode rejection for the loop antenna system could not be directly measured or adjusted with any degree of accuracy since it was not possible to construct a good balanced dummy antenna. Measurements did indicate that the common-mode rejection was in excess of 40 db at all frequencies.

4. Current Sensors

The current sensors were calibrated by placing a known current

through a single conductor in the sensor opening. This conductor was permanently placed on the sensor and terminated in a coax connector. For current sensor calibrations the calibration attenuator (HP attenuator) termination (600 ohms) was placed in series with the calibration cable to provide a known calibration current (voltage/600 ohms). This calibration current was compared with known currents in long conductors of various sizes (diameters) in all parts of the sensor openings. For the low-frequency sensor (Mo-permalloy), the calibration current and test current produced identical responses, giving $K_I = 600$. For the high-frequency sensor, the response to the calibration current differed from the response to current through all straight conductors by a constant, giving $K_I = 426$. This difference was due to the structure of the high-frequency sensor. The calibration and output windings were close together and on the same half of the toriod, so that coupling to the calibration winding was stronger than to a conductor through the window.

A measurement was made to determine whether the pickup device influenced the cable current. By using the ferrite pickup to monitor the current in the test wire, the response was observed as the Mo-permalloy pickup was clamped over the test wire about 100 feet down the line from the ferrite pickup. No change could be detected in the receiver output as the Mo-permalloy pickup was clamped over the wire or removed. Tests with spacings as close as 5 feet between the pickups produced similar results, leading to the conclusion that the presence of the core did not significantly affect the wire current.

The sensitivity of the current pickups to the electromagnetic fields of the transmitting antenna were also determined in the course of the measurement program. At radial distances of 500, 1000, 2000, and 3000 feet from the transmitter, the current pickups were placed on the ground in the position that was normally used when current in a radial conductor was being measured. With the transmitter on, the response of the pickup to the fields (principally azimuthal magnetic field) was measured. This response is shown in Fig. 18, where the solid curves are the response of the low-frequency (Mo-permalloy) pickup and the dashed curves are the response of the high-frequency (ferrite) pickup. A similar set of response curves was obtained with the pickups in the position that was normally used when current in azimuthal arcs was being measured.

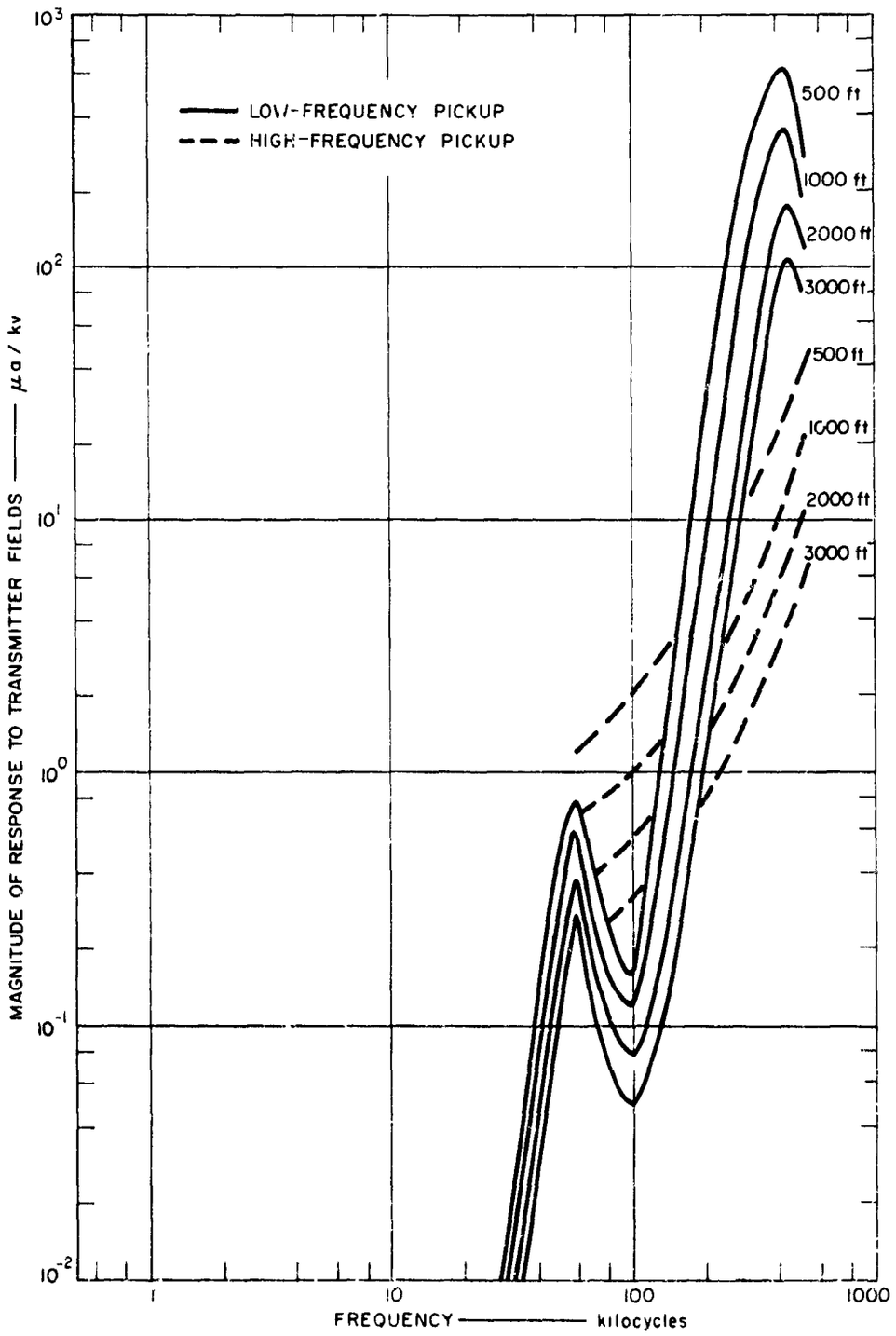

FIG. 15 RESPONSE OF CURRENT SENSORS TO TRANSMITTER FIELDS

These curves were almost identical to those of Fig. 18 except that the response was an order of magnitude (20 db) lower in this (azimuthal arc) position.

E. CW System Performance

Measurements yielding over 1700 individual data points were made to determine the system characteristics and develop operating procedures described above. These measurements were made at the location shown in Fig. 1. Upon completion of this developmental phase of the program, a series of measurements were made over a three-day period to demonstrate system performance prior to moving the system to the site shown in Fig. 2. Electric and magnetic fields were measured at 1000 and 2000 feet. These data are shown in Figs. 19 and 20. As can be seen, electric field measurements and predicted fields agree to better than 5%. Magnetic fields agree to better than 10%. These percentages do not include any averaging among data points. The good agreement between theory and measurements indicates the accuracy of both.

Cable current measurements were repeated over a three-day period and showed a maximum amplitude variation, at any one frequency, of 1.6 db or 20 percent, part of which was undoubtedly due to variations in soil conditions (see Sec. VI-B).

Phase measurements with respect to E_θ are only reliable on current measurements, on E_θ and on H_ϕ (phase during null is not easily described or measured, as is shown in Sec. II-G). Phase for these data is no better than ±5 degrees and may be ±10 degrees at the three lowest frequencies since the accuracy with which phase can be determined is a function of the zero beat accuracy between calibrate signal and transmitter frequency.

The measured null for the plate antenna was 4 degrees wide between points 20 db above the null. In normal operation the three readings near a null were made usually within one degree so that orientation of the total electric field was determined to better than one degree, referenced to the antenna mount which was accurate to about one degree. Electric field orientations were accurate to one degree from one antenna set-up to another set-up. For measurements using a single antenna set-up, the change in field orientation with frequency was accurate to about 1/4 degree.

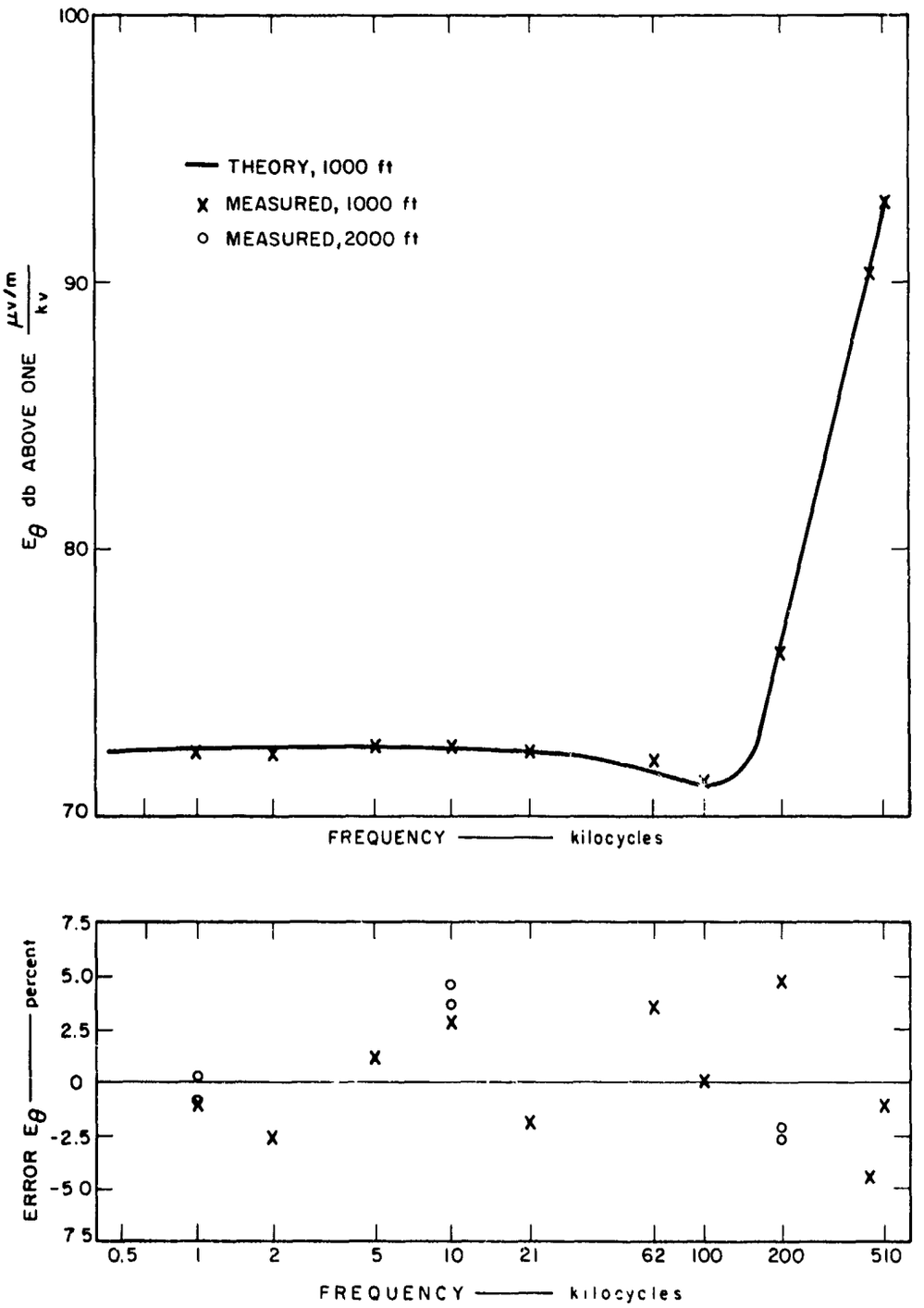

FIG. 19 SYSTEM PERFORMANCE E FIELD

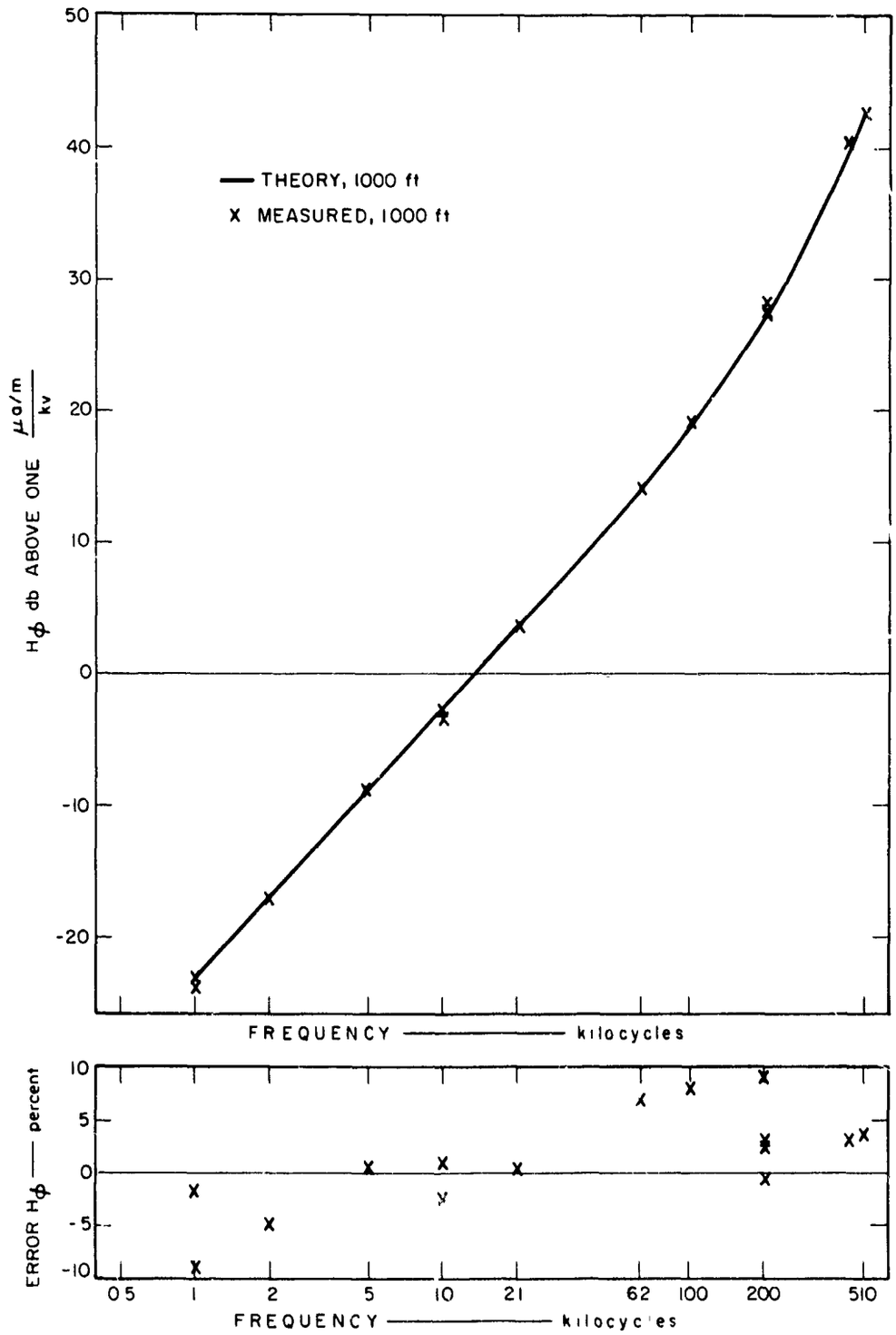

FIG. 20 SYSTEM PERFORMANCE H FIELD

The measurement of magnetic field orientation was only accurate to 2 or 3 degrees. This lesser accuracy is due to the loop null being generally 20 db above the plate null and due to the geometry of the loop. (The diameter of one side subtends a 1.5-degree angle viewed from the center of the opposite side.)

VI

WIRE-CURRENT MEASUREMENTS ON THE SURFACE

A. General

Initial wire-current measurements were made on an insulated solid copper wire lying on the surface of an unimproved roadway extending radially from the transmitting antenna in the test area shown in Fig. 1. Since this roadway had apparently been made by grading the vegetation and a few inches of surface soil off the open range land, the roadway surface was essentially equivalent to the undisturbed range land. The surface of the soil appeared to be dry and powdery, but moisture was visibly evident within two inches of the surface. During the initial wire-current measurements, a U. S. Geological Survey team measured the soil resistivity at dc, to a depth of 300 feet at the four field measurement sites along the road (i.e., at 1000, 2000, 4000, and 6000 feet from the transmitter).[1] In addition, the resistivity was measured to a depth of 4000 feet at the 2000-foot distance. While the apparent resistivity varies somewhat with depth and distance from the transmitter, the mean resistivity was of the order of 250 Ω-m.

The procedure for laying the wire was to reel the full length of the wire off onto the roadway, then stretch the wire to remove bends. When the wire was reasonably straight, the tension was removed and the wire was allowed to assume the contour of the road surface. The surface of the wire insulation was thus in physical contact with the surface of the roadway throughout its length, except at a few short dips in the roadway where the sag of the wire did not quite bring it in contact with the soil. The wire-current experiments were performed with insulated 10-gauge AWG solid copper wire of the type ordinarily used for interior house wiring. The plastic insulation (Polyvinyl chloride) on this wire is about 47 mils thick, so the outside diameter of the insulation is approximately 196 mils.

For the current pickup to be clamped about the wire, the wire had to be lifted about 4 inches off the ground and supported in the window of the pickup. The wire generally sagged enough to touch the ground within 5 feet of the pickup. Checks similar to those made with the pickup devices (see Sec. V-D-4) were made to ascertain that this slight discontinuity did not affect the wire currents.

In all cases, the wire currents were measured at frequencies of 2, 10, 62, 200, and 510 kc. All measured data presented in this section are tabulated in Appendix C, Tables C-1, C-2, and C-3.

B. Radial Insulated Wire with Ends Floating

Several experiments were conducted using insulated 10-gauge AWG wire with the ends floating (open-circuited). In the first experiment, the wire extended from a point 300 feet from the transmitter to a point 4000 feet from it. The wire current was measured at both ends and at each 100 feet along the wire at frequencies of 62, 200, and 510 kc. At the low frequencies, the current was measured at the ends and at 500-foot intervals.

The magnitude of the wire currents in the insulated, floating wire extending from 300 to 4000 feet are shown in Fig. 21, where the wire current induced by 1.0 kv of transmitter voltage is plotted as a function of distance from the transmitter for each frequency. Also indicated in Fig. 21 is the sensitivity limit of the current sensor when the sensor was 300 feet from the transmitter. The phase of the wire current relative to the phase of the local vertical electric field is shown in Fig. 22.

Since the wire was insulated and the ends were open circuited, the line is only moderately lossy. Current injected along the line therefore propagates for a considerable distance at the lower frequencies before it is dissipated through line losses. Since coupling to the line is primarily through the capacitance between the wire and ground, the coupling increases with frequency. In addition, as the frequency is increased, the electrical length of the line and the line attenuation increase. Hence, at frequencies below 10 kc the line is less than one-half wavelength and it is almost lossless, while at 200 kc and above, the line is more than one-half wavelength and the losses have become significant. At these frequencies, standing waves are apparent, and the magnitude of the current is limited by line losses rather than by degree of coupling.

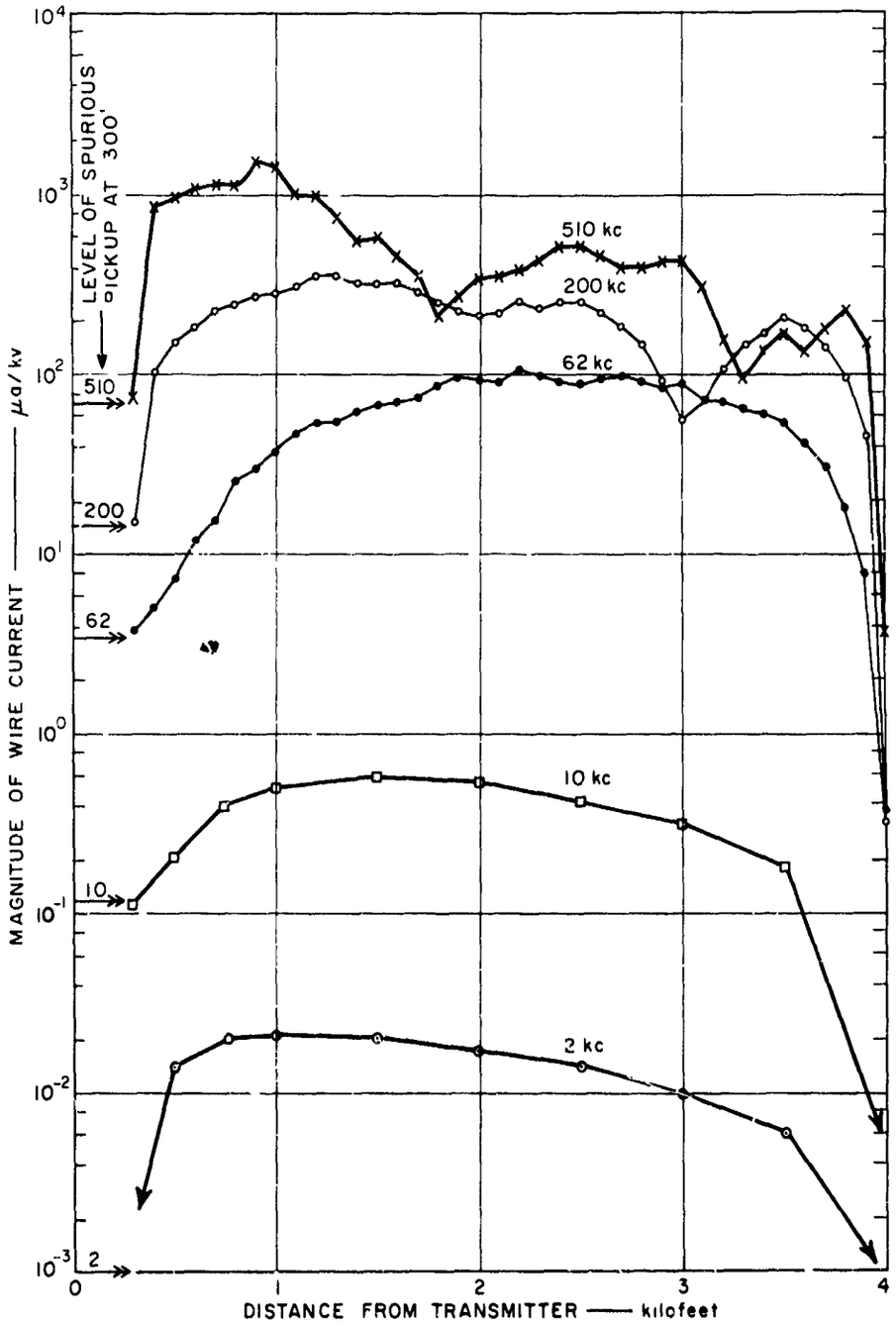

FIG. 21 MEASURED MAGNITUDE OF CURRENT INDUCED IN 10-GAUGE INSULATED WIRE

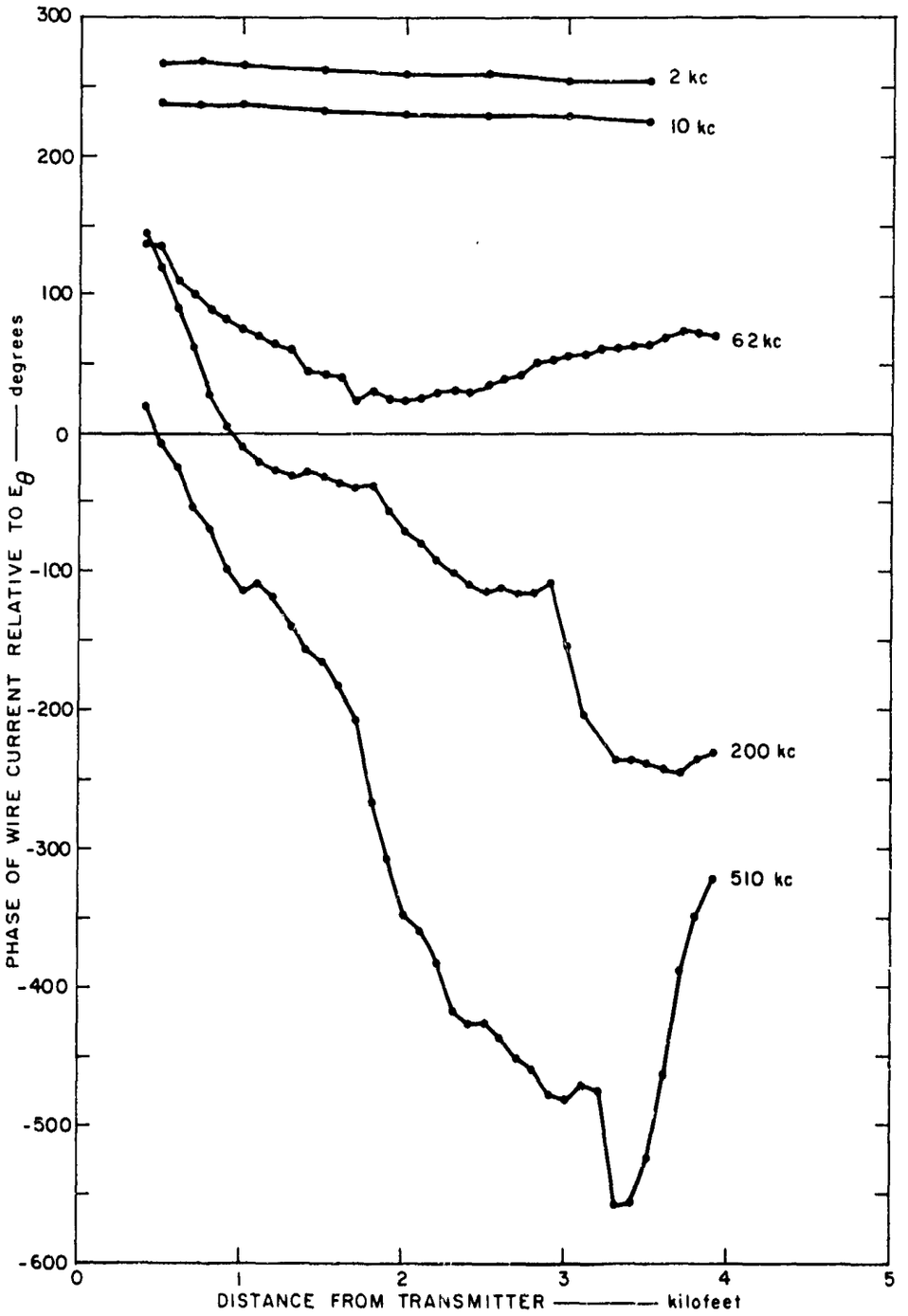

FIG. 22 MEASURED PHASE OF CURRENT INDUCED IN 10-GAUGE INSULATED WIRE

The plot of the phase of the current as a function of distance in Fig. 22 illustrates the difference between the free-space wavelength and the line wavelength. Since the phase of the current was measured using the phase of the local vertical electric field, E_θ, as a reference, only the difference between the phase of the current wave and the free-space wave was obtained. This difference is relatively constant at the lower frequencies where the line is short and entirely in the near field of the antenna. At 62 kc the phase changes considerably along the line, partly because the line length is a significant fraction of a wavelength at 62 kc, and partly because the antenna fields go through the transition from near field to far field along the length of the wire. At the higher frequencies (200 and 510 kc) the current phase changes even more rapidly with distance because of the greater electrical length of the line at these frequencies. It is also noted that the phase meanders considerably at the higher frequencies. Some of this meandering is caused by interference between the current wave propagating down the line and the current injected by the radial electric field along the line.

At 62 kc, the line appears to be somewhat longer than one-half wavelength. It was therefore decided to adjust the length of the line until it resonated at 62 kc. This was done by monitoring the magnitude and phase of the current at the center of the wire as segments of the wire were cut off and removed. Figure 23 is a polar plot of the current at the center of the wire as the wire length was shortened from 3700 feet to 2500 feet. From the polar plot, it appears that the half-wave resonance occurs at 62 kc when the wire is approximately 3250 feet long.

While the line length was 2500 feet, the current was measured as a function of distance along the line. The line length was then increased to 3250 feet and the current was again measured as a function of distance along the line. These data are plotted in Fig. 24 with the 62-kc data from Fig. 21. Comparison of the amplitudes of the current at the center of the 3250-foot-long wire in Fig. 23 with those of Fig. 24. indicate that a discrepancy exists between these current magnitudes. It is suspected that the properties of the wire as a transmission line vary considerably because of changes in the surface of the soil. If the surface of the soil dries out during the day, the effective height of the conductor

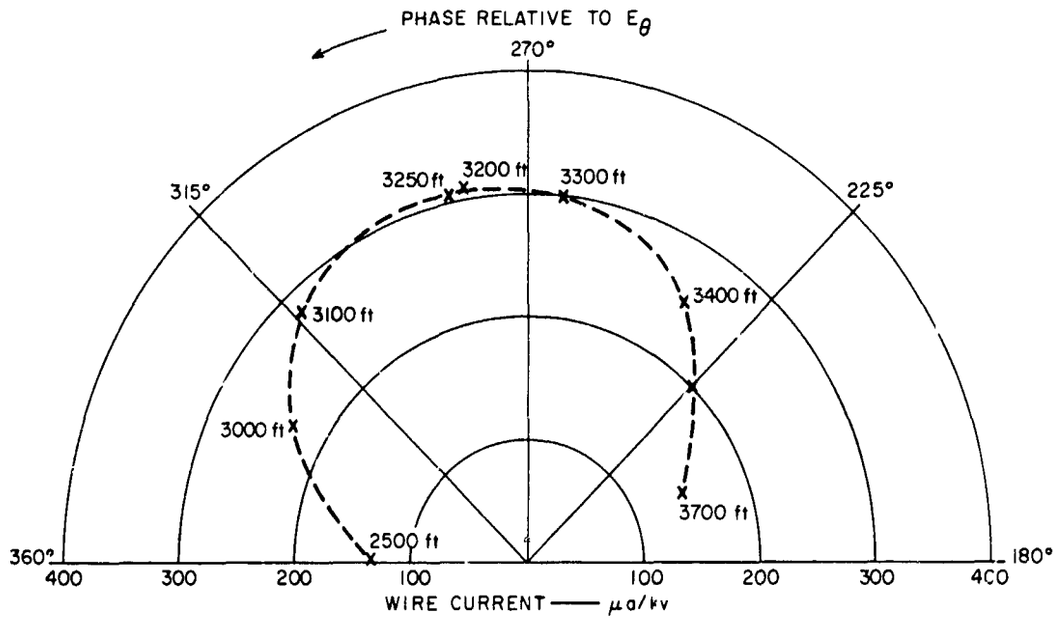

FIG. 23 POLAR PLOT OF CURRENT MEASURED AT CENTER OF WIRE AS WIRE LENGTH IS VARIED (f = 62 kc)

above the conducting soil increases and the capacitive admittance and propagation factor are correspondingly altered. Overnight, however, the surface soil may be rendered conductive by moisture absorbed from the subsoil. Thus, measurements made early in the morning of a sunny day may not be consistent with measurements made in the afternoon. The currents shown in Fig. 24 were measured on the morning after the currents of Fig. 23 were measured.

For comparison with the currents of Figs. 21 and 22, the currents were computed from Eq. (28), using Eqs. (48) and (49) to estimate the propagation factor γ. The imaginary part of γ was adjusted to agree with the value obtained from the resonant length at 62 kc. This was done by adjusting the capacitance and inductance per unit length of the line in such a manner that $\sqrt{L/C}$ remained constant. Thus, only the imaginary part of the propagation factor and the coefficient A in Eq. (29) were affected. The magnitude and phase of the computed currents are shown in Figs. 25 and 26, respectively.

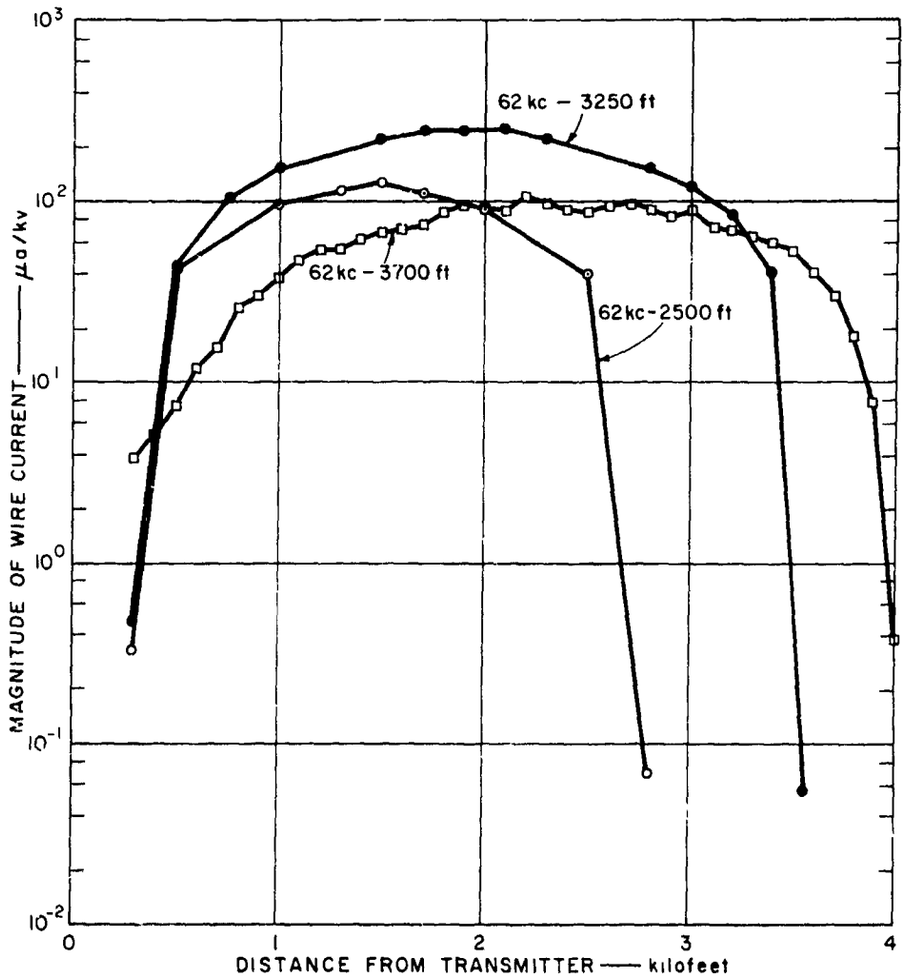

FIG. 24 INDUCED CURRENT MEASURED AT 62 kc FOR RESONANT LENGTH AND 2500-FOOT LENGTH

The form of the computed current magnitudes is remarkably similar to the form of the measured currents, particularly at 200 kc and lower frequencies. The computed current magnitudes are slightly lower than the measured currents at frequencies of 62 kc and higher and are considerably lower at 2 and 10 kc. This implies that the coefficient A in Eq. (29), which depends on the capacitance per unit length, is too small. The computation was not rerun with the corrected values of capacitance and coefficient A since it was felt that results shown in

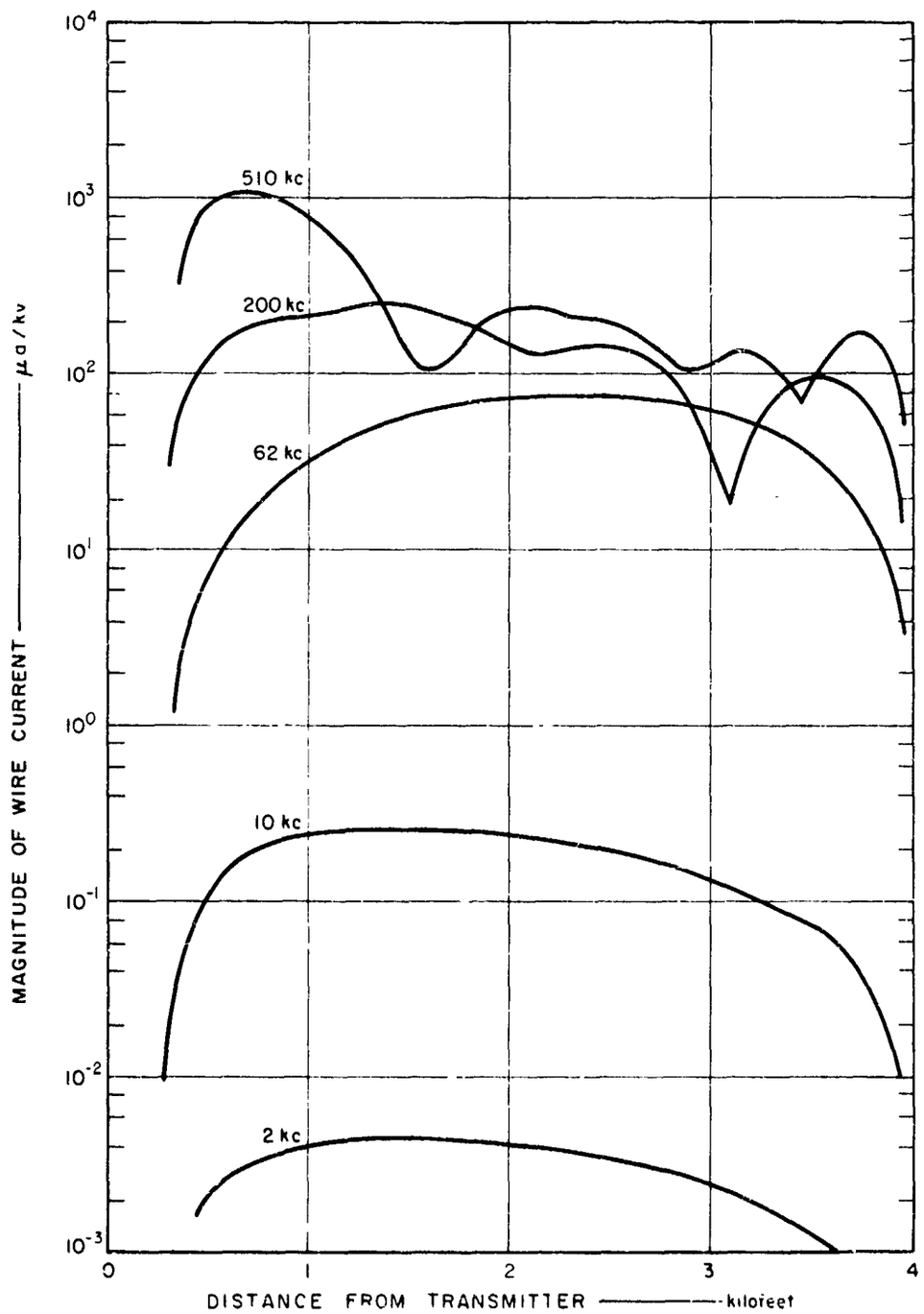

FIG. 25 COMPUTED MAGNITUDE OF CURRENT INDUCED IN 10-GAUGE INSULATED WIRE

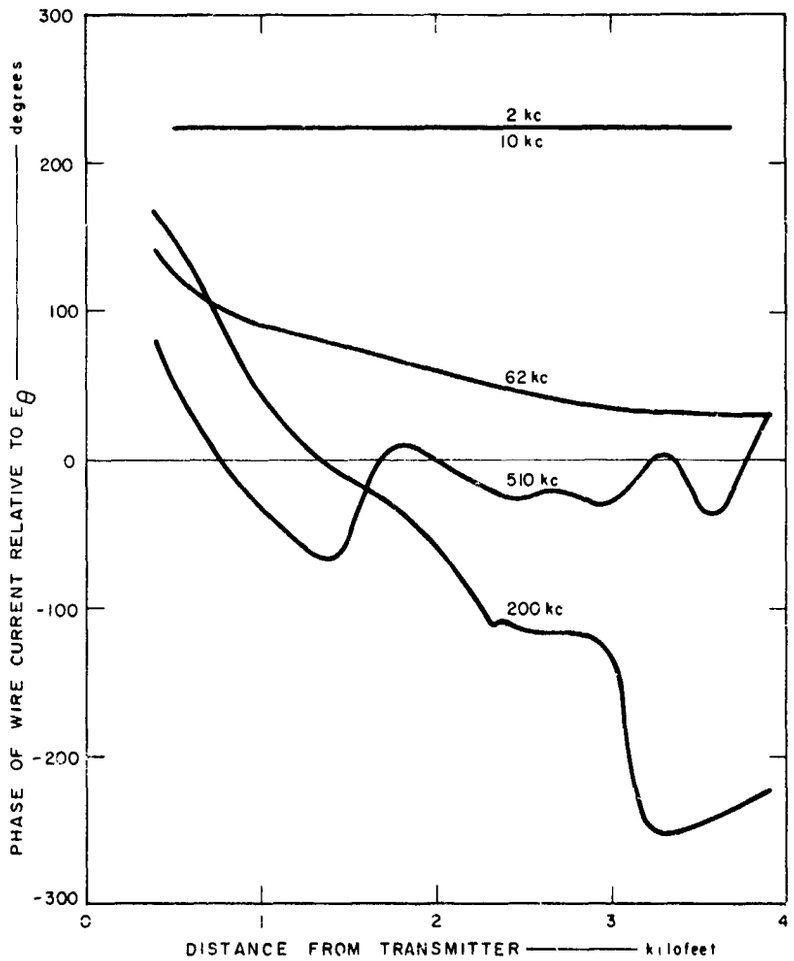

FIG. 26 COMPUTED PHASE OF CURRENT INDUCED IN 10-GAUGE INSULATED WIRE

Figs. 25 and 26 were adequate to demonstrate the validity of the cable current theory. It is noted, however, that if the capacitance were increased by a factor of about 2.3 and the inductance were reduced by the same factor, so that $(LC)^{1/2}$ remained constant, the computed currents for frequencies of 10 kc and higher would be in excellent agreement with the measured currents in both magnitude and standing wave-form. Such an adjustment of the inductance and capacitance would alter the attenuation factor, the real part of γ, but as will be discussed below, a reduction in attenuation factor is desirable at the higher fre-

quencies for better agreement with the measured phase. Even with these changes, the computed current at 2 kc will be lower than the measured current. This discrepancy is probably attributable to the high radial electric field that exists within a skin depth of the transmitting antenna. At 2 kc and lower frequencies, the end of the wire is within this high-field region.[13]

The computed phase of Fig. 26 is also in good agreement with the measured phase of Fig. 22 except at 510 kc. At 510 kc, the measured phase relative to the local vertical electric field decreased rapidly between 1000 and 2000 feet, but the computed phase increased in this interval. Thus, as the end of the wire at 4000 feet is approached, the measured phase is about 360 degrees less (more negative) than the computed phase. The reason for this peculiar behavior of the phase at 510 kc is that the line attenuation used in computing the current was higher than the actual line attenuation. Thus, in the theoretical case, the current induced in the line in the first few hundred feet of the line was so greatly attenuated in propagating a few hundred feet that it was no longer of sufficient magnitude to be the predominant factor in determining the phase. In the actual wire, however, the attenuation at 510 kc was much lower, and the large current induced in the first few hundred feet of the wire was still large enough after propagating to 2000 feet and beyond, to be the predominant current in determining the phase of the line current. This behavior is depicted more clearly in a polar plot of the magnitude and phase of the line-current phasor. In Fig. 27, the contour swept out by the current phasor at 510 kc is plotted for the measured current (dashed curve) and the computed current (solid curve). In Fig. 27, the phase angle is measured relative to the voltage applied to the transmitting antenna, and the magnitude is in microamperes of line current for each kilovolt of transmitter voltage. (The measured magnitudes have been suppressed at 900 and 1000 feet to smooth the contour). Note that the measured current phasor of Fig. 27(a) spirals around the origin twice between 500 feet and 2500 feet to produce a 720-degree phase change. In particular between 1000 feet and 2000 feet the contour encloses the origin and the current accumulates over 360 degrees of phase. The computed current phasor of Fig. 27(b) encircles the origin only once between 500 feet and 2500 feet, and between 1000 feet and 2000 feet the loop formed by the computed current does not enclose the origin; hence only about 100 degrees is accumulated in this range. Had the computed line

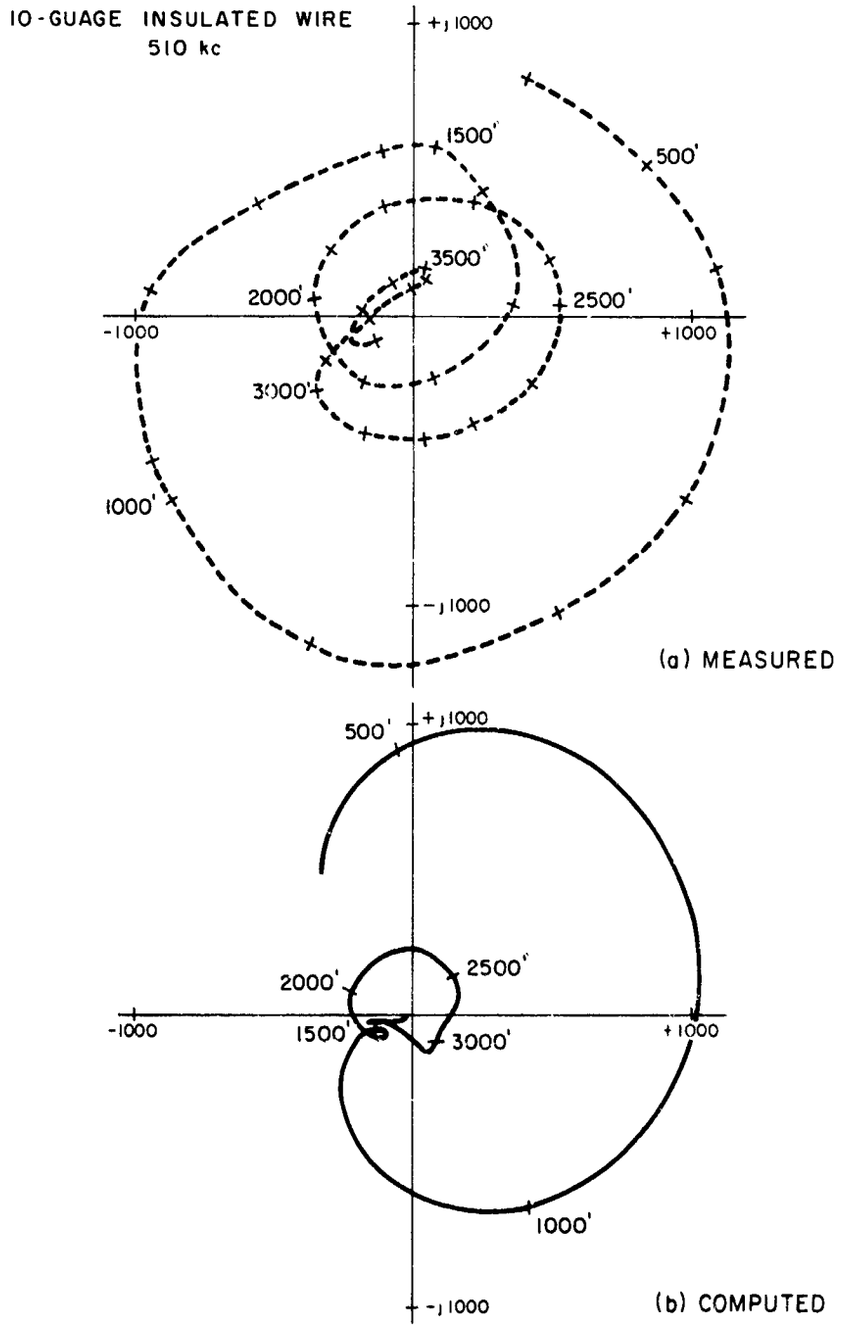

FIG. 27 POLAR PLOT OF CURRENT IN 10-GAUGE INSULATED WIRE AT 510 kc

attenuation been less, the loop between 1000 feet and 2000 feet in Fig. 27(b) would have been large enough to enclose the origin (i.e., the amplitude would not have decayed so rapidly after the first maximum) and the computed phase and magnitude would have been in better agreement with the measured phase.

It is worth nothing in this connection that Eqs. (48) and (49) lead to an attenuation factor that increases more rapidly with frequency than the propagation factor does in the 200-to-500-kc range. With the other formulas, Eqs. (40), (42), (43), and (44), the ratio of attenuation constant to propagation constant varies only slightly with frequency. For all subsequent computation, therefore, the latter formulas have been used.

C. 100-Foot-Diameter Loop

A 100-foot-diameter closed loop of insulated 10-gauge copper wire was laid out on the surface of the ground with its center 750 feet from the transmitter. The terrain in this region was typical of the undisturbed range land of the area. The surface soil was loose and sandy, and the principal vegetation was sagebrush. The sagebrush was removed along the path of the wire in an effort to bring the wire in contact with the soil, but the irregularity of the cleared surface prevented continuous contact with the soil. Imperfections in the geometry of the loop also resulted from the difficulty of stretching the wire to remove small bends in the copper. By weighting the wire down with rocks, contact with the soil was improved. The loop is estimated to have been within 8 inches of a perfect circle at all points. The insulated wire used for the loop had slightly thinner insulation than the wire used for the radial line. The outside diameter of the insulation was 170 mils.

Wire current was measured at four points on the loop -- two points at the intersection of the circle by a radial from the transmitter through the center of the circle and two points at the intersection of the circle by a line perpendicular to the radial and passing through the center of the circle. These points are illustrated in Fig. 28 and have been labeled according to the approximate bearing of the points from the center of the loop. The measured wire currents are also plotted in Fig. 28.

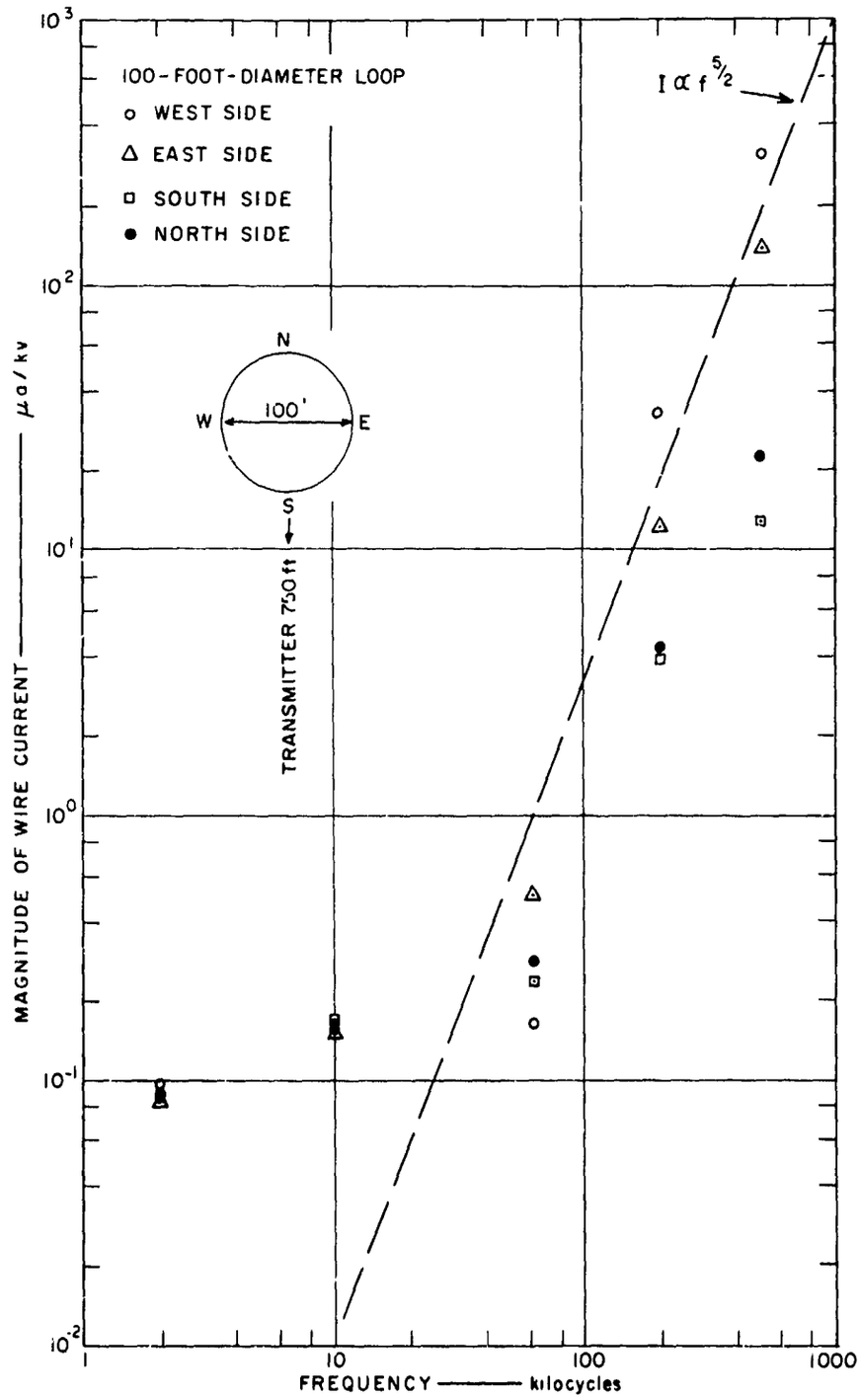

FIG. 28 MEASURED MAGNITUDE OF CURRENT IN 100-FOOT-DIAMETER LOOP

If the loop were a perfect circle lying in the plane interface between the air and the soil, one would expect that equal current would be induced in each semicircle formed by splitting the loop along the north-south diameter. At frequencies such that $\pi d/2$ = 157 feet is less than one-half wavelength on the line (i.e., below about 1.2 Mc), these currents would be maximum at the center of the semicircles (at the east and west points) and would exactly cancel each other at the ends of the semicircles (at the north and south points). Furthermore, because of the capacitive coupling between the soil and the wire, the current at a given point on the loop should increase approximately as the 5/2 power of frequency for frequencies below the first resonance. A 5/2 power line has also been drawn on Fig. 28. It should be noted that the measured high-frequency currents fall close to the 5/2 power line, but that they are not equal in magnitudes and do not cancel exactly at the north and south points.

Two imperfections in the loop probably account for most of the deviation of the actual loop currents from the ideal loop currents. One is the variation in coupling between the wire and the radial electric field in the ground resulting from irregularities in the position of the wire relative to the surface of the ground. Such irregularities affect the characteristic impedance of the line as well as the coupling. The other imperfection is the imperfect decoupling of the loop from the azimuthal magnetic field of the transmitting antenna. This coupling would predominate at the lowest frequencies, where the coupling to the radial electric field (which is frequency-dependent to the 5/2 power) is the smallest. Coupling to the azimuthal magnetic field would produce circulating currents in the closed loop, while variations in coupling to the radial electric field would tend to produce asymmetrical currents in the sides of the loop. At the low frequencies (2 and 10 kc) the current appears to originate almost entirely from coupling to the magnetic field since the magnitude of the current is the same at all points about the loop and well above the sensitivity limit of the current sensor. As the frequency is increased, however, the current appears to follow the 5/2 power curve, indicating that coupling to the radial electric field is producing the current. The inequality of the currents at the east side and west side and the failure of the currents to cancel at north and south ends

is probably caused by non-uniform coupling between the wire and the radial electric field at 200 and 510 kc. At 62 kc the measured currents are near the sensitivity limit of the current sensor, so that these data are of doubtful significance.

D. Summary

Measurements on a long radial wire on the earth's surface are shown to be in general agreement with the transmission-line theory for wire currents developed in Sec. III. This theory predicts wire currents caused by the radial electric field. Values for constants in the theory were not optimized for maximum agreement; however, suggested values to improve agreement are presented.

Wire currents in a circular loop on the earth's surface are shown to be caused by two processes. The transmission-line theory predicts the radially flowing currents in the loop. In addition, the azimuthal magnetic field (H_ϕ) couples into the loop (due to imperfect loop orientation) causing a circulating uniform current. At the higher frequencies the radially flowing currents predominate. At the lower frequencies where the radial currents are small the circulating currents predominate.

This page intentionally left blank.

VII

WIRE CURRENT MEASUREMENTS BELOW THE SURFACE

A. General

After the preliminary measurements with wires on the surface were completed, some modifications were made on the current sensors and the test system was moved to a site where a variety of buried wire and cable configurations had been installed. The low-frequency current pickup was modified so that the full 260-turn winding was used at all frequencies from 0.5 kc through 20.6 kc. This modification was made to make the sensor less sensitive to the azimuthal magnetic field of the transmitter. The electrostatic shielding of the high-frequency pickup was improved by replacing the conductive silver paint with copper-coated dielectric (printed-circuit board), and the calibration loops on both pickups were reduced in size to accommodate the larger cables.

Eight cable types or configurations were available. These included both bare and insulated cables, radial and tangential cable runs, and three loop configurations (see Fig. 2). The cable currents were measured at various distances from the transmitter at frequencies ranging from 0.5 to 510 kc. Soil resistivity[2] at the site was about 50Ω-m. All measured data presented in this section are tabulated in Appendix C, Tables C-4 through C-12.

B. Bare 10-Gauge Copper Wire (Cable Z)

This wire extended radially from a point 725 feet from the transmitter to a point 3000 feet from the transmitter. The wire was buried approximately 1 foot deep. Pits were dug to expose the wire at the points where the current was to be measured. Measurements were made at both ends and at points 1000, 1750, and 2380 feet from the transmitter.

The magnitude and phase of the wire current as a function of frequency for 1.0 kv on the transmitting antenna are shown in Figs. 29 and 30, respectively.

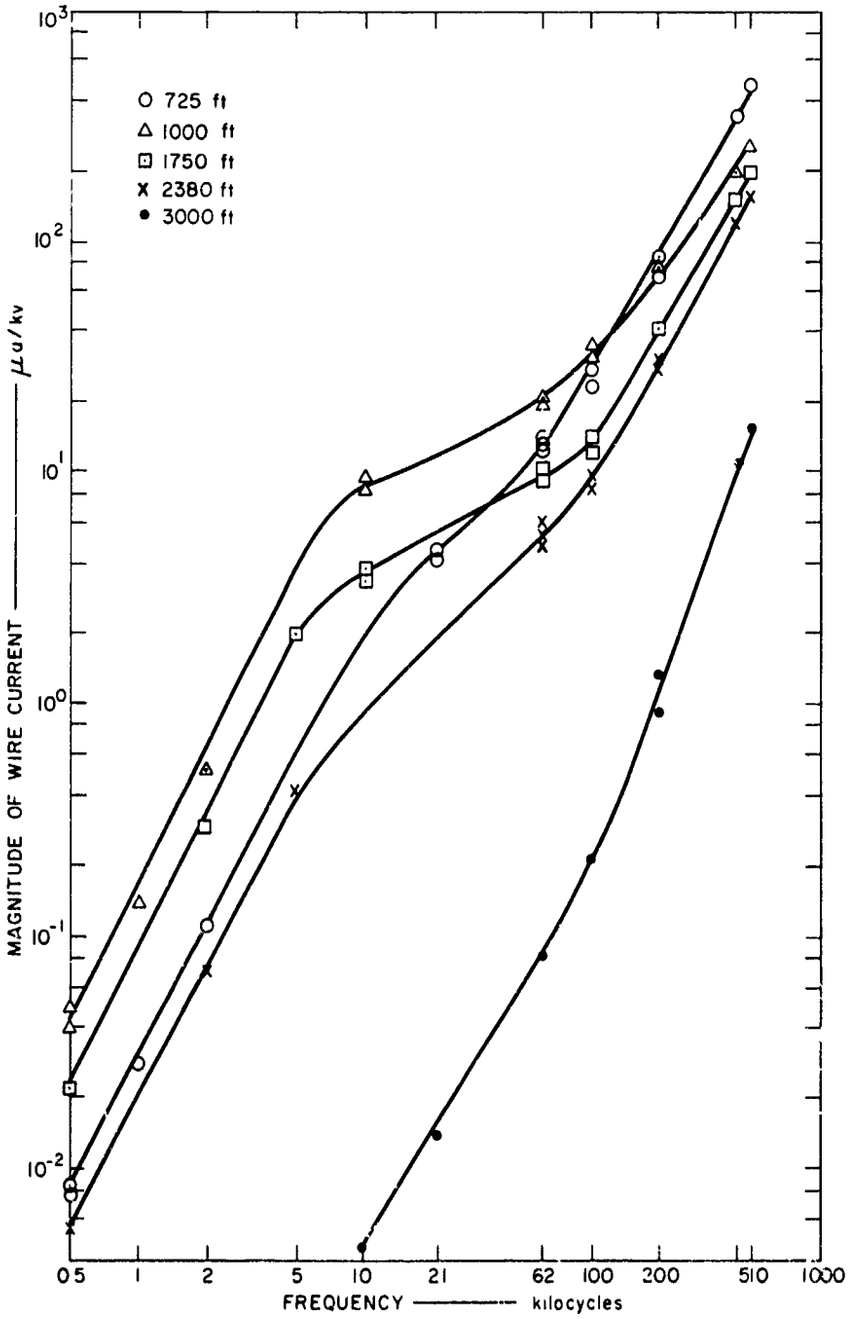

FIG. 29 MEASURED MAGNITUDE OF CURRENT IN BARE 10-GAUGE COPPER WIRE

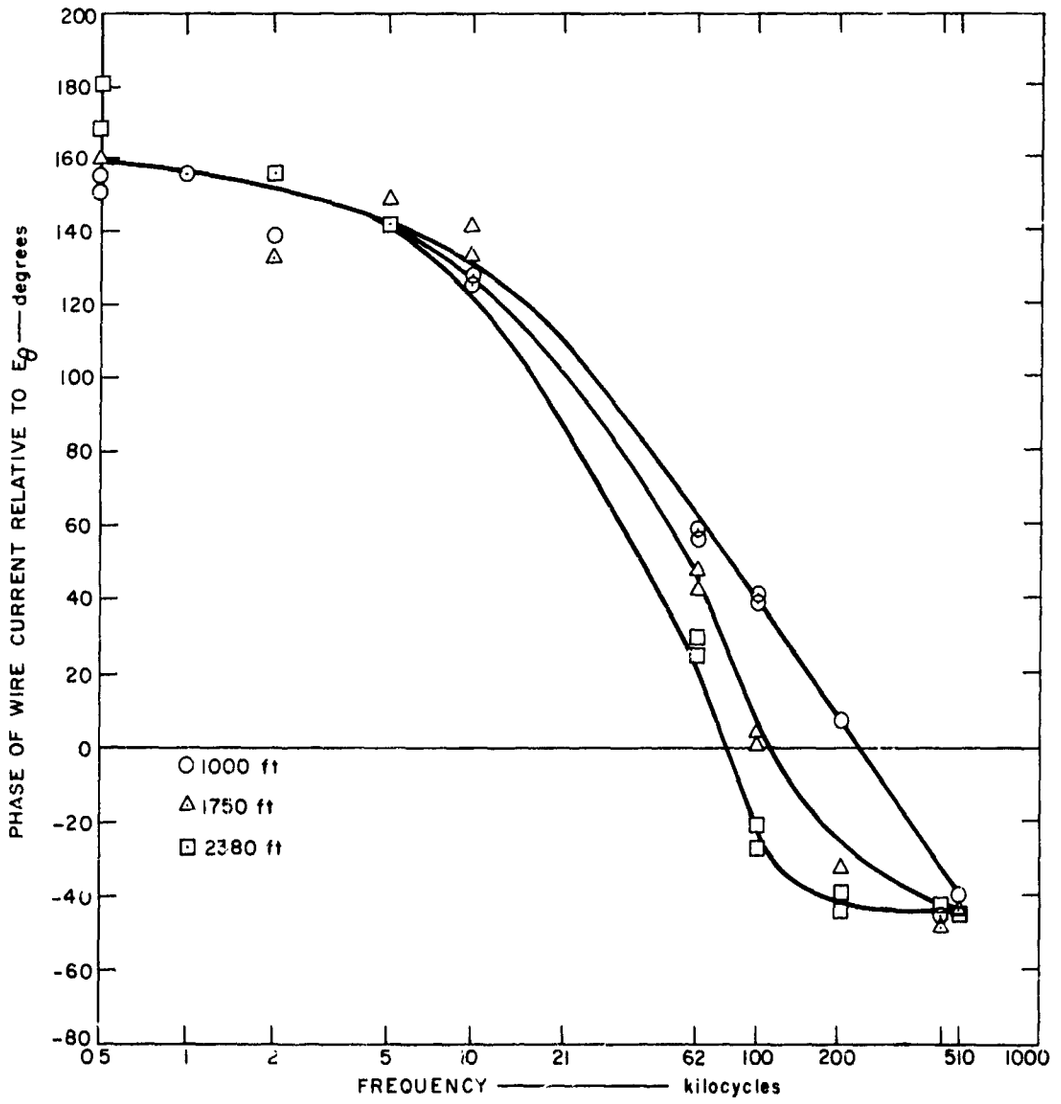

FIG. 30 MEASURED PHASE OF CURRENT IN BARE 10-GAUGE COPPER WIRE

The magnitude of the current appears to increase as the 3/2 power of frequency, although there is an offset in the curve in the 10-to-100-kc frequency range. (For a further discussion of this offset, see Sec. VII-E.)

The impedance per unit length and the admittance per unit length of the bare 10-gauge copper wire are defined by Eqs. (44) and (40). From these, the propagation factor γ and the characteristic impedance Z_0 were computed and are plotted in Fig. 31. It is noted that the real and imaginary parts of the

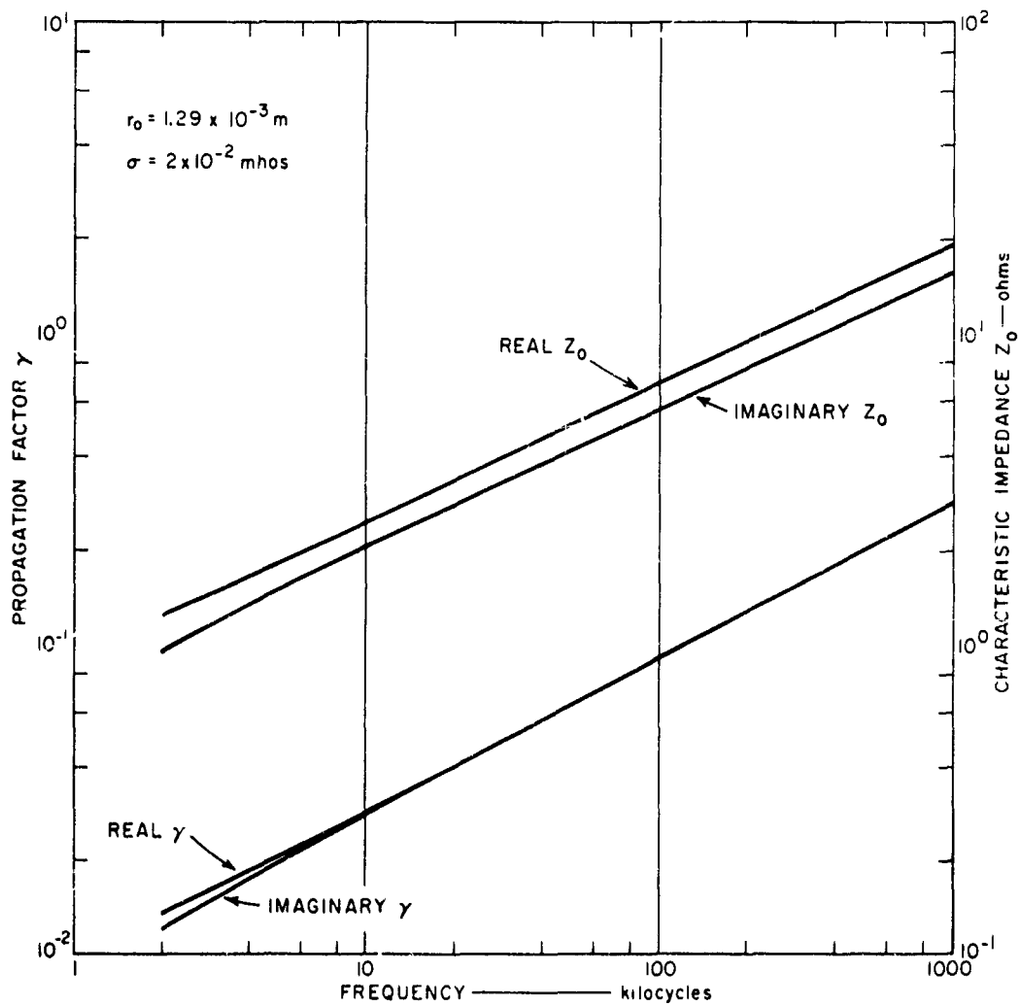

FIG. 31 CHARACTERISTIC IMPEDANCE AND PROPAGATION FACTOR FOR BURIED, BARE 10-GAUGE COPPER WIRE

propagation factor are almost equal, and that the real part is greater than 10^{-2} for almost the entire frequency range. This implies that a current in the wire is reduced by a factor of 1/3 in propagating 100 meters or less down the line (at 500 kc the current is reduced by 1/3 in propagating only 5 meters). The current at a particular point along the line is therefore dependent only on the current and fields in the immediate vicinity. Reflections are of concern only very near the end of the wire, and resonances are too heavily damped to be detected.

Using the approximation of Eq. (A-35)*, the magnitude and phase of the wire current were computed and are shown in Figs. 32 and 33, respectively. For comparison with Fig. 30, the phase relative to the local vertical electrical field (E_θ) is shown in Fig. 34. The computed magnitude of the wire current varies very nearly as the 3/2 power of frequency (for a constant antenna voltage), and the magnitude is in general agreement with the measured current magnitude. The computed phase executes a 180-degree change between 10 kc and 500 kc (see Fig. 34), agreeing well with the measured phase of Fig. 30. The theory leading to Eq. (A-35), therefore, appears to describe the bare 10-gauge-copper-wire case rather well.

C. Insulated Cable (Cable N)

Cable N was a double-shielded multi-conductor (19 pair) cable with an outer insulating jacket (polyethylene). The mean outside diameter of the outer shield (copper) was 4.4 cm, and of the plastic sheath, 5.1 cm. The cable extended radially from a point about 400 feet from the transmitter to a point 3300 feet from the transmitter.* The cable was buried about 3 feet deep. The end of the cable nearest the transmitter had been cut off, exposing the end of the shields and core wires. This end was buried without any protective cover over the exposed conductors. At the other end of the cable (at 3300 feet) the outer shield was connected to the grounded steel case of an underground bunker and the core wires were open-circuited. Measurements were made of the total current in the cable (shields and core wires) at 550, 1050, 1550, 2050, and 3050 feet from the transmitter.

*This cable originally started at 300 feet; however, because the first 100 feet had been badly damaged by earth-moving equipment, this section was removed.

*See Appendix A.

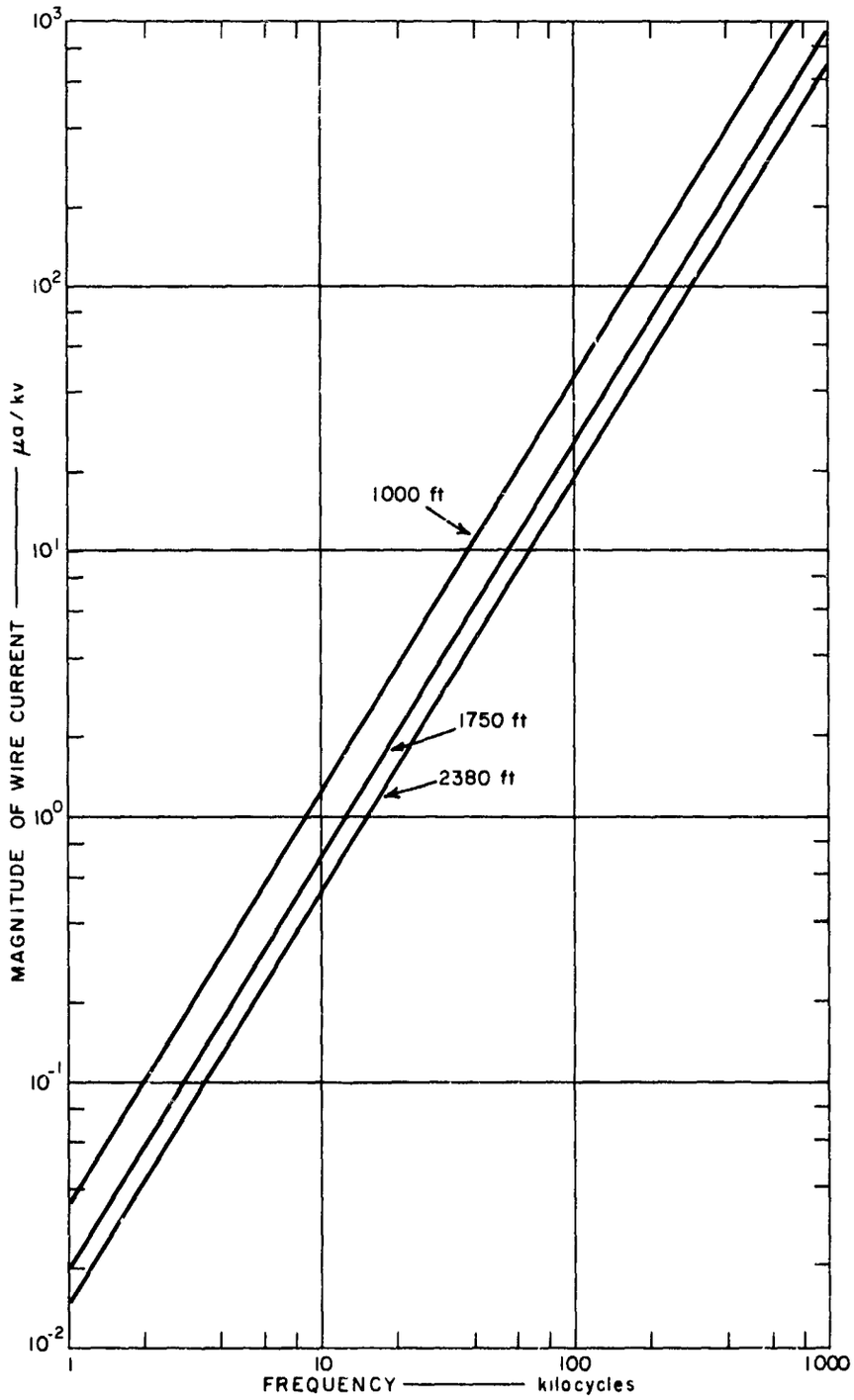

FIG. 32 COMPUTED MAGNITUDE OF CURRENT IN BARE 10-GAUGE COPPER WIRE

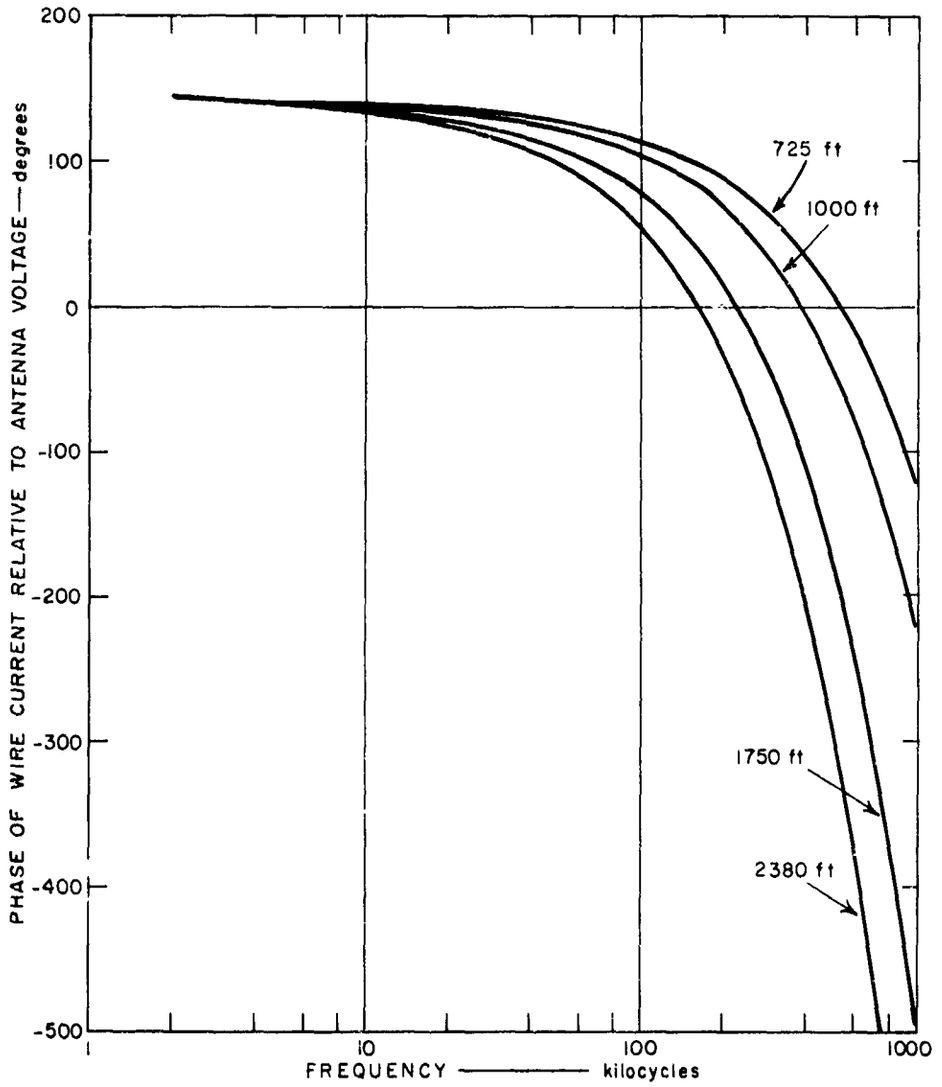

FIG. 33 COMPUTED PHASE (Relative to Antenna Voltage) OF CURRENT IN BARE 10-GAUGE COPPER WIRE

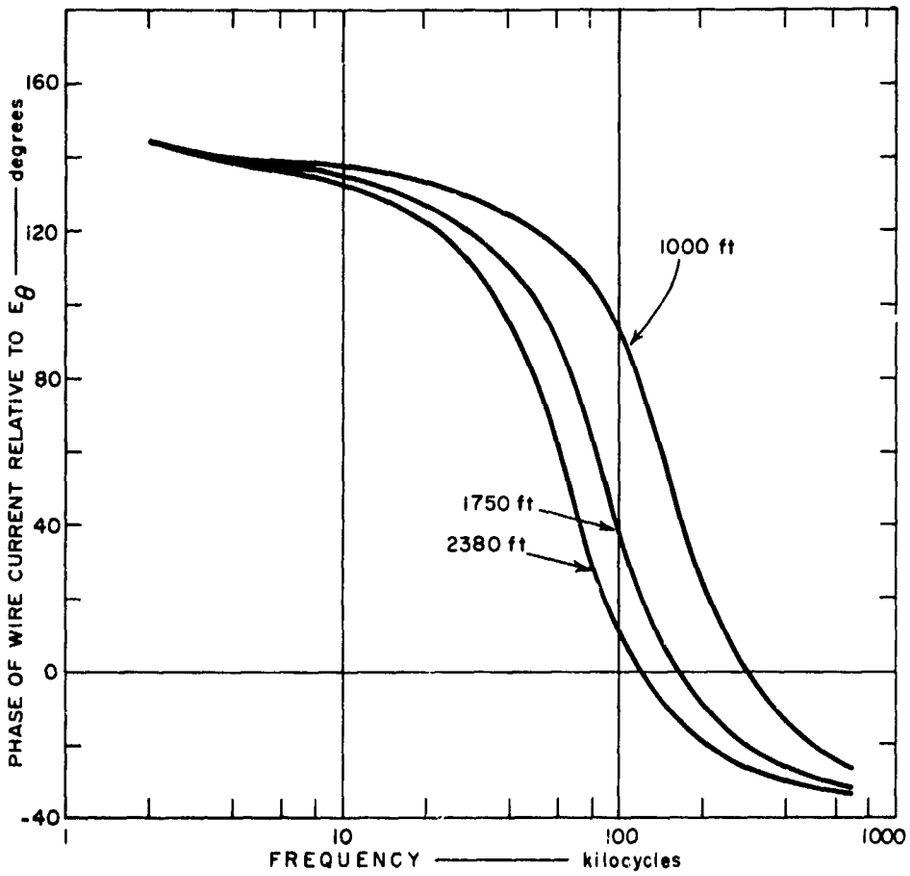

FIG. 34 COMPUTED PHASE OF CURRENT IN BARE 10-GAUGE COPPER WIRE

The measured magnitude of the current in the entire cable--core wires as well as shields--is shown in Fig. 35 for an antenna voltage of 1.0 kv. Below 10 kc, the current appears to increase as the 5/2 power of frequency, as would be expected for an insulated conductor [see Eq. (A-4), Appendix A]. Above 10 kc the magnitude of the current fluctuates somewhat with both frequency and distance from the transmitter. It was initially thought that these fluctuations indicated a discontinuity in the cable, but subsequent analysis of the cable currents indicated that such fluctuations were to be expected. A splice in the cable

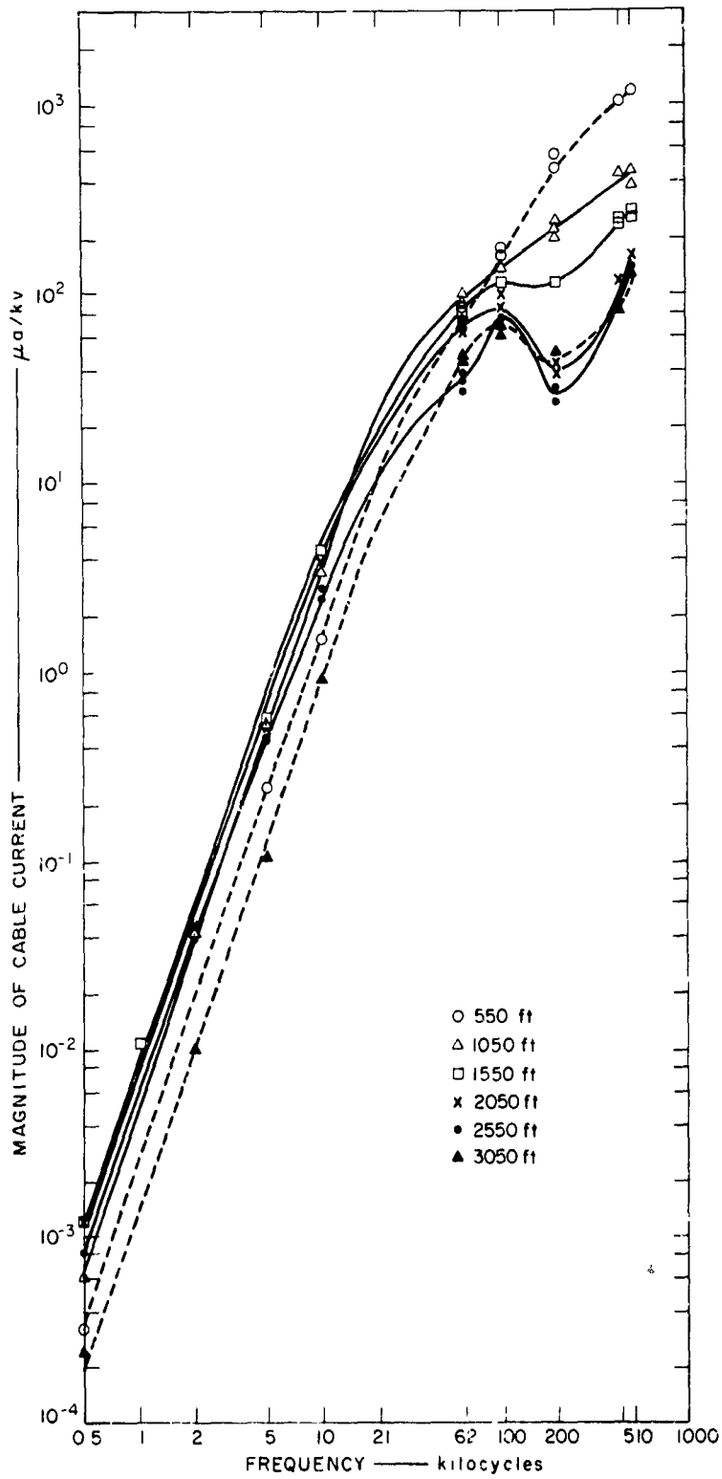

FIG. 35 MEASURED MAGNITUDE OF CURRENT IN INSULATED CABLE

was found at 2350 feet from the transmitter, and it is possible that the shields were grounded at this point. The junction box was found to contain water when it was unearthed. Because the act of unearthing the splice disturbed the contact between the cable and the soil, it is uncertain whether or not the wet splice served as a good ground. The measured phase of the current relative to the phase of the local vertical electric field is shown in Fig. 36. Above 20 kc, the actual phase is subject to a 360-degree uncertainty, since the measurement system indicates an angle of only -180 degrees to +180 degrees. Additional increments of -360 degrees were added on the basis of computed results described in the following paragraphs.

The admittance per unit length and the impedance per unit length of the insulated copper shield were computed from Eqs. (43) and (44), respectively. The propagation factor and characteristic impedance computed from these admittance and impedance values are shown in Fig. 37. In computing the impedance and admittance, it was assumed that the copper shield was a solid copper conductor, so that the impedance per unit length was somewhat in error at the low end of the frequency range. It was also assumed that the admittance of the soil was large compared to the admittance of the insulation, so that the admittance per unit length was slightly in error at the high end of the frequency range.

The magnitude and phase of the current in the shield of the insulated cable were computed from Eqs. (28) and (A-23) with 1000 ohms for the terminating impedance Z_1. The cable was assumed to extend from 300 feet to 3260 feet from the transmitter. (Note that this differs slightly from the experimental cable, which extended from 400 feet to 3300 feet from the transmitter.) The computed results are shown as a function of frequency at a distance of 2050 feet from the transmitter in Figs. 38 and 39. Of particular interest in Fig. 38 are the resonances and the high currents associated with resonances. At very low frequencies the current increases as the 5/2 power of frequency, but as the first resonance at 11.3 kc is approached, the current rises more steeply. From the first resonance frequency to about 500 kc the current amplitude fluctuates with frequency as higher-order resonances are encountered, but the mean amplitude increases only slightly with frequency. At the first resonance the current is almost two orders of magnitude higher than the current in the bare 10-

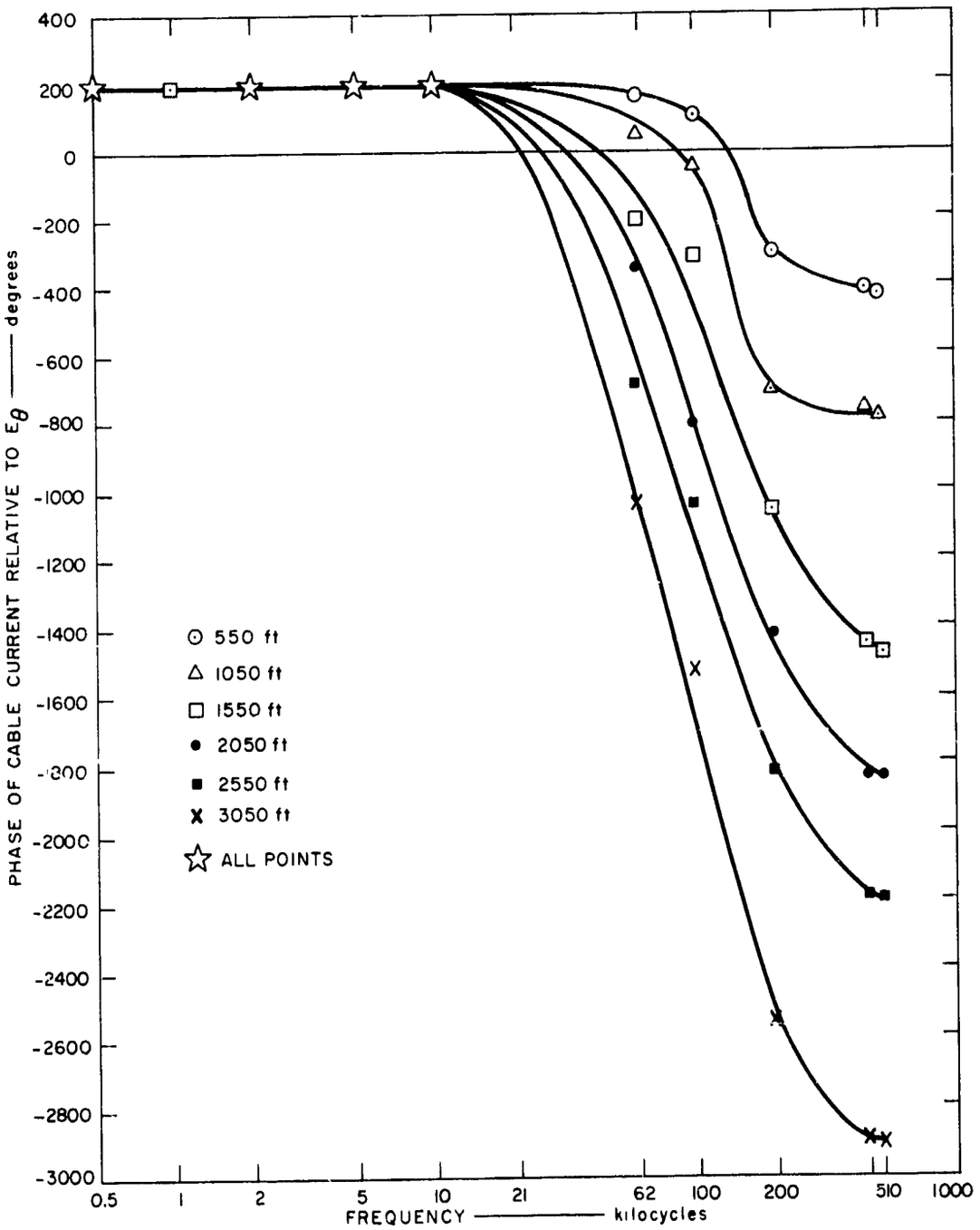

FIG. 36 MEASURED PHASE OF CURRENT IN INSULATED CABLE

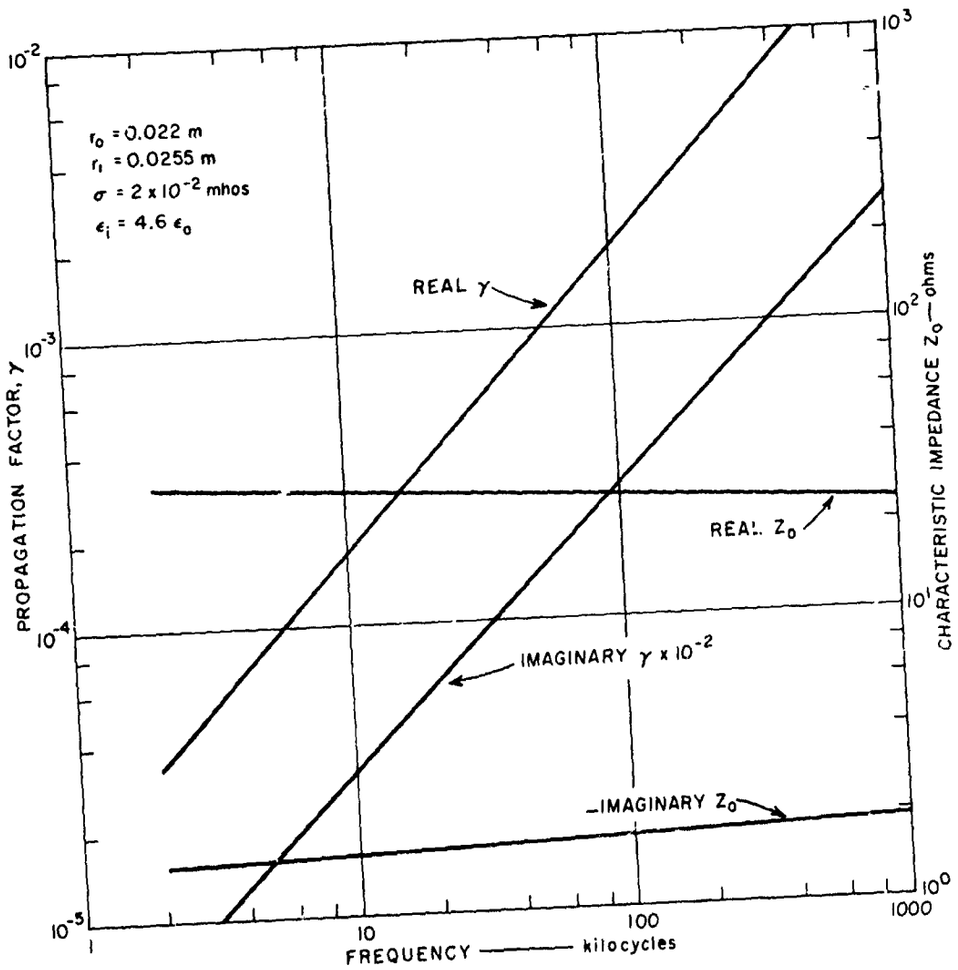

FIG. 37 CHARACTERISTIC IMPEDANCE AND PROPAGATION FACTOR FOR INSULATED CABLE

gauge copper wire at the same frequency, however. The amplitude at this resonance is dependent upon the terminating impedance and the dissipation of the insulation (the dissipation factor was assumed to be zero in the computation). It is noted from Fig. 37 that the characteristic impedance is 30 ohms or less, so that the terminating impedance Z_1, which was arbitrarily assumed to be 1000 ohms, reflects almost as well as an open circuit. It should also be pointed out that the cable on which the data of Fig. 35 were taken was terminated in a much lower impedance at 3300 feet; in fact, the actual termination may

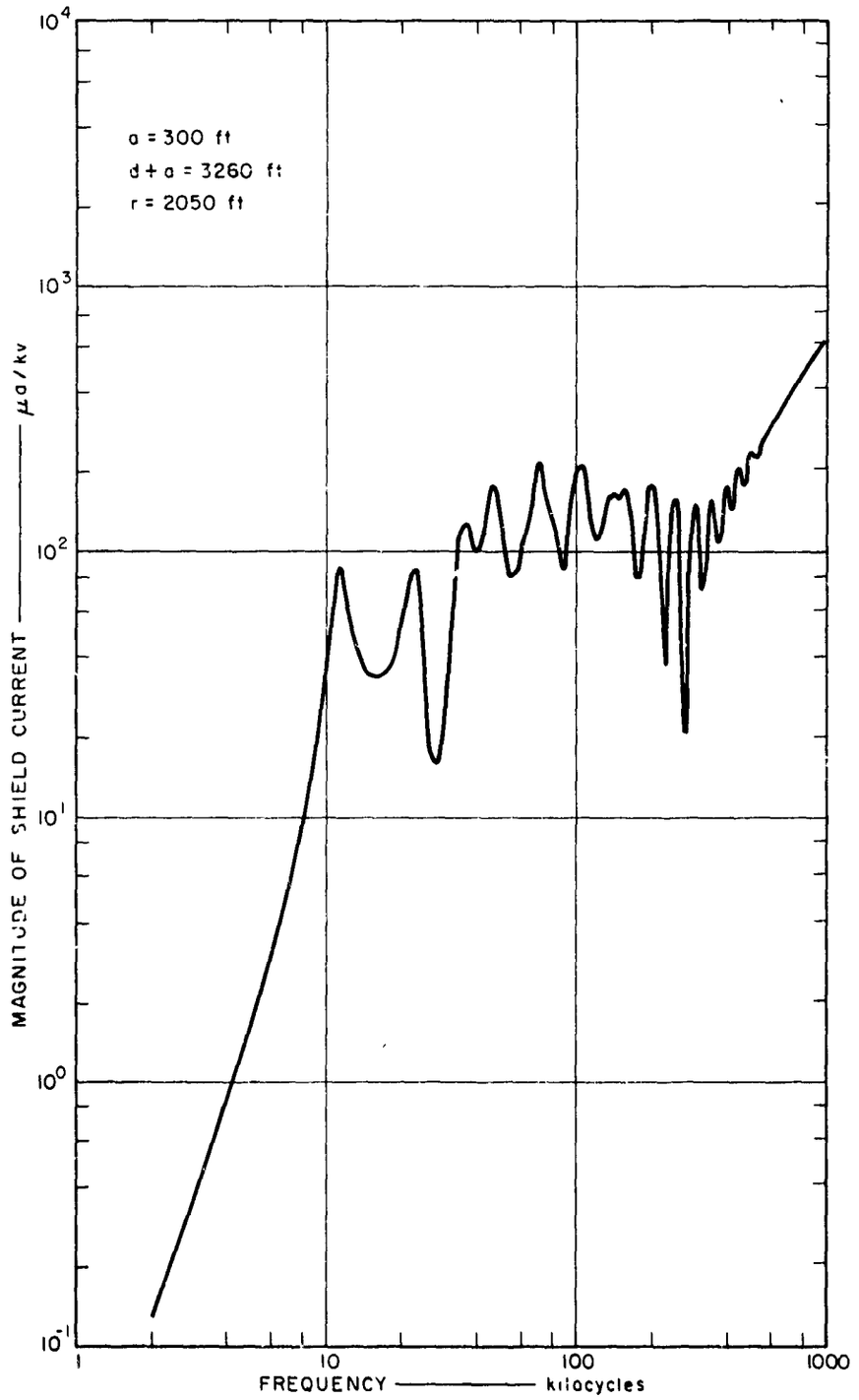

FIG. 38 COMPUTED MAGNITUDE OF CURRENT IN INSULATED CABLE

have been sufficiently close to the characteristic impedance (about 25 ohms) that reflections were minimal. At frequencies above 500 kc, the capacitive admittance per unit length becomes so high that the cable begins to behave almost as though it were bare. In this frequency range, a better approximation would have been obtained if the complete admittance function of Eq. (45) had been used instead of jB_e. Even using $Y = jB_e$, however, the current appears to approach the 3/2 power frequency variation observed on the bare 10-gauge copper wire.

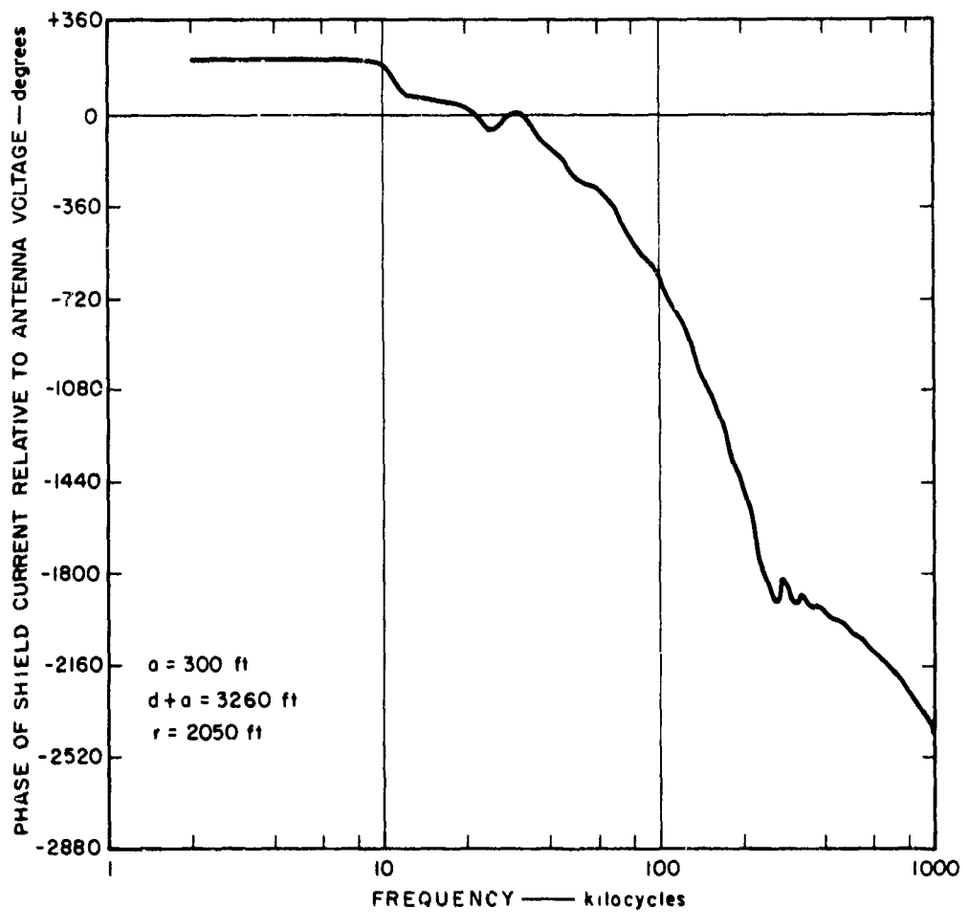

FIG. 39 COMPUTED PHASE OF CURRENT IN INSULATED CABLE

The phase of the computed shield current shown in Fig. 39 is typical of a low-loss transmission line until the frequency approaches 250 kc. At this point the rate of change of the phase changes and the phase oscillates as a new rate of change is established. It is believed that the explanation of this behavior of the phase is that above 250 kc the line attenuation is such that currents propagating from either end toward the 2050-foot point are greatly attenuated so that they do not appreciably alter the current at 2050 feet (which is assumed to have been induced in the shield near the 2050-foot point). Below 250 kc, however, the line attenuation is less, and current induced near the ends or reflected from the ends propagates without severe attenuation. Below 250 kc, therefore, the phase at a given point on the line is determined by the line length and the integrated effect of the current induced at all points along the line propagating to the point of interest, in some cases after being reflected from the terminations. It should be pointed out that the computed phase shown in Fig. 39 is the phase relative to the transmitting antenna voltage, whereas the measured phase shown in Fig. 36 is the phase relative to the local vertical electric field. Comparison of the computed and measured phases, therefore, must take into account the phase of the vertical electric field relative to the transmitting antenna voltage.

Comparison of the computed magnitude of the current in Fig. 38 with the measured magnitude at 2050 feet in Fig. 35 indicates that these currents are in reasonable agreement (within a factor of 2 or 3) except at 10 kc, where the computed current is an order of magnitude too high. It is noted that at 10 kc the computed current is on the rapidly rising approach to the first resonance, and that the current magnitude is strongly influenced by the proximity of the resonance. The frequency of the first resonance depends on the dielectric constant of the insulation, the length of the cable, and the shield termination. The height of the resonance is also a function of the dielectric loss and terminating impedance. Since the properties of the dielectric and the terminations assumed in computing the current magnitude shown in Fig. 38 were somewhat arbitrary, the frequency and current magnitude shown for the first resonance (and higher-order resonances) are not necessarily representative of the values that would be obtained in a practical installation.

D. Conducting Sheath Cable (Cable L)

This cable was identical to Cable N (Sec. VII-C) except that the outer shield of corrugated copper was covered with a sheath of conductive plastic. The mean outside diameter of the copper shield was 4.4 cm and the mean outside diameter of the plastic sheath was 5.1 cm. The cable extended radially from a point 300 feet from the transmitter to a point 3300 feet from the transmitter and was buried about 3 feet deep. The exposed end of the cable was buried without protection at 300 feet, and the shield was terminated at a grounded steel bunker case at 3300 feet. The core wires were open-circuited in the bunker. Current measurements were made at 550, 1050, 1550, 2050, and 3050 feet from the transmitter.

The magnitude and phase of the total cable current are shown in Figs. 40 and 41, respectively. Since the resistivity of the conductive plastic sheath on this cable was supposed to be much lower than the soil resistivity, it would be assumed that the outer shield would behave as a buried bare conductor. Comparison of the current magnitudes of Fig. 40 with the currents obtained for the bare 10-gauge copper wire in Fig. 29 (measured) or Fig. 32 (computed) indicates that the magnitudes and the rate of change with frequency are comparable only above 100 kc. Below 100 kc, the conducting sheath cable currents are higher than the currents in the bare 10-gauge copper wire, the discrepancy becoming greater as the frequency decreases. The current phase also exhibits a peculiar behavior. Whereas the phase of the bare copper wire current (see Figs. 30 and 34) starts at 140 to 150 degrees at the low frequencies, executes a 180-degree shift, and approaches -40 degrees at the high frequencies, the phase of the conducting sheath cable current starts at about 50 degrees at the low frequencies, executes a 90-degree phase shift and approaches -40 degrees at the high frequencies.

Because the properties of the conducting sheath cable current are also characteristic of the current in the lead sheath cable discussed in Sec. VII-E below, further discussion of this case will be deferred until the lead sheath cable measurements have been presented.

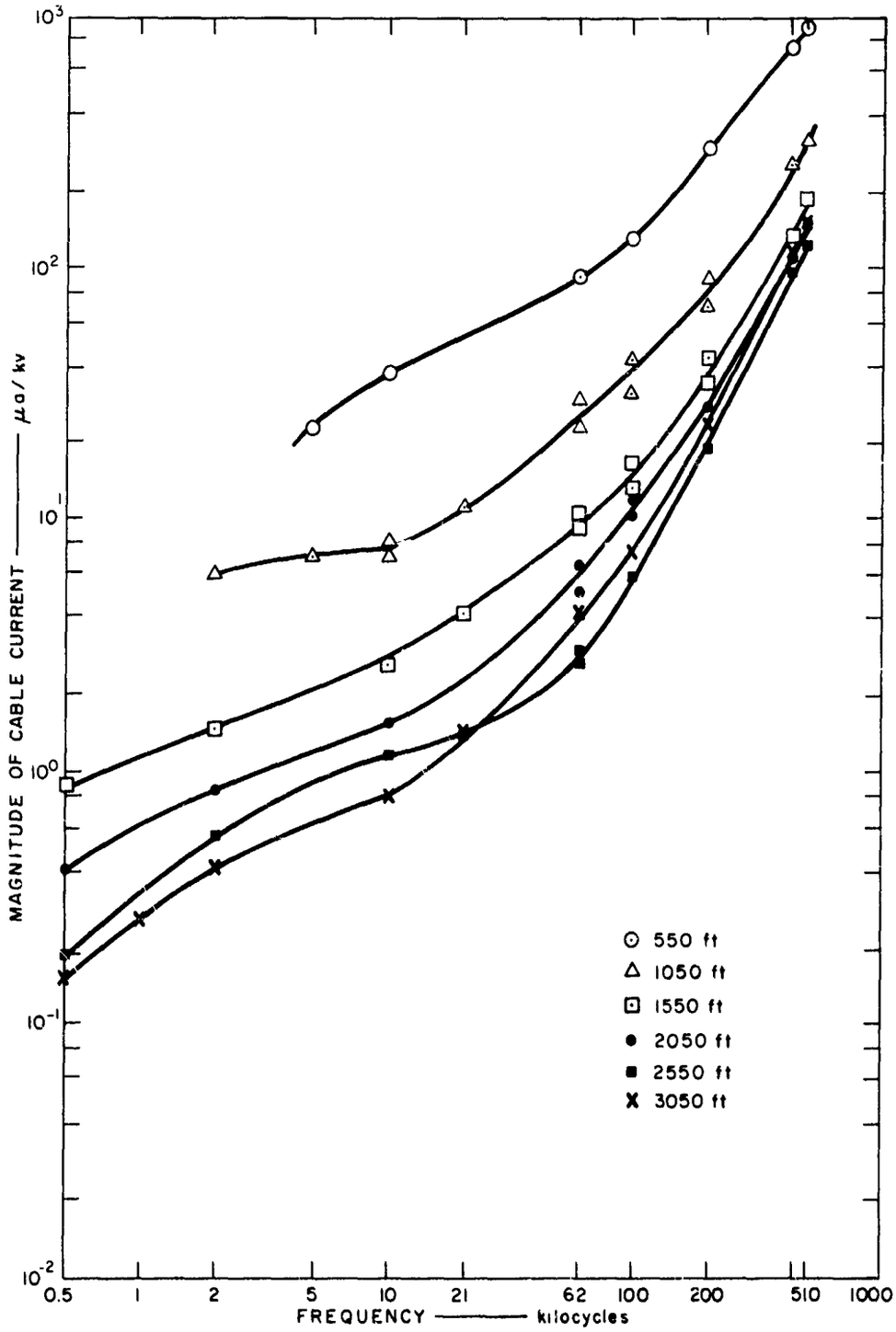

FIG. 40 MEASURED MAGNITUDE OF CURRENT IN CONDUCTING SHEATH CABLE

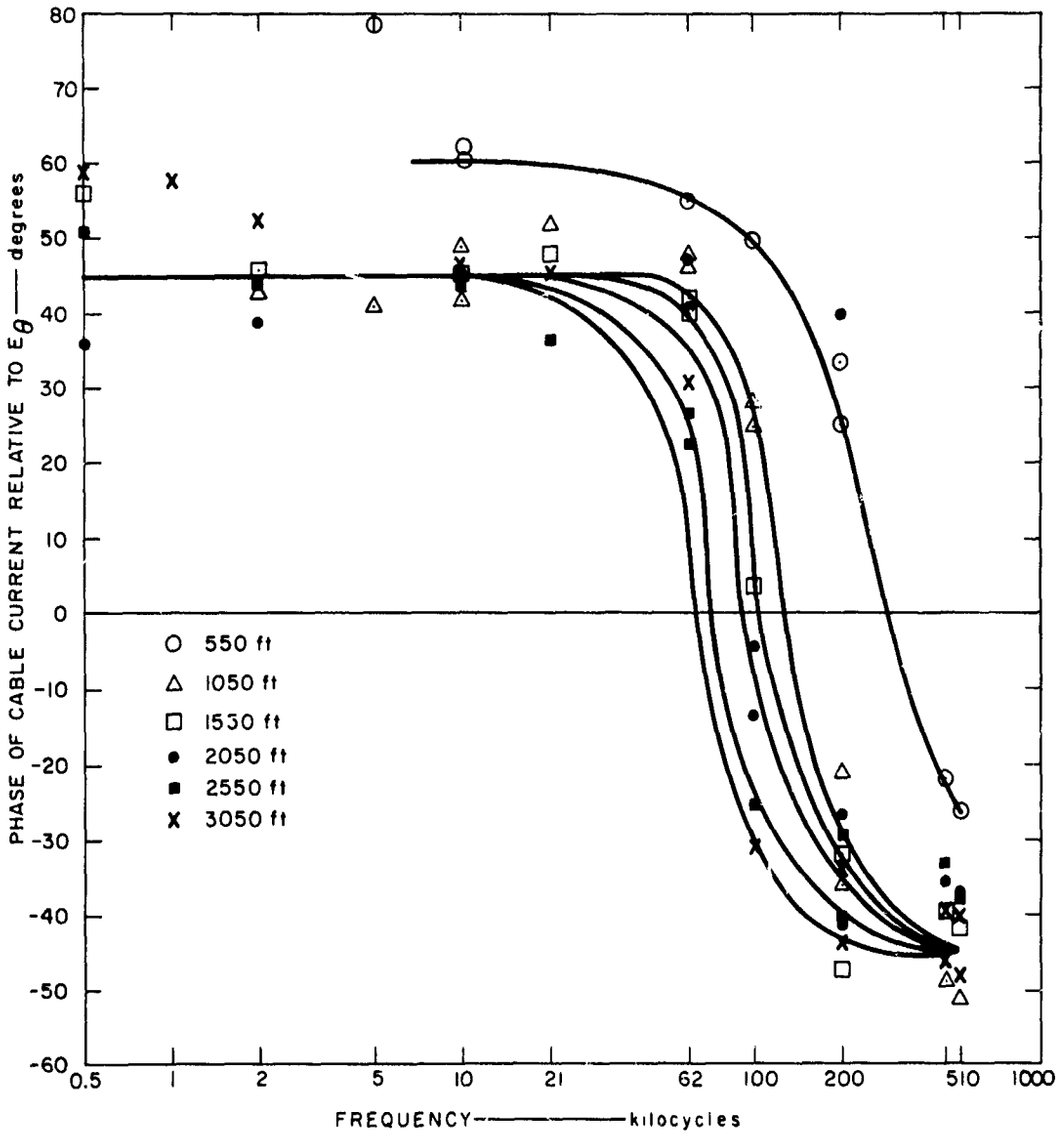

FIG. 41 MEASURED PHASE OF CURRENT IN CONDUCTING SHEATH CABLE

E. Lead Sheath Cable (Cable A)

The lead sheath cable was composed of insulated copper core wires (100 pairs) surrounded by a plastic sheath and fiber wrapper. The cable was encased in a lead sheath having an outside diameter of 4.1 cm and a thickness of about 0.3 cm. The cable extended radially from a point 170 feet from the transmitter to 6000 feet from the transmitter. The cable appeared to be continuous out to 4000 feet, but it was not determined whether or not it was continuous beyond 4000 feet. The cable was buried 4 feet deep. At 170 feet the cable end was sealed off with lead, and all conductors terminated. Currents were measured at 500, 1000, 1500, 2000, and 4000 feet.

The magnitude and phase of the currents measured in the lead sheath cable are shown in Figs. 42 and 43, respectively. As can be seen, the magnitude and phase of the lead sheath cable currents are remarkably similar to the currents in the conducting sheath cable, in spite of the fact that neither appears to be consistent with the bare copper wire data. As with the conducting sheath cable, the magnitude of the lead sheath cable current is higher (relative to the current in the bare copper wire) at the low frequencies and the discrepency becomes greater as the frequency decreases. The phase of the lead sheath cable current is also characterized by a 90-degree shift similar to that of the conducting sheath cable.

The propagation factor and the characteristic impedance of the lead sheath cable have been computed from the impedance and admittance per unit length. The admittance and impedance per unit length were computed from Eqs. (40) and (44), respectively, assuming that the lead sheath was a solid lead conductor. The computed propagation factor and characteristic impedance are shown in Fig. 44. The cable current was then computed from the approximate formula of Eq. (A-35). The computed magnitude and phase are shown in Figs. 45 and 46, respectively. As in the case of the bare copper wire, the computed magnitude varies almost as the 3/2 power of frequency, and the phase (relative to the vertical electric field) displays a 180-degree shift between 10 and 1000 kc.

Since both theory and intuition indicate that the lead sheath cable currents should be similar to the bare copper currents, one is inclined toward seeking differences in the installations that would account for the discrepancies between

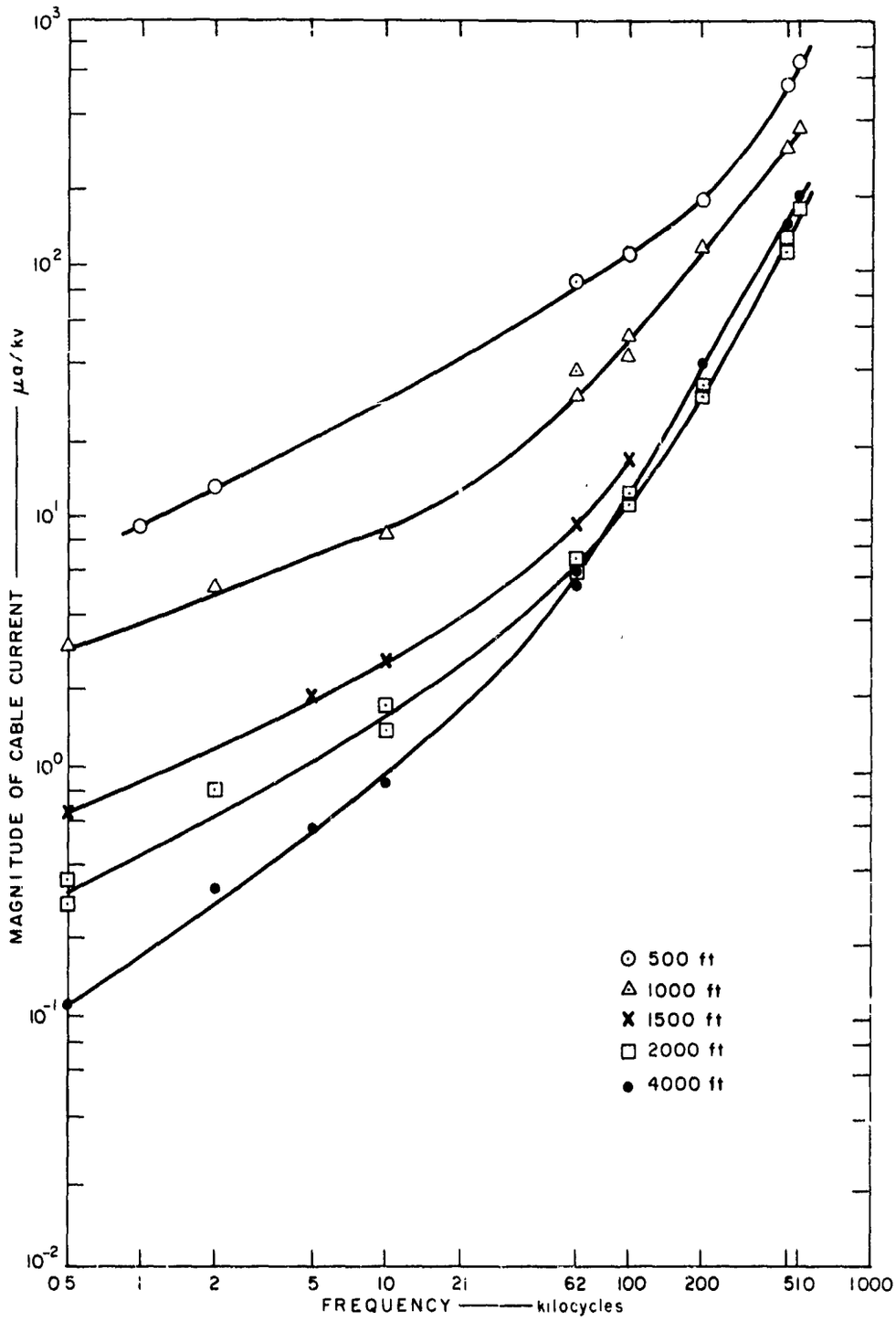

FIG. 42 MEASURED MAGNITUDE OF CURRENT IN LEAD SHEATH CABLE

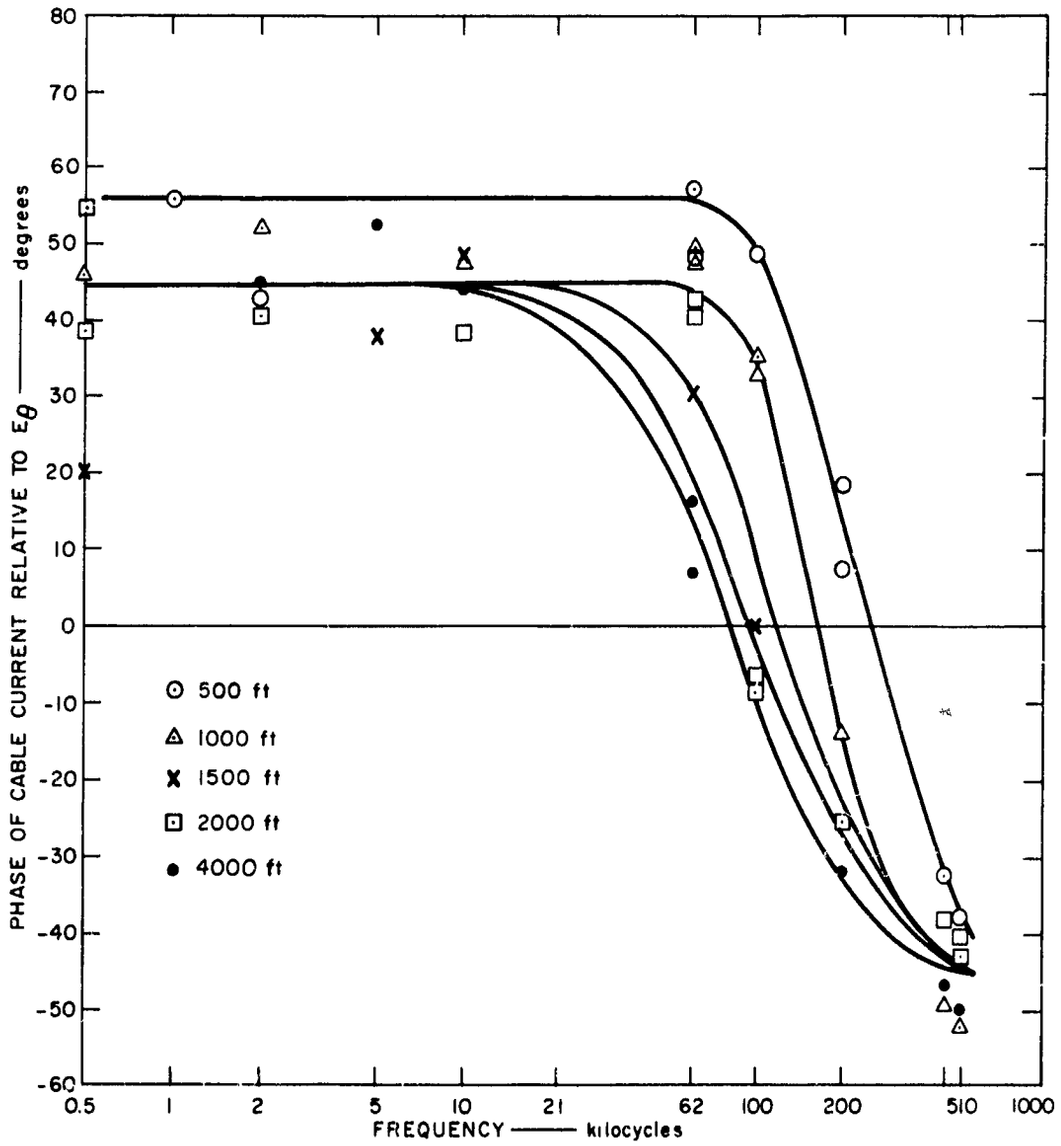

FIG. 43 MEASURED PHASE OF CURRENT IN LEAD SHEATH CABLE

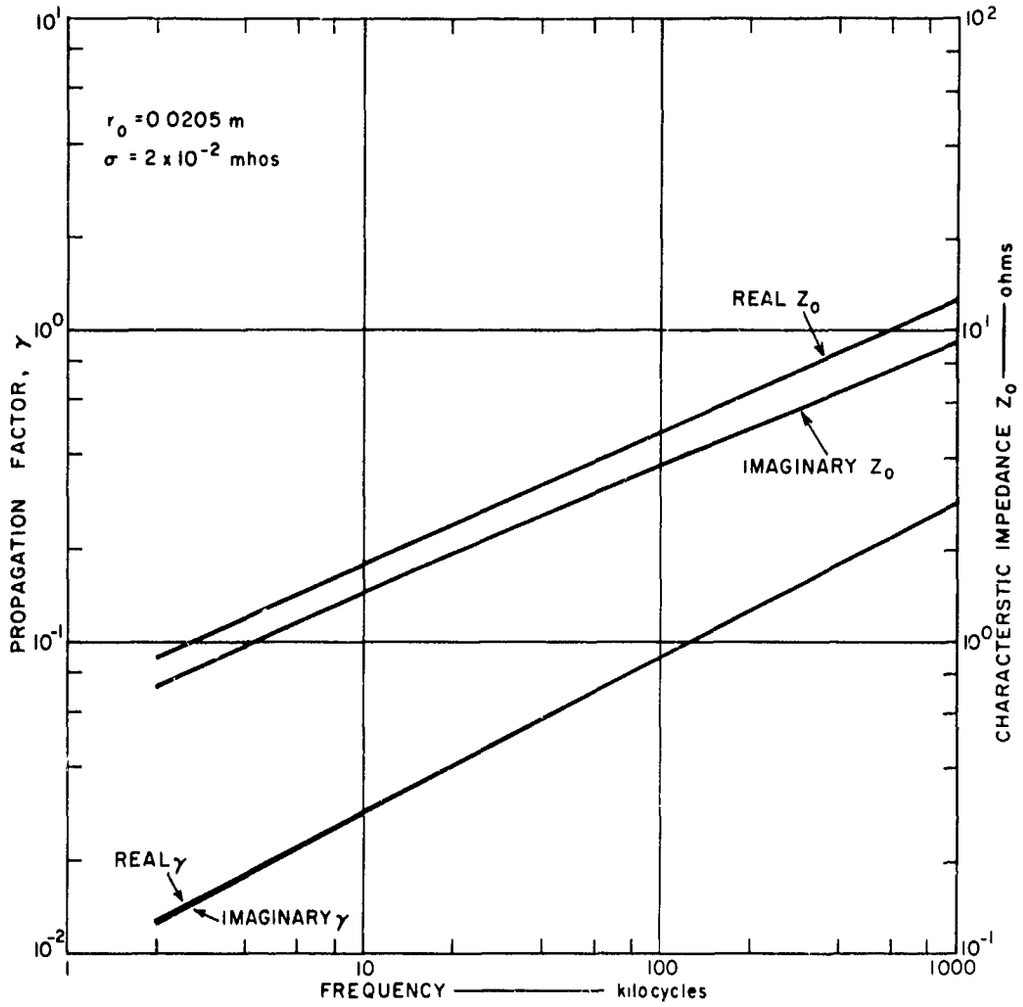

FIG. 44 CHARACTERISTIC IMPEDANCE AND PROPAGATION FACTOR FOR LEAD SHEATH CABLE

the measured currents. The principal differences between the bare copper wire and the other two cables appeared to be (1) the cross section of conductor, (2) the proximity of the near end of the conductor to the transmitter, (3) the material between the metal conductor and the soil, and (4) the depth at which the conductors are buried. These differences are summarized in Table III below.

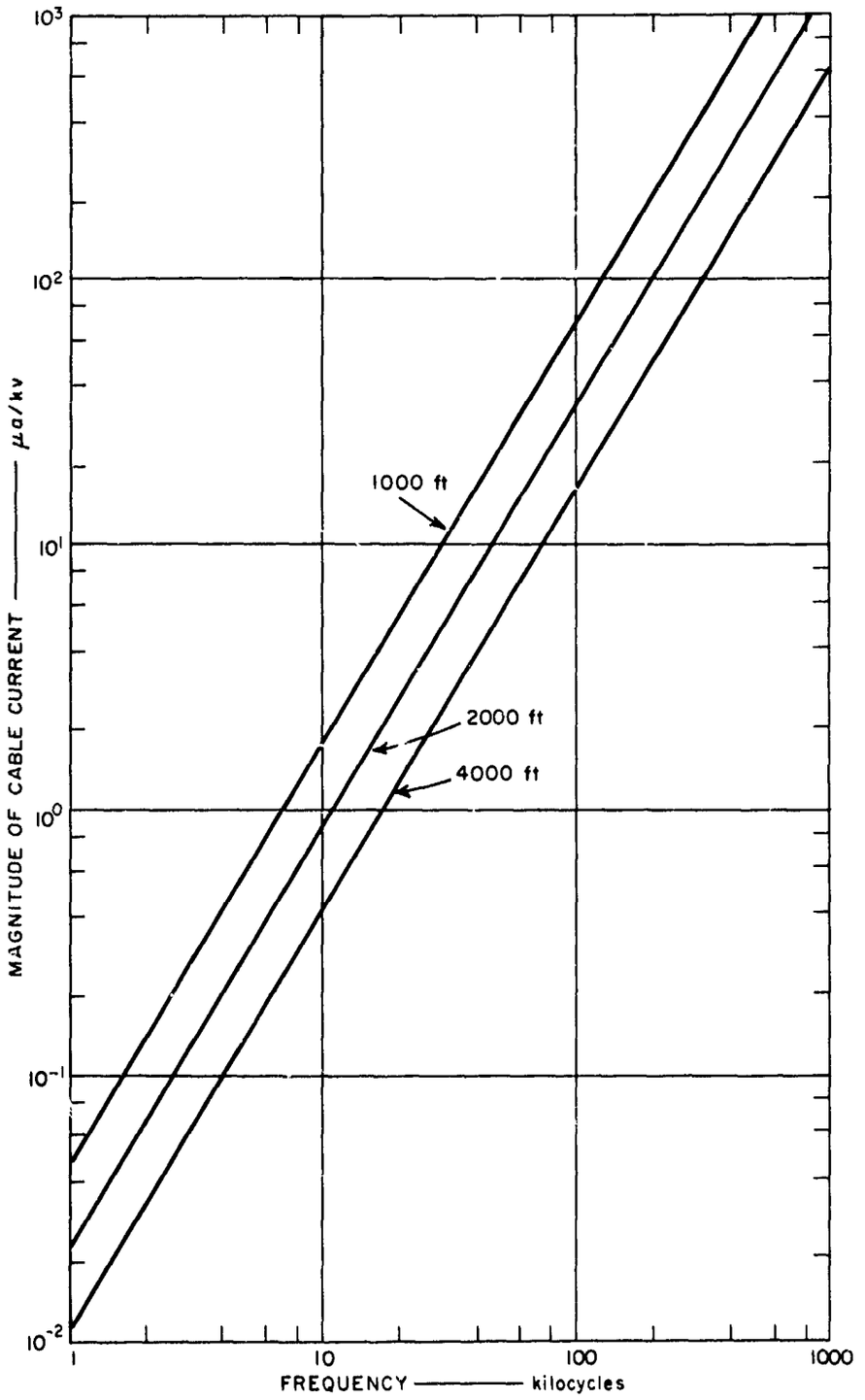

FIG. 45 COMPUTED MAGNITUDE OF LEAD SHEATH CURRENT USING TRANSMISSION LINE THEORY

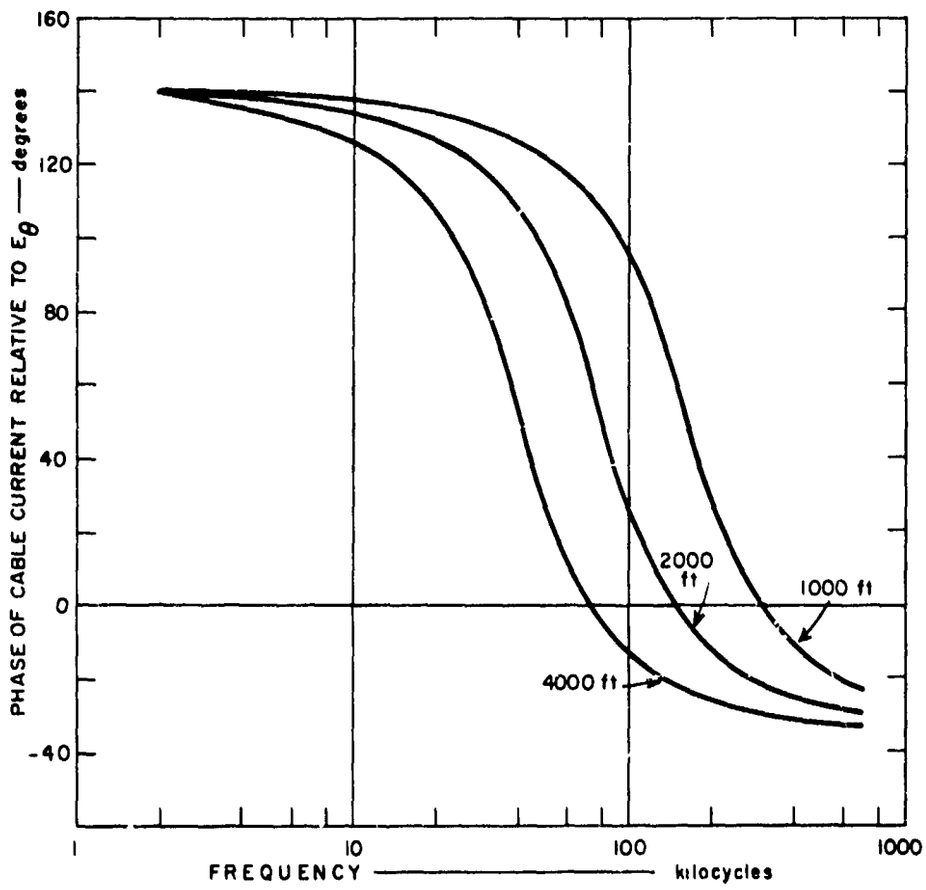

FIG. 46 COMPUTED PHASE OF LEAD SHEATH CURRENT USING TRANSMISSION LINE THEORY

Table III

PROPERTIES OF BARE CABLES

Conductor	Conductor Cross Section (sq. inch)	Closest Approach To Transmitter (feet)	Depth Buried (feet)	Conductor Contacts Soil Through
#10 copper	0.0082	725	1	Oxides or salts of copper
Lead sheath	0.47	170	4	Oxides or salts of lead
Conducting Sheath	0.17	300	3	Conductive plastic

If the conductor were actually coupled to the soil capacitively (e.g., through an oxide coating), in such a manner that the wavelength on the line so formed were very much shorter than a free space wavelength, the behavior in the 0.5-to-100-kc frequency range could be approximated by resonance phenomena similar to that shown in Fig. 38 between 10 and 500 kc. This explanation of the high currents below 100 kc is inconsistent with the constant phase observed on both the conducting and lead sheath cables. It is consistent with the observation that the lead sheath cable is long, so that if it were insulated by an oxide film it would resonate at a very low frequency. The conducting sheath cable could also meet the "long line" criterion if the "conductive" plastic sheath were improperly compounded so that the plastic was only slightly conductive but was sufficiently loaded with conductive solids to raise the effective dielectric constant to a very high value. Because this theory does not explain the behavior of the phase, and because of the extremely high dielectric constants inherent in this theory, it is felt that this theory does not satisfactorily explain the low-frequency currents.

It was also considered possible that, because the conducting and lead sheath cables were terminated much closer to the transmitter than the copper wire, the higher low-frequency currents might be caused by the higher radial electric fields existing within a skin depth of the transmitting antenna base. At distances within a skin depth of the antenna base, the radial electric field strength is of the order of δ/r times the field strength computed from Eq. (12).

The current is attenuated by a factor exp. $(-x/\delta)$ in propagating down the line, however. The higher radial electric field due to the spherical distribution of current at the antenna base is thus significant only close to the transmitter and at the lowest frequencies, and cannot account for the higher cable currents at frequencies from 2 to 100 kc.

Consideration may also be given to the possibility that a copper-cuprous oxide junction at the surface of the wire might rectify the alternating current flowing to the wire and produce anomalous effects. Such action would cause the wire to charge to a negative dc potential, but it does not appear likely that this would have a significant effect on the ac characteristics of the conductor. It is assumed that the line would charge to a negative equilibrium potential within a few cycles of the applied alternating field. Subsequently, the junction would appear to alternating signals as a large capacitance per unit length.

Examination of the wire spacing was made to determine whether the transmission line theory or Wait's wave impendance theory was applicable. The lead sheath cable and the conducting sheath cables are only 15 degrees apart and are only 15 degrees from other cables in the area. Hence, at 0.5 kc, where δ = 520 feet, the cables are separated by a skin depth or more at radial distances greater than 1980 feet, while at 50 kc the cables are separated by a skin depth or more at distances greater than 198 feet. It thus appears that the cable spacing is less than one skin depth for significant radial distances at frequencies below 50 kc, and that Wait's wave impedance theory might be more appropriate than the transmission line theory over a limited range of frequencies and distances. Accordingly, the magnitude of the cable currents was computed from Eq. (38) with $N = 24$ (15 degree spacing) and $r_o = 0.02$ meter. Rather than stopping at the frequency and distance at which the cable spacing is equal to the skin depth, however, the computation was carried out until the current magnitude curve from Eq. (38) intersected the current magnitude curve from Eq. (A-35). These curves are shown in Fig. 47 for distances of 1000, 2000, and 4000 feet from the transmitter. The dashed portion of the curve is computed from Wait's theory $\left|\text{Eq. (38)}\right|$ and the solid curves were obtained from the transmission line theory $\left|\text{Eq. (A-35)}\right|$. Comparison of these curves with the curves obtained from the measurements on the lead sheath and conducting sheath cables, Figs. 40 and 42, reveal the similarity of both the general shape

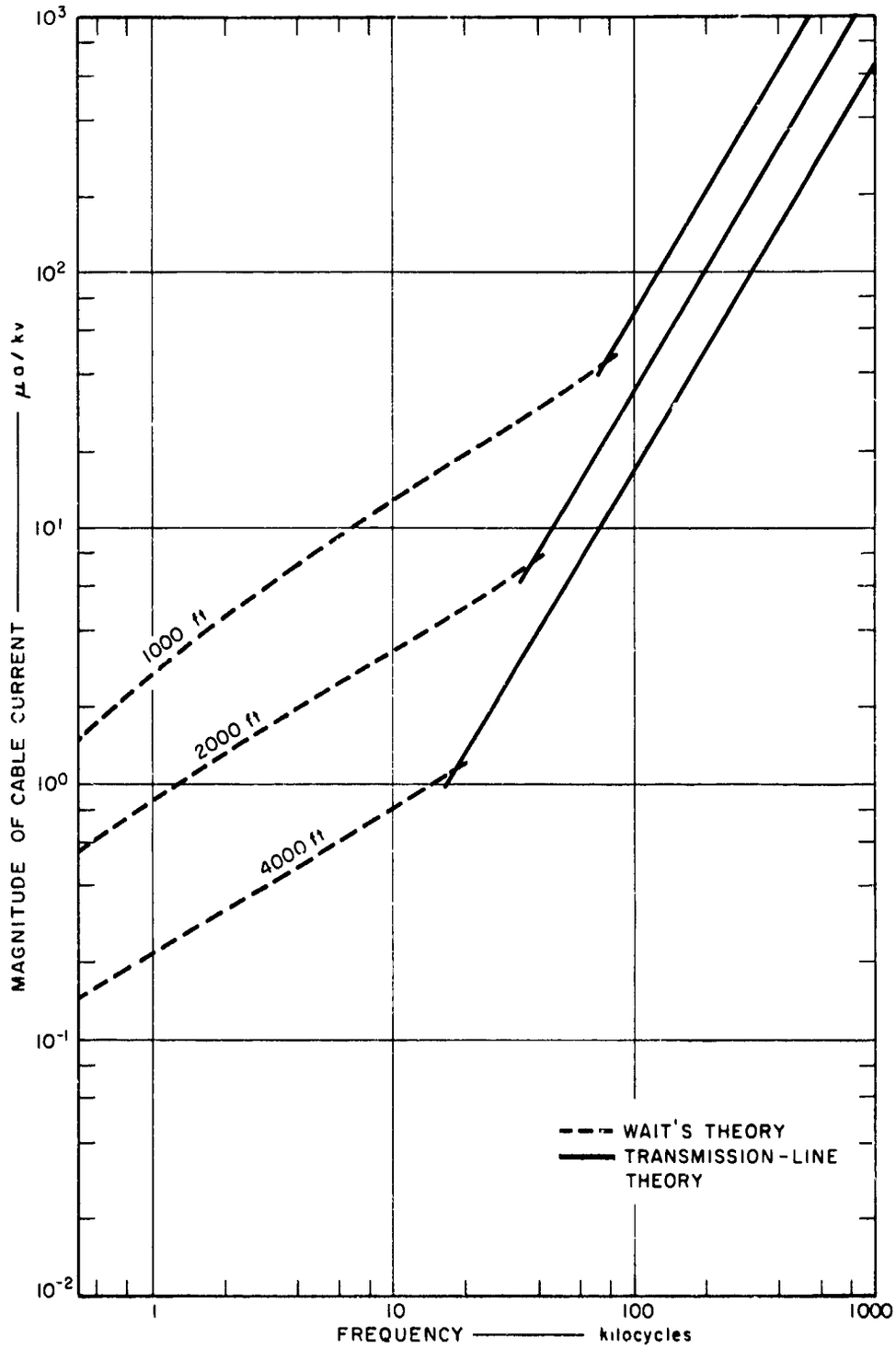

FIG. 47 COMPUTED MAGNITUDE OF CURRENT IN LEAD SHEATH OR CONDUCTING SHEATH CABLE USING WAIT'S THEORY AND TRANSMISSION LINE THEORY

and the magnitude of the curves. The computed curves appear to drop a little faster below 2 kc, particularly at 1000 feet, than the experimental curves, but this discrepancy may be at least partially accounted for by correcting for the high radial fields that exist within a skin depth of the antenna. The phase of the current relative to the local vertical electric field computed from Wait's theory is relatively constant at 230 to 240 degrees for frequencies out to 20 kc, beyond which the phase begins to decrease. This phase is roughly 180 degrees more than the phase of the measured currents in the lead sheath and conducting sheath cables. This 180-degree discrepency has not been satisfactorily resolved. Above about 50 kc, the measured phase tends to agree with the phase computed from the transmission-line theory.

It is also peculiar that the lead sheath and conducting sheath cables should obey Wait's theory while the bare 10-gauge copper wire obeys the transmission-line theory. This is particularly disturbing when it is recognized that the 10-gauge copper wire is only 9.5 degrees from another bare lead sheath cable (not shown on Fig. 2). There were, in fact, three lead sheath cables spaced 15 degrees apart, the closest of which was 9.5 degrees counterclockwise from the 10-gauge copper wire. Hence, although the copper wire was 20 degrees from the insulated cable (cable N), it was very close to an array of bare lead sheath cables having the same spacing as the array including the conducting and lead sheath cables. A possible explanation for this behavior is that the large lead sheath cable adjacent to the copper wire acts as a guard wire for the copper wire, shorting out the radial electric field about the copper wire at low frequencies where the skin-depth is large. It is noted in Fig. 29 that the magnitude of the current in the copper wire appears to follow the trend set by the larger bare cables as frequency is decreased, but at 10 kc the current begins to drop more rapidly with decreasing frequency, suggesting that some other effect begins to occur. This new effect could be the almost exponential decrease in field strength about the copper wire as the range of influence of the lead sheath cable increases with decreasing frequency. It is also difficult to justify the application of Wait's theory to distances as great as 4000 feet from the transmitter with the 15-degree spacing, although one would expect a smooth transition from wave-impedance theory (for closely space cables) to the transmission-line theory (for isolated cables).

It should also be remarked that if Wait's theory is applicable to the lead sheath and conducting sheath cables (as it appears to be) the theory should be restricted to conductors tightly coupled to the conducting soil, since the grid of conductors does not effectively shunt the ground impedance unless low-impedance contact between the conductor and soil exists. Thus, if the conductors are above ground or have thick insulation, the relatively high-impedance (low-admittance) capacitive coupling between the conductor and ground limits and shunting action of the conductors at low frequencies. At high frequencies where the coupling impedance is low, the skin depth in the soil is small so that the conductors are effectively isolated (unless the spacing is very close).

F. Pie-Shaped Loop

A loop formed by two radial lines 30 degrees apart and two arcs, one at 340 feet and one at 1500 feet from the transmitter (see Fig. 2), was formed of the conducting sheath cable used for cable L (see Sec. VII-D). The radially directed sides of the loop passed through underground bunkers at 900 feet from the transmitter and the arc at 1500 feet passed through a similar bunker. A hole was dug about 20 feet from the counterclockwise end to expose the cable at one point on the arc at 340 feet. The cable was buried 3 feet deep. In the bunkers, the shields were connected to the grounded steel bunker case, and the core wires passed through the bunker without shielding other than that provided by the bunker. Current in both the shields and the core wires was measured in the three bunkers, and total current was measured at the hole on the 340-foot arc.

Some difficulty was experienced with the pie-shaped loop because of deterioration of the cable installation. The cable had been cut in two places close to Bunker 523.09. Splices were made at these cuts, but instead of splicing individual core wires, all core wires were connected together and spliced with one large conductor. For the length of the splices (2 feet and 10 feet), the core wires were unshielded. Where the cable entered the burkers, it passed through a 4-inch-diameter plastic pipe about 6 inches long that was intended to isolate the cable from the steel bunker case. At the end of the plastic pipe inside the bunker were the terminal fittings for the shields and an opening through which

the core wires passed into the bunker. The shield terminal fittings were found to be shorted to ground through a low resistance when the site was first examined. The terminal fittings were removed, and it was found that the plastic pipe and the end of the cable were filled with mud. The plastic pipe sections were all cleaned to restore the isolation between the terminal fittings and the grounded steel bunker case. There was apparently moisture and mud inside the cable, however, and the core-to-shield resistance was found to vary from several megohms to 50 kilohms during about six months. This core-to-shield resistance change had a noticeable effect on the current induced in the core wires.

The magnitude and phase of the currents measured in the shield of the cable are shown in Figs. 48 and 49, respectively. The magnitude and phase of the currents measured in the core wires are shown in Figs. 50 and 51, respectively. The core-wire currents seem to be exceptionally high, particularly along the outer arc at 1500 feet. Because of the poor and variable isolation between the core wires and the shields, however, the significance of the core-wire currents is somewhat questionable. Two sets of core wire data are shown in Figs. 50 and 51. One set was taken when the core-to-shield resistance (as measured with a dc ohmmeter in one of the bunkers) was 50 kilohms, and the other set was taken when the core-to-shield resistance was 500 kilohms. The current magnitude differed by an order of magnitude for these two sets of measurements. Because of such irregularities, little credence is given to trends that might be suggested by the core wire current measurements.

The currents measured in the shields should be somewhat more reliable, but the circuit arrangement is so complex that it is difficult to establish a quantitative theoretical explanation of the measured values. The cable formed a closed loop, and if the loop were isolated and perfectly nulled so that no azimuthal magnetic field linked the loop (a doubtful condition), the only currents induced in the cables would have been those produced by the radial electric field in the soil. These currents would have been equal in the radial sides of the loop and would have cancelled at the centers of the azimuthal arcs. Since neither of the current measurements on the arcs was made at the center, however, this property of the loop was not checked. Although the bunkers along the sides of the loop were at the same distance from the transmitter, the currents

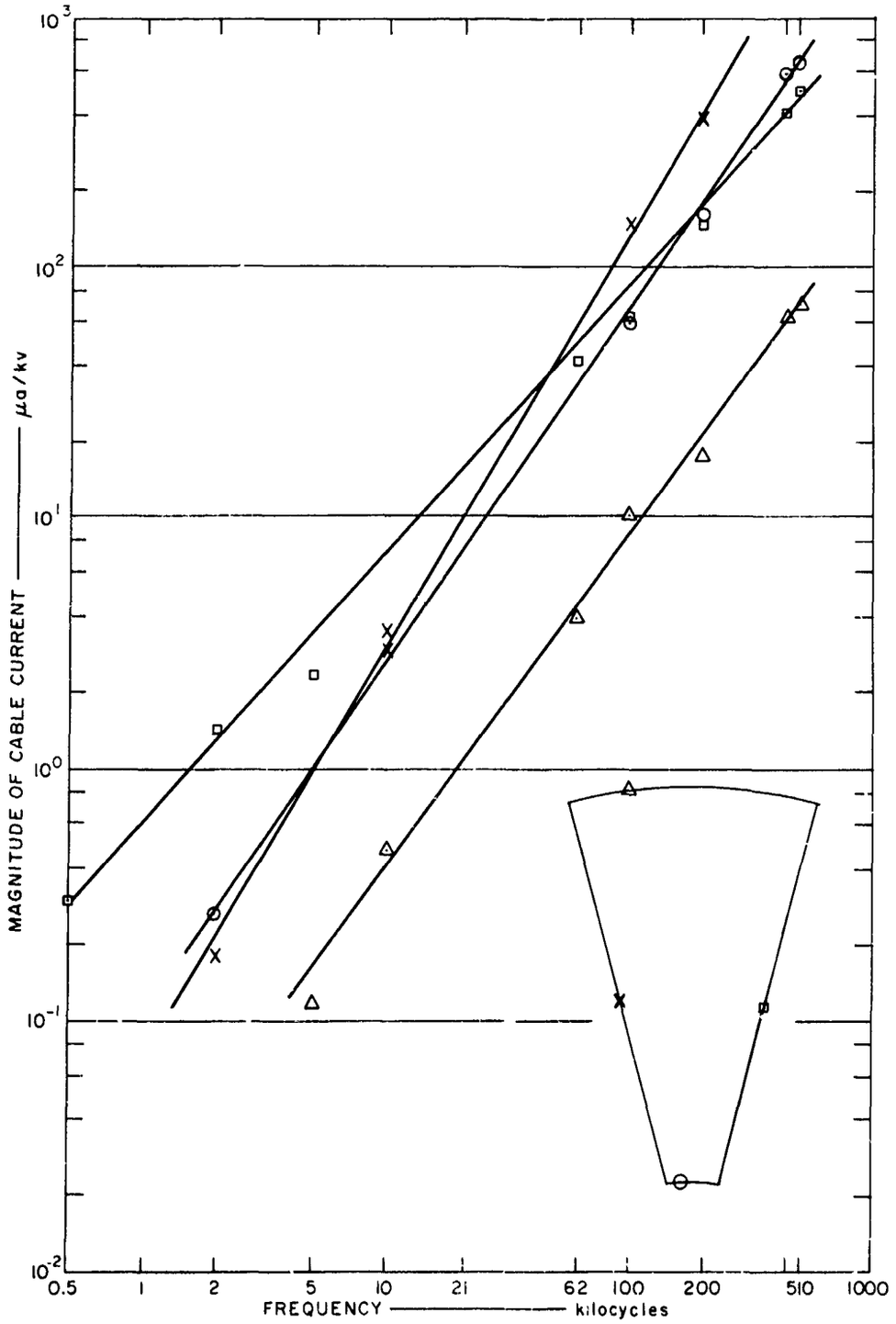

FIG. 48 MEASURED MAGNITUDE OF SHIELD CURRENT IN PIE-SHAPED LOOP

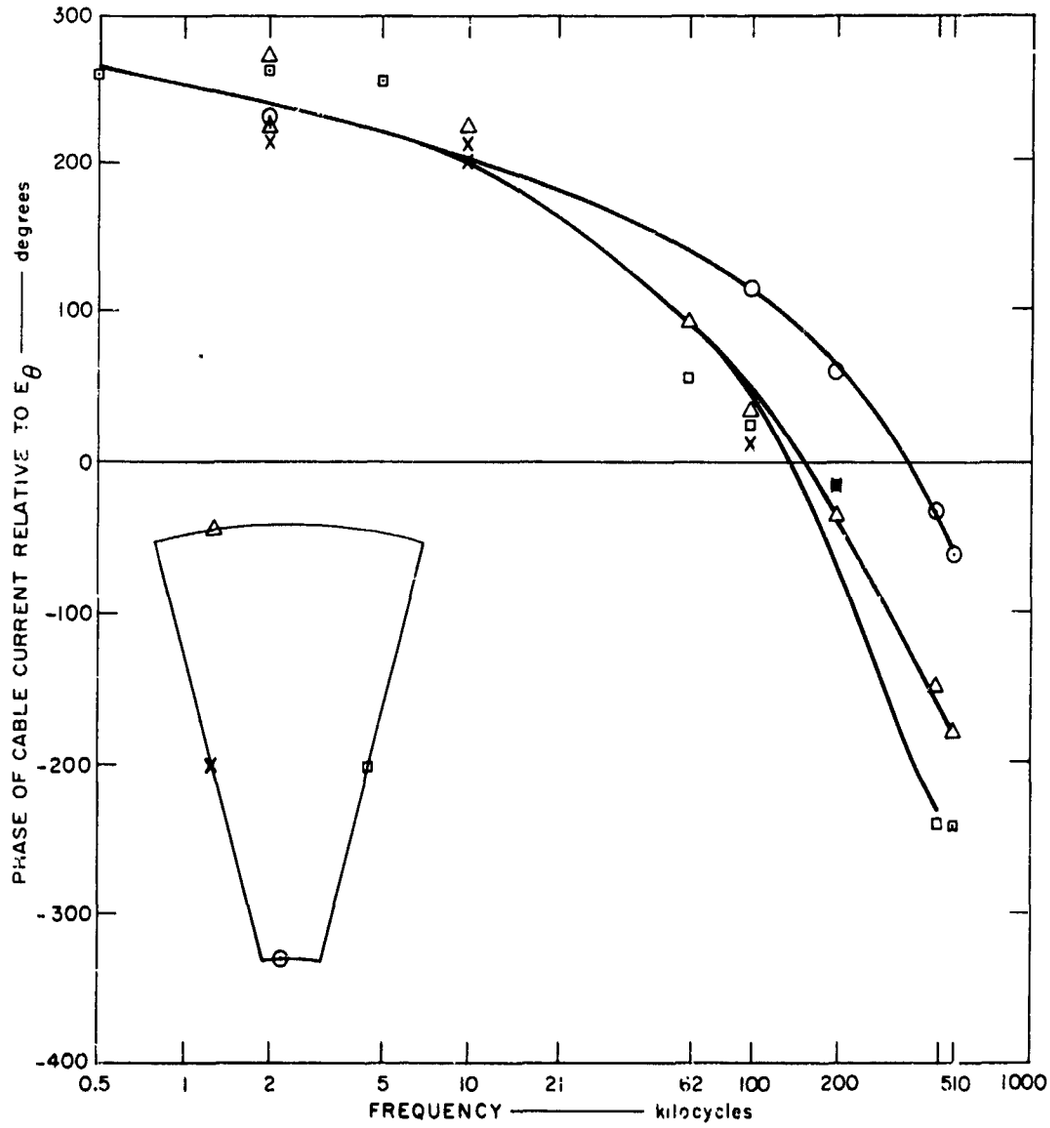

FIG. 49 MEASURED PHASE OF SHIELD CURRENT IN PIE-SHAPED LOOP

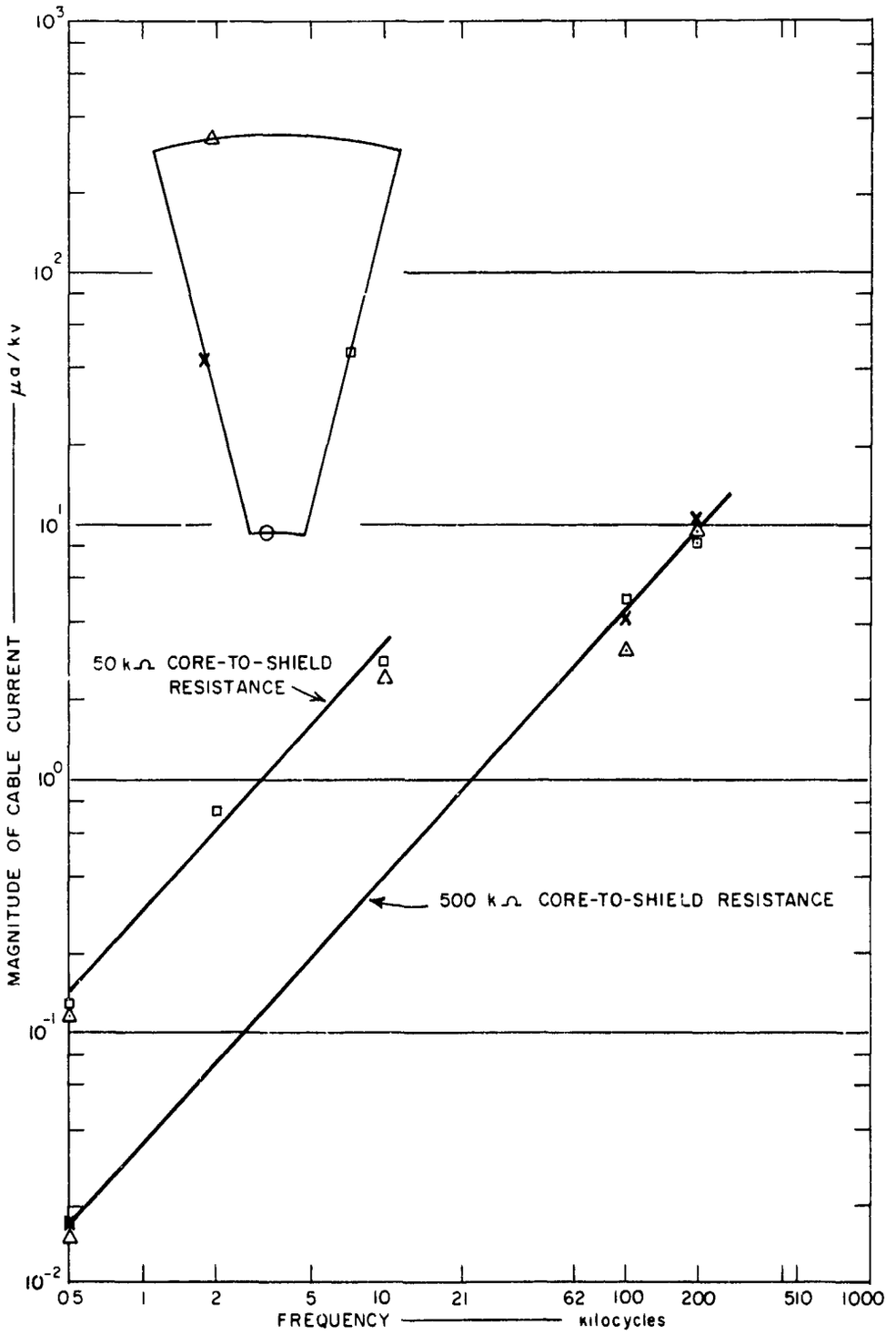

FIG. 50 MEASURED MAGNITUDE OF CORE-WIRE CURRENT IN PIE-SHAPED LOOP

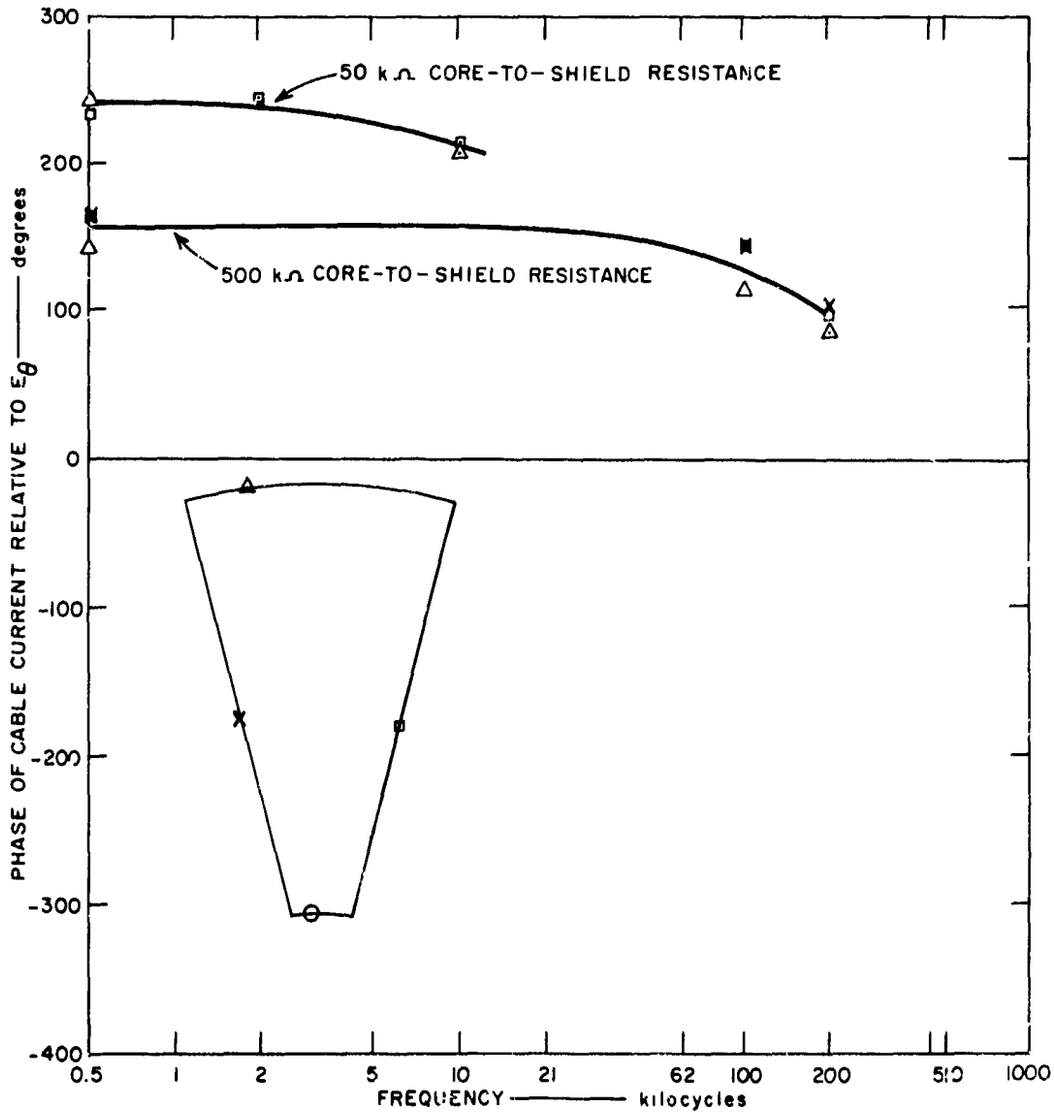

FIG. 51 MEASURED PHASE OF CORE-WIRE CURRENT IN PIE-SHAPED LOOP

in the cable were not exactly equal, and at 2 kc these currents differed by almost an order of magnitude. It is perhaps significant that the pie-shaped loop was adjacent to the cable array that included the lead sheath cable and the conducting sheath cable discussed in the preceding paragraphs (one side of the loop was only 15 degrees from the lead sheath cable). The shield currents in the pie-shaped loop were also influenced by the low-impedance grounds that were intentionally installed at each steel bunker case. Since the bunker on the arc at 1500 feet is not in the center of the arc, the ground connection at this bunker undoubtedly contributes to asymmetrical currents. Late in the measurement program it was found that a radial cable was buried along a line besecting the pie-shaped loop. The ends of this cable were not located. The entire loop might thus be within the range for which Wait's wave impedance theory applies at low frequencies, but because of the length of the sides of the loop and the manner of terminating, the validity of applying this theory is doubtful even if the other complicating factors are overlooked.

The current in the arc at 340 feet (see Fig. 48) seems at first glance to be rather high, but when it is taken into consideration that the cable from which the loop was made has a low-resistance conductive plastic sheath so that the cable behaves as a bare conductor, this high current seems more plausible. The inner arc serves as a large, essentially equipotential ground connection for the two radial sides of the loop. The current flow into this ground connection is distributed over the arc length, and since the measurement was made near the corner, a large fraction of the current flowing from the arc into the radial conductors flows through the cable where the current was measured. The current in the radial side cables at 340 feet may be comparable to, or even greater than, the current at 900 feet where the current was measured in the bunkers. At 1500 feet the current in the arc was measured in the bunker, which is over 150 feet from the corner, so that the current at this point is much lower than the current in the sides, because of both the radial distances from the transmitter and the arc length from the corner.

G. 100-Foot Diameter Loop

A closed circular loop of insulated 12-gauge copper wire was located with its center 750 feet from the transmitter. The wire was buried about one foot deep except where it entered a bunker on the side opposite the transmitter. Where it entered the bunker, the wire was approximately 8 feet underground. The wire current was measured at four equally spaced points on the loop, including a measurement in the bunker.

The magnitude and phase of the currents measured in the loop are shown in Figs. 52 and 53, respectively. Comparison of Fig. 53 with Fig. 28 in Sec. VI, which shows the currents measured in a 10-gauge wire loop lying on the surface of the ground, indicates the similarity between the current magnitudes in these two cases. As in the earlier case, the low-frequency currents appear to be caused by coupling to the azimuthal magnetic field, while the high-frequency currents are caused primarily by coupling to the radial electric field. The high-frequency currents are somewhat higher in the 12-gauge loop because the loop is buried and, therefore, better coupled to the radial electric fields than was the 10-gauge wire lying on the surface of the soil. The phase of the high-frequency current appears to substantiate the assumption of capacitive coupling to the radial electric field. At the low frequencies (10 kc and lower) the current is in phase at all four measurement points, as would be expected if these were circulating currents induced by the azimuthal magnetic field. The currents are assumed positive when flowing in the counterclockwise direction. At the high frequencies, the currents are 180 degrees out of phase at the sides of the loop, indicating that these currents are induced by the radial electric field. The phase of the high-frequency currents at the ends of the loop is somewhat erratic, as might be expected if these were the residual currents remaining after the interference of the currents coming in from the two sides of the loop. At the low frequencies one would expect currents induced in a loop in a vertical plane to be 90 or 270 degrees out of phase with the local vertical electric field, rather than the 190 degrees observed. Capacitive coupling to the ground and the shunting effect of the ground have some effect on the phase, however. Coupling to the radial electric field at these frequencies will also have a slight effect.

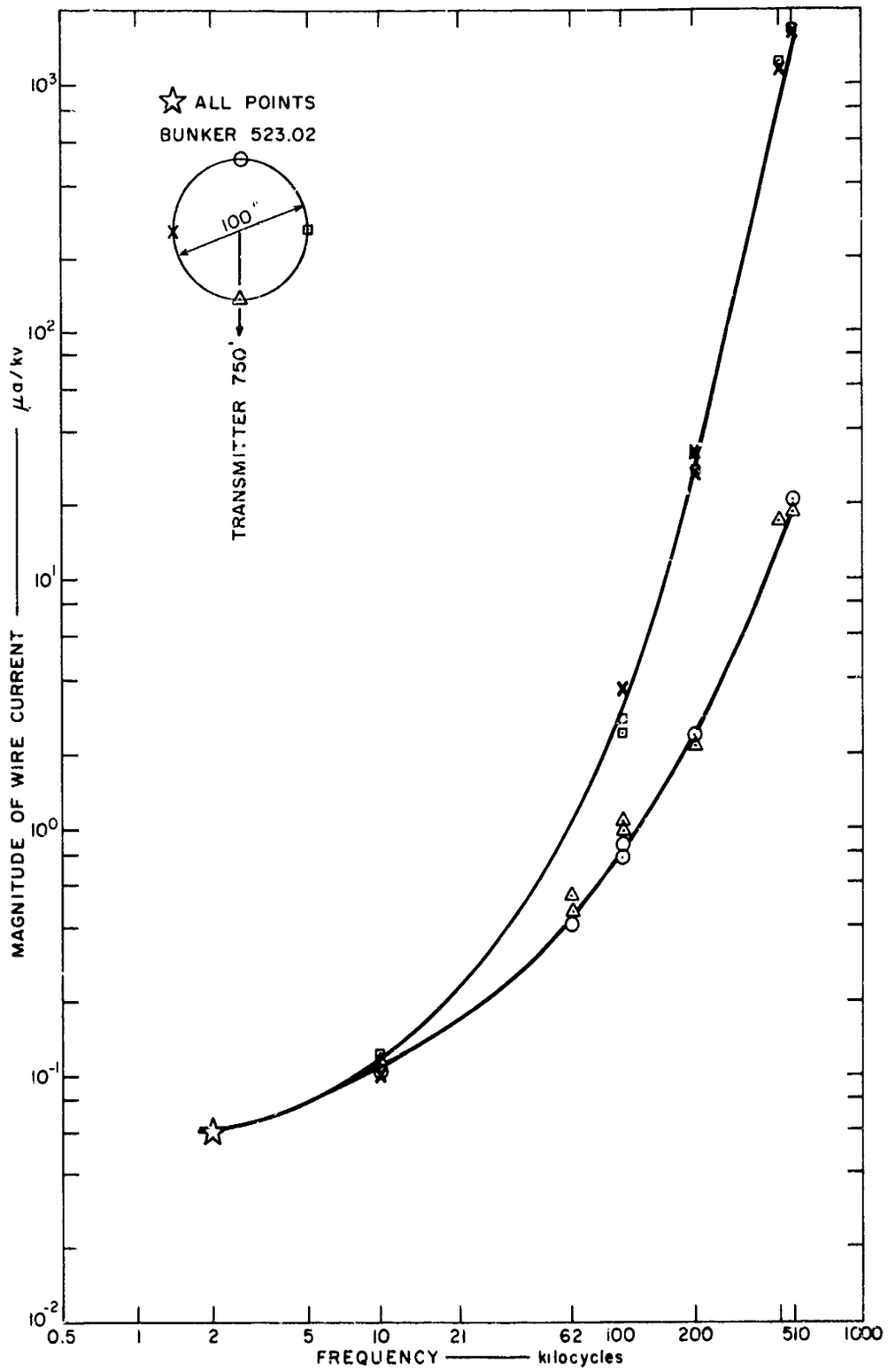

FIG. 52 MEASURED MAGNITUDE OF CURRENT IN 100-FOOT-DIAMETER LOOP

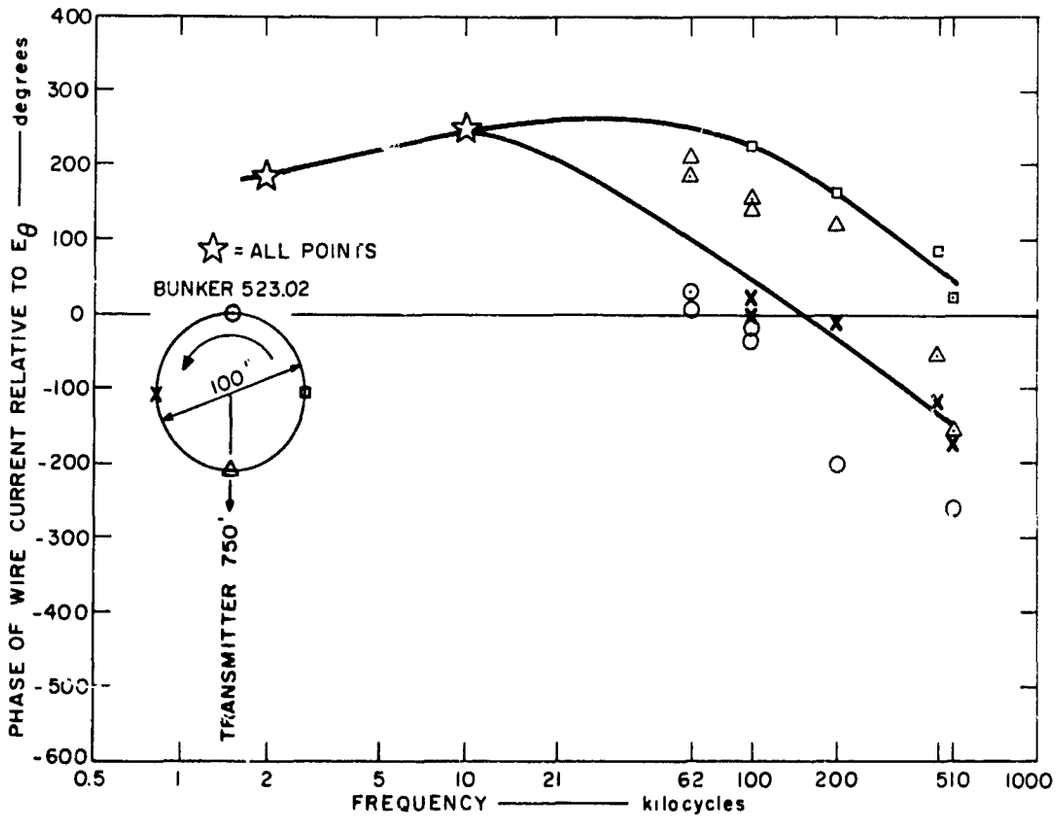

FIG. 53 MEASURED PHASE OF CURRENT IN 100-FOOT-DIAMETER LOOP

H. 100-Foot Diameter Loop with Guard Ring

A second closed circular loop of insulated 12-gauge copper wire, identical to the first, was installed with a closed loop of insulated 4/0-gauge copper wire. The installation was the same as for the first loop, except that the 4/0-gauge wire was taped to the 12-gauge wire. Current measurements were made on each wire individually, and on the two wires together.

The magnitudes of the currents measured in the wires are shown in Figs. 54, 55, and 56. Figure 54 shows the total current induced in both the 10-gauge and the 4/0-gauge wire. This current is similar in magnitude and variation

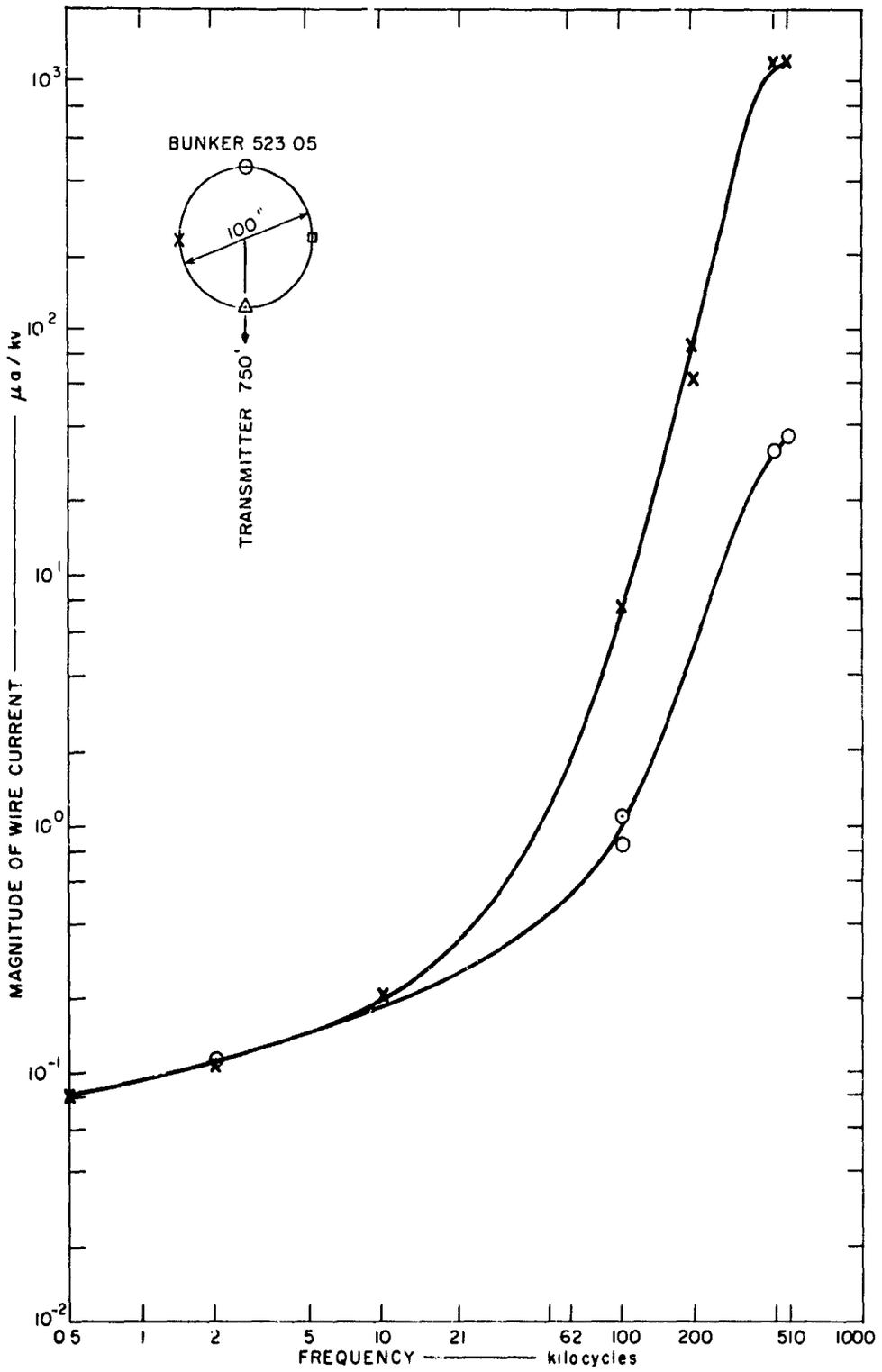

FIG. 54 MEASURED MAGNITUDE OF CURRENT IN 100-FOOT-DIAMETER LOOP WITH GUARD RING (Total Current)

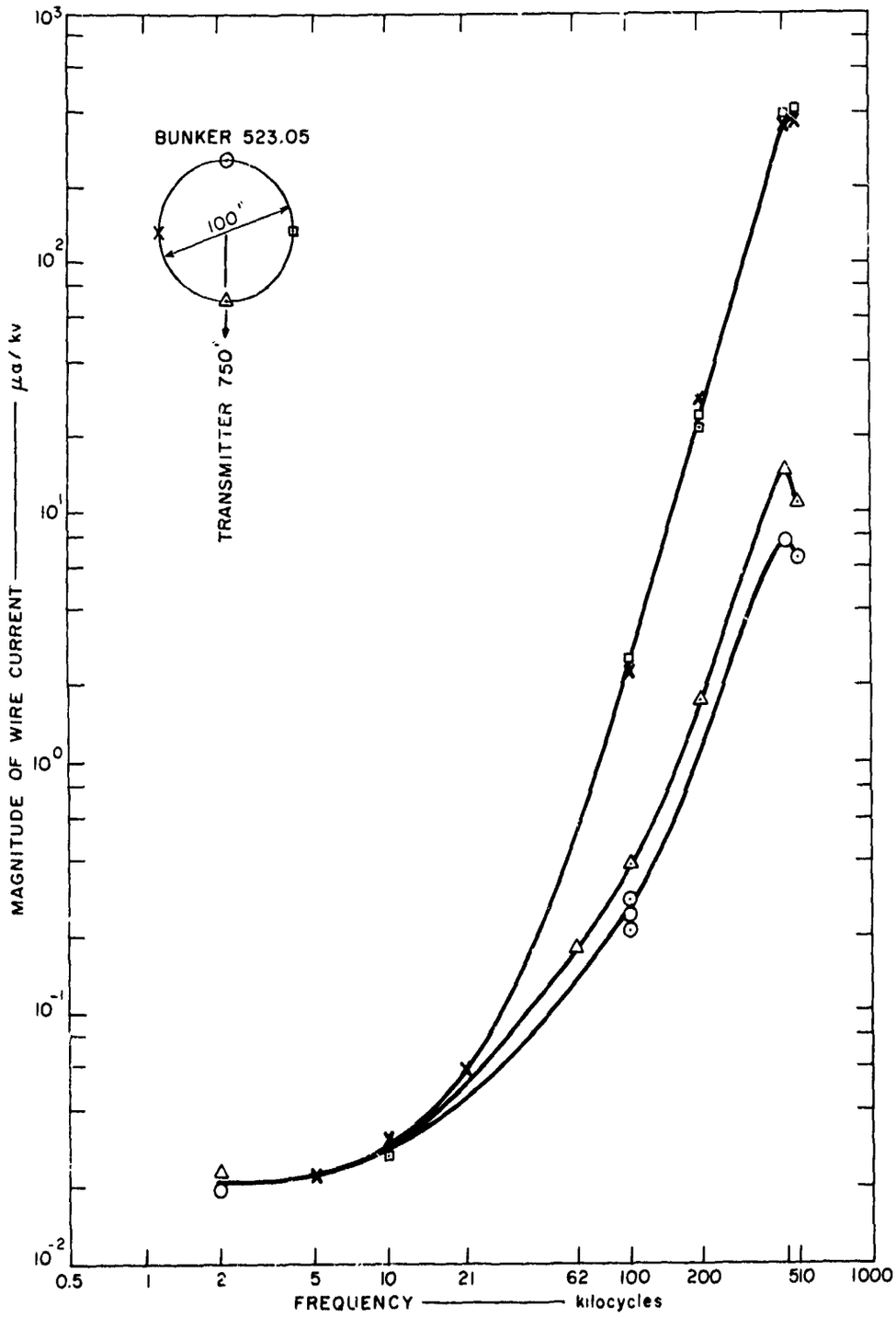

FIG. 55 MEASURED MAGNITUDE OF CURRENT IN 100-FOOT-DIAMETER LOOP WITH GUARD RING (12-Gauge Wire Only)

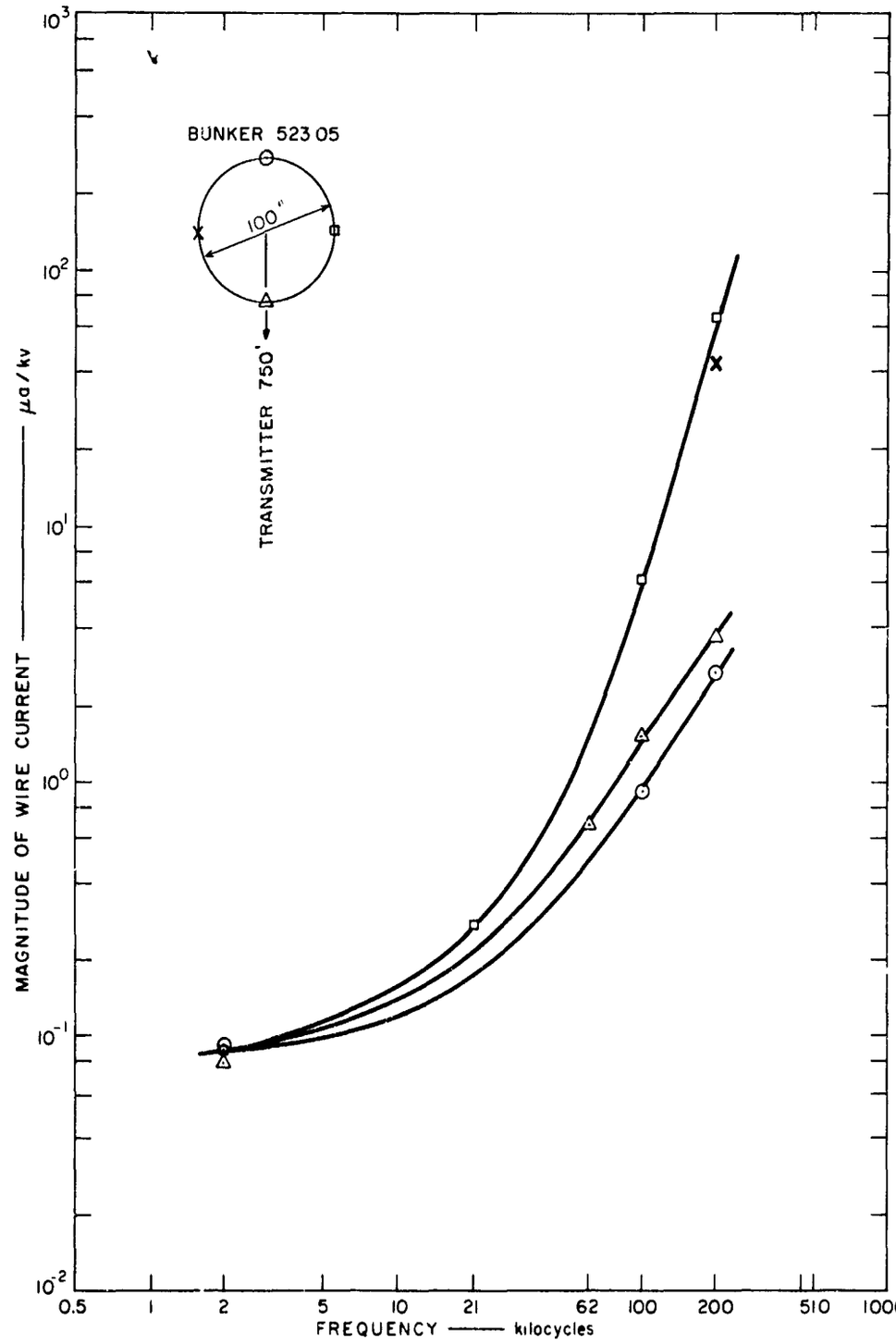

FIG. 56 MEASURED MAGNITUDE OF CURRENT IN 100-FOOT-DIAMETER LOOP WITH GUARD RING (4 0-Gauge Wire Only)

with frequency to the current induced in the 10-gauge and 12-gauge loops discussed previously. Figure 55 shows the current measured in the 12-gauge wire, and the current in the 4/0 gauge is shown in Fig. 56. It is observed that the current induced in the 12-gauge wire is generally less than that induced in the 4/0-gauge wire, particularly at frequencies of 10 kc and lower. This result is consistent with the contention that the low-frequency currents are circulating currents induced by the azimuthal magnetic field. The large 4/0 shorted turn thus reduced the magnetic field linking the 12-gauge loop. At the higher frequencies (100 kc and higher) the currents are induced by the radial electric field, and although the 4/0 wire also tends to short circuit the radial electric field, it is less effective because of the low capacitive admittance of the insulation (i.e., a large part of the voltage per unit length along the wire is dissipated across the insulation capacitance).

The phase of the measured currents is shown in Figs. 57, 58, and 59. Figure 57 shows the phase of the total current in both wires, and Figs. 58 and 59 show the phase of the 12-gauge wire current and the 4/0-gauge wire current, respectively. The currents are assumed to be positive when flowing in the counterclockwise direction. It is noted that the currents at frequencies of 10 kc and lower are in phase, in agreement with the theory that there are circulating currents induced by the azimuthal magnetic field. At 100 kc and above, the currents are 180 degrees out of phase, in accordance with the theory that these currents are produced by the radial electric field.

The manner of coupling to the 4/0-gauge guard ring has important implications relative to the effectiveness of the guard ring in limiting the current induced in the circuit to be protected (the 12-gauge wire in this case). The installation described is fairly effective in protecting the 12-gauge loop against currents induced by magnetic field linking the loop, but it is less effective against currents induced by a radial electric field because of the poor coupling to the soil through the insulation. If the 4/0-gauge loop had been a bare conductor, it would have been much more efficient in short-circuiting the electric field in the vicinity of the 12-gauge wire.

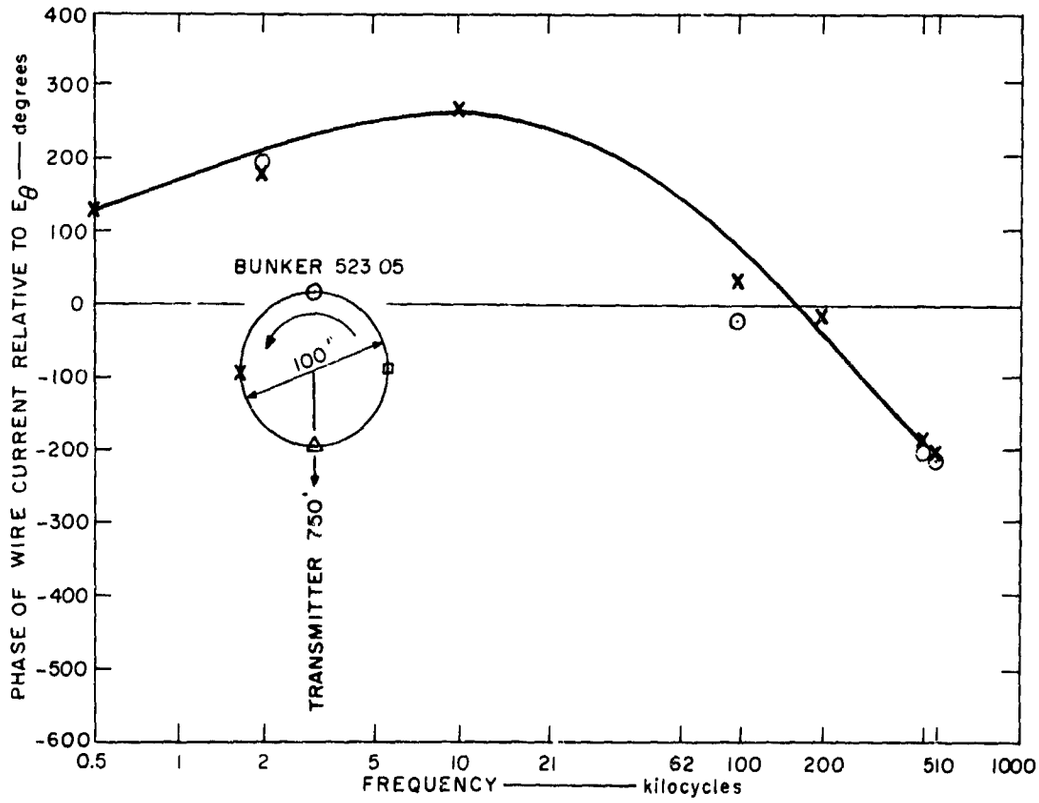

FIG. 57 MEASURED PHASE OF CURRENT IN 100-FOOT-DIAMETER LOOP WITH GUARD RING (Total Current)

I. Aluminum Sheath Arcs (Cables T_1 and T_2)

Two aluminum sheath cables were buried along arcs subtended by 30-degree angle located at 500 and 2000 feet from the transmitter. The aluminum sheath was 8 mils thick and was covered with an outer jacket of polyethylene 65 mils thick. The outside diameter of the cable was 0.78 inch. Current measurements were made at three points approximately 7.5 degrees apart on each arc (see Fig. 2).

The magnitude and phase of the current measured in the arc 500 feet from the transmitter are shown in Figs. 60 and 61, respectively. The magnitude of

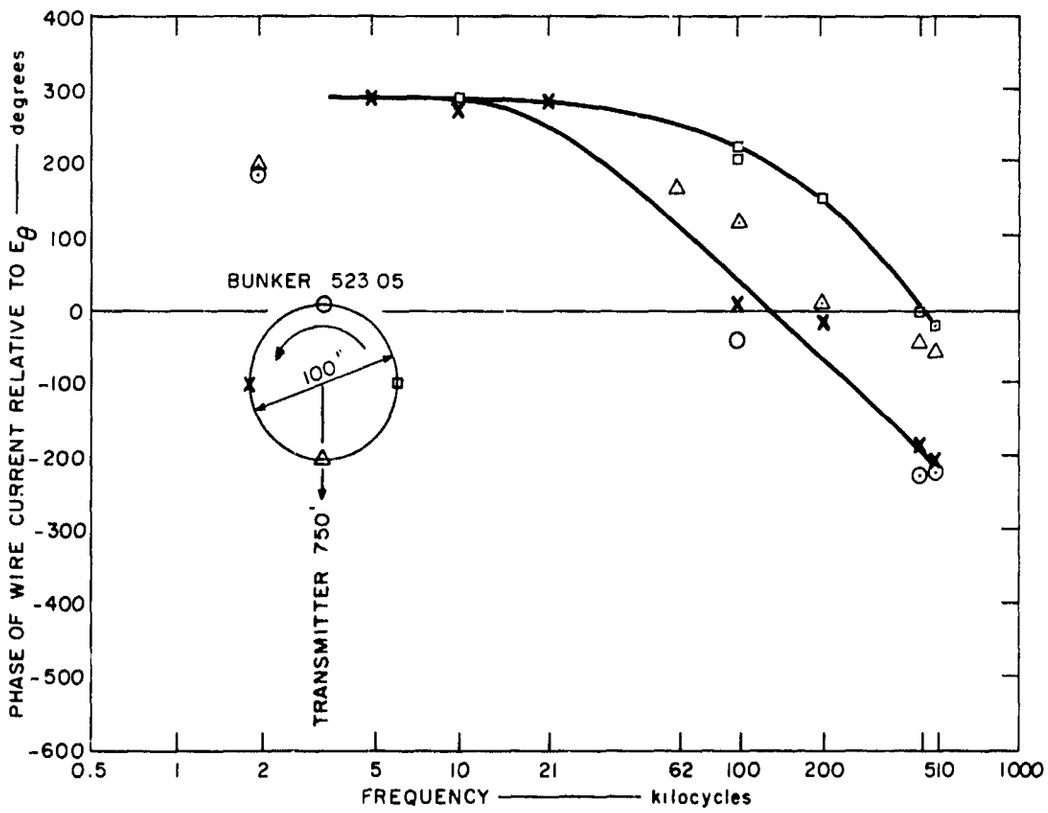

FIG. 58 MEASURED PHASE OF CURRENT IN 100-FOOT-DIAMETER LOOP WITH GUARD RING (12-Gauge Wire Only)

the current is at least an order of magnitude lower than the current measured in insulated radial cables at similar distances (compare Fig. 60 with Fig. 35, for example). If the arc had been perfectly laid out and the ground had been perfectly uniform and smooth, this current should have been zero. If we visualize the conductor as an electric dipole antenna, however, a comparison of the current in the arc to the current in a similar radial conductor indicates that the null response of this dipole is over 20 db down from the main-lobe response. Such a null response is fairly typical of dipole antennas that are not carefully constructed to produce good null characteristics.

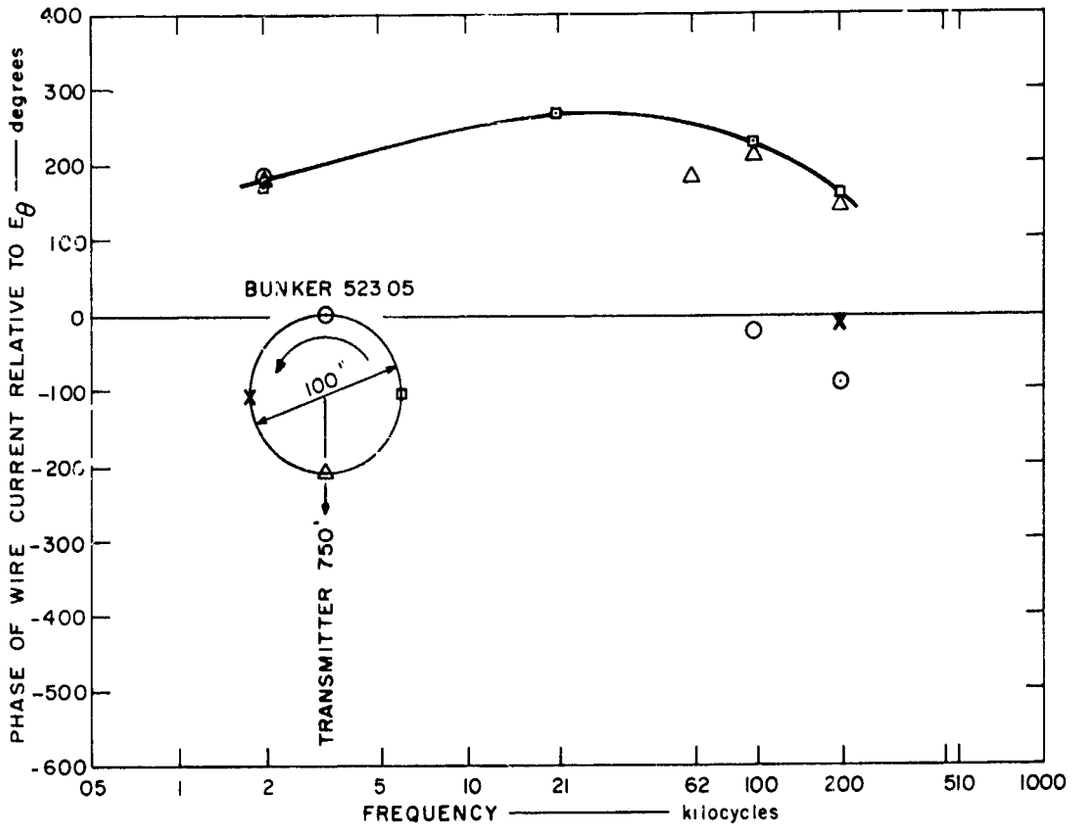

FIG. 59 MEASURED PHASE OF CURRENT IN 100-FOOT-DIAMETER LOOP WITH GUARD RING (4/0-Gauge Wire Only)

The magnitude and phase of the current in the arc at 2000 feet are shown in Figs. 62 and 63, respectively. Comparing the magnitude of the current in this arc with the current at a similar distance in the radial conductor (see Fig. 35) shows that the current in the arc is about 2 orders of magnitude below the current in the radial conductor. The currents in the arc at 2000 feet were so low that they were barely measureable.

J. Summary

Currents were measured in four kinds of long buried cables running radially from the transmitter:

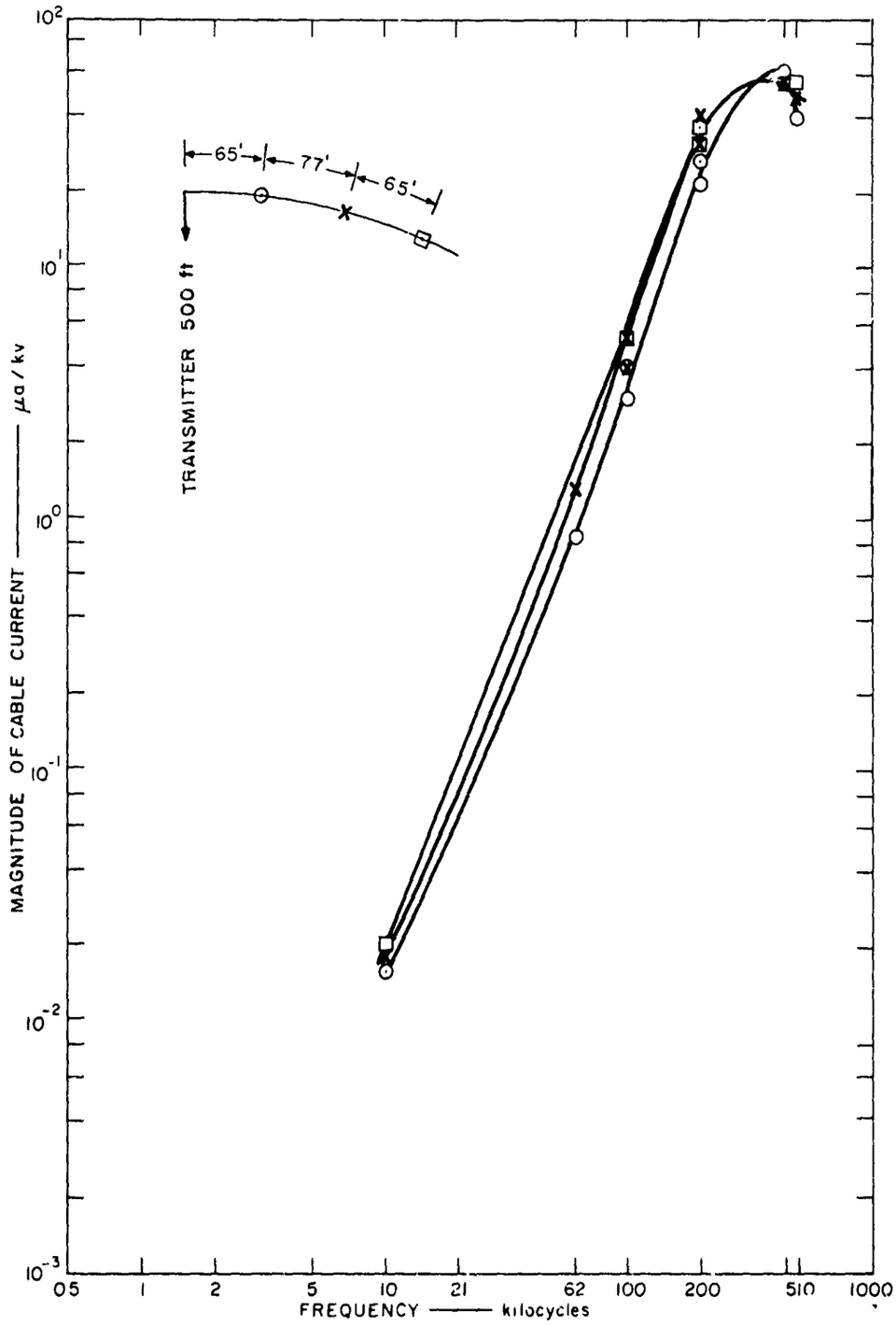

FIG. 60 MEASURED MAGNITUDE OF CURRENT IN ARC 500 FEET FROM TRANSMITTER

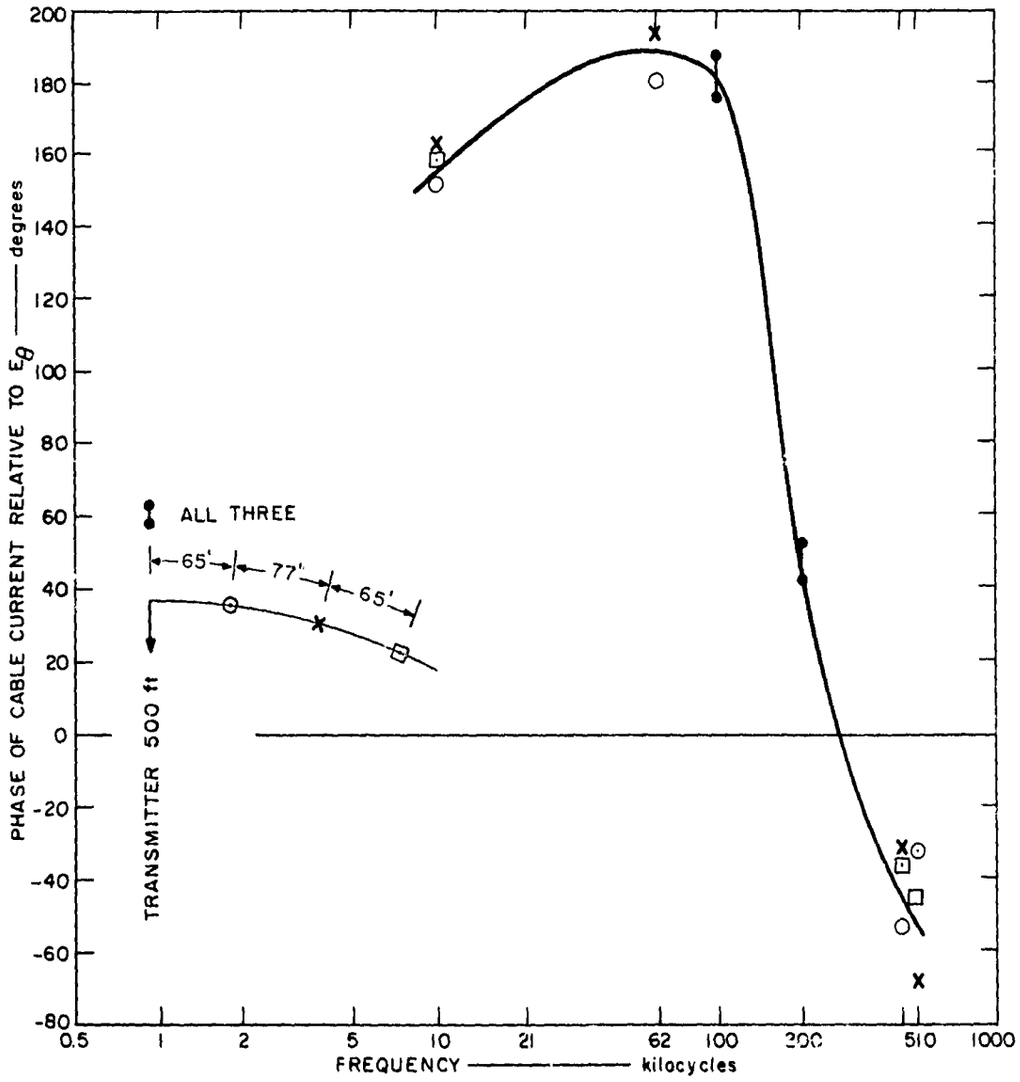

FIG. 61 MEASURED PHASE OF CURRENT IN ARC 500 FEET FROM TRANSMITTER

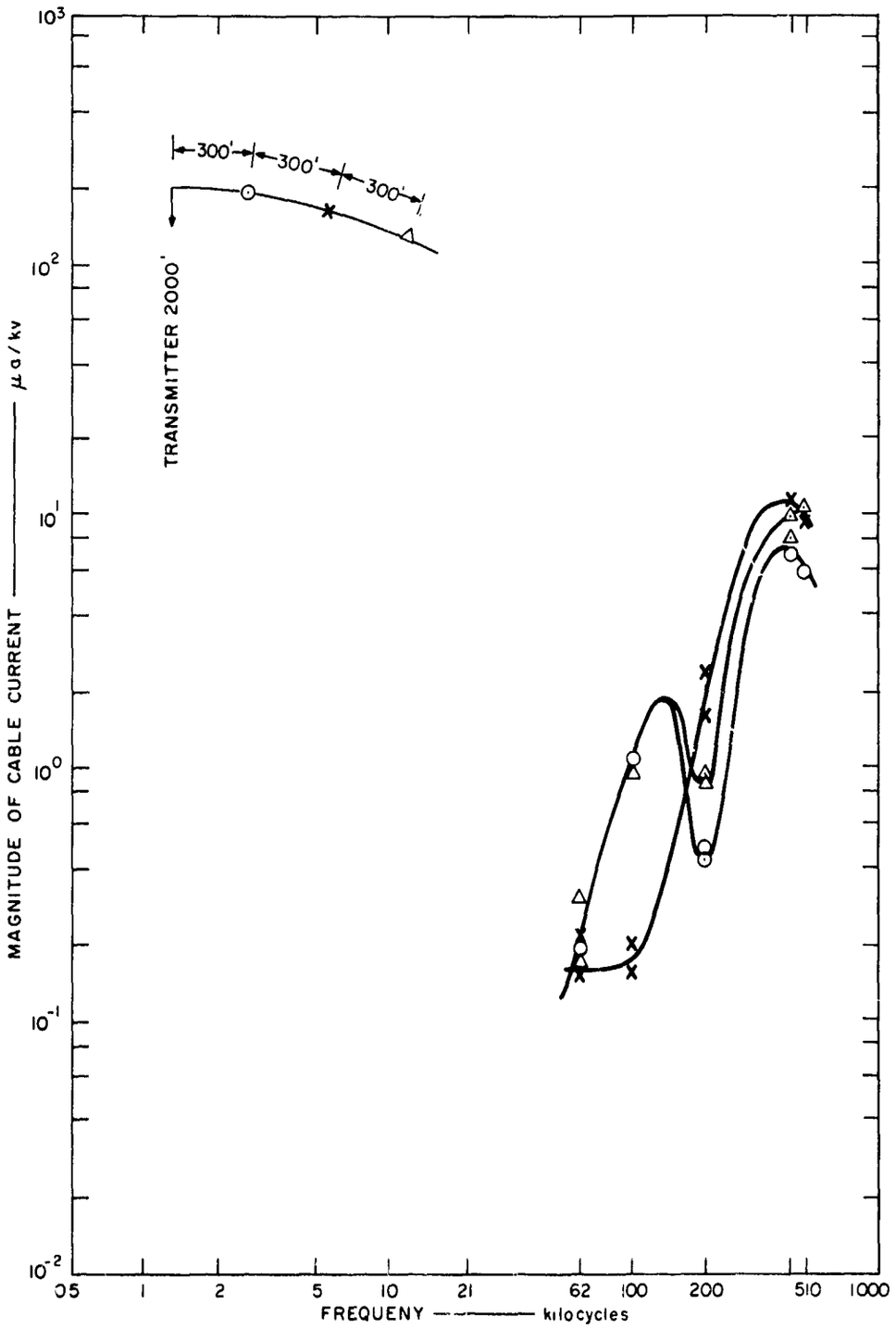

FIG. 62 MEASURED MAGNITUDE OF CURRENT IN ARC 2000 FEET FROM TRANSMITTER

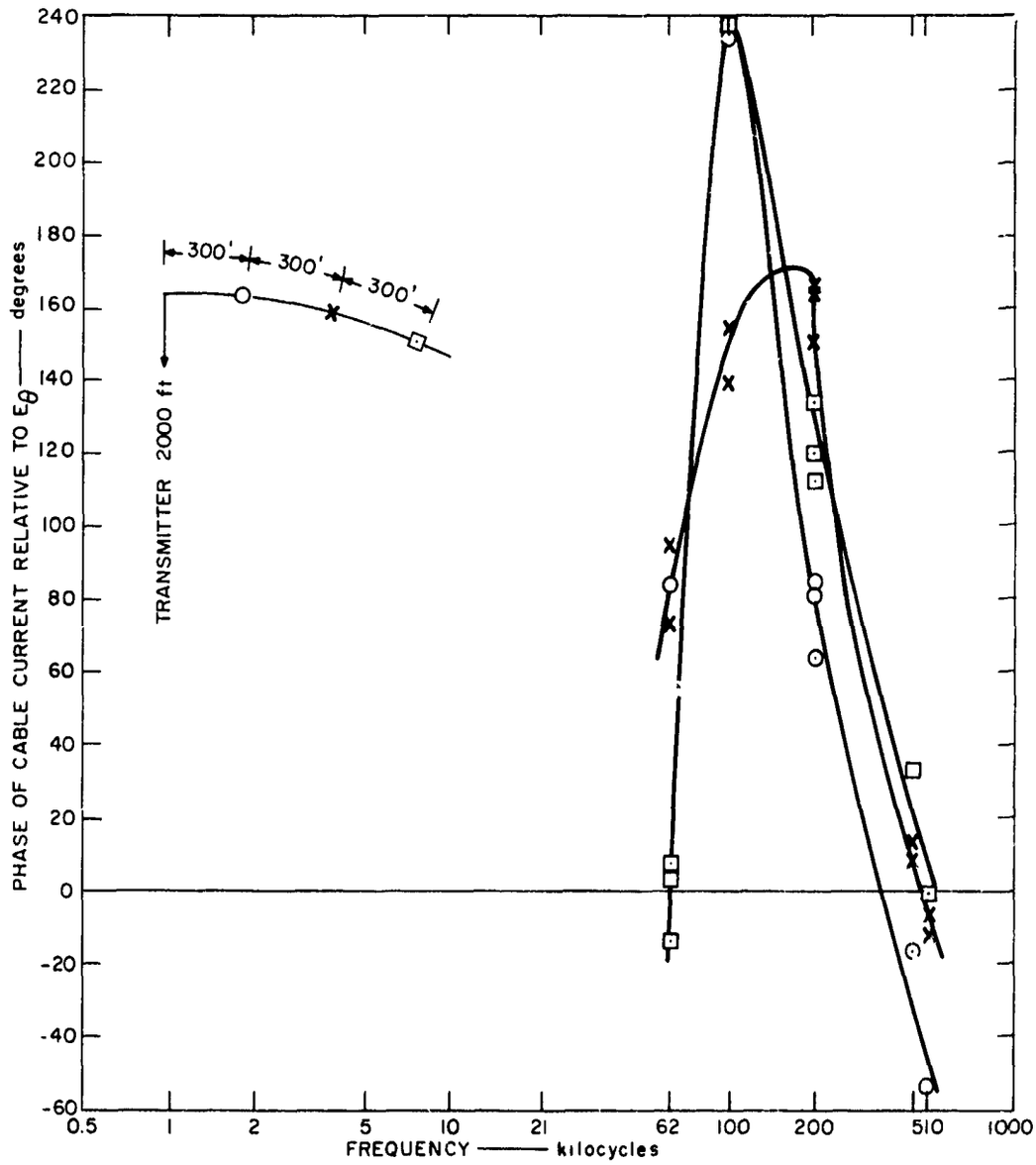

FIG. 63 MEASURED PHASE OF CURRENT IN ARC 2000 FEET FROM TRANSMITTER

(1) Bare 10-gauge copper wire one foot below the surface

(2) Copper shield cable with outer insulating plastic sheath three feet below the surface

(3) Copper shield cable with outer conducting plastic sheath three feet below the surface

(4) Lead sheath cable four feet below the surface.

The measured currents in the insulated cable could be predicted fairly well using the transmission line theory developed in Sec. III. This cable, being insulated from the ground, contained resonances above 10 kc. Below 10 kc, current increased as the 5/2 power of frequency, as would be expected from the theory for an insulated conductor [see Eq. (A-4), Appendix A]. The resonances, being complex functions of the dielectric constant of the insulation, length of cable, and cable terminations were not exactly as predicted; however, general agreement between theory and measurements was indicated.

The currents in the bare wire and cables with outer conducting sheaths could be predicted (using the transmission line theory) for cables that could be considered as single buried radial conductors. For such cables, both theory and measurements show that current increases as the 3/2 power of frequency. When more than one cable was buried in an area, so that cables were within a skin depth of each other, then Wait's wave impedance theory (see Sec. III) would predict the cable currents. Generally, at the higher frequencies and large distances from the transmitter, the cables were sufficiently isolated from each other to be considered as single cables. Near the transmitter at low frequencies, the cables had to be considered as an array. For the bare 10-gauge wire at frequencies below 2 kc the measured currents did not behave as predicted by either current theory. It was thought that a nearby large-diameter lead sheath cable was acting like a guard cable at these frequencies and was effectively shorting out the radial electric field near the 10-gauge wire.

Currents were measured in three buried loop structures:

(1) 100-foot diameter circular loop of insulated 12-gauge wire one foot below the surface

(2) 100-foot diameter loop of insulated 12-gauge wire with insulated 4/0-gauge guard loop, both one foot below the surface

(3) Large pie-shaped loop of multi-conductor cable with conducting outer sheath three feet below the surface.

The measured currents in the circular loops indicated that two current sources existed. At the higher frequencies the measured currents were in agreement with the transmission line theory, causing radially flowing currents in either side of the loop. At low frequencies, the loop response to the azimuthal magnetic field due to imperfect loop orientation causes circulating currents that are larger than the radially flowing currents.

Comparison of the currents in the guarded and unguarded 12-gauge loops indicate that the insulated 4/0-gauge guard loop shields the low-frequency currents caused by the azimuthal magnetic field, reducing these currents by a factor of about ten. The radially flowing currents in both loops are nearly alike, indicating little or no shielding for currents caused by the radial electric field. To improve shielding, the guard ring should have been uninsulated to provide a more effective short for the radial electric field.

Measured currents in the large pie-shaped loop were made in each radial leg and to one side of center in each azimuthal arc (340 and 1500 feet). At three locations the cable entered bunkers with the core wires continuous through the bunker and the shield connected to the bunker case. Deterioration of the cable had caused leakage between the shield and core wires that varied with soil and weather conditions. The measured core and shield currents were not very repeatable or predictable; however, the general behavior was like that observed on the 100-foot loops.

Currents measured on two azimuthal buried cables indicate that such cables appear as electric dipoles with their pattern null in the electric field direction so that the currents induced in such cables are reduced by one to two orders of magnitude compared to radial cables at similar distances. The amount of reduction appears to be dependent upon the effective null of the dipole.

This page intentionally left blank.

VIII
FIELD MEASUREMENTS NEAR CABLES AND BUNKERS

A. General

CW field measurements were made near selected buried cables and bunkers shown in Fig. 2 to determine magnitude, phase, and spatial differences from field measurements in an open (free space) area (also shown in Fig. 2). These measurements were made with the electric and magnetic field systems described in Secs. IV and V. At each measurement location the sensor was first oriented with a maximum sensitivity in the direction of the major field component--θ direction (vertical) for electric field (E_θ) and ϕ direction (azimuthal) for magnetic field (H_ϕ). The sensor was then oriented to obtain two null readings, one in each of the remaining orthogonal directions. This procedure produced the major field magnitude and phase with respect to E_θ and the spatial orientation of the total electric or magnetic field. The measurements during a null do not represent the fields orthogonal to the major field components (see Sec. II-G). In the null, this measurement technique gives a phase that is very sensitive to antenna orientation and is consequently sufficiently inaccurate to be meaningless as phase of the null component. Magnitude in the null is only meaningful when the null signal is greater than the sensor common-mode signal from the major field. (For example, at the higher frequencies and greater distances, E_r--radial E--is about 25 db below E_θ. The sensor common-mode signal in the null is about 50 db below E_θ. Thus, the signal magnitude in the null, called E_r null, is mostly due to E_r and not common mode and is meaningful as a magnitude only.)

Measurements were made along a radial line (N15°50'E--see Fig. 2) from the transmitter at 1000, 1600, and 2000 feet. This area was selected to have no known man-made inhomogenities in the immediate area. These measurements indicated that the electric and magnetic fields around the CW transmitter were as predicted using Eqs. (10), (11), and (12).

B. Bare 10-Gauge Copper Wire (Cable Z)

Magnetic field measurements were made at 0.5, 10, 62, 100, 200, and 510 kc along an arc at 1760 feet from the transmitter (10 feet beyond a hole where wire currents were measured.) Measurements were made above the wire (buried 1 foot) and at distances of 10, 20, 40, and 80 feet along an arc to the left of the wire facing in the direction of propagation (counter-clockwise from the wire). Measurements above the wire were repeated after a two-week interval.

The magnitude of H_ϕ is shown in Fig. 64 along with free-space theory and data. The free-space data are at 1600 and 2000 feet. The data at 1760 feet should fall between these free-space data if there are no magnetic field distortions above the wire. At the three higher frequencies, H_ϕ is essentially independent of the wire. At the three lower frequencies, H_ϕ is enhanced due to the presence of the wire. However, the field enhancement does not follow any particular pattern as a function of distance from the wire.

The phase of H_ϕ referenced to E_θ is shown in Fig. 65 along with the H_ϕ free-space phase at 1600 and 2000 feet. The phase shows a maximum variation at 10 kc and smaller variations at the higher frequencies. Phase accuracy is no better than ±5 degrees. The maximum phase deviation from theoretical phase occurs over the wire. At 10 kc, phase retards (decreasing phase angle) as the cable is approached. This tendency occurs at 62 kc but is not evident at other frequencies.

The magnitude of H_θ null (vertical) is shown in Fig. 66 along with the theoretical value of H_ϕ at 1600 feet. As can be seen, H_θ null approaches the magnitude of H_ϕ, indicating a large anomalous vertical magnetic field. (For the free-space measurements, H_θ null and H_r null were of the order of 40 db below H_ϕ.) At all frequencies except 10 kc the H_θ null magnitude is a minimum over the wire (0 feet), maximum near the wire (10 feet), and decreases smoothly with distance approaching the 0-foot magnitude at 80 feet. At 10 kc the distance dependance is the same as at other frequencies if the measurements over the wire are neglected. At 10 kc, H_θ null over the wire is the maximum signal recorded.

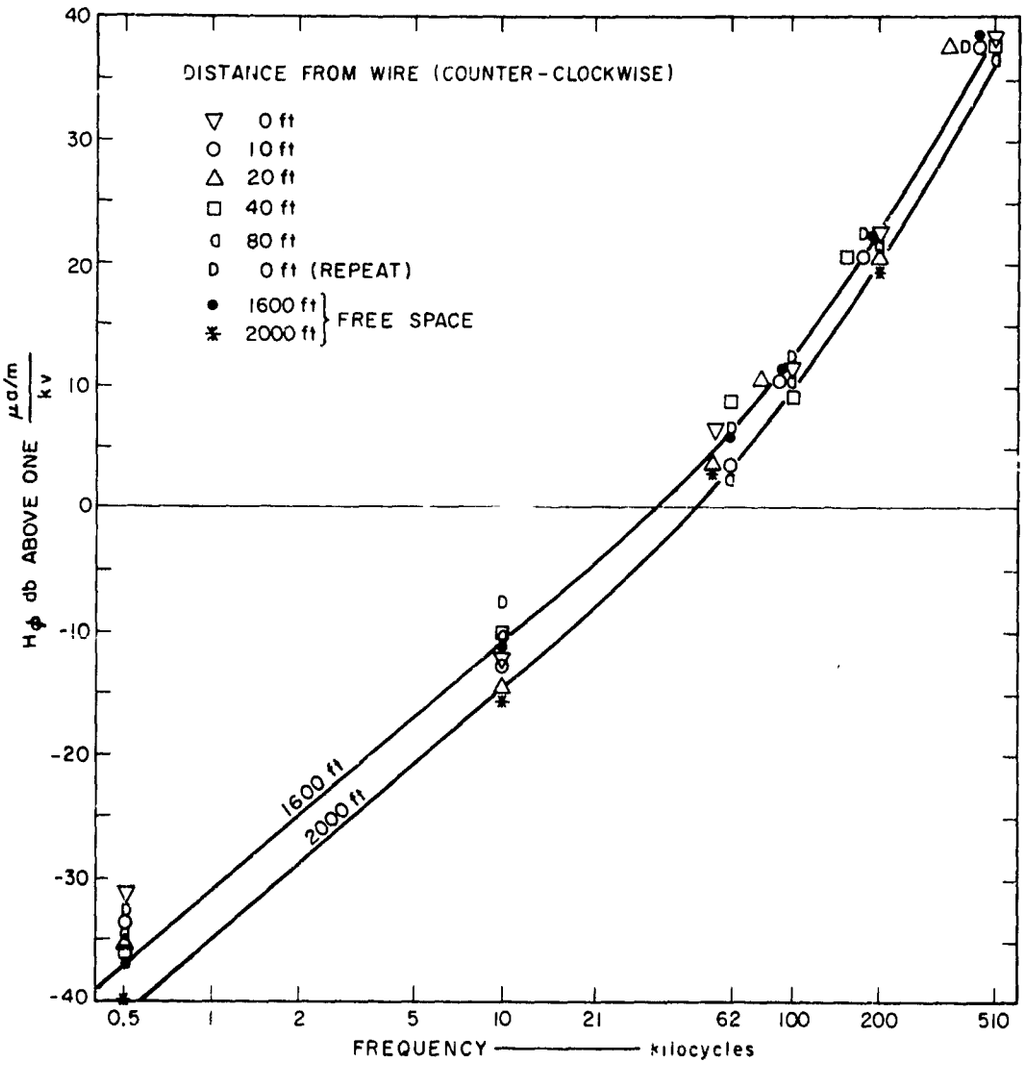

FIG. 64 H_ϕ MAGNITUDE NEAR 10-GAUGE COPPER WIRE AT 1760 FEET

The H_r null magnitude is shown in Fig. 67 along with theoretical H_ϕ for 1600 feet. H_r null magnitudes are generally less than H_θ null (being 20 db below H_ϕ) but are greater than H_r null in free space at 1600 feet. The data are closely grouped except at 10 and 62 kc. There is no smooth pattern as a function of distance from the wire.

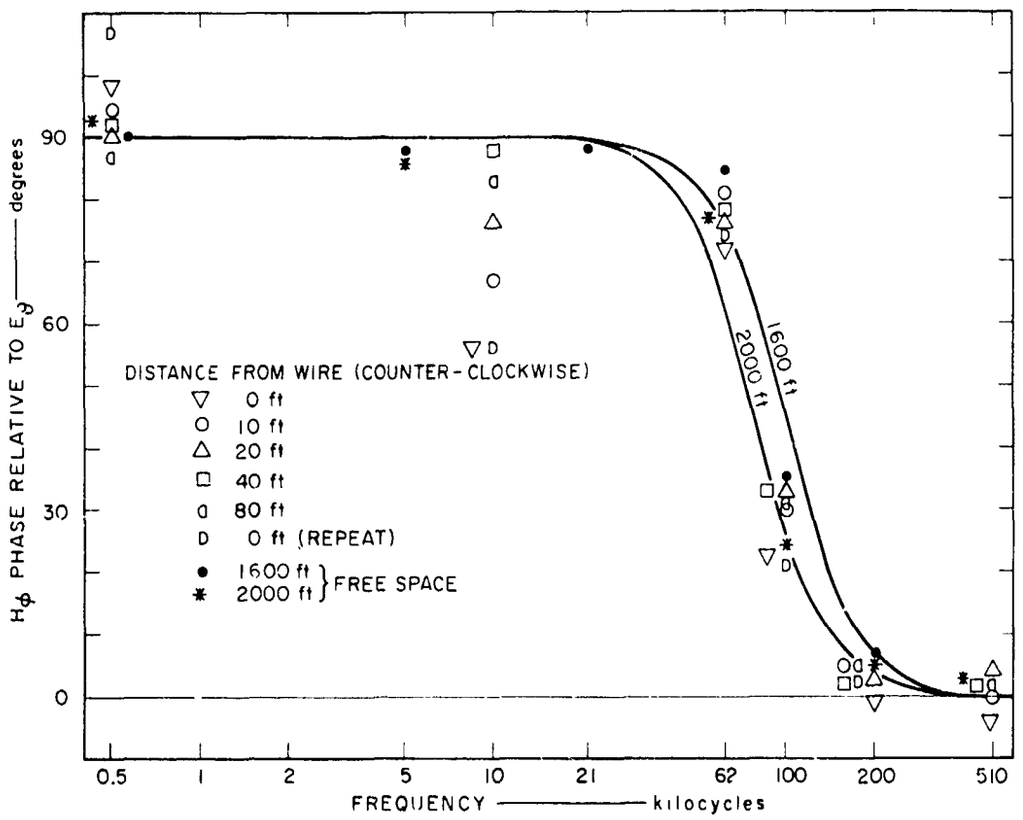

FIG. 65 H_ϕ PHASE NEAR 10-GAUGE COPPER WIRE AT 1760 FEET

The H_ρ null and H_r null data presented in Figs. 66 and 67 were the minimum readings obtained in the null. Three readings were obtained near each null. The orientation of the sensor for the smallest magnitude reading defines the orientation of the total H field (see Sec. II-G). For the magnetic field, the remaining two readings were at angles greater than ±1 degree from this minimum (see Sec. V), and the magnitudes were not always greatly different from the minimum magnitude. The angular orientation of the H field near the buried 10-gauge wire is shown in Figs. 68 and 69. The angle associated with the minimum magnitude is shown as the probable null. The angles for the remaining two readings are shown by the vertical line through the probable null. H-field orientation is shown as change in orientation from the theoretical negative H_ϕ

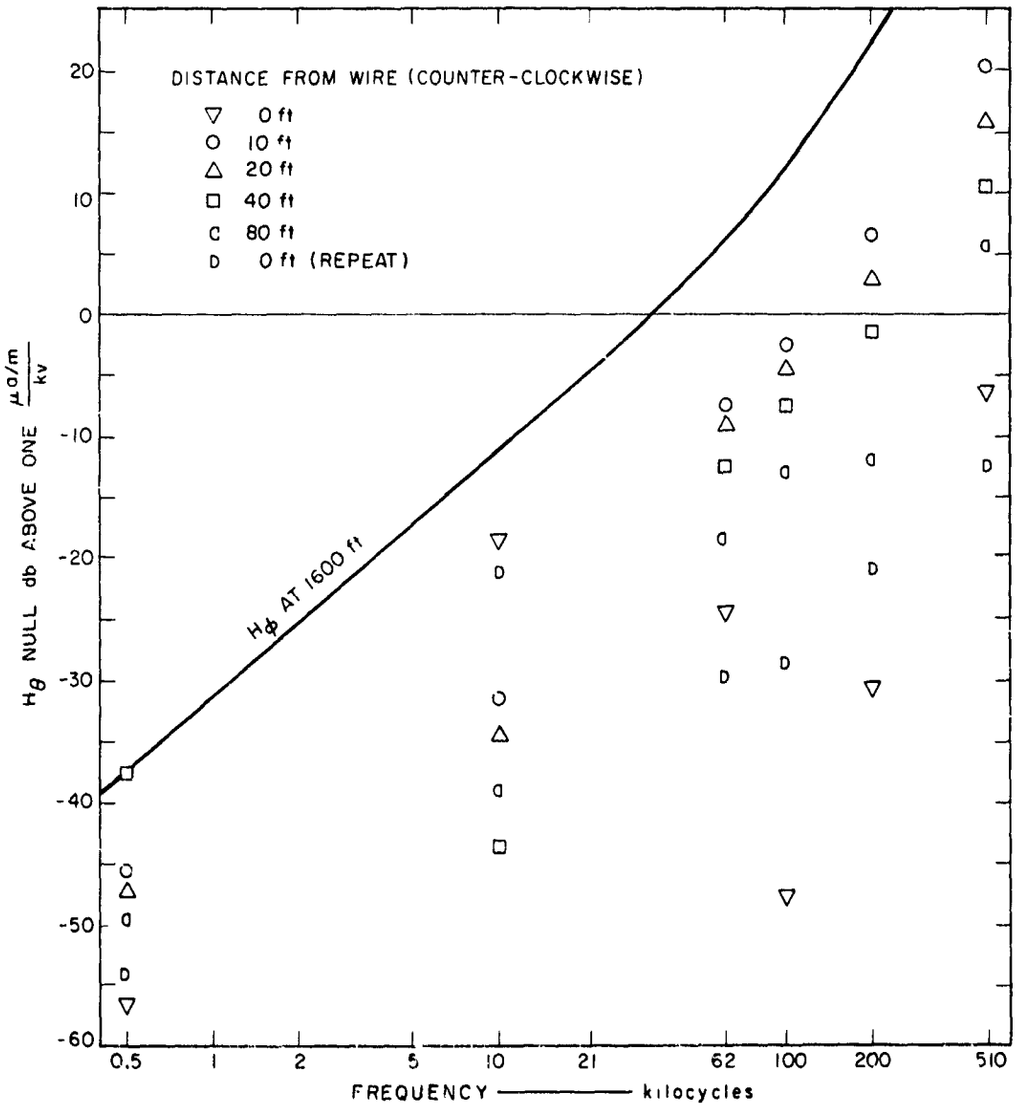

FIG. 66 H_θ NULL MAGNITUDE NEAR 10-GAUGE COPPER WIRE AT 1760 FEET

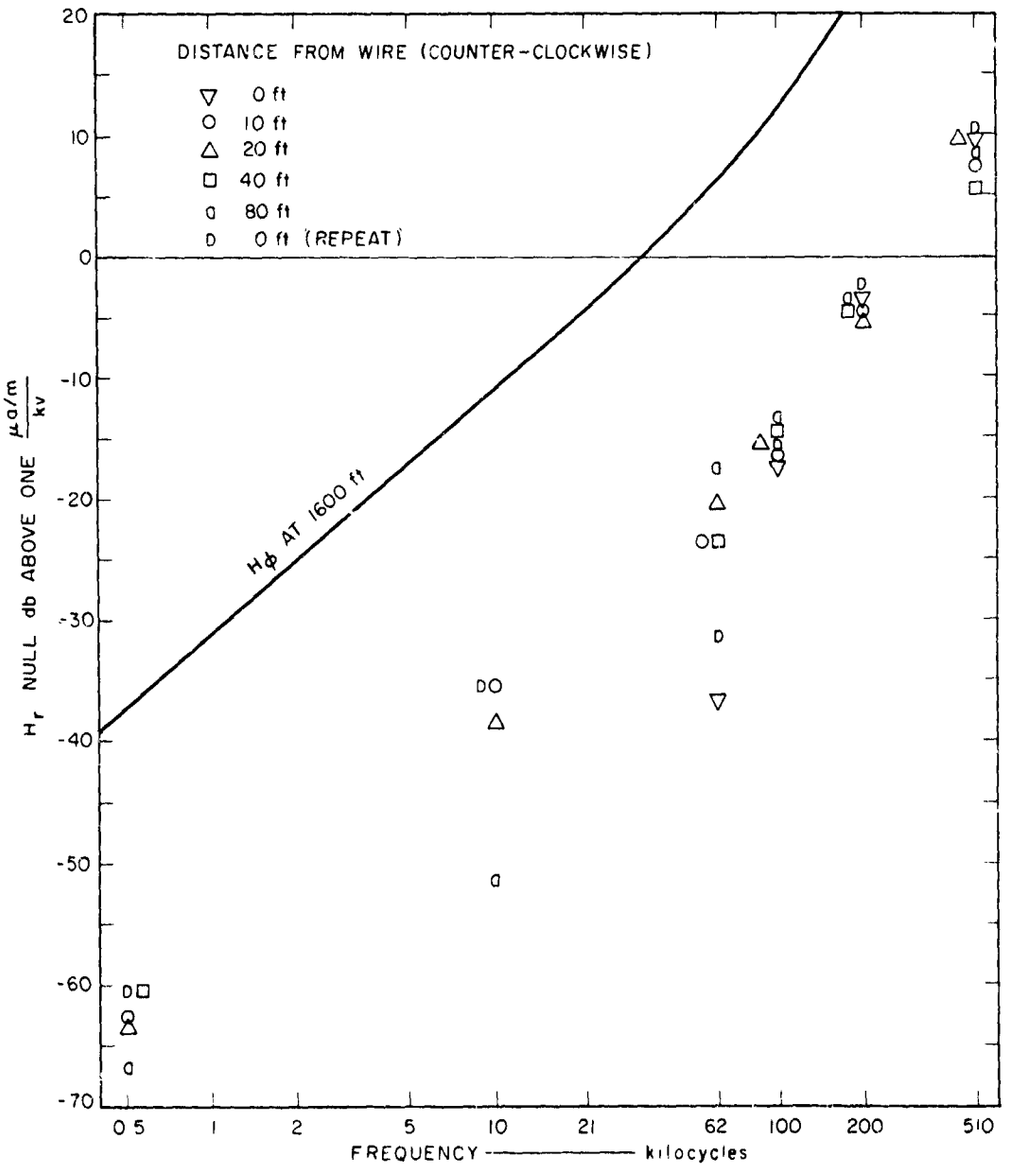

FIG. 67 H_r NULL MAGNITUDE NEAR 10-GAUGE COPPER WIRE AT 1760 FEET

direction.* H tilt is the change in the vertical direction (positive change down) and H yaw is the change in the horizontal direction (positive change toward the transmitter).

Figure 68 shows H tilt and H yaw as functions of frequency for the measurements near the 10-gauge copper wire along with the free-space data. The H field shows a negative tilt (up) at most frequencies with the maximum tilt at 10 kc. Yaw is evident at 10, 62, and 100 kc. Figure 69 shows the tilt and yaw as a function of distance from the wire. Tilt shows definite distance dependence that can be related to current in the wire. A current flowing toward the transmitter in a long radial wire will create a magnetic field H_I counterclockwise around the wire looking in the direction of propagation. This field will add to the propagating field H_ϕ to cause an elliptic polarization of the H vector more general than that shown for the E vector in Sec. II-G because H_I and H_ϕ need no longer be orthogonal in space. The effect for currents flowing toward the transmitter (positive current) is a negative H tilt counter-clockwise from the wire and positive H tilt clockwise from the wire. H tilt should be zero above the cable, however, the magnitude of H_I should add (using proper phase) to H_ϕ magnitude. The H-tilt data in Fig. 67 shows the general behavior described above. In Fig. 70 are shown the H_ϕ predicted at 1600 feet and H_I at 10 feet from the wire from the measured wire currents at 1750 feet (Fig. 29). Obviously, maximum field distortion effects in the form of H tilt and H_ϕ magnitude and phase should occur at 10 kc with minimum effects at the lowest and highest frequencies. The magnitude and phase observations shown in Figs. 64, 65, and 66 generally agree with the assumption that the field distortion is caused by the measured radial wire current. The geometry and relative phase of H_ϕ and H_I effect the general description outlined above and can cause considerable variations with distance and frequency.

Radial uniform currents in the wire cannot cause radial magnetic fields or H-yaw distortions. However, all current is not confined to the wire.

---

*The data presentation format described here and shown in the figures is used throughout this report and was selected for easy presentation of both E and H spacial distortions.

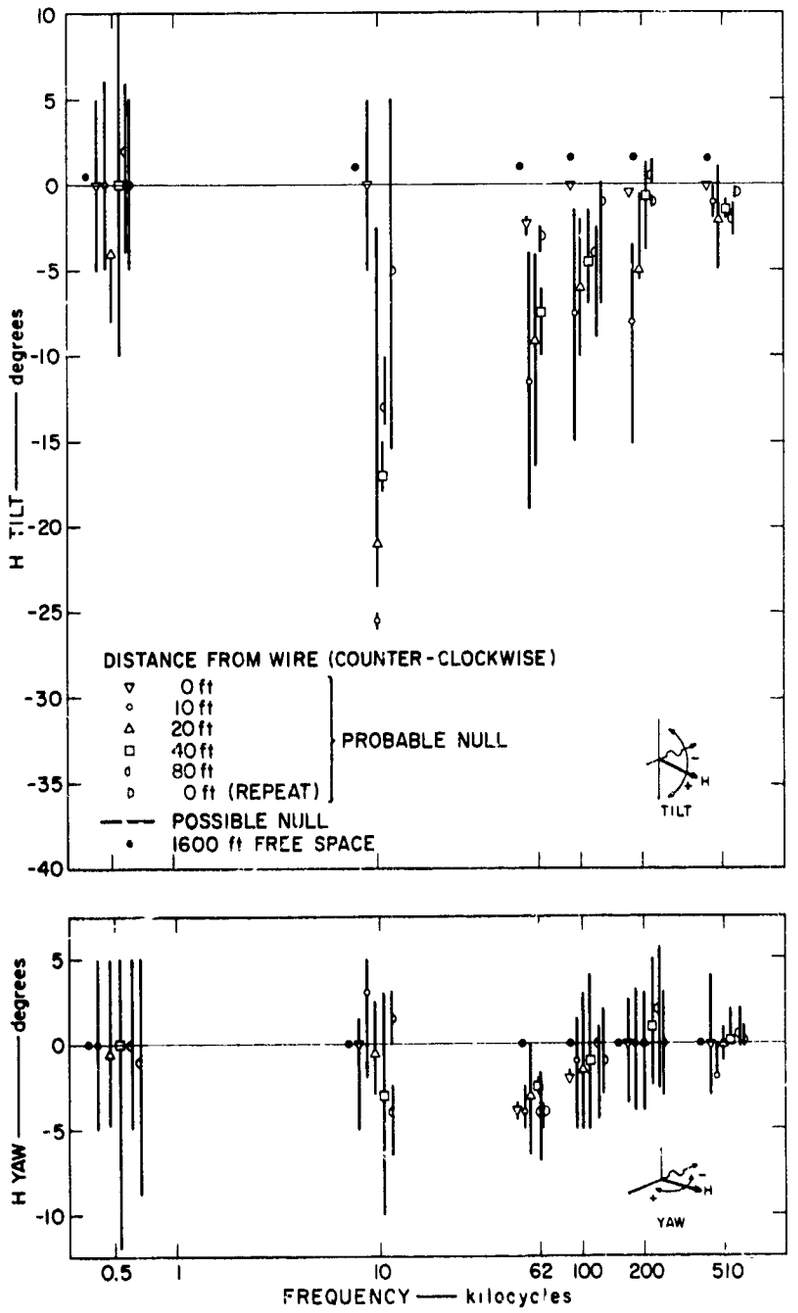

FIG. 68 H TILT AND H YAW NEAR 10-GAUGE COPPER WIRE AT 1760 FEET

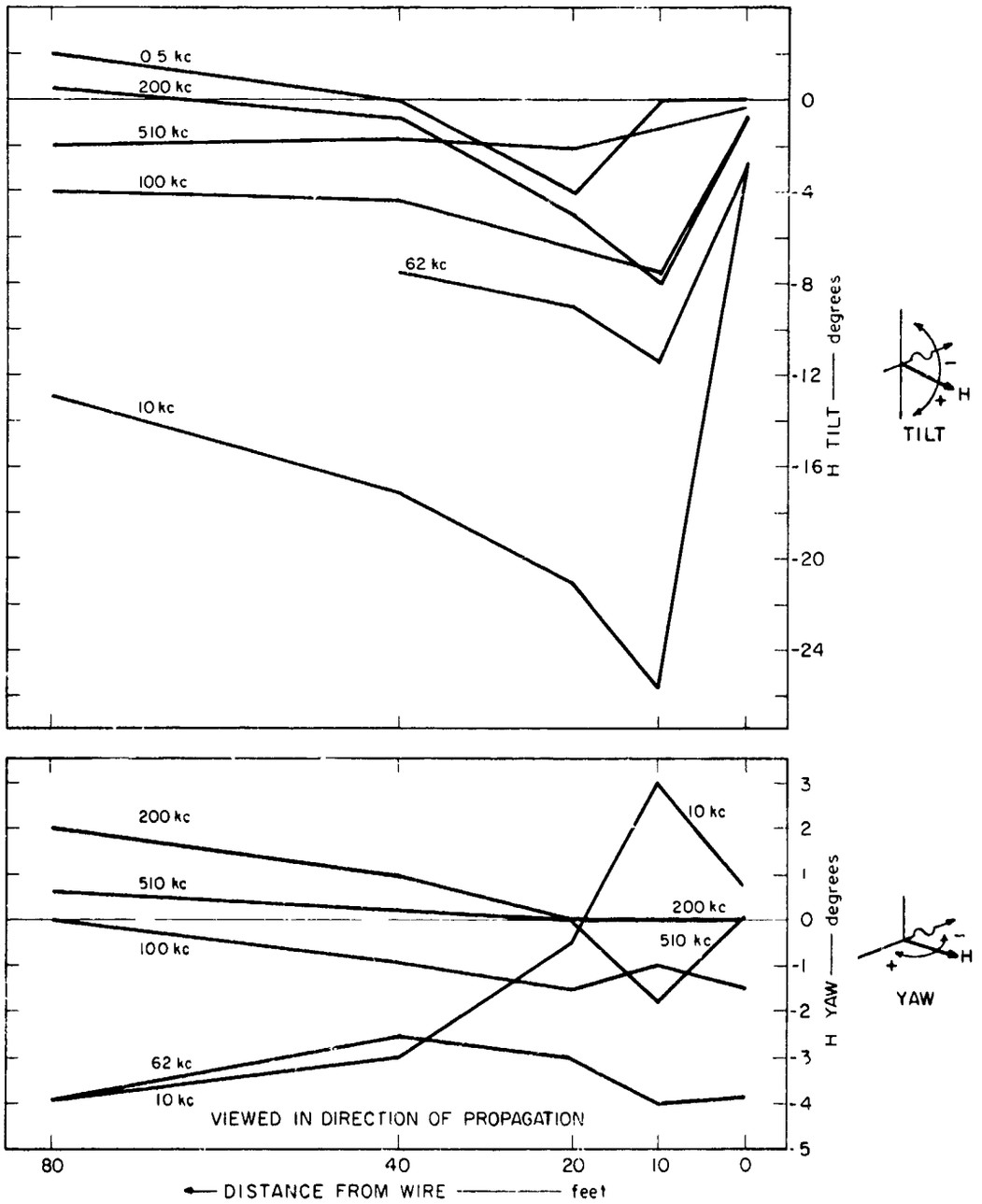

FIG. 69 H TILT AND H YAW NEAR 10-GAUGE COPPER WIRE AT 1760 FEET

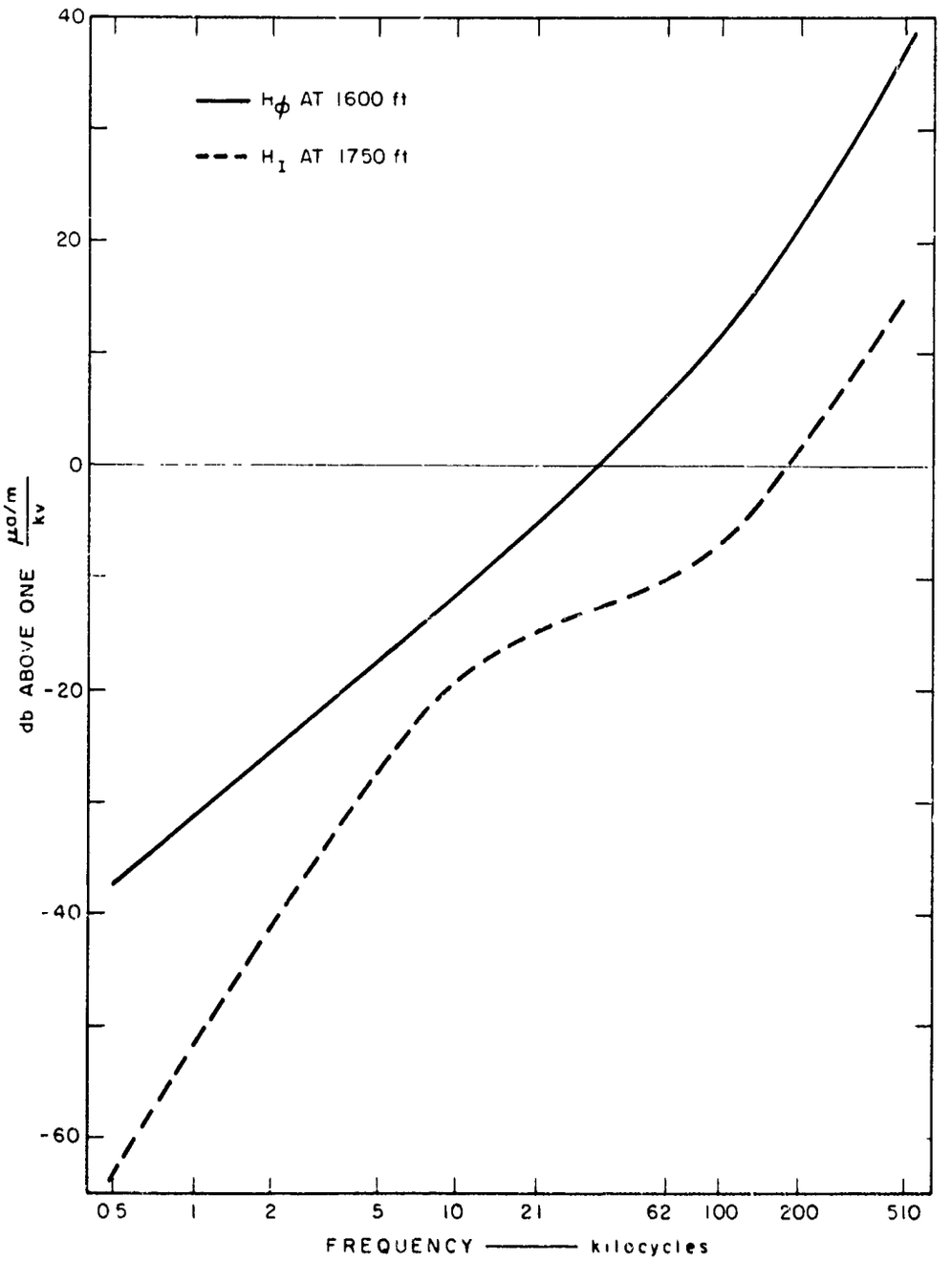

FIG. 70 H_ϕ AND H_I MAGNITUDES 10 FEET FROM 10-GAUGE COPPER WIRE

Currents flow in the ground that converge on the wire which is a better conductor than the ground. These ground currents that are not totally radial can cause H yaw. Figures 67, 68, and 69 show evidence of a H-yaw distortion between 10 and 62 kc whose exact cause is unknown.

C. Conducting Sheath Cable (Cable L)

Magnetic field measurements were made at 0.5, 10, 62, 100, 200, and 510 kc along an arc at 2030 feet from the transmitter (20 feet toward the transmitter from a hole where cable current measurements were made). Measurements were made above the cable (buried 3 to 4 feet) and at distances of 10, 20, 40, and 80 feet along an arc to the left of the cable facing in the direction of propagation.

The magnitude and phase of H_ϕ (reference to E_θ) are shown in Figs. 71 and 72. Both magnitude and phase are very nearly equal to the free-space measurements. The magnitude at 10 kc shows an enhancement at all distances except at 80 feet and a large phase difference from free-space measurements at 2000 feet. The data at 0.5 kc is limited but does show a large signal enhancement and a phase distortion.

The magnitude of H_θ null (vertical) is shown in Fig. 73 along with the predicted curve for H_ϕ at 2000 feet. Except for 0.5 kc where H_θ null exceeds predicted H_ϕ, H_θ is about 20 db below H_ϕ and 40 db above H_θ null in free space. H_θ null is a minimum over the cable, a maximum at 10 feet, and decreases with distance from the cable. H_r null (radial) shown in Fig. 74 generally is of the same magnitude as H_θ null; however, there does not seem to be a uniform distance dependence to the variation in magnitude.

Magnetic field distortion angles H tilt and H yaw are shown versus frequency in Fig. 75 and versus distance in Fig. 76. H tilt (distortion in vertical direction) shows some distortion at all frequencies, with the greatest distortion at the low frequencies. Maximum tilt (up) occurs at 10 feet (Fig. 76) and is increasing with decreasing frequency. Figure 77 shows H_ϕ in free space at 2000 feet and the magnetic field H_I at 10 feet from the cable, calculated from the measured cable currents at 2050 feet shown in Fig. 40. The summation of these two fields would cause maximum H tilt at the lowest fre-

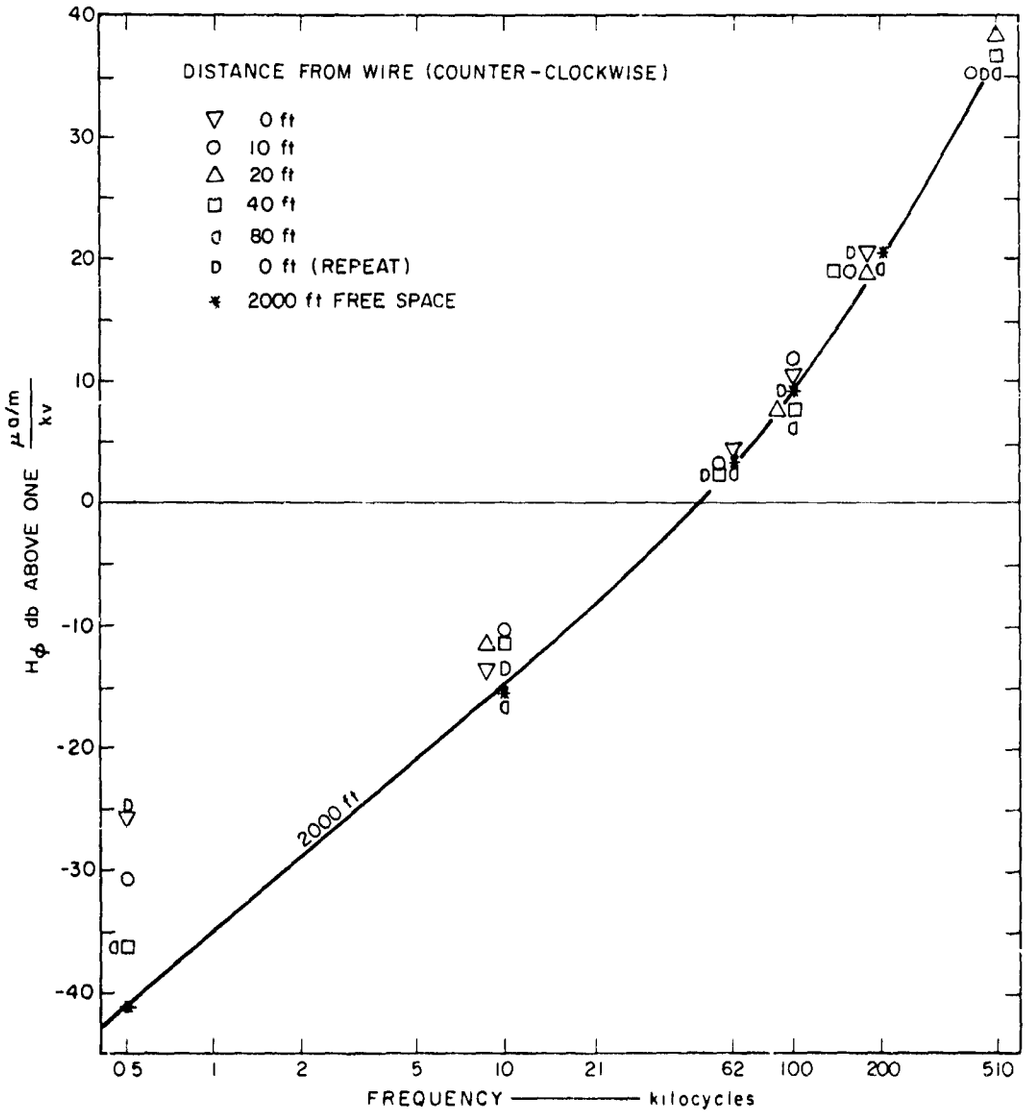

FIG. 71 H_ϕ MAGNITUDE NEAR CONDUCTING SHEATH CABLE AT 2030 FEET

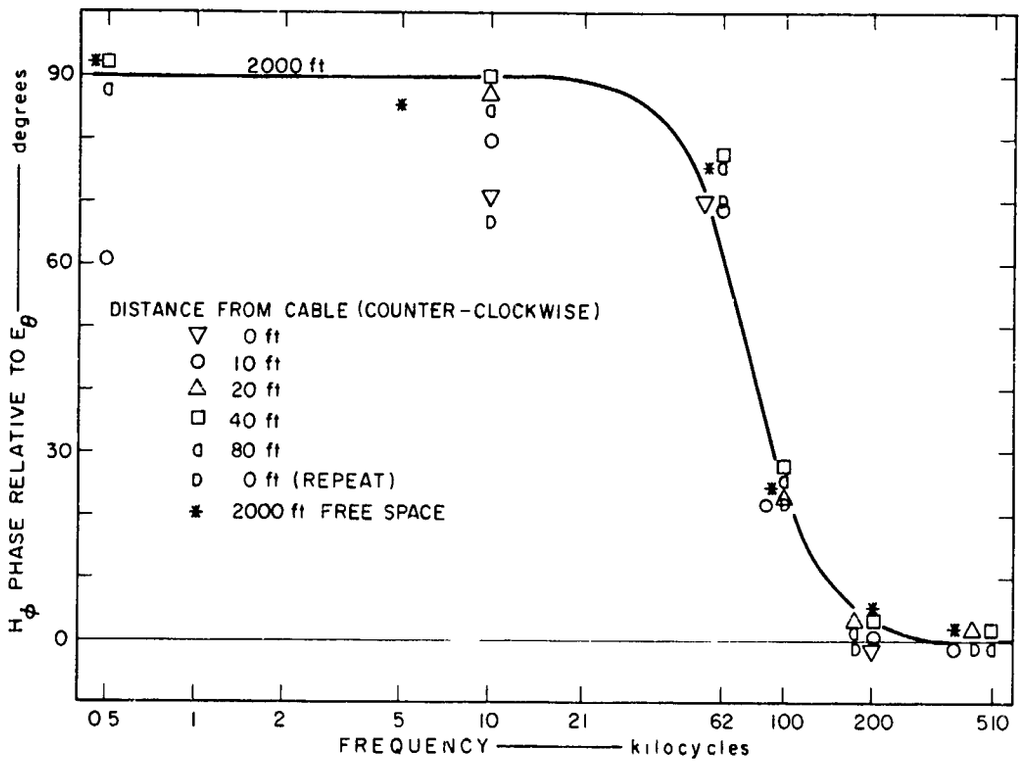

FIG. 72 H_ϕ PHASE NEAR CONDUCTING SHEATH CABLE AT 2030 FEET

quency that is compatible with the measured H tilt. H tilt is apparently caused by the radial current in the buried cable.

H yaw shows little distortion at the higher frequencies. The lowest frequencies show maximum distortion. H yaw behavior is similar to H tilt, indicating a common cause for the two distortions.

D. Pie-Shaped Loop

Magnetic and electric field measurements were made at 0.5, 10, 62, 100, 200, and 510 kc at 600, 900, and 1200 feet along a radial from the transmitter that dissected the pie-shaped loop shown in Fig. 2. The inner and outer loop arcs are at 340 and 1500 feet so that all measurements were within the loop area. A buried cable of undetermined length ran on a radial beneath the measurements at a depth of 1 foot. The pie-shaped loop cable was in poor physical

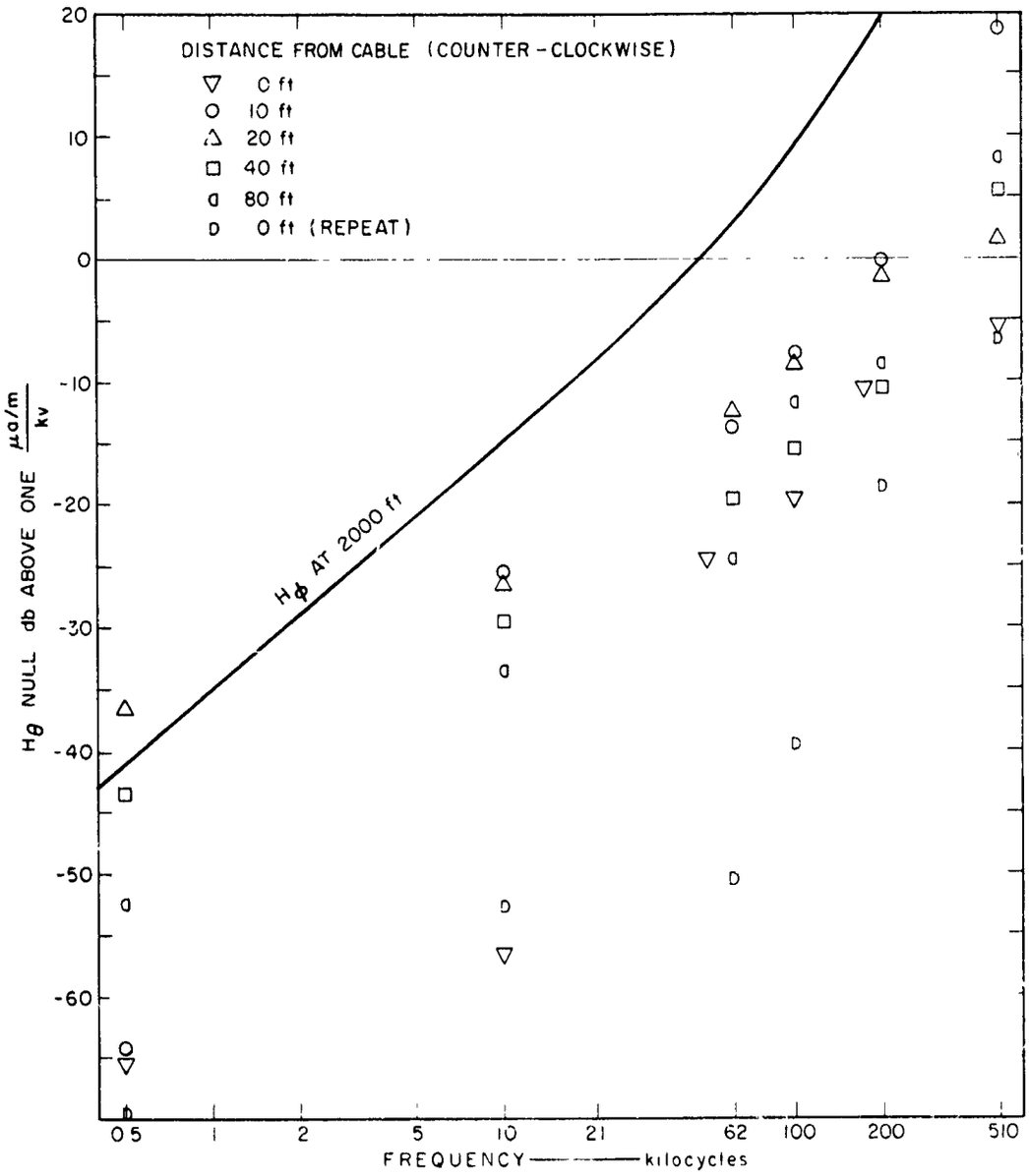

FIG. 73 H_θ NULL MAGNITUDE NEAR CONDUCTING SHEATH CABLE AT 2030 FEET

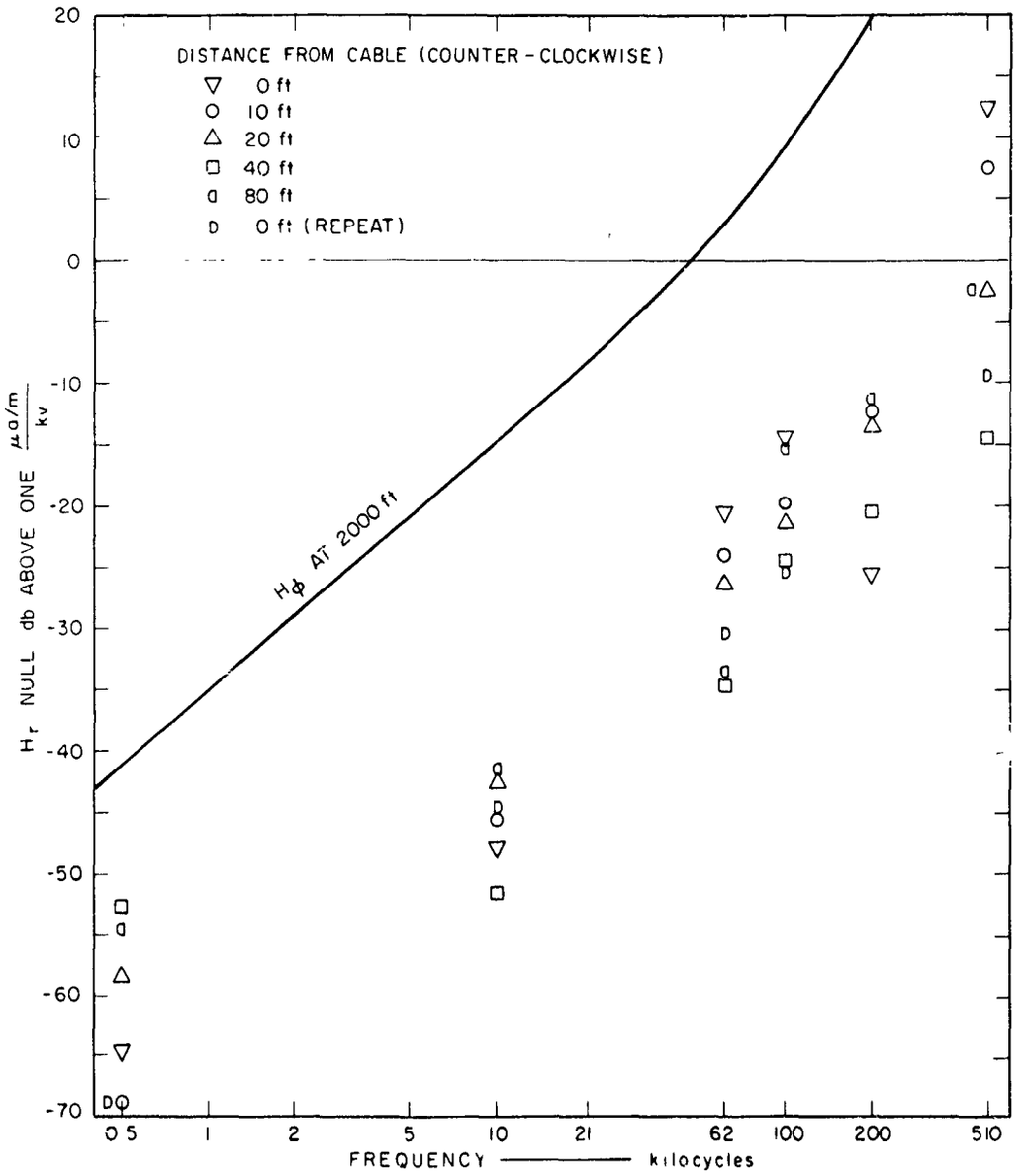

FIG. 74 H_r NULL MAGNITUDE NEAR CONDUCTING SHEATH CABLE AT 2030 FEET

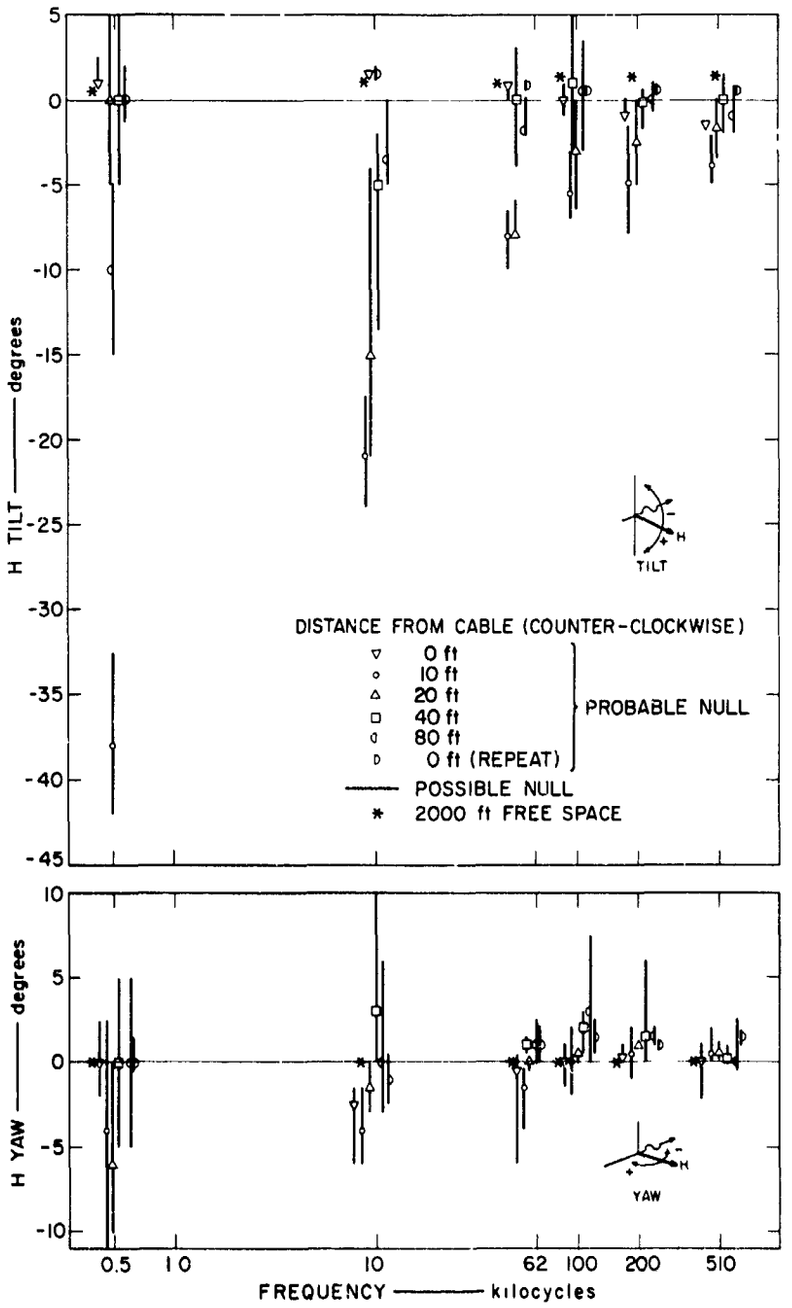

FIG. 75 H TILT AND H YAW NEAR CONDUCTING SHEATH CABLE AT 2030 FEET

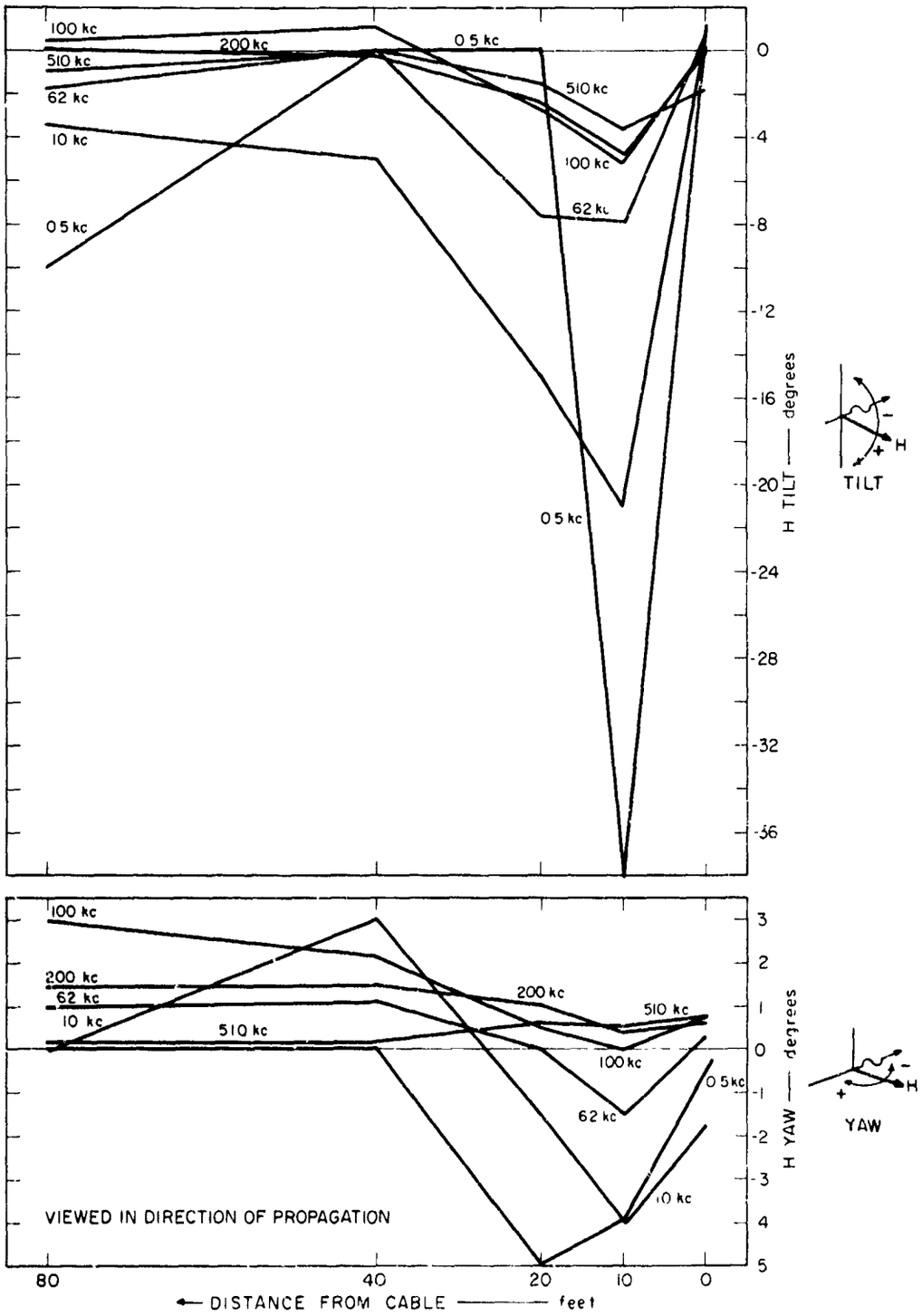

FIG. 76 H TILT AND H YAW NEAR CONDUCTING SHEATH CABLE AT 2030 FEET

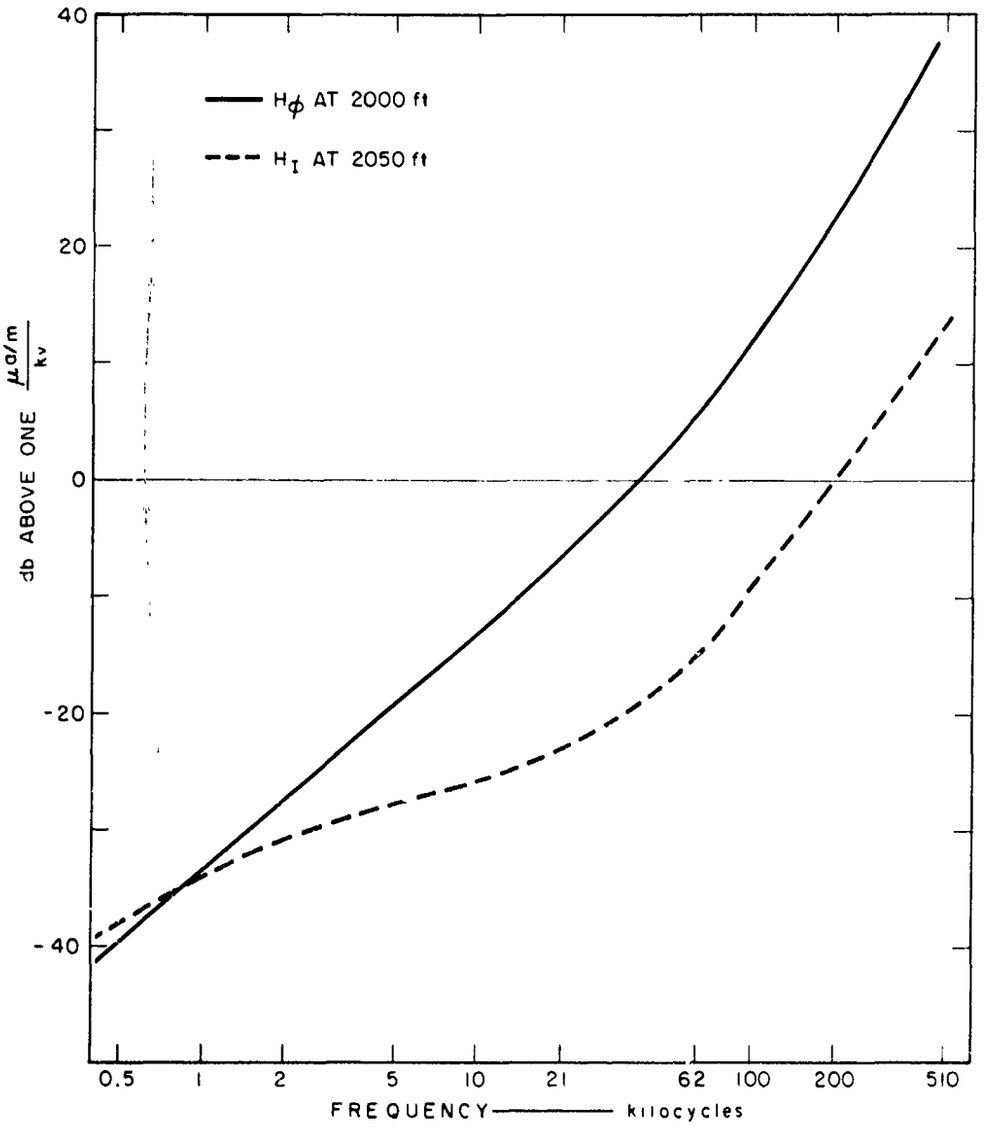

FIG. 77 H_ϕ AND H_I MAGNITUDES 10-FEET FROM CONDUCTING SHEATH CABLE

shape, having several repaired breaks and a time-varying (slow) sheath-to-core resistance (see Sec. VII-F).

The magnitude of H_ϕ is shown in Fig. 78 with predicted H_ϕ for 600, 900, and 1200 feet. At 600 and 900 feet and above 100 kc the measured field is nearly the free-space predicted field. Below 100 kc for 600 and 900 feet, H_ϕ is increasingly enhanced with decreasing frequency and distance from transmitter. This enhancement may be due to inadequacies in the field theory.* The H_ϕ measurements at all frequencies at 1200 feet are some 10 db below predicted free space H_ϕ. The phase of H_ϕ (not shown) did not agree with predicted free-space phase for any distance. All phase data were below (more negative) predicted phase. The frequency-distance dependence shown in the magnitude data was not displayed in any manner in the phase data. The magnitude of H_θ null and H_r null are shown in Fig. 79 with predicted H_ϕ for 600, 900, and 1200 feet. H_θ null is generally larger than H_r null and is nearly equal to the predicted H_ϕ, indicating a distorted H field. H_θ null decreases with distance from transmitter except at 0.5 kc. H_r null does not follow a distance function for all frequencies.

The magnetic field distortions in the form of H tilt are shown in Fig. 80. H tilt (vertical) shows a large field distortion at 0.5 kc that decreases with increasing frequency. At 600 and 1200 feet the H field is tilted up and at 900 feet the tilt magnitude is the same magnitude as other distances but is in the down direction. A uniform radial current in the radial cable directly beneath the field measurements cannot cause the observed H tilt. The pie-loop current measurements shown in Figs. 48 through 51 do not show any correlation with the H-tilt field distortions shown in Fig. 80. However, H tilt and H_ϕ show similar patterns (low-frequency distortion).

H yaw (not presented) showed no distortion at 600 and 1200 feet and showed a small H yaw (one degree) toward the transmitter at 900 feet at all frequencies. Assuming a ±1° accuracy, the H yaw may have only existed at 62 and 100 kc.

---

*The field theory used is increasingly invalid as the transmitter is approached where the antenna cannot be considered a point source. Near the antenna (in wavelengths) the theory used will give field magnitudes that are too small.

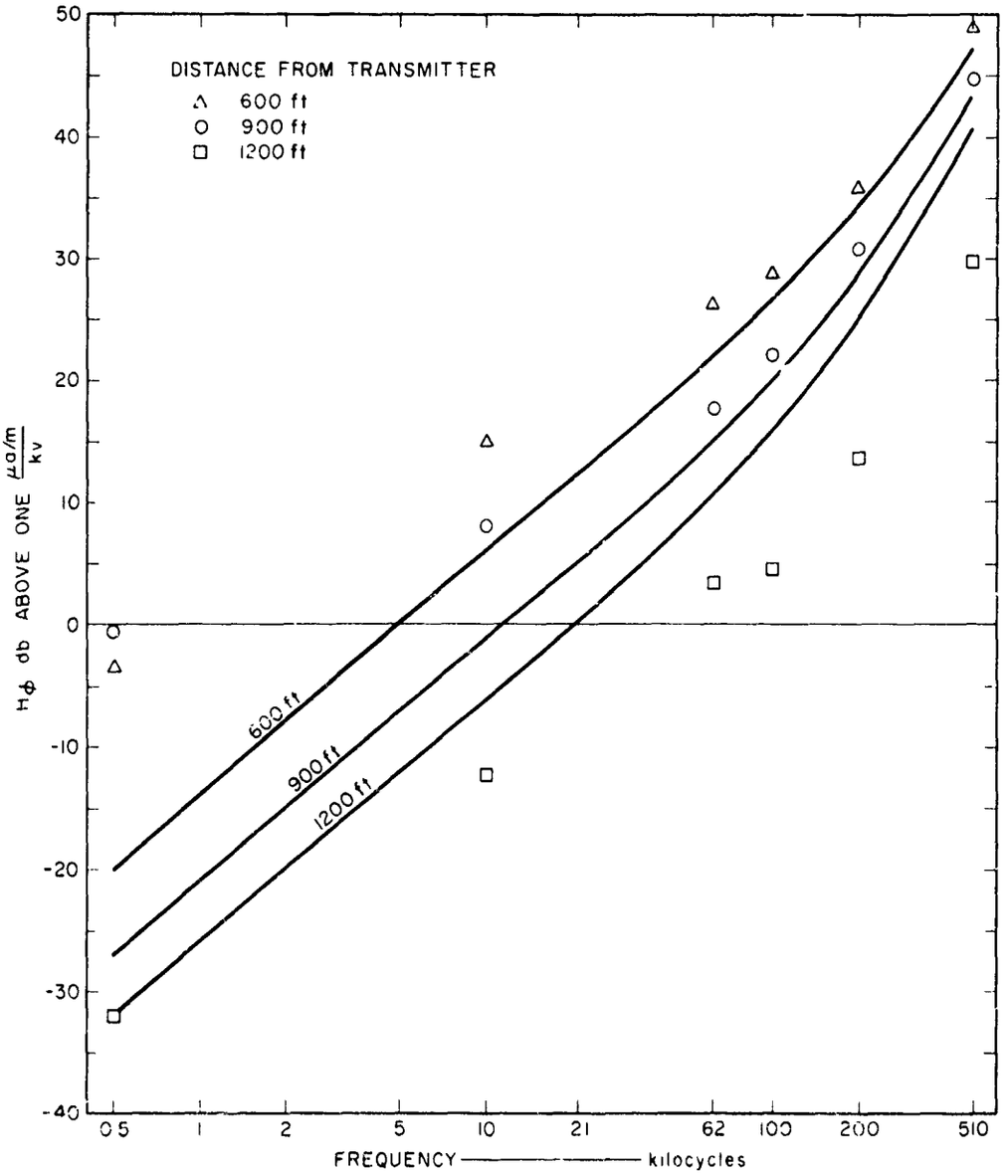

FIG. 78 H_ϕ MAGNITUDE IN PIE-SHAPED LOOP

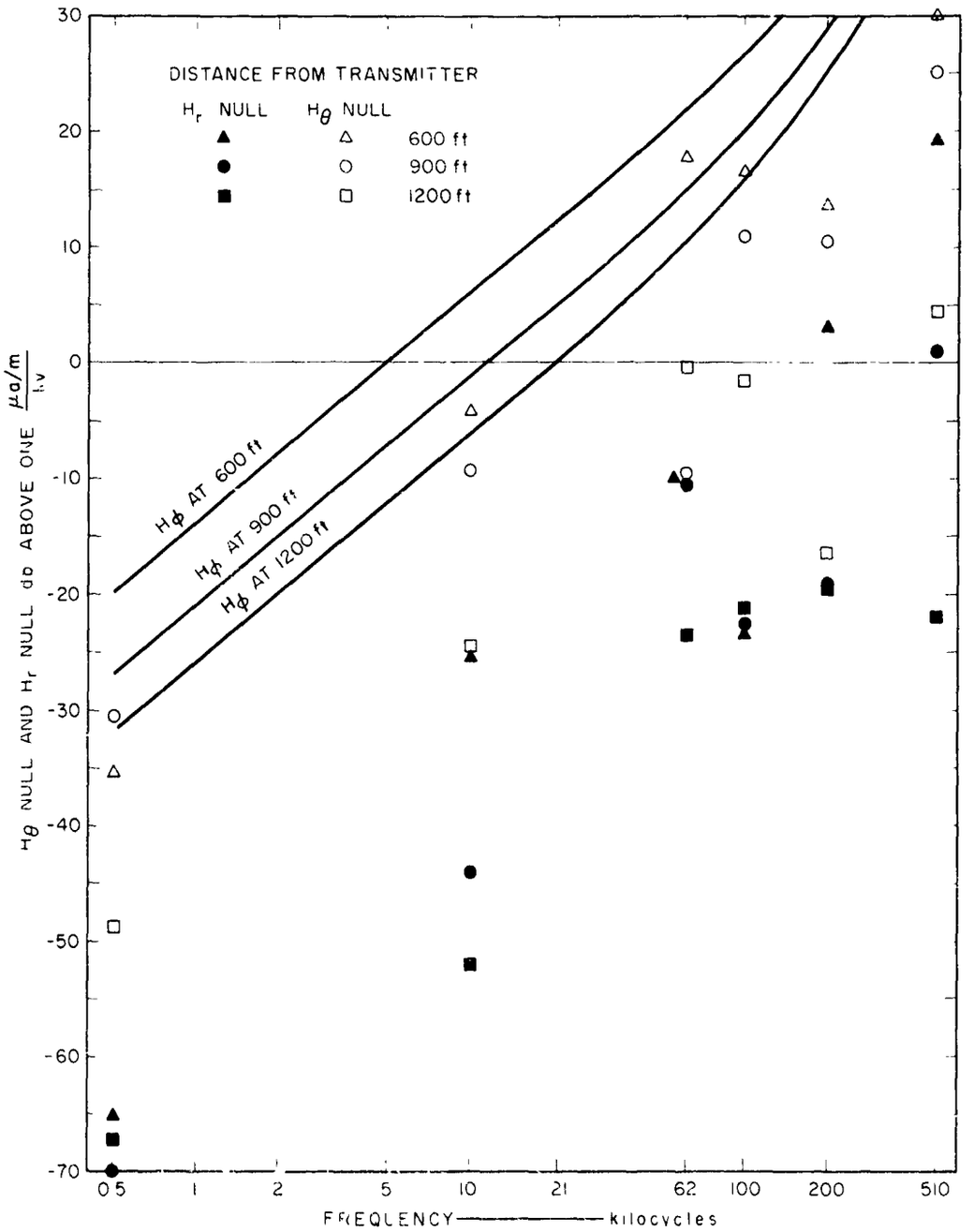

FIG. 79 H_θ NULL AND H_r NULL MAGNITUDE IN PIE-SHAPED LOOP

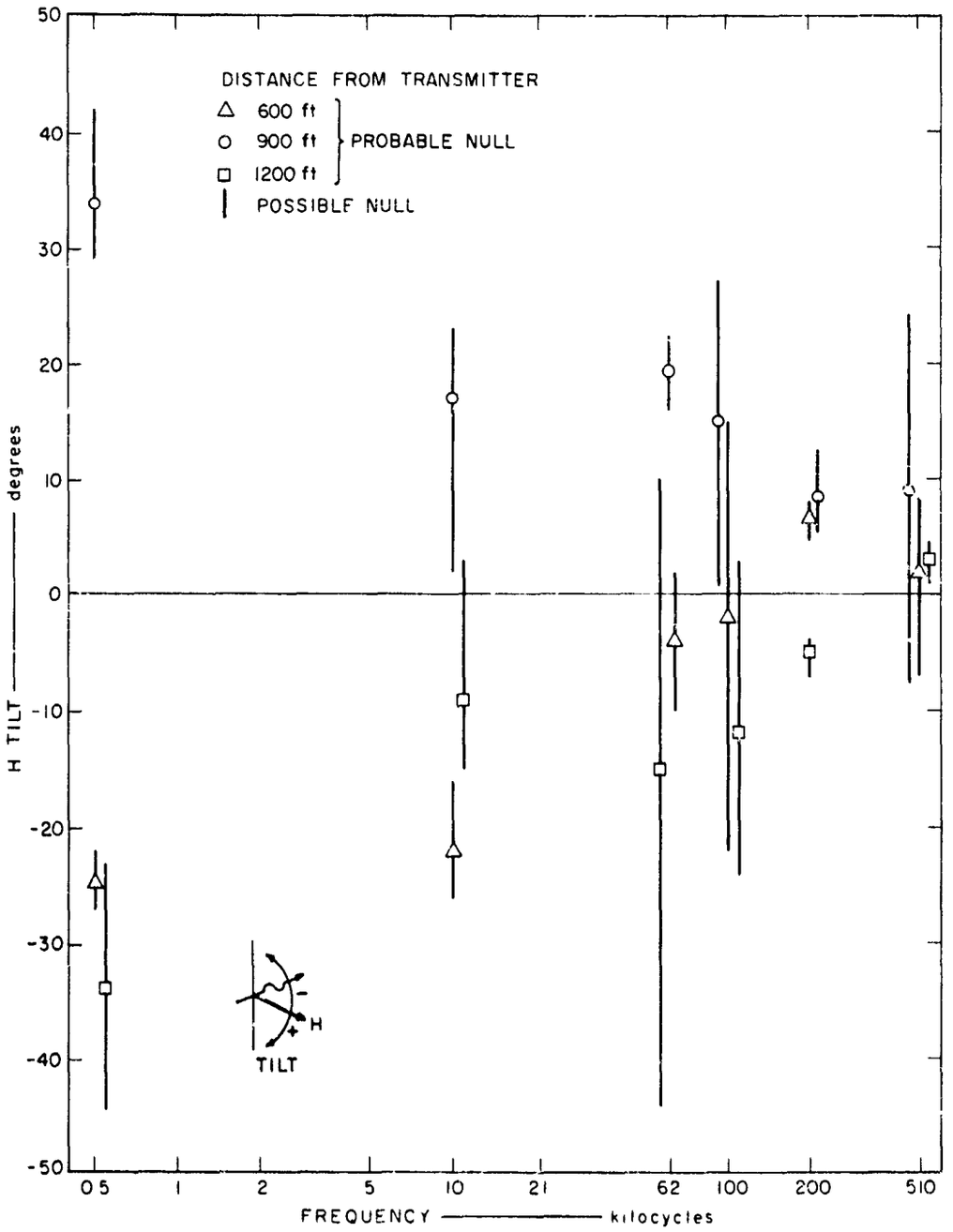

FIG. 80 H TILT IN PIE-SHAPED LOOP

The magnitude of the E_θ measurements within the pie-shaped loop are shown in Fig. 81 with the predicted free-space E_θ. Free-space E_θ data at 1000 feet are shown and they agree with predicted E_θ for this distance. The measurements within the pie-shaped loop are all some 5 db above predicted free-space E_θ.

The magnitude of E_r null and E_ϕ null is shown in Fig. 82. For the distances shown, the predicted electric field ellipse formed by E_θ and E_r varies from a near-field backward-leaning (toward the transmitter) to far-field forward-leaning ellipse (see Sec. II-G). Thus, E_r null will equal E_r in the intermediate zone when $kr = 1$, providing E_r magnitude is greater than the sensor null response to E_θ. Predicted E_r and E_r null are shown in Fig. 82; the two curves meet at $kr = 1$. Far-field conditions occur only at the highest frequencies at 900 and 1200 feet. Measured E_r null agrees fairly well with theory at the four higher frequencies, where the common-mode signal from E_θ is smaller than E_r. At 0.5 and 10 kc, E_r null is not measurable since the sensor common-mode signal is above predicted E_r null. E_ϕ null is generally 15 to 20 db below E_r null but above the sensor threshold at the higher frequencies. E_ϕ null is a maximum at 600 and 1200 feet and a minimum at 900 feet. (This behavior is similar to some of the H-field behavior described above, and is unexplained.)

Spatial orientation of the total electric field is defined by the electric field sensor orientation when measuring E_r null and E_ϕ null. As was done with the magnetic field sensor, three readings were made for each null. The minimum magnitude is the null magnitude. All three orientations were generally within ±0.1 degrees for readings taken with the same sensor base set up. For readings between separate set-ups, orientation was accurate to about ±0.7 degree. The orientation associated with E_r null measurements is shown in Fig. 83 as E pitch with positive being a field ellipse leaning away from the transmitter* (far field). Theoretical E pitch from Sec. II-G is also shown.

*E-pitch reference is taken from the negative E_θ vector (see Fig. 83) for convenience of presentation.

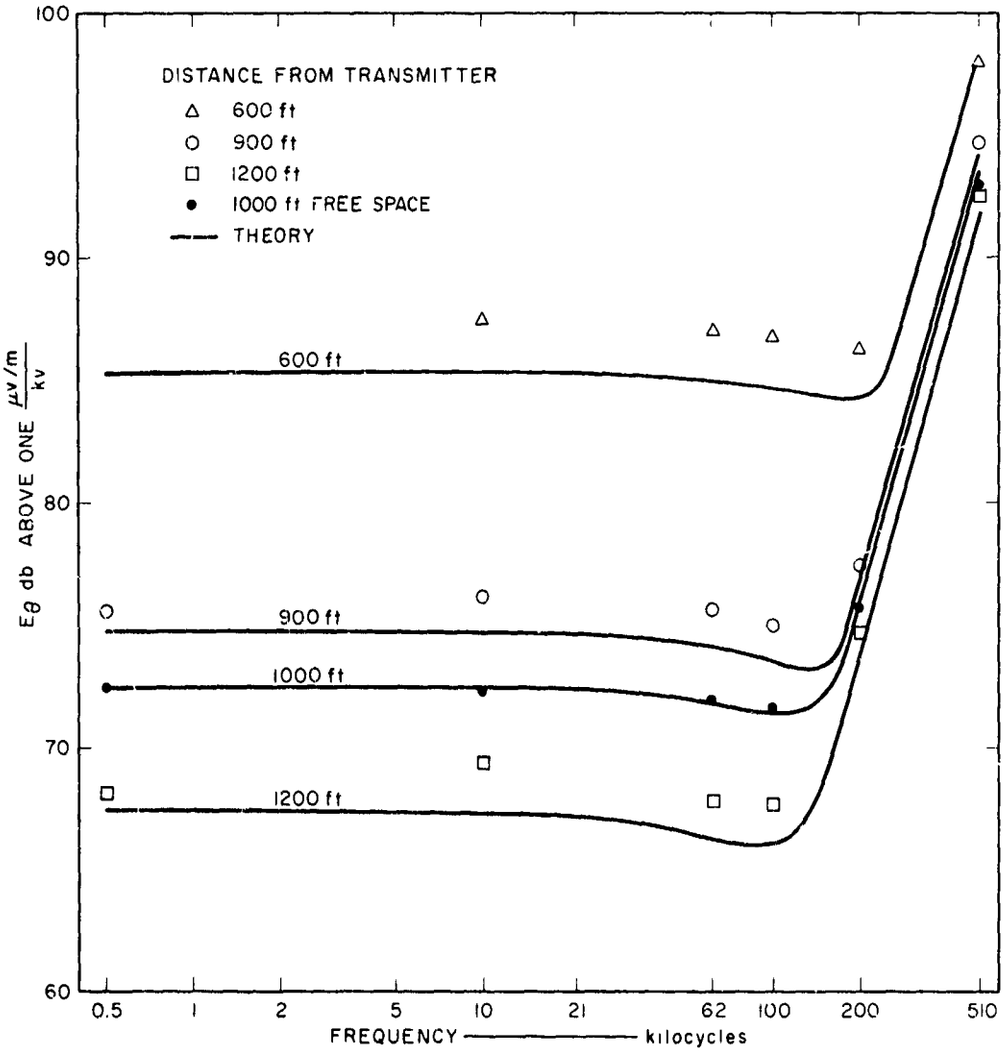

FIG. 81 E_θ MAGNITUDE IN PIE-SHAPED LOOP

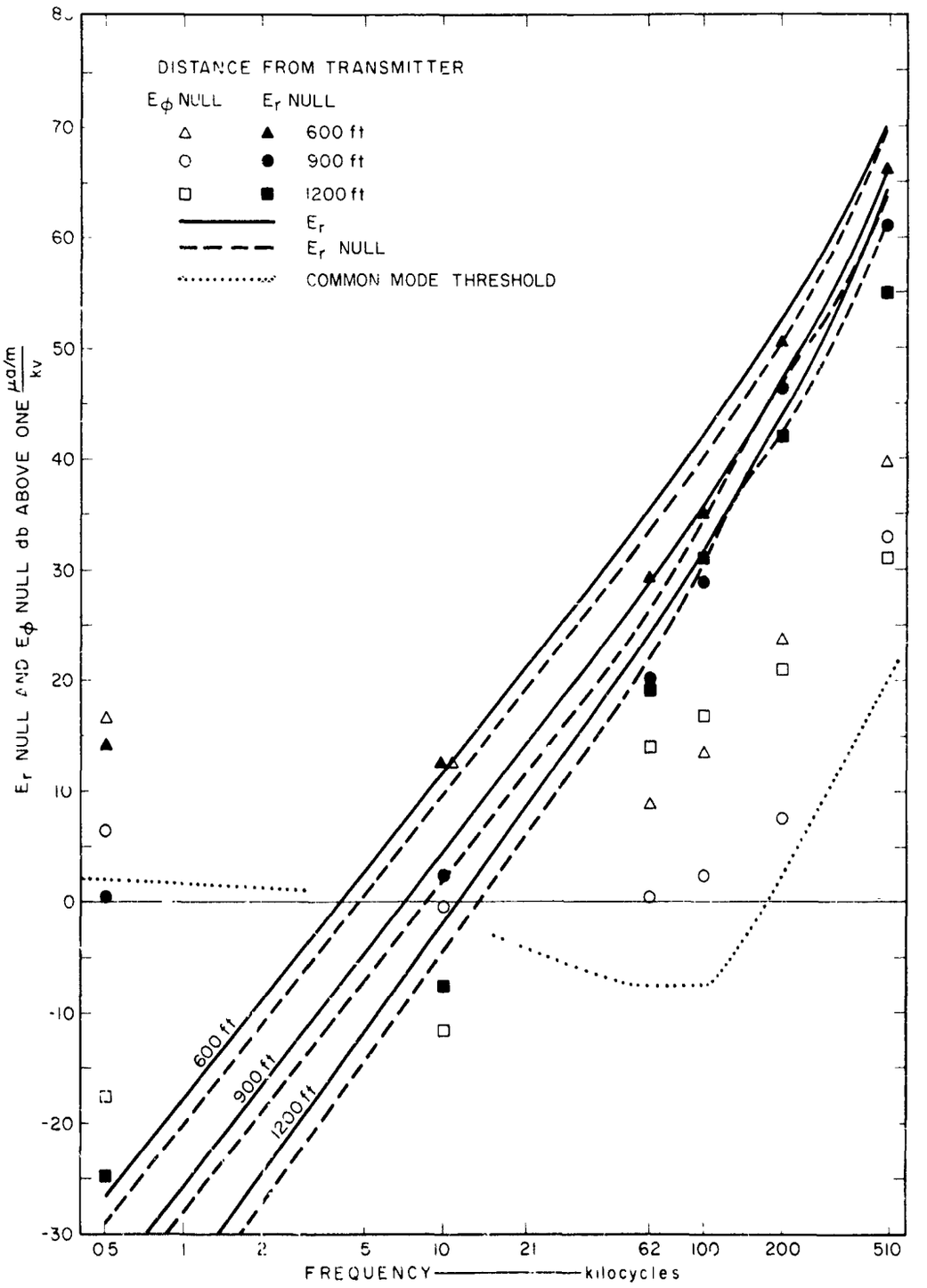

FIG. 82 E_r NULL AND E_ϕ NULL MAGNITUDE IN PIE-SHAPED LOOP

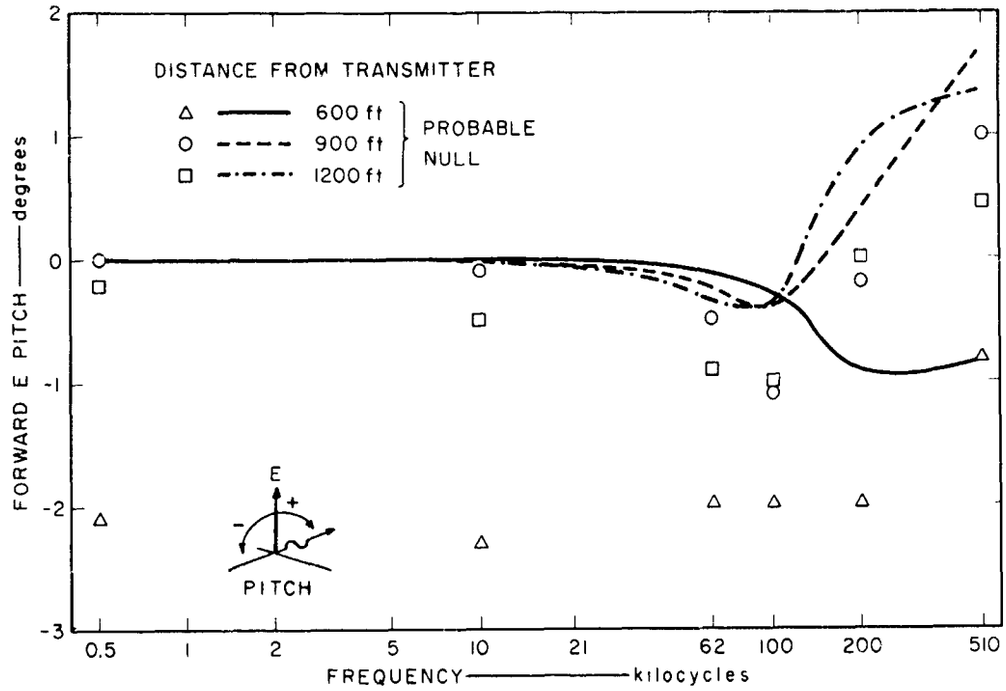

FIG. 83 E PITCH IN PIE-SHAPED LOOP

The measurements show remarkable agreement (constant 0.5 degree error) with theory at 900 and 1200 feet. The 600-foot data shows little agreement with theory, the exception being 510 kc.

Orientation associated with E_ϕ null measurements is labeled "E tilt" with positive tilt being a clockwise rotation of the E field facing in the direction of propagation. E tilt (not shown) did not differ from zero for the 900- and 1200-foot measurements. For 600 feet, all frequencies were about -0.5 degree, indicating a possible error in sensor base orientation.

E. Bunkers 5.601 and 519.03

Magnetic and electric field measurements were made near bunkers 5.601 and 519.03 shown in Fig. 2. Bunker 5.601 at 1600 feet from the transmitter consisted essentially of metal and could be considered as a box flush with the surface 36 feet wide, 43 feet long, and some 36 feet deep. The top surface of this bunker is shown in Fig. 84, with the various locations for the field measurements indicated.

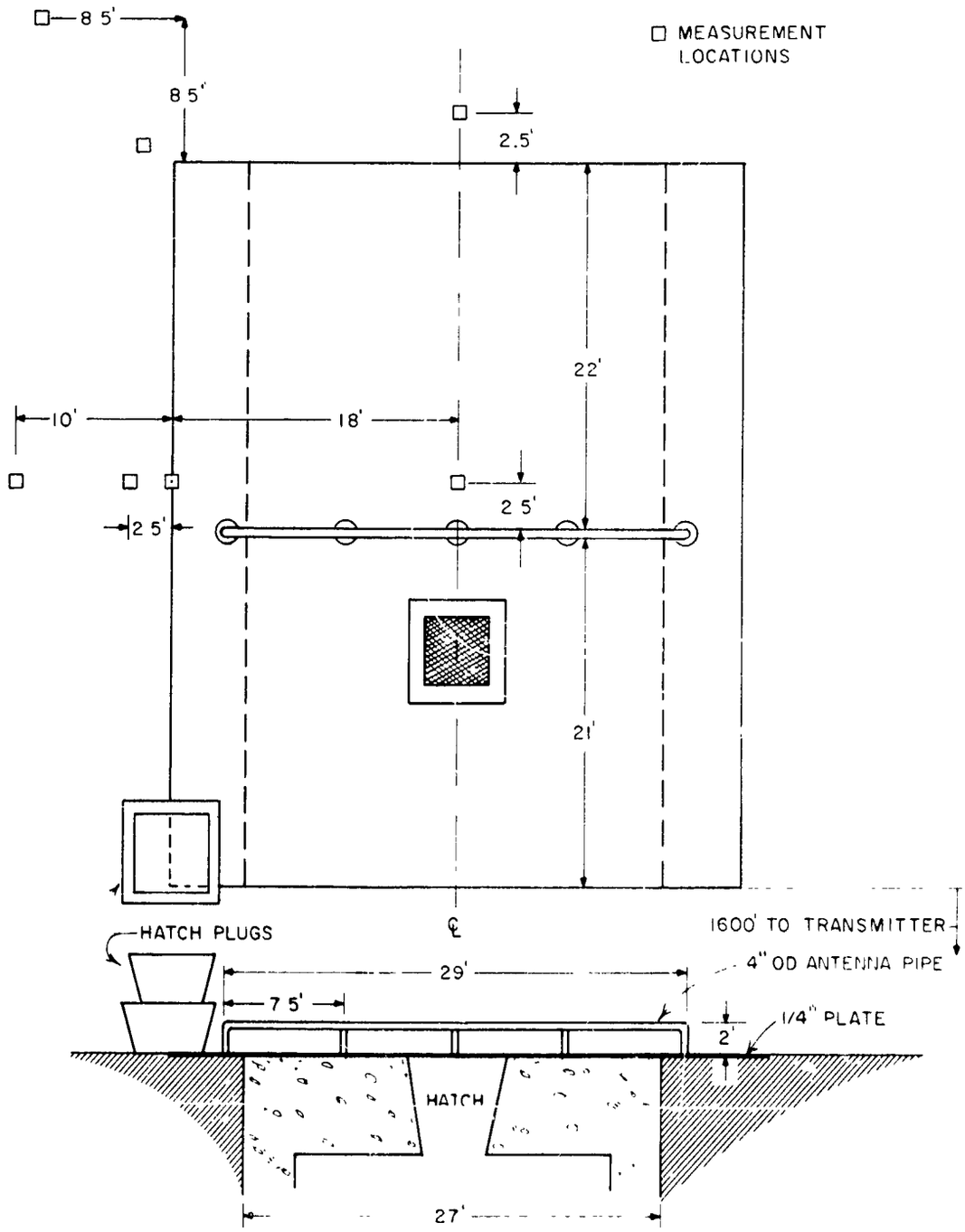

FIG 84 BUNKER 5.601 PLAN VIEW

Bunker 519.03, also at 1600 feet from the transmitter, was a small concrete bunker near other concrete bunkers all flush with the earth's surface. This bunker and the field measurement locations are shown in Fig. 85.

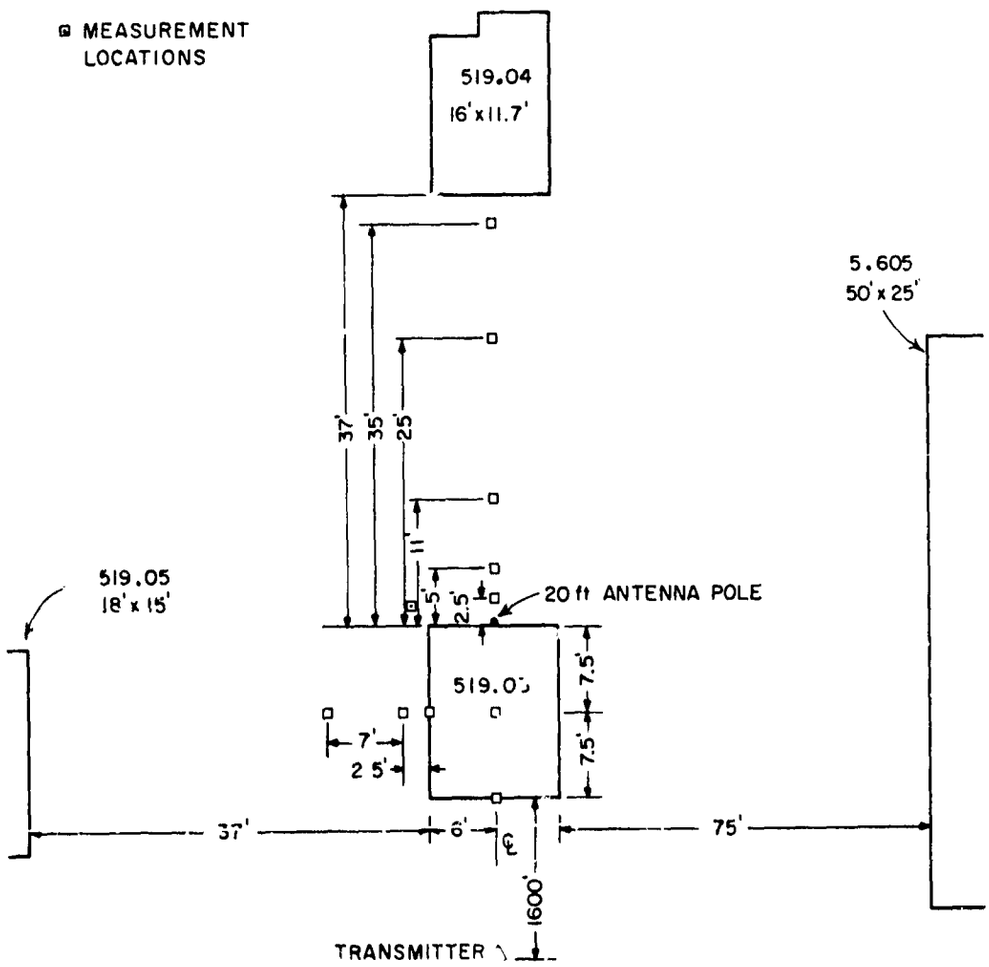

FIG. 85 BUNKER 519.03 PLAN VIEW

The magnitudes of the measurements of the azimuthal magnetic field, H_ϕ, near the two bunkers are shown in Fig. 86 along with free-space H_ϕ at 1600 feet. Except for a few data at 10 kc, all measurements are in essential agreement with the measurements in free space and with theory. The phase (not shown) of all H_ϕ data (including 10 kc) were within 3 or 4 degrees of the H_ϕ phase measurements in free space. In addition, H_θ null and H_r null magnitudes at all frequencies for all measurements around both bunkers were of the same order of magnitude as the free-space H_ϕ null and H_r null, indicating no abnormal out-of-phase magnetic field components. The null readings at 0.5 kc were barely greater than the free-space null readings for some selected locations.

Sensor orientation for the H_θ null and H_r null measurements near bunker 5.601 are shown as H tilt (vertical) in Fig. 87 and H yaw (horizontal) in Fig. 88. H tilt at the higher frequencies shows an up-tilt (-) for all measurements except those over a radial line through the center of the bunker. As frequency is decreased, H tilt is decreased. Maximum H tilt occurs over the azimuthal line through the bunker. H yaw shows a yaw (-) away from the transmitter for the measurements not over the bunker and essentially no yaw for measurements over the bunker. H yaw decreases with frequency and is in the opposite direction at 0.5 kc.

The H-tilt and H-yaw data show a field distortion that tends to bend the azimuthal magnetic field lines away from the bunker. The H_ϕ magnitude and phase and the H_θ and H_r null magnitudes indicate that magnetic fields in spatial directions different from the predicted H_ϕ direction can only exist as fields in-time-phase (or out-of-time-phase) with H_ϕ. (Linear polarization is equivalent to a single field at a new direction. For this field, orientation is affected more than magnitude for small field distortions.) Thus, the cause of the distortion must be associated with or caused by the H_ϕ field. If bunker 5.601 could be considered to be a large loop oriented to respond to H_ϕ,* the

*The loop assumption does not require the bunker to appear physically as a loop. A solid conducting structure will appear to an impinging magnetic field as a loop type structure in that circulating currents will flow in a continuous loop.[14]

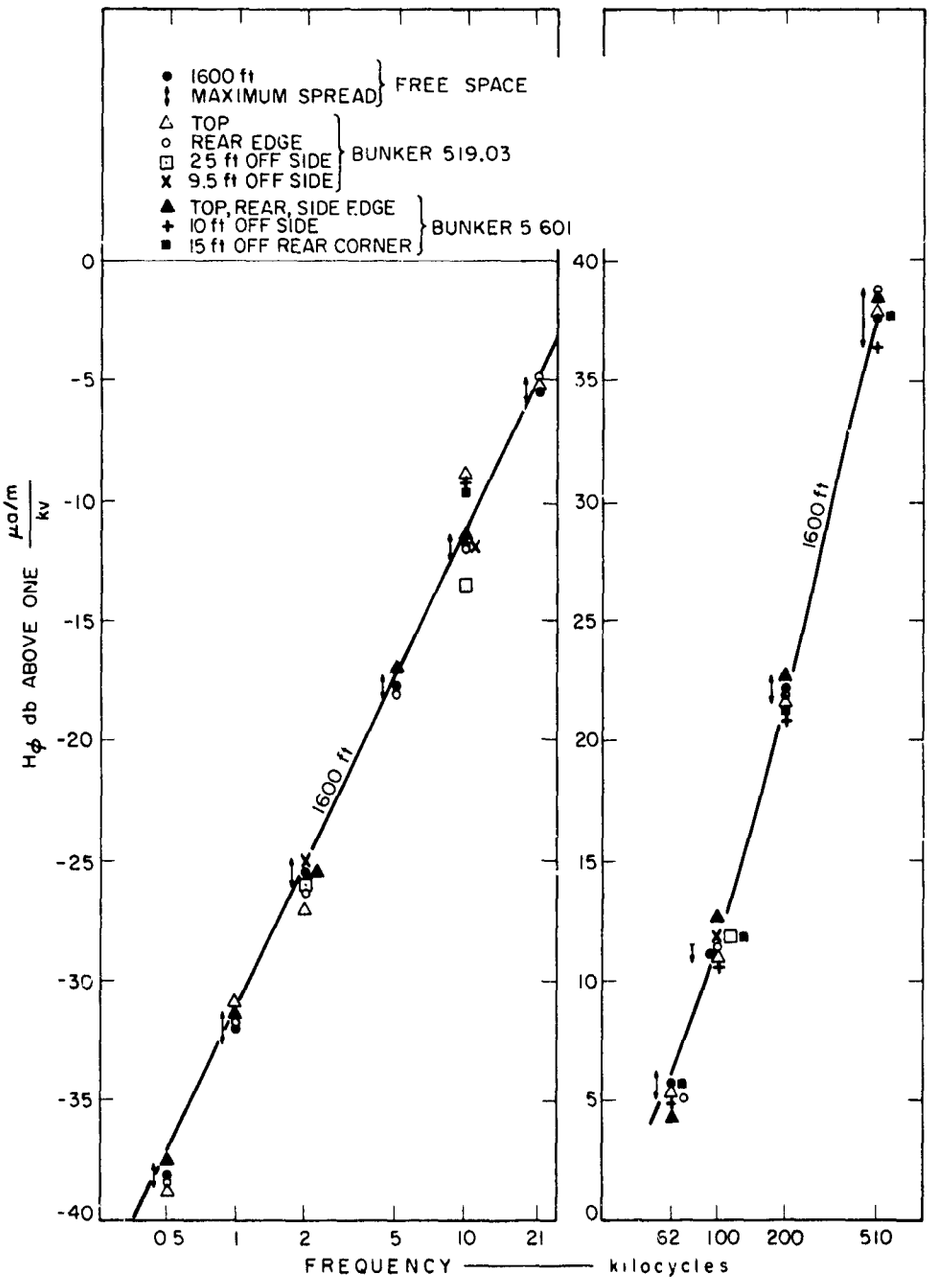

FIG. 86 H_ϕ MAGNITUDE NEAR BUNKERS

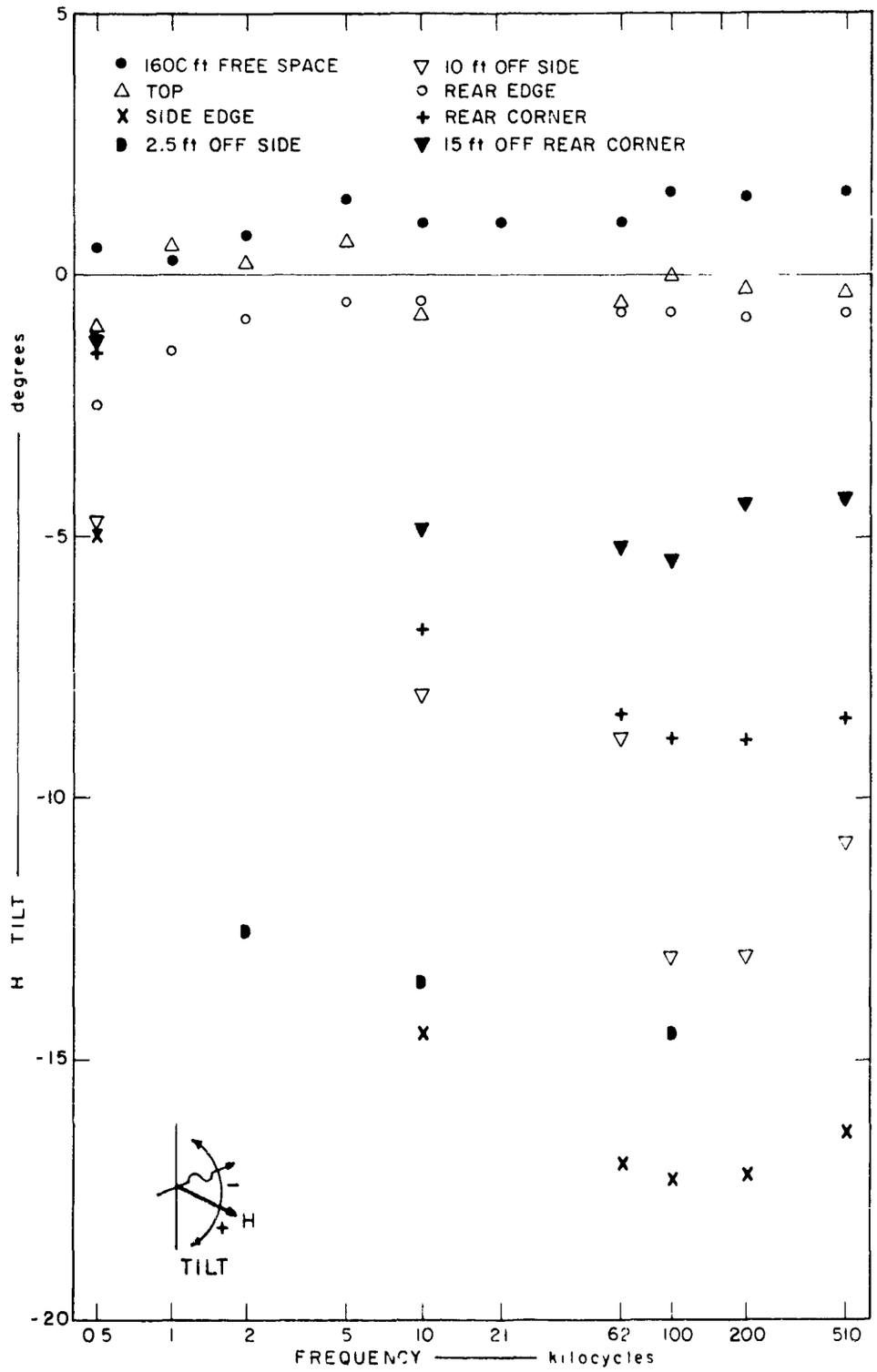

FIG. 87 H TILT NEAR BUNKER 5.601

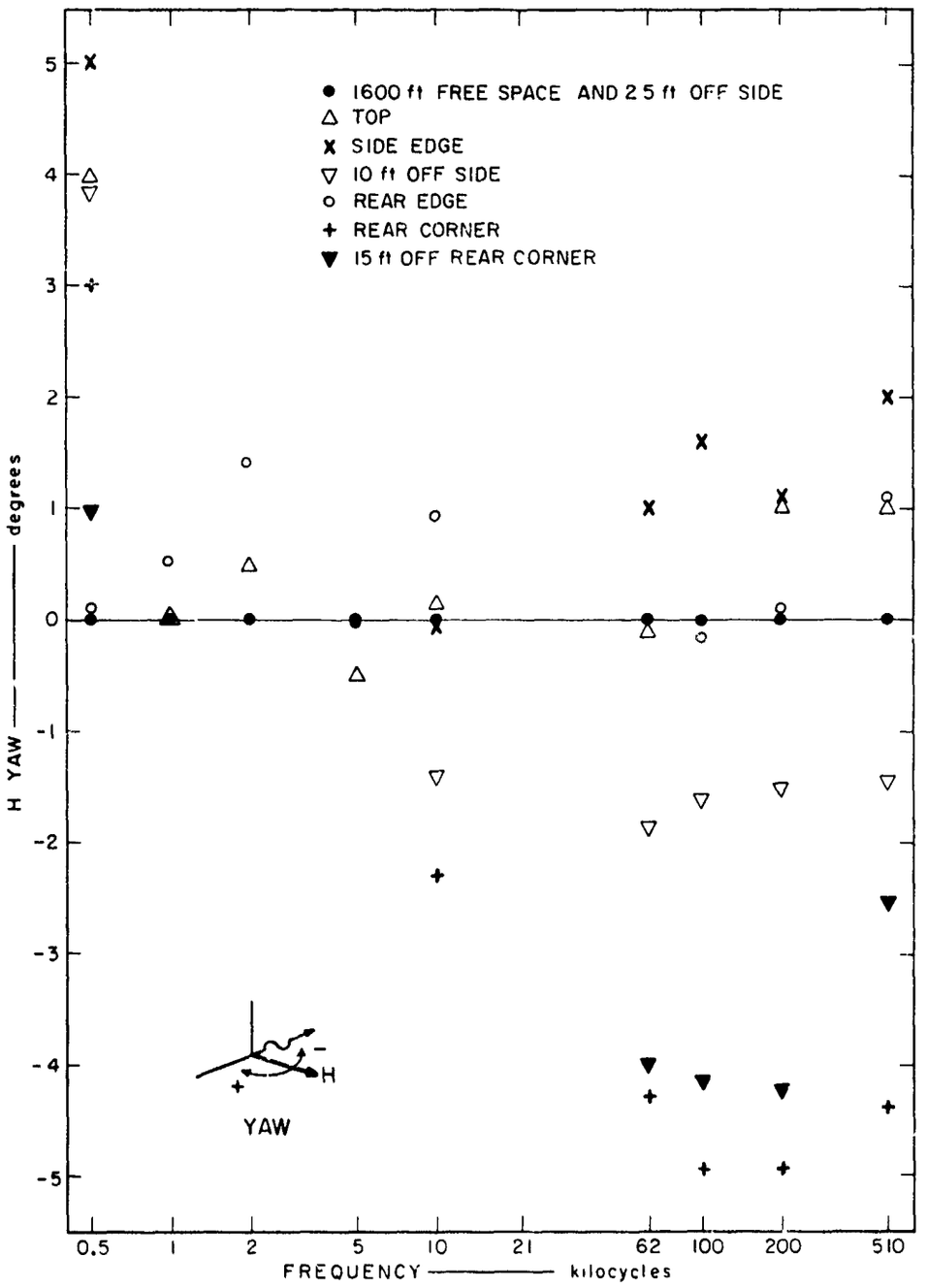

FIG. 88 H YAW NEAR BUNKER 5.601

circulating current in this hypothetical loop would cause the H_ϕ field to be repelled in the observed manner. Furthermore, at low frequencies, the reduced efficiency of the loop (lower Q) would cause the effect to be reduced. For the distortion to be caused by a loop type structure, the magnitude of H_ϕ over the bunker should be enhanced particularly at the higher frequencies. Such an enhancement is possibly indicated in the data shown in Fig. 86. The behavior of H yaw at 0.5 kc is not explained by the assumption that the bunker acts like a loop.

The H-tilt and H-yaw orientations from the H_θ null and H_r null measurements near bunker 519.03 are shown in Fig. 89. Both H tilt and H yaw are within ±1 degree of the theoretical H_ϕ, indicating essentially no H-field distortion. (All H-tilt data above 0.5 kc is about 2 degrees negative compared to the free-space measurements; however, since this difference is constant for all locations, the data appears to be a sensor orientation problem and not a field phenomena.)*

The vertical electric field E_θ magnitudes near bunkers 5.601 and 519.03 are shown in Fig. 90 along with free space data at 1000, 1600, and 2000 feet. E_θ near bunker 5.601 was in good agreement with the theory and free-space E_θ. All data were between the two values (top and rear edge) shown in Fig. 90.

E_θ magnitude near bunker 519.03 shows considerable change (in the form of signal reduction) from free-space measurements. Maximum reduction (minimum magnitude) occurs at the rear edge of the bunker (behind the pole--see Fig. 85) and appears to be symmetrical about this measurement along the radial line through the bunker center. Measurements along the radial beyond the data shown in Fig. 90 are not presented since they were essentailly at free-space E_θ magnitudes. Measurements azimuthal from the center of the bunker were like the free-space magnitudes except for the measurement at 2.5 feet off the side of the bunker, which fell just above the top data shown in Fig. 90.

*The sensor is oriented to the earth's gravitational field and H_ϕ is oriented to the local earth's surface.

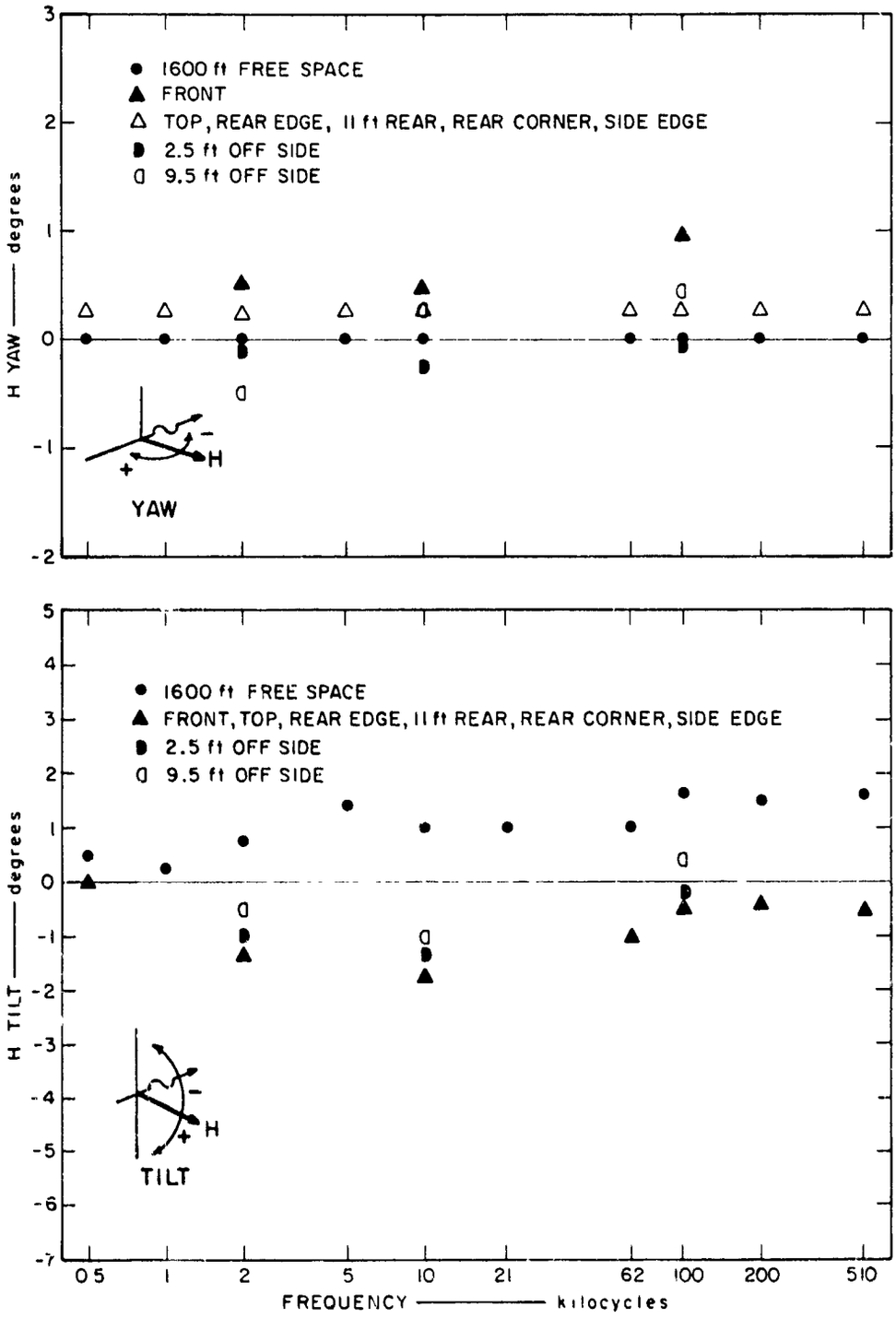

FIG. 89 H TILT AND H YAW NEAR BUNKER 519 03

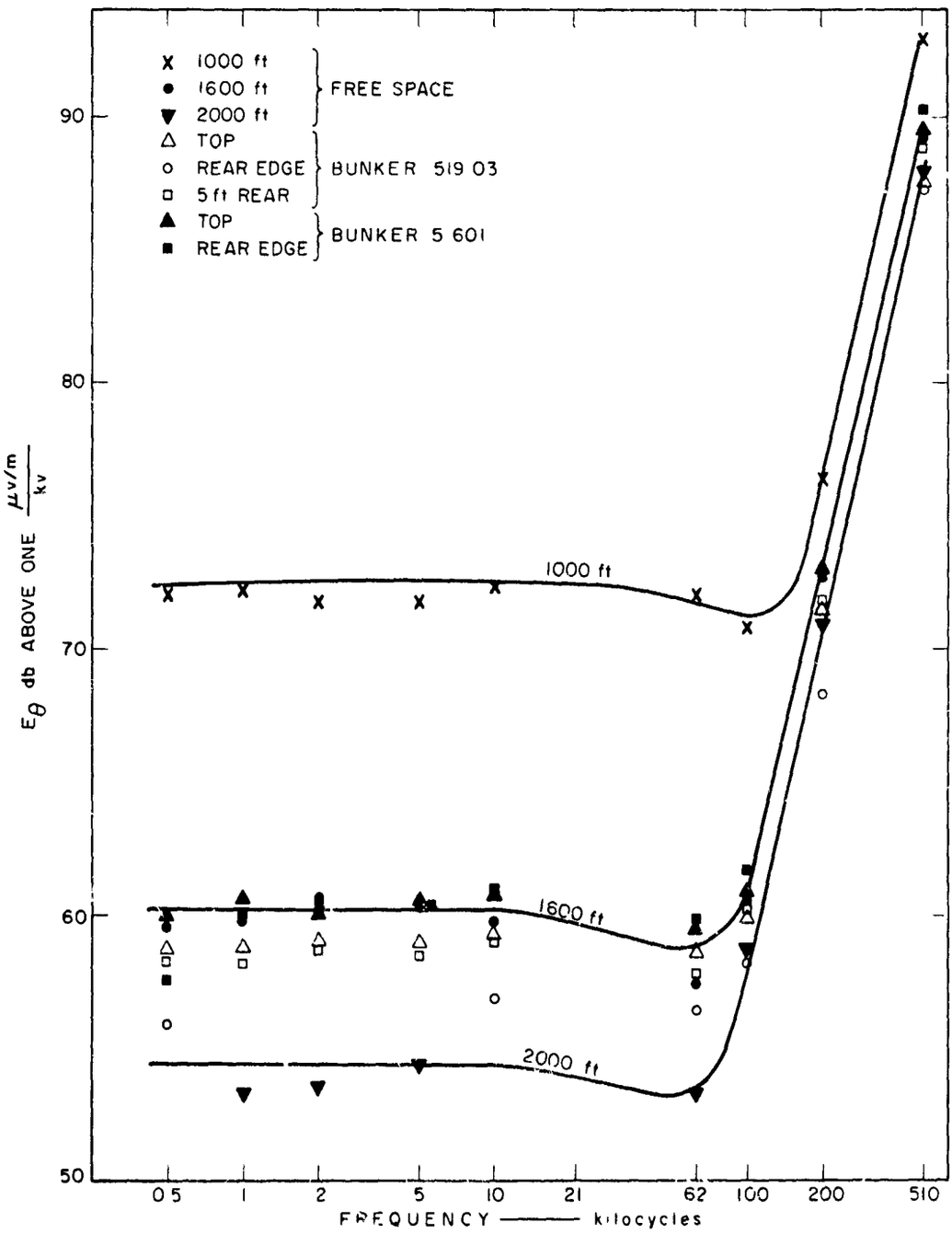

FIG. 90 E_θ MAGNITUDE NEAR BUNKERS

The magnitude of E_ϕ null near both bunkers did not differ from free-space E_ϕ null. The magnitude of E_r null near both bunkers is shown in Fig. 91 for the measurement locations listed in Fig. 90. At the lower frequencies, E_r null is above free-space E_r null for all data near bunker 519.03. Maximum field occurs nearest to the rear edge, with apparent symmetry along a radial about this point. At the higher frequencies, E_r null does not follow a decent pattern; however, the field appears to be enhanced over free-space measurements. All other E_r null measurements near bunker 519.03 were in agreement with the free-space E_r null shown in Fig. 91.

E_r null magnitudes near bunker 5.601 were only above the sensor common-mode threshold at the higher frequencies. All data except the data taken over the bunker agrees with the rear-edge data shown, and is in agreement with free-space E_r null. Over the bunker, E_r null is reduced by about 10 db, probably due to the presence of a better conducting ground plane.

E pitch and E tilt associated with E_r null and E_ϕ null measurements near 5.601 are shown in Fig. 92. Theoretical E pitch from Sec. II-G is plotted for 1600 feet as the solid curve. Free-space E pitch agrees well with theory. All data near the bunker are displaced in the positive direction from free-space E pitch. The data appears to follow the shape of the theory curve if the curve is displaced (dashed curve), except at the highest frequency. The data appears to contain a sensor base orientation error with respect to the local ground.* E pitch at 510 kc appears to be more negative than free-space E pitch. E tilt near bunker 5.601 shows a tilt of the E field away from the bunker (measurements off side of bunker) and no tilt over the bunker. The E tilt may be caused by the H tilt distortion shown in Fig. 87.

E pitch from the E_r null data near bunker 519.03 is shown in Fig. 93. The data show pitch away (+) from the transmitter for data taken behind (further from transmitter) the rear edge of the bunker and pitch toward (-) the transmitter for data ahead of the rear edge. The pole at the rear edge of bunker 519.03 (see Fig. 85) contains a cable with a grounded shield. All E-pitch data

*Sensors are oriented to earth's gravitational field.

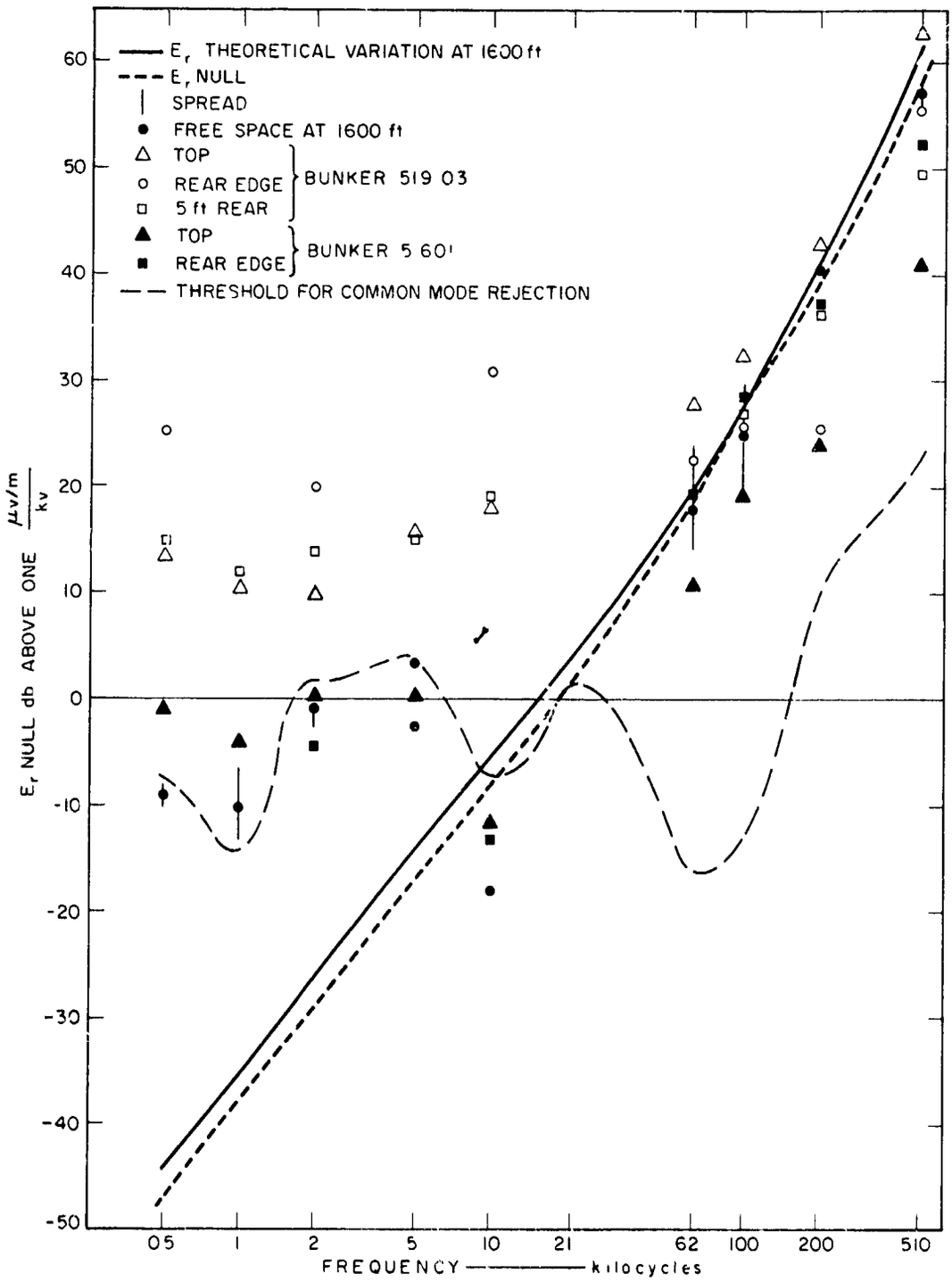

FIG. 91 E_r NULL MAGNITUDE NEAR BUNKERS

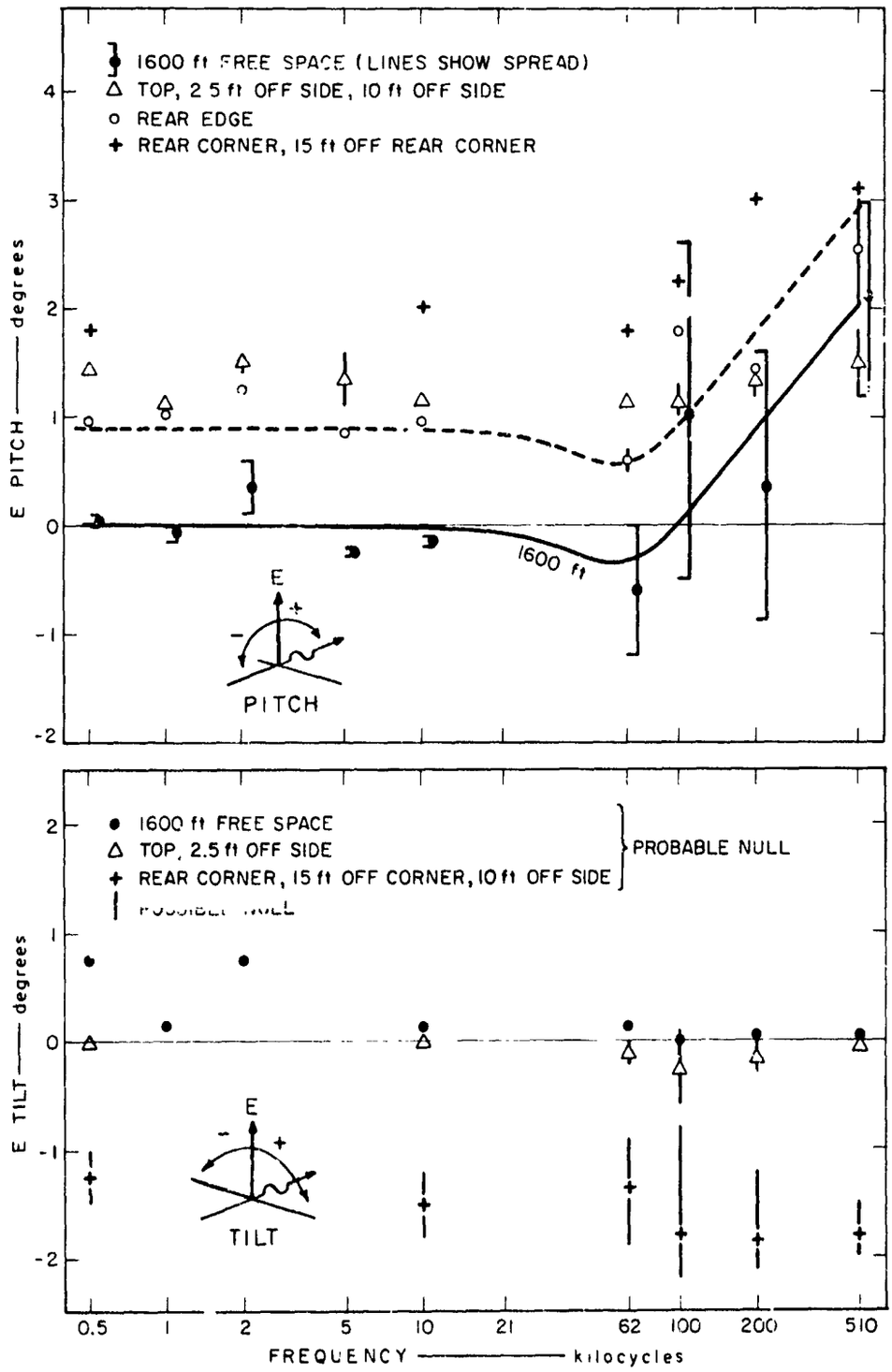

FIG. 92 E PITCH AND E TILT NEAR BUNKER 5 601

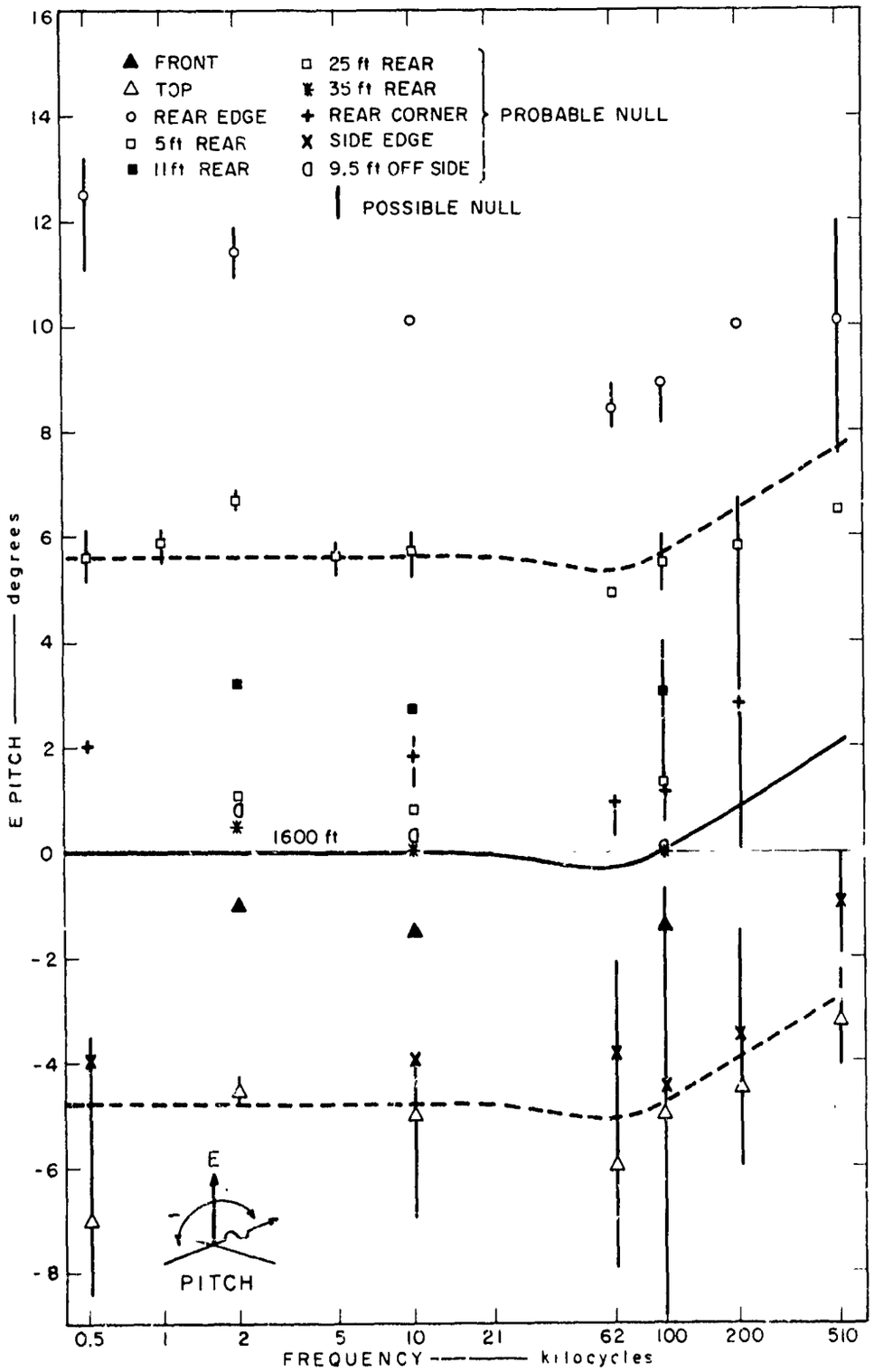

FIG. 93 E PITCH NEAR BUNKER 519 03

around this bunker is compatible with the E_θ field terminating on the grounded pole cable shield, causing a field distortion symmetrical around the pole.

E tilt near bunker 519.03 from the E_ϕ null measurements is shown in Fig. 94. This data confirms that angular distortion around this bunker is caused by the presence of the conducting vertical pole at the bunker rear edge. The distortion due to the pole will cause E_θ magnitude to be reduced as the pole is approached (see Fig. 90). Furthermore, in the far field (100 kc and up at 1600 feet) the E_θ angular distortion will alter the ellipse formed by E_θ and E_r (see Sec. II-G) and will result in an increase in E_r null magnitude near the pole toward the transmitter and a decrease in magnitude near the pole away from the transmitter. Figure 91 shows this tendency. In the near field (low frequencies) the ellipse is normally tilting toward the transmitter (see Fig. 4), and the change in E_r null magnitude should decrease on the transmitter side of the pole and increase on the far side. E_r null at low frequencies is normally not of sufficient amplitude to exceed the sensor common mode threshold so that this near-field distortion cannot be observed. However, E_r null at low frequencies (see Fig. 91) was measured near bunker 519.03 as being some 10 to 20 db above the common mode threshold near the pole. The phase of E_r null with respect to E_θ cannot be measured accurately; however, all E_r null signals measured near the pole over the bunker (toward the transmitter) were around -100 degrees and the phase behind the pole was around +100 degrees at low frequencies and near -100 degrees at high frequencies. The phase reversal at the lower frequencies and the abnormally high magnitude of E_r null at low frequencies indicates that the pole is reradiating the E_θ field and creating a new radial electric field around the pole. Near the pole, this re-radiated field will vary with frequency in a manner very nearly the same as E_θ.* Thus, at low frequencies the re-radiated radial field can predominate, and at high frequencies the transmitter radial field E_r can predominate, which is observed.

*For distances very near to a vertical radiator with constant voltage the radial voltage is nearly independent of frequency (see Eq. (12)).

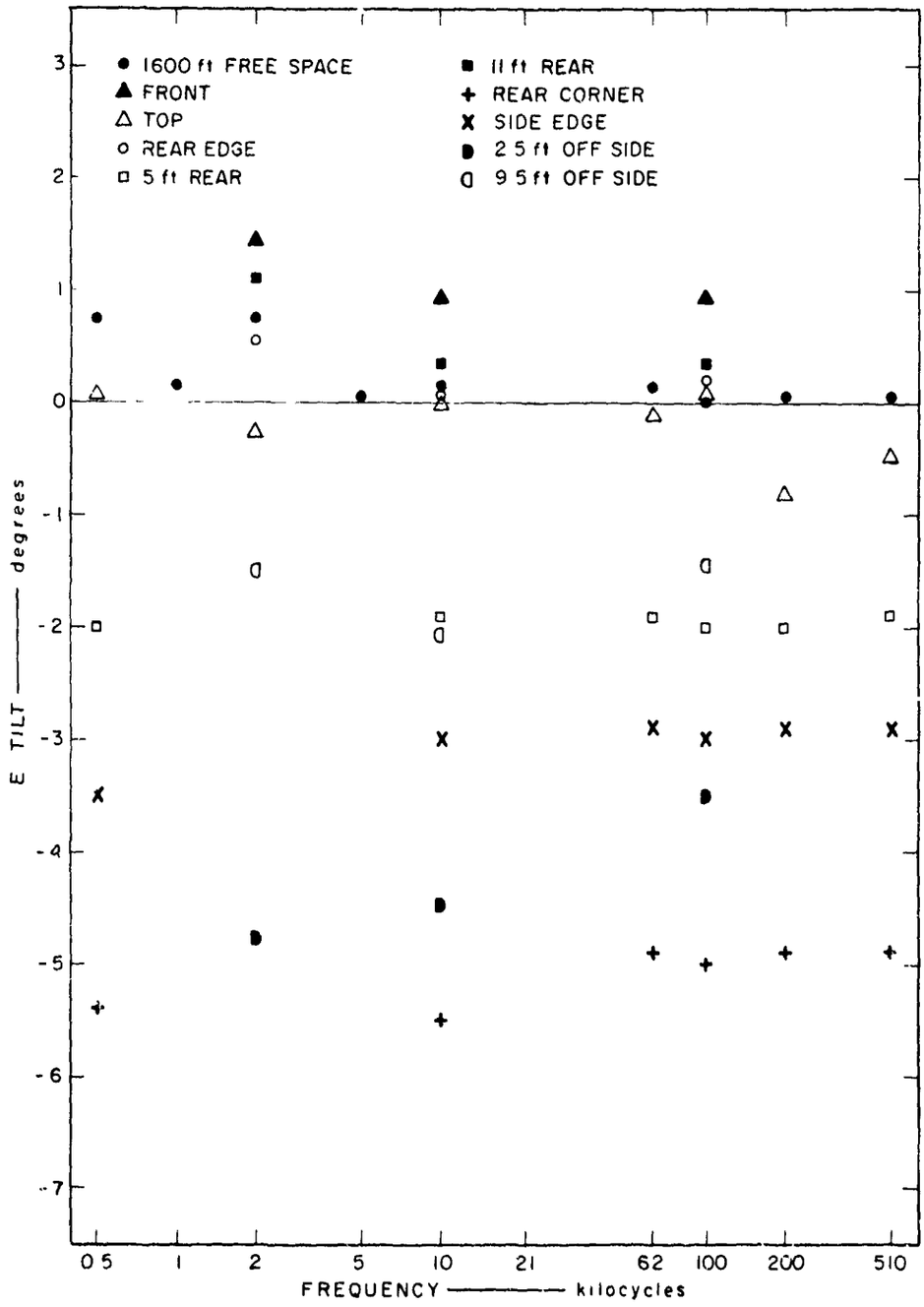

FIG. 94 E TILT NEAR BUNKER 519.03

F. Summary

Electric and magnetic field measurements in the area shown in Fig. 2 indicate that the fields are in agreement with the theory developed in Sec. II except near buried structures. The magnetic field near radial cables is distorted due to the magnetic field produced by radial currents in the cable. This disturbing field adds spatially to the azimuthal magnetic field from the transmitter to give an elliptically polarized field in the plane normal to the radial wire. For cables buried to a depth of four feet, the magnetic field distortion is discernible to about 80 feet from the cable using a system that is accurate in magnitude to 10 percent and in spatial orientation to 1 degree. The electric field near buried cables was not measured. Measurements near cables on the earth's surface indicated that field lines terminate on the cable and are detectable as spatial distortions out to ten feet from the cable. For buried cables this distortion should be less noticeable.

Measurements along a radial line bisecting a large pie-shaped loop (see Fig. 2) within the loop area indicate both magnetic and electric field distortions. The magnetic field showed relatively large magnitude and phase distortions of the azimuthal field component and the presence of a vertical component that caused the field to tilt ±20 degrees as functions of both distance and frequency. A buried radial cable at a depth of one foot also bisected the pie-shaped loop; however, the currents in this cable should not tilt the magnetic field directly over the cable. The magnitude of the vertical electric field showed a consistent enhancement. The orientation of the ellipse formed by the vertical and radial field components generally behaved as predicted. (That is, the total electric field near--in wavelengths--the transmitter leans toward the transmitter and as distance is increased the total field goes through vertical to an away-leaning field at great distances.) Considerable azimuthal electric field was observed. The cause of all field distortions is not known; however, due to the complex structures in the immediate area (pie-shaped loop and radial cables) and due to poor and changing conditions of the pie-shaped loop with soil conditions (cable had varying sheath-to-core leakage), complex field distortions are possible.

Measurements near two buried bunkers showed that for a conducting (metal) bunker near the surface the azimuthal magnetic field was "repelled" away from

the bunker due to induced currents in the bunker structure. The orientation of the magnetic field was observed to deviate from the azimuthal direction by as much as 15 degrees. The increased conductivity directly over this bunker caused a decrease in radial electric field magnitude and a small spatial electric field orientation distortion near the bunker edge due to field termination on the bunker. For a small buried concrete bunker, the magnetic field was essentially unaffected by the bunker. Due to a vertical conductor near this bunker, effects of the bunker on the electric field could not be determined. The electric field was observed to terminate on the vertical conductor above the earth's surface, causing a cone-shaped electric field distortion discernible to 25 feet from the conductor. The re-radiated electric field from the vertical conductor was observed to distort the radial electric field near the conductor.

This page intentionally left blank.

IX PULSE MEASUREMENTS

A. General

The pulse transmitter and receiving systems described in Secs. IV-D and IV-E were used to make pulse measurements of cable current, major electric field (vertical), and major magnetic field (azimuthal) at selected locations where CW measurements were made. The received pulse signal was observed on a self-triggering oscilloscope and photographed on Polaroid transparent film at several sweep speeds (typically 0.5, 1, 2, 5, 10, and 20 μsec/cm) so that both rapid and slow variations could be recorded. Also placed on film were amplitude calibrations at 50 kc (± 2 percent) using a sweep speed of 20 μsec/cm. Thus, calibrations of nonlinearities in the oscilloscope time sweep were made along with the amplitude calibrations. Pictures were taken at each observation point using receiving bandwidths of 100 and 500 kc.

The recorded transmitted pulse was well above the noise, and produced good repeatable pictures using a single oscilloscope sweep.* The received pulses could often be recorded on a single sweep; however, noise (interference) was always observable. In some instances the received pulse had to be photographically integrated using several sweeps, to separate sweeps triggered by interference and sweeps triggered by the wanted pulse. Self triggering of the oscilloscope always eliminates some portion of the pulse leading edge. Triggering was tried on both negative-going and positive-going portions of the wanted pulse and most often resulted in a triggering level at less than 10 percent of peak pulse amplitude.

---

*The transmitter pulse was continually monitored and photographed throughout the pulse measurements program using the pulse monitor circuit shown in Fig. B-4. The pulse shape did not noticeably change with time.

B. Data Processing

The waveform pictures recorded were the result of the transmitted pulse modified by the transfer function $|G(\omega)|$ from the transmitter to the receiving point and the transfer function of the receiving and recording system $|P(\omega)|$. The receiving systems were band-limited (100 kc and 500 kc) and consequently had a non-constant amplitude and phase response as a function of frequency. To obtain the true received pulse the recording characteristics had to be removed from the data. This was accomplished as described below on an IBM 7090 computer, using the Fourier transforms described in Appendix D.

The time pictures for the transmitted pulse are shown in Fig. 95 for sweep speeds of 0.5, 1, 5, and 10 μsec/cm along with two calibration levels. (The calibration frequency for this set of data was 100 kc and not the normal 50 kc used at the receivers.) The calibration signal for the transmitted pulse recordings was applied directly to the oscilloscope since the transmitter monitor system consists of a plate antenna and simple passive filter (see Fig. B-4). The transmitter monitor output was measured (using the CW probe calibration scheme described in Sec. V-B) to be 0.1 volts per kv on the transmitting antenna at frequencies below 110 kc. Thus, the peak-to-peak amplitude of the two calibration signals of 0.5 and 2.5 volts rms in Figs. 95(e) and 95(f) correspond to 14.1 and 70.7 kilovolts on the transmitting antenna.* This gives an oscilloscope deflection of 28.8×10^3 volts/cm. The dot at the left edge of the pulse pictures corresponds to zero volts on the transmitting antenna and a line parallel to the peaks of the calibration signal through this dot represents zero volts for all times in each picture. The distance between peaks gives the time scale.** The zero volt line was transferred to the pulse picture shown in Fig. 95(a). The time calibrations were transferred to the zero volt line with the intercept of the zero volt line and the extrapolated pulse beginning being

*As can be seen the oscilloscope gain is set so that on 2 volts/cm, the deflection is approximately 2.8 volts/cm. This was done to give a pulse amplitude near peak deflection.

**The calibration signal in Fig. 95(f) is at 100 kc (period 10 μsec) using a sweep of 20 μsec/cm. Thus, the peaks are spaced 10 μsec for a 20-μsec/cm sweep and represent 0.1-, 0.5-, 1-, and 5-μsec spacing for 0.2-, 1-, 2- and 10-μsec/cm sweeps respectively.

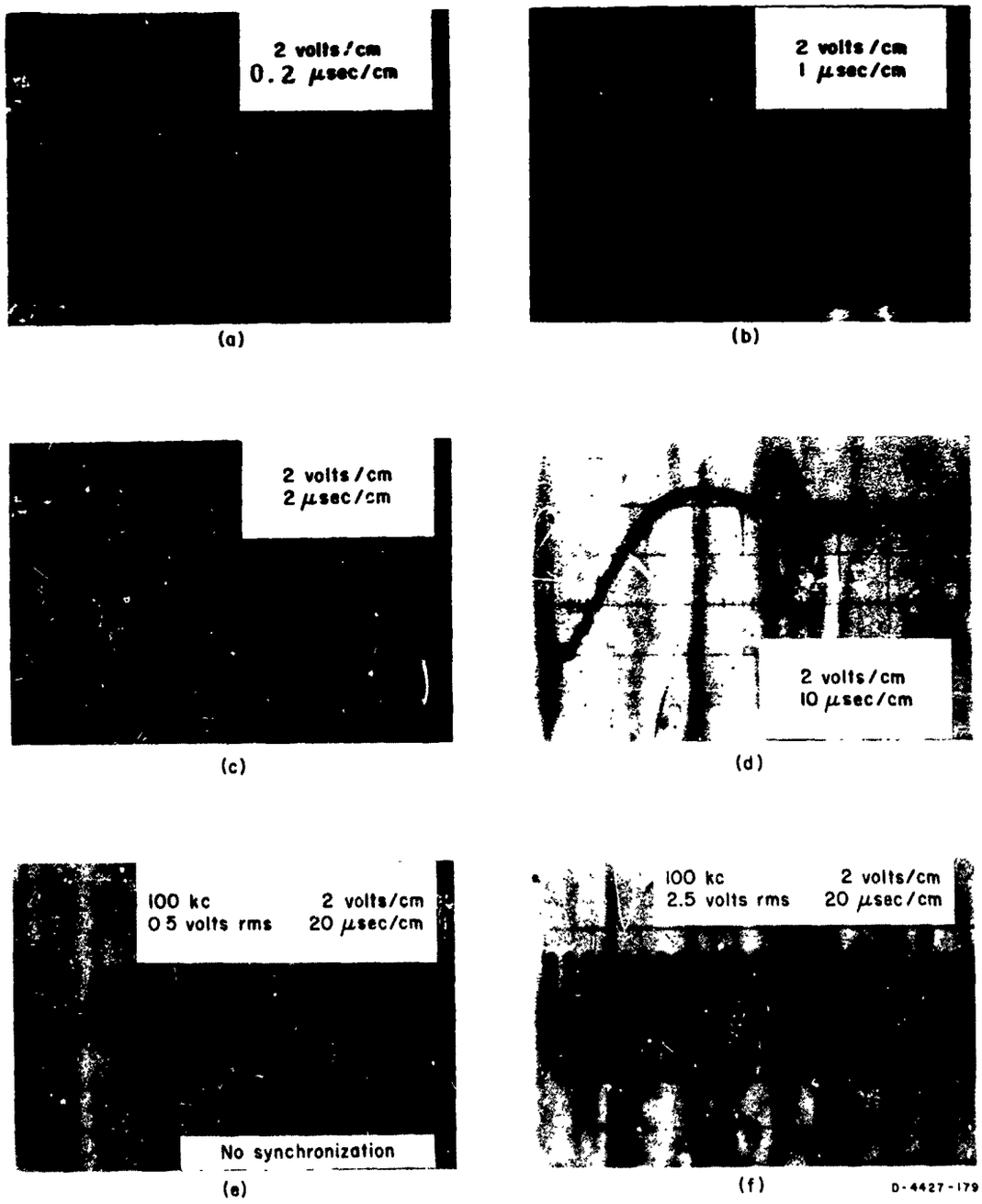

FIG. 95 PULSE RECORDINGS WITH CALIBRATIONS

time equal zero ($t = 0$). Figure 95(a) was then scaled each 0.1 μsec after $t = 0$ for the amplitude in transmitter antenna volts. The scaled amplitude was the smoothed pulse waveform shown by the fine line drawn on Fig. 95(a). Scaling was accomplished on a Benson-Lehner Oscar F analog-to-digital system. Scaling on Fig. 95(a) gave the first 16 scaling points ($t = 1.6\,\mu$sec). Figure 95(b) was then scaled after first matching the data from Figs 95(a) and (b) for the times $t = 1$ to 1.6 μsec. Figure 95(b) was scaled each 0.1 μsec. to $t = 5\,\mu$sec for a total of 50 time points. Thereafter all scalings were at 0.2-μsec spacings. Scalings were continued with matching from one picture to another out to where the waveform returned to the zero line which was 100 μsec for the waveform shown in Fig. 95. Thus, for the transmitted pulse, 526 times (including $t = 0$) and their associated waveform amplitude values were punched on cards. This scaling procedure was used for all waveforms recorded. Scaling was terminated whenever the waveform being scaled had returned to the zero volt line, indicating the end of the pulse waveform. Thus, a different number of time points were scaled for each waveform.

The time waveform data obtained from Fig. 95 was transformed to a frequency spectrum using the computer program outlined in Appendix D. Amplitude and phase were calculated each 2 kc from 0 to 1000 kc. As a check on the computer processing, the frequency spectrum was inverse transformed back to time at the same time points as the original scaling. This inverse transform time function and the original scaled time function (2 curves) are both plotted in Fig. 96. As can be seen, the two curves in Fig. 96 are nearly indentical. Where the two curves differ, the error (indicated in Fig. 96) is less than 0.5 percent of peak amplitude.

The time waveform shown in Fig. 96 is the result of the voltage-time function on the transmitting antenna modified by the recording filter characteristic. This filter characteristic $P(\omega)$ was measured in both amplitude and phase and was transferred to cards as $1/P(\omega)$ at each 2 kc from 0 to 1000 kc. The shape of $1/P(\omega)$ and the corresponding plate, loop, and cable current recording characteristics for 100- and 500-kc bandwidths are indicated in Table IV. The product of $1/P(\omega)$ and the frequency spectrum obtained by transforming the scaled time waveform, is the transmitted spectrum, and the inverse trans-

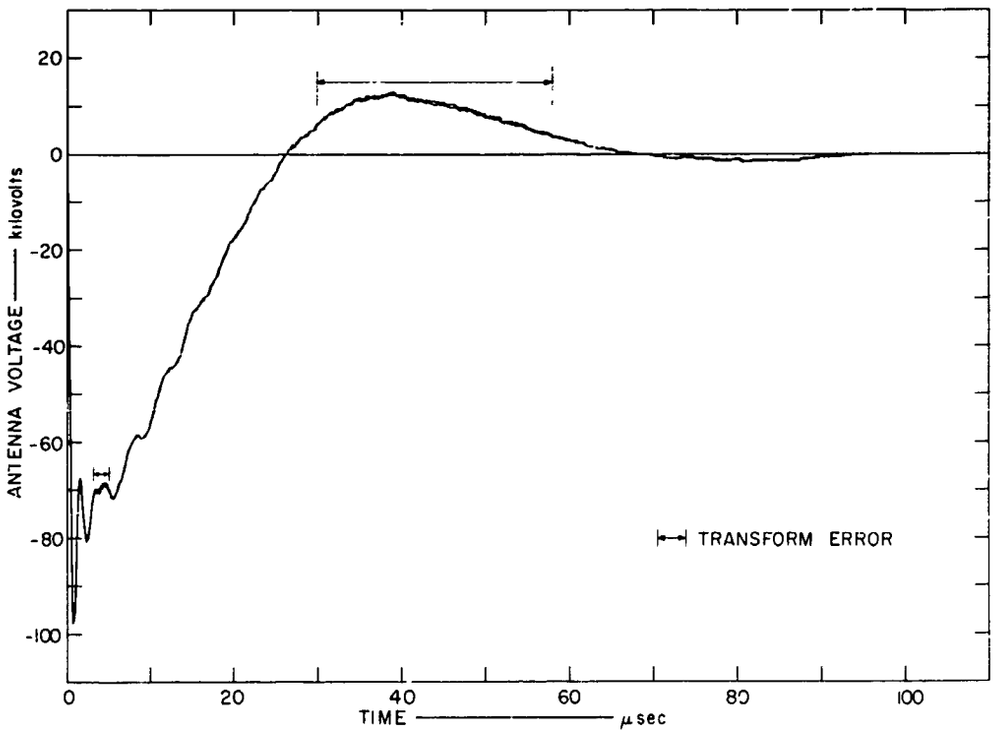

FIG. 96 FOURIER TRANSFORM PROCESSING ERROR

form of this transmitted spectrum is the transmitted time waveform. The transmitted time waveform and spectrum (magnitude and phase) for the recorded waveform in Fig. 96 are shown in Fig. 97. The time waveform is very similar to the recorded waveform in Fig. 96 since the filter function in Table IV is relatively constant with frequency. The transmitted spectrum is peaked near 12 kc, has a secondary peak near 260 kc,* and appears to contain energies

*Reactance measurements on the pulse transmitting antenna system showed a secondary resonance between 250 and 260 kc caused by self resonance in the antenna load inductance.

Table IV

PULSE SYSTEMS INVERSE FREQUENCY RESPONSE

Freq. (kc)	Transmitter Monitor		Cable Current System				Plate System				Loop System			
			100 kc		500 kc		100 kc		500 kc		100 kc		500 kc	
	Rel. Mag.	Phase (rad.)	Rel. Mag.	Phase (rad.)	Rel. Mag.	Phase (rad.)	Rel. Mag.	Phase (rad.)	Rel. Mag.	Phase (rad.)	Rel. Mag.	Phase (rad.)	Rel. Mag.	Phase (rad.)
2	1.000	0	1.190	5.550	1.364	5.550	1.000	6.109	1.000	6.109	1.160	5.847	1.188	5.864
10	1.000	0	1.000	0	1.000	0	1.000	0.157	1.000	0	1.010	0	1.010	6.198
50	1.000	0.040	1.025	0.541	1.001	0.248	1.113	0.750	1.000	0.240	1.047	0.559	1.000	0.087
100	1.000	0.150	1.190	1.012	1.012	0.559	1.460	1.379	1.000	0.384	1.118	0.997	1.000	0.263
200	1.016	0.276	1.739	1.728	1.072	1.012	2.469	2.199	1.000	0.768	1.678	1.693	0.988	0.559
300	1.057	0.379	2.667	2.286	1.147	1.484	3.650	2.827	1.000	1.168	2.342	2.269	0.954	0.838
400	1.107	0.487	3.676	2.793	1.205	1.885	4.808	3.403	1.000	1.536	2.950	2.810	0.954	1.082
500	1.168	0.600	4.831	3.361	1.202	2.304	5.952	3.979	1.010	1.929	3.509	3.299	0.978	1.309
600	1.244	0.740	5.988	3.787	1.135	2.827	7.143	4.538	1.000	2.391	4.115	3.787	1.026	1.588
700	1.332	0.890	7.194	4.294	0.957	3.491	8.310	5.117	1.031	2.862	4.681	4.210	1.136	1.902
800	1.433	1.047	8.475	4.800	0.952	4.363	9.434	5.655	1.515	3.334	5.181	4.555	1.266	2.164
900	1.598	1.204	9.709	5.306	1.529	5.201	10.52	6.074	1.754	3.805	5.697	4.901	1.429	2.478
1000	1.686	1.361	10.99	5.812	2.825	6.109	11.23	6.283	1.923	4.276	6.211	5.236	1.621	2.827

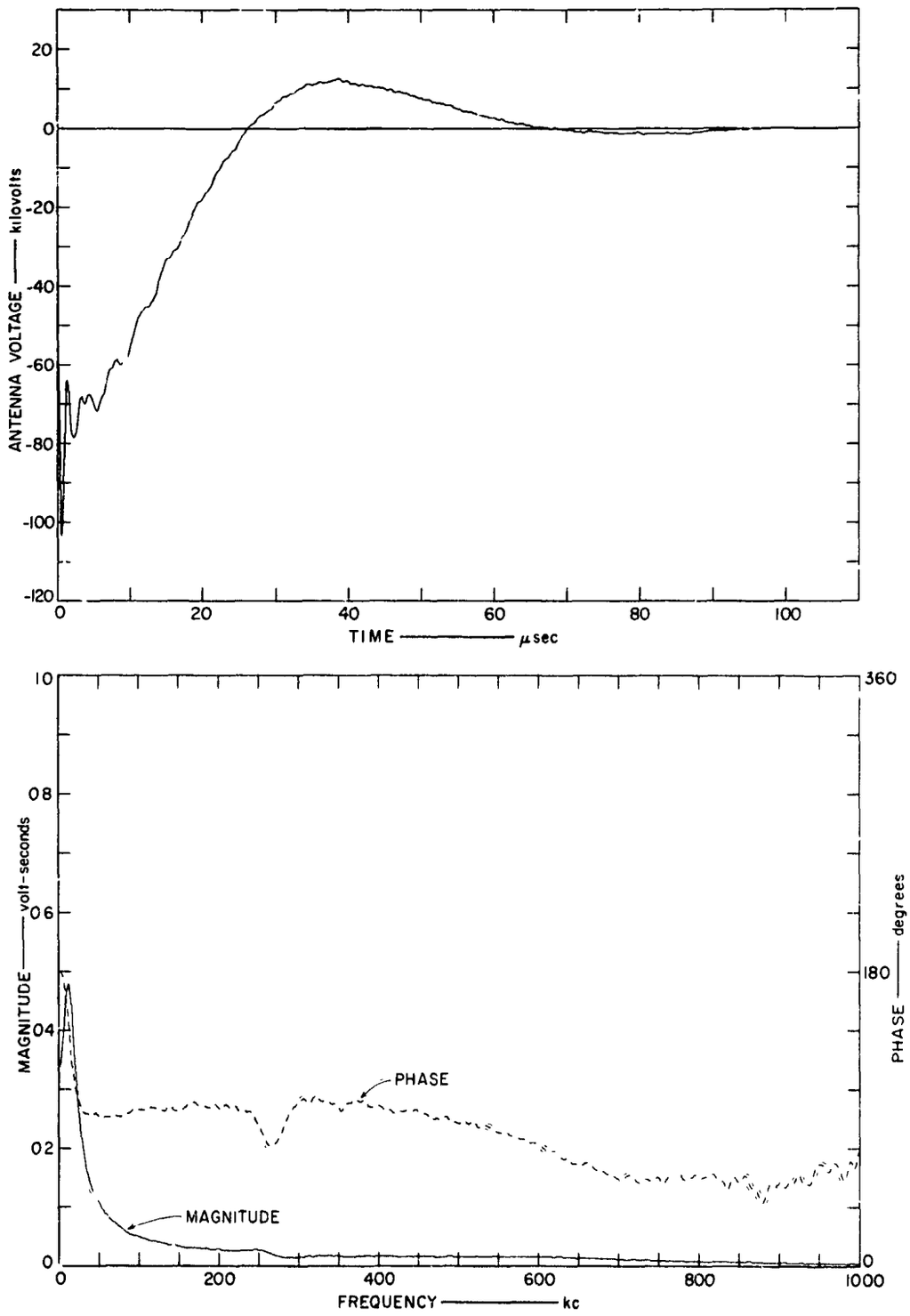

FIG. 97 TRANSMITTED PULSE TIME WAVEFORM AND FREQUENCY SPECTRUM

out to about 650 kc. This spectrum from 0 to 1000-kc has a magnitude variation in excess of 40 db. The film recording scaling accuracy is probably accurate over a 20-db dynamic range and may be usable but inaccurate to 30 db. Consequently, the transmitted spectrum is accurately defined over a 20-db amplitude range or for frequencies up to about 100 kc. For frequencies up to 275 kc (30 db below the spectrum peak), the spectrum is usable but inaccurate. Above 275 kc (over 30 db below the spectrum peak), the transmitted spectrum presented in Fig. 97 is considered to be noise.

For the received pulse data, processing similar to that described above was used to obtain the actual received time waveform and spectrum. Since two recordings were made for each received pulse (100- and 500-kc bandwidths) two waveforms and two spectrums were obtained. Theoretically the two waveforms and two spectrums should be identical after the recording filter characteristics are removed, and often they were nearly identical. Figure 98 shows the results of the recorded and processed time waveforms for the 100-kc and 500-kc bandwidth pulse current recordings at 2050 feet on Cable L when the pulse of Fig. 96 was transmitted. The scaled waveforms show considerable differences due to the reduction of the higher frequencies in the 100-kc bandwidth recording. The processed waveforms show good agreement between the 100-kc and 500-kc recordings. The 100-kc processed time waveform appears to contain higher frequencies. This is caused by the data processing, which multiplies the low-amplitude recorded high-frequency energy by a large number to correct for the recording filter characteristic. This portion of the 100-kc recording is very inaccurate, as can be seen in Fig. 99 which shows the 100-kc and 500-kc spectrums for the processed time waveforms in Fig. 98. The processed 100-kc spectrum enhances frequencies above 200 kc; consequently, the higher-frequency portion of the 100-kc recording is very inaccurate. For the data in Figs. 98 and 99, the 500-kc waveform and spectrum are selected to represent the received signal.

The spectrums in Fig. 99 show several features that limit the usefulness of the pulse data. The transmitted spectrum has two predominant frequency components at 12 and 260 kc. These show as the major frequencies in Fig. 98 and consequently as magnitude peaks in the spectrums shown in Fig. 99. The

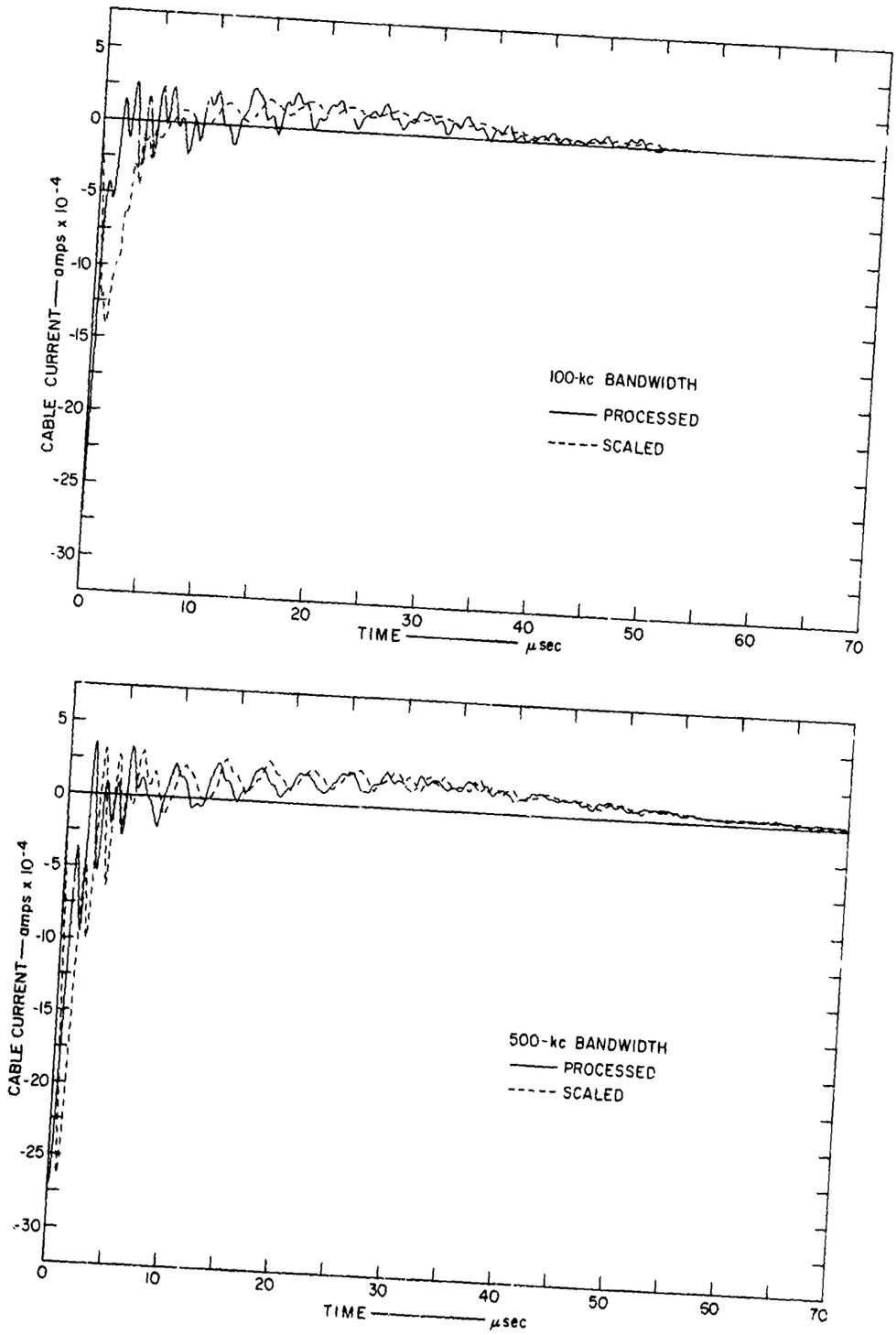

FIG. 98 COMPARISON OF 100-kc AND 500-kc PROCESSED TIME WAVEFORMS

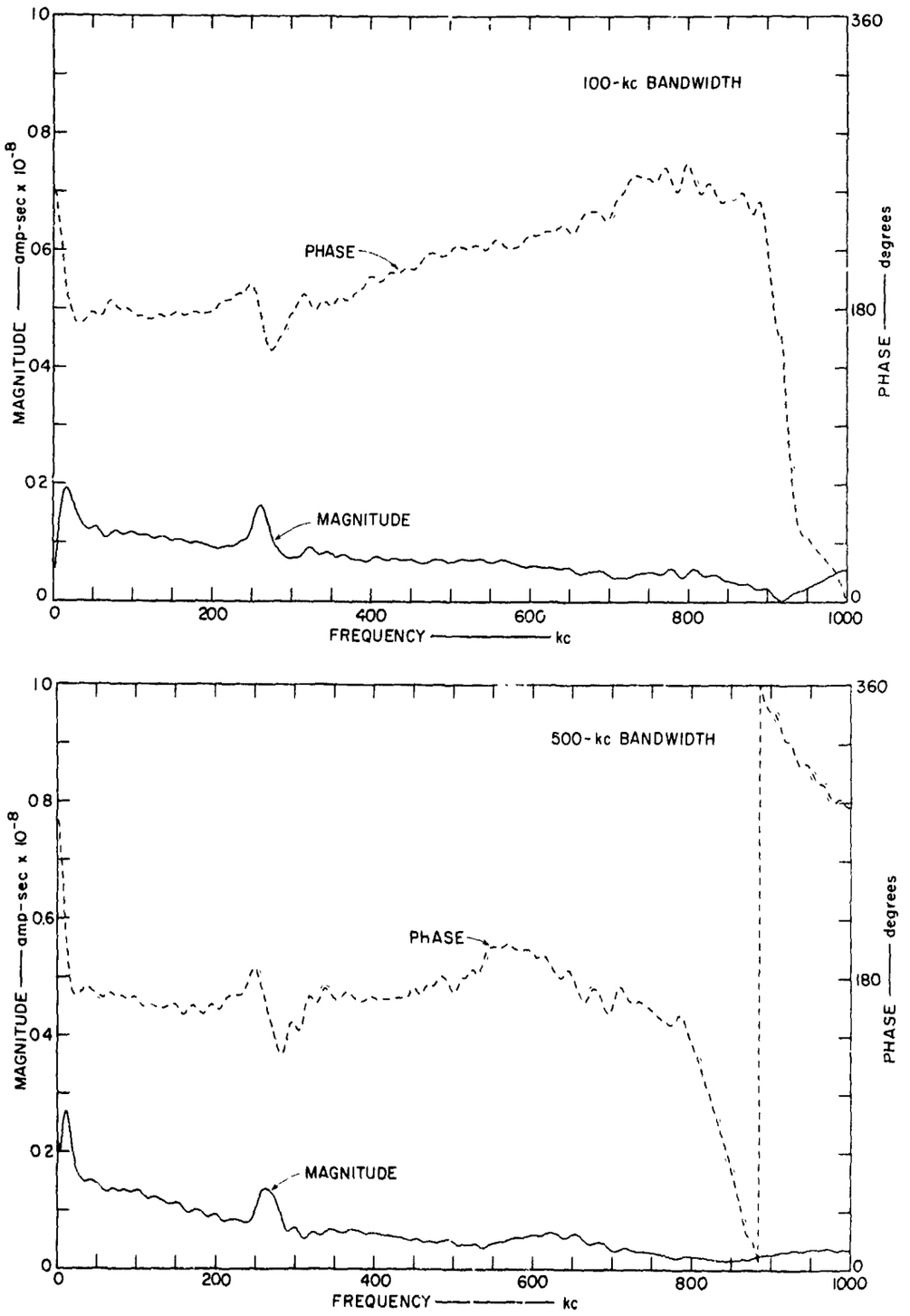

FIG. 99 COMPARISON OF 100-kc AND 500-kc PROCESSED FREQUENCY SPECTRUMS

spectrum at these two frequencies is probably scaled very accurately, with a decreasing scaling accuracy away from either frequency. In addition, the recording filter response limits scaling accuracy above either 100 or 500 kc out to about the maximum transmitted frequency of 650 kc. Above 650 kc the spectrums presented are considered to be invalid.

The comparison and selection process described above was made for each set of data and generally resulted in selecting the processed 500-kc data as representing the actual received pulse. In some instances the received pulse was predominantly composed of high frequencies. For these pulses, the 100-kc recordings gave sufficient high-frequency accuracy and sufficient low-frequency signal so that the 100-kc recording was selected to represent the received pulse.

The spectrum selected as representing the received pulse spectrum was further processed to obtain the transfer function $G(\omega)$ from the pulse transmitter to the receiving location so that the CW and pulse data can be compared. $G(\omega)$ was obtained by dividing the received spectrum by the transmitted spectrum shown in Fig. 97. For the CW measurements, the magnitude of $G(\omega)$ is presented as the magnitude of the received signal per unit transmitter volt. This is the data presentation form used for all CW data.

This 6-step data processing for all pulse data presented is summarized below.

Step 1--The data from each set of photographs were semi-automatically placed on cards at time points 0.1 and 0.2 μsec apart.*

Step 2--The time cards were plotted and compared with the photographs.

Step 3--The time cards were transformed to amplitude and phase and multiplied by the inverse of the transform of the recording system to create the received pulse amplitude and phase spectrum.

*Amplitude calibrations were corrected for the filter characteristics listed in Table IV.

Step 4--The spectrum obtained in Step 3 was transformed to time to give the received time waveform.

Step 5--The spectrums and time waveforms obtained from the 100- and 500-kc recordings were compared and one selected for presentation in this report.

Step 6--The spectrum selected in Step 5 was divided by the transmitted spectrum to obtain the transfer function $G(\omega)$.

C. CURRENTS IN BURIED RADIAL CABLES

Measurements of pulse current were made at 1000, 1750, and 3000 feet in the buried bare 10-gauge copper wire (cable Z) and at 1050, 2050, and 3050 feet in the conducting sheath cable (cable L) shown in Fig. 2. The computer-processed data, in the form of a received pulse time waveform and its associated transmitter voltage (V_a)-to-wire current transfer function (magnitude and phase), for the bare 10-gauge copper wire are shown in Figs. 100, 101, and 102. The three processed time waveforms show a reasonable pattern with distance. All waveforms show considerable 260-kc* energy. The first positive pulse is recognizable as the same pulse in each time waveform. Details prior to this pulse are not discernible with the recording and data processing techniques used.** The high-frequency part of the time pulse is about equal at 1000 and 1750 feet and about one order of magnitude down at 3000 feet. The low-frequency component of the pulse decreases with distance, being nondiscernible at 3000 feet. This low-frequency behavior is indicated by the recorded pulse time duration shown as t_{max} in each figure.

The transmitter voltage-to-wire current transfer function for the bare 10-gauge copper wire is shown in the lower half of Figs. 100, 101, and 102 as

*Secondary peak in transmitted spectrum (see Fig. 97).

**Pictures were obtained with self triggering at about 10% of peak pulse amplitude. Processing to eliminate recording system frequency functions from the data enhances the high frequencies. Thus, the processed time waveforms start at some arbitrary time and magnitude after the actual pulse beginning.

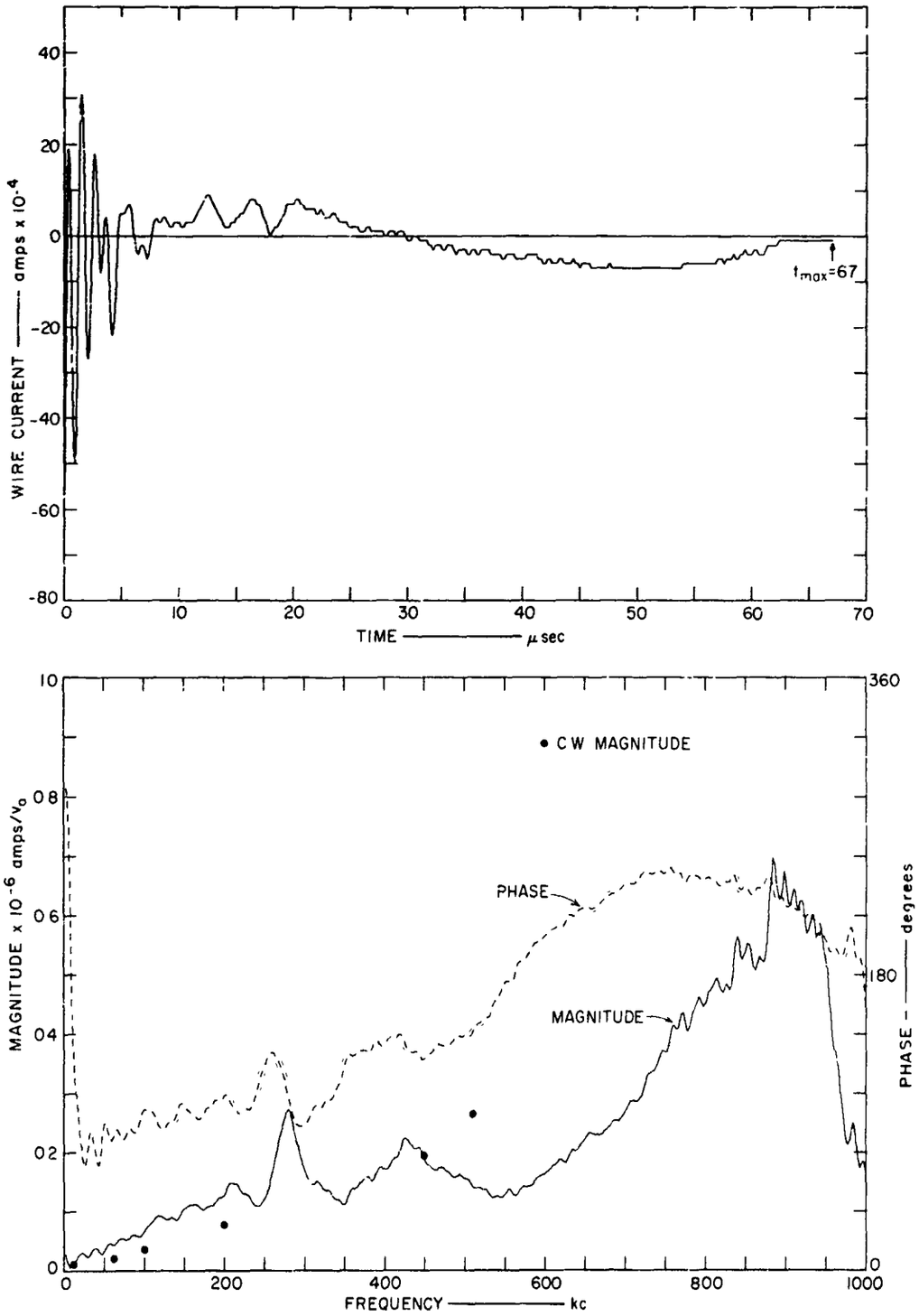

FIG. 100 PULSE WIRE CURRENT AT 1000 FEET IN BARE 10-GAUGE COPPER WIRE

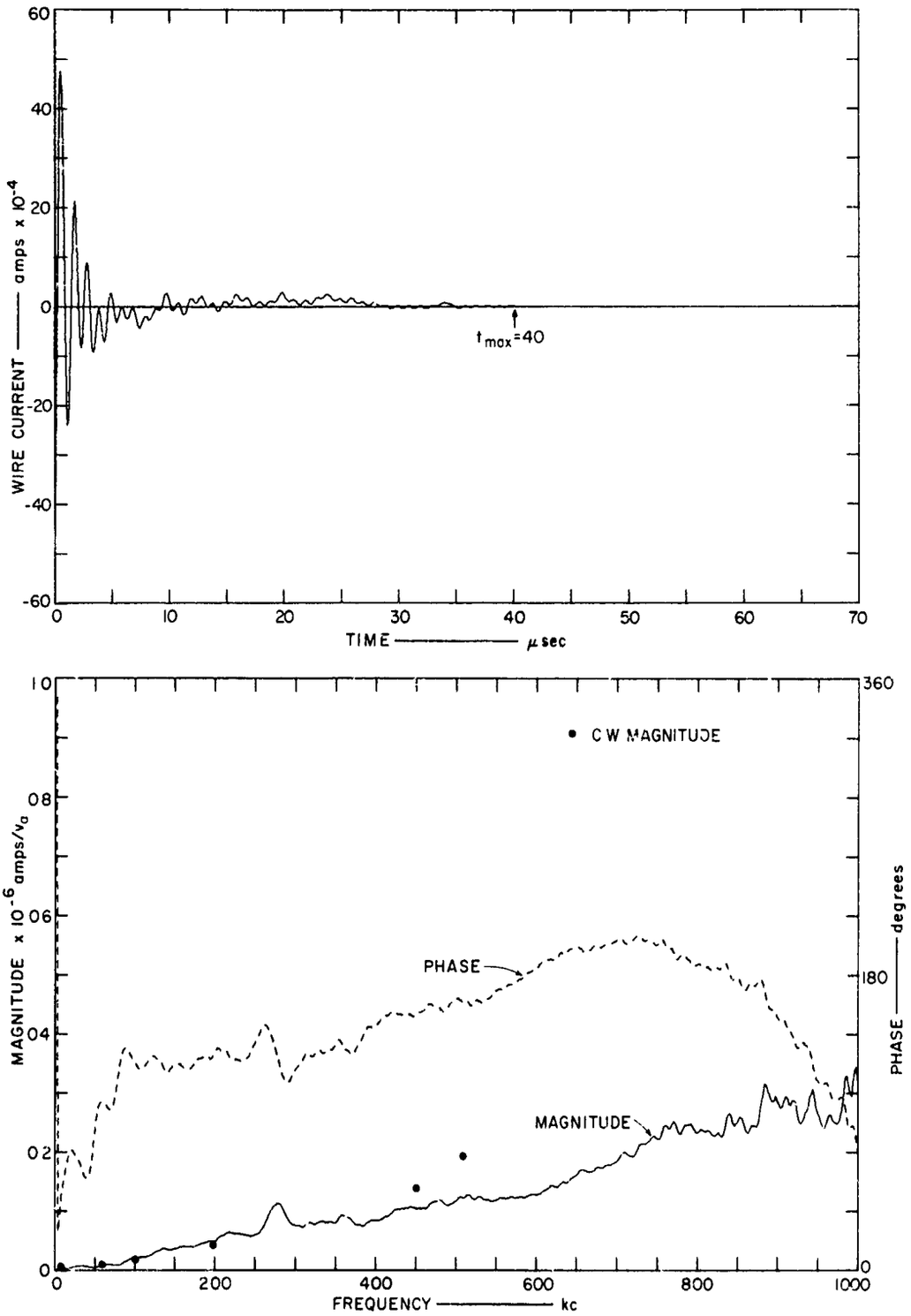

FIG. 101 PULSE WIRE CURRENT AT 1750 FEET IN BARE 10-GAUGE COPPER WIRE

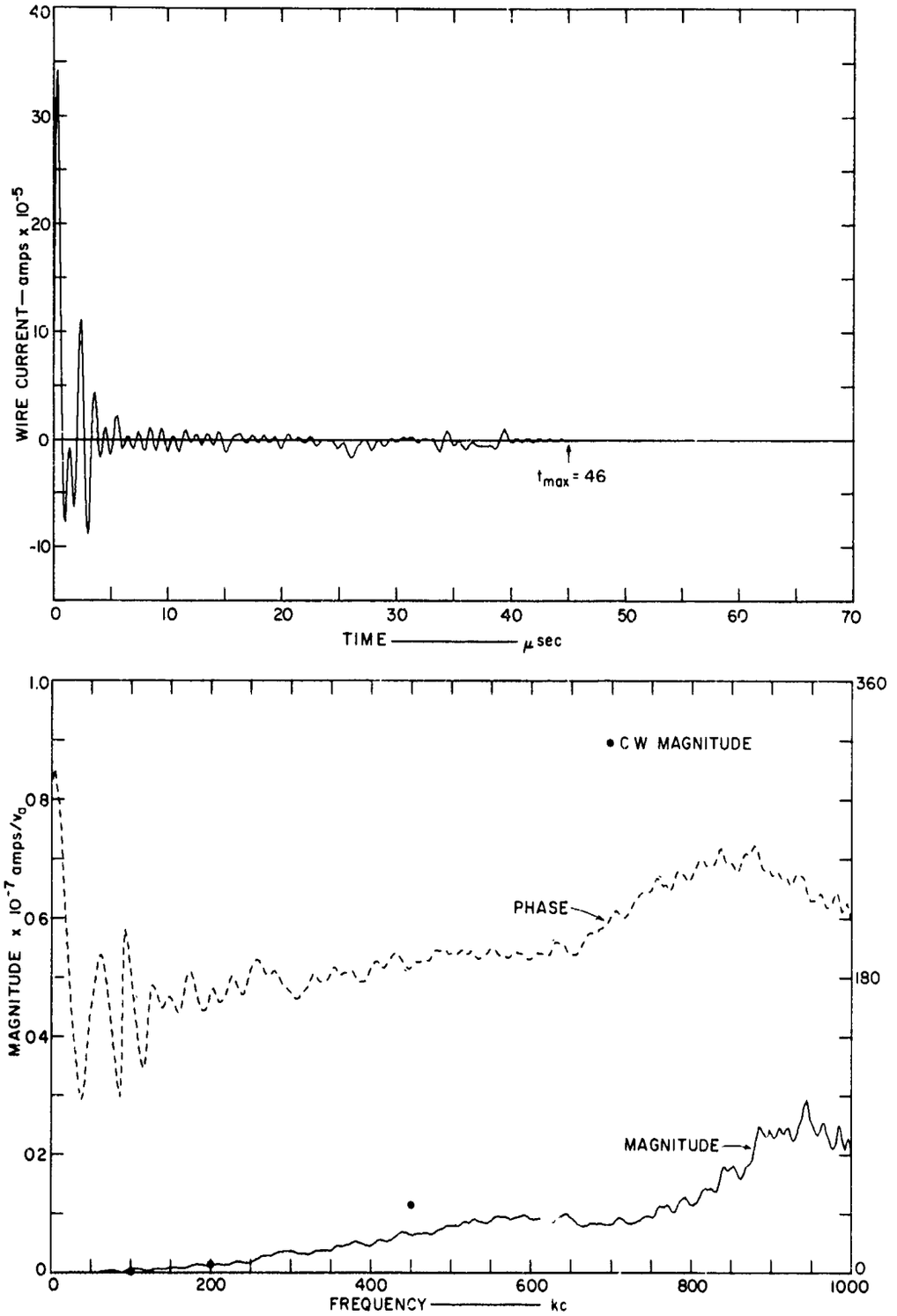

FIG. 102 PULSE WIRE CURRENT AT 3000 FEET IN BARE 10-GAUGE COPPER WIRE

magnitude (solid line) and phase (dashed line). These transform functions demonstrate some of the inherent limitations in the pulse transform functions presented. First, there is little transmitter energy beyond about 650 kc; therefore, the received data above this frequency is probably noise. In addition, the transmitted spectrum contains considerable energy near 260 kc. This energy is the predominant received energy in Figs. 100, 101, and 102, resulting in an enhancement in the received spectrum accuracy around this frequency. The CW magnitude data from Sec. VII, Fig. 29 is shown in Figs. 100, 101, and 102. Both the pulse and CW transmitter-to-wire current transfer functions show magnitude increasing with frequency out to the validity of the pulse data (650 kc). Both the pulse and CW data agree fairly well up to about 200 kc, indicating that the dynamic range for the accurate portion of the transmitted spectrum shown in Fig. 97 may be slightly greater than the assumed 20 db. The inaccuracies in the transmitter spectrum above 200 kc are evident, particularly near 260 kc.

The pulse current data in the conducting sheath cable (cable L) are shown in Figs. 103, 104, and 105 for 1050, 2050, and 3050 feet from the transmitter, respectively. For all three distances, the initial negative impulse is alike, as is the higher-frequency ringing that follows. At 1050 feet there is definite evidence of a low-frequency component (10 to 20 kc) that decreases as a function of distance from the transmitter. The general shape of the pulse current in this cable is like that of the transmitter.

The transfer functions for transmitter voltage-to-cable currents, along with the CW magnitude data from Fig. 40, are shown in the lower portions of Figs. 103, 104, and 105. The CW data indicates that the magnitude is smoothly increasing with frequency. The pulse data generally agrees with the CW data up to 200 or 300 kc. The transmitted pulse spectrum is inaccurate above this frequency and the data presented are probably invalid. The magnitude peak of 260 kc is probably caused by scaling inaccuracies in the transmitted and received pulses in the vicinity of this frequency, and indicates some of the inherent limitations of the pulse data. The magnitude of the 260-kc peak and the magnitude below about 150 kc show good agreement with the CW data.

The measured pulse and CW transfer functions for two buried radial cables (bare 10-gauge copper and conducting sheath) show sufficient agreement (smooth-

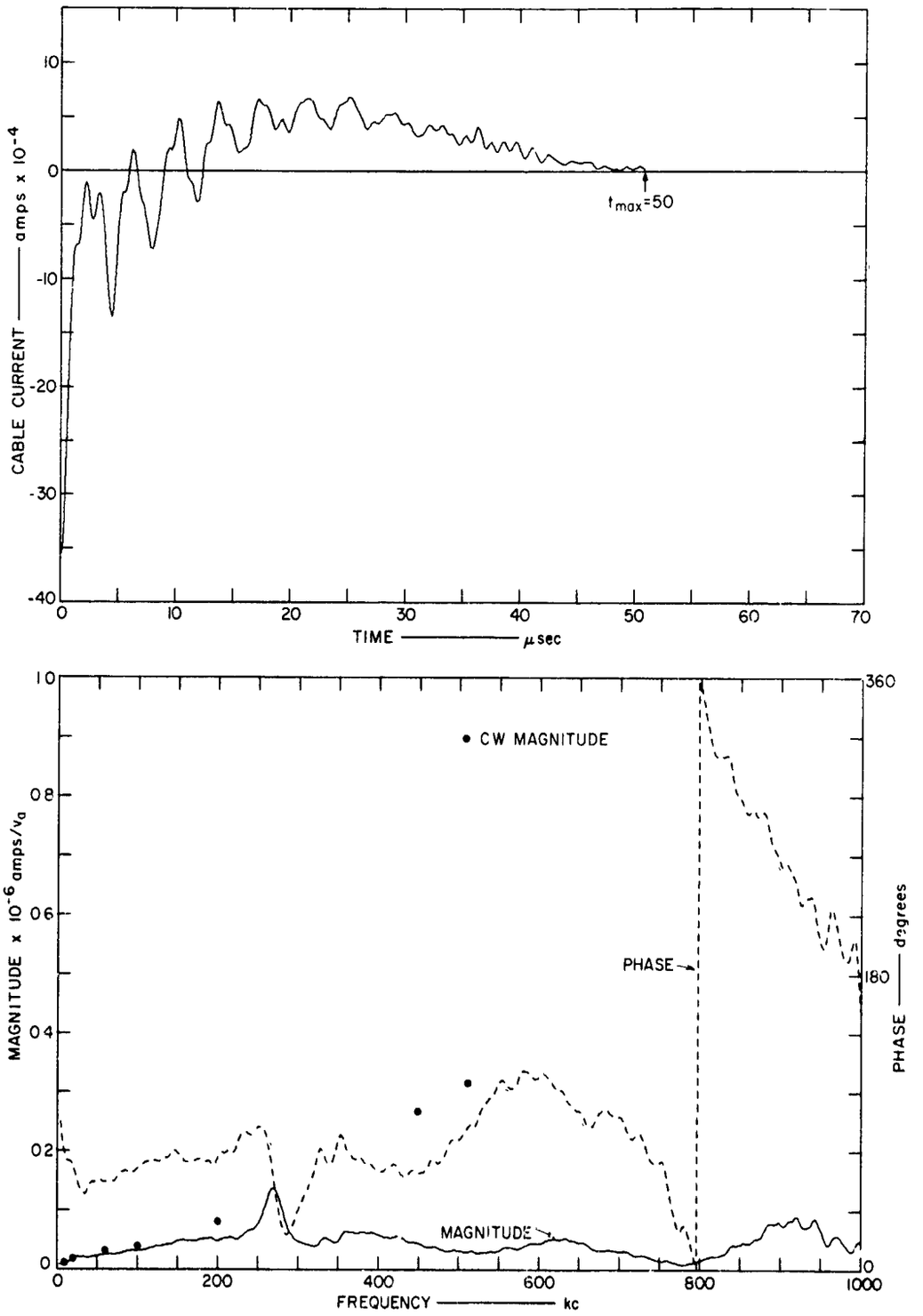

FIG. 103 PULSE CURRENT AT 1050 FEET IN CONDUCTING SHEATH CABLE

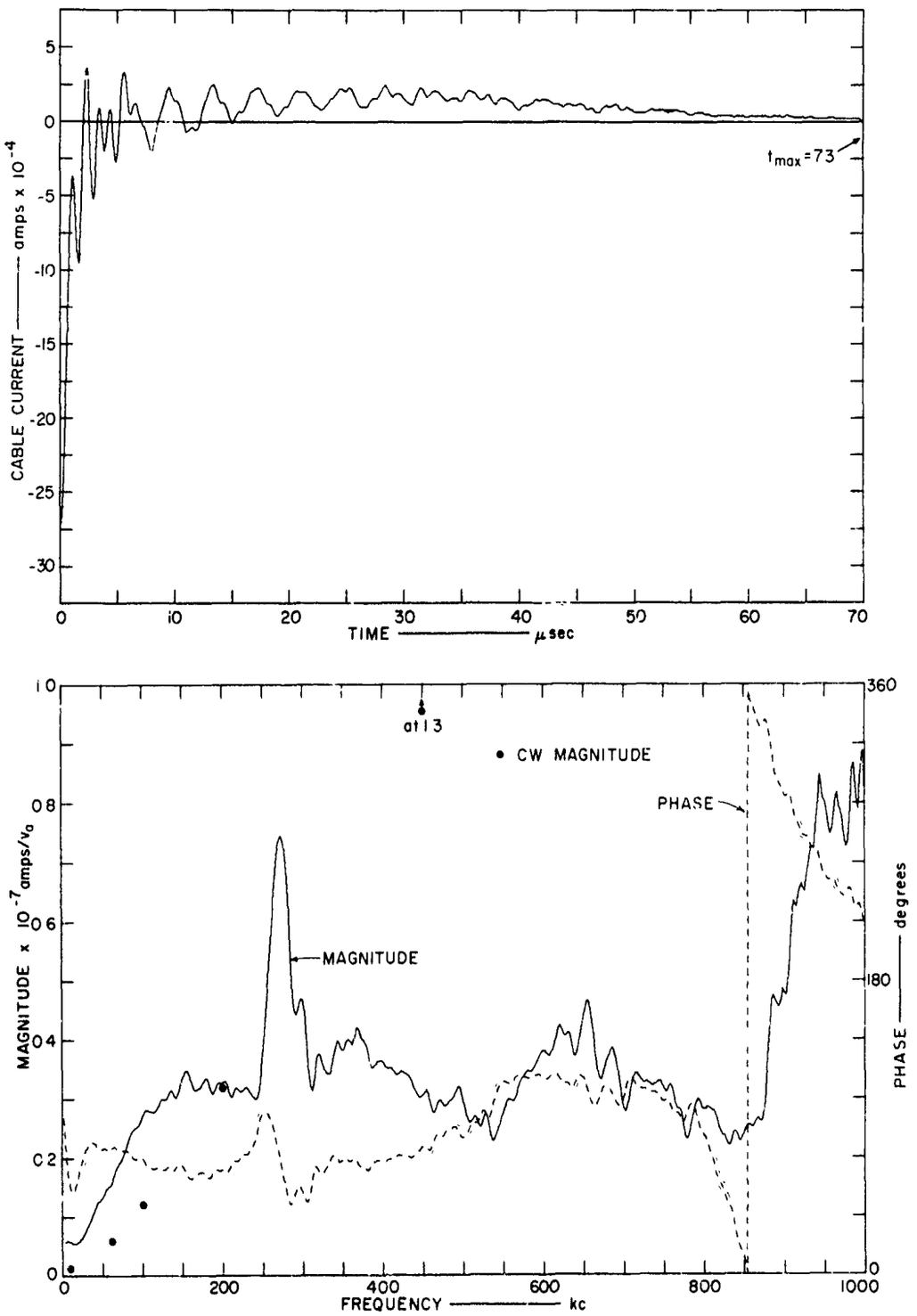

FIG. 104 PULSE CURRENT AT 2050 FEET IN CONDUCTING SHEATH CABLE

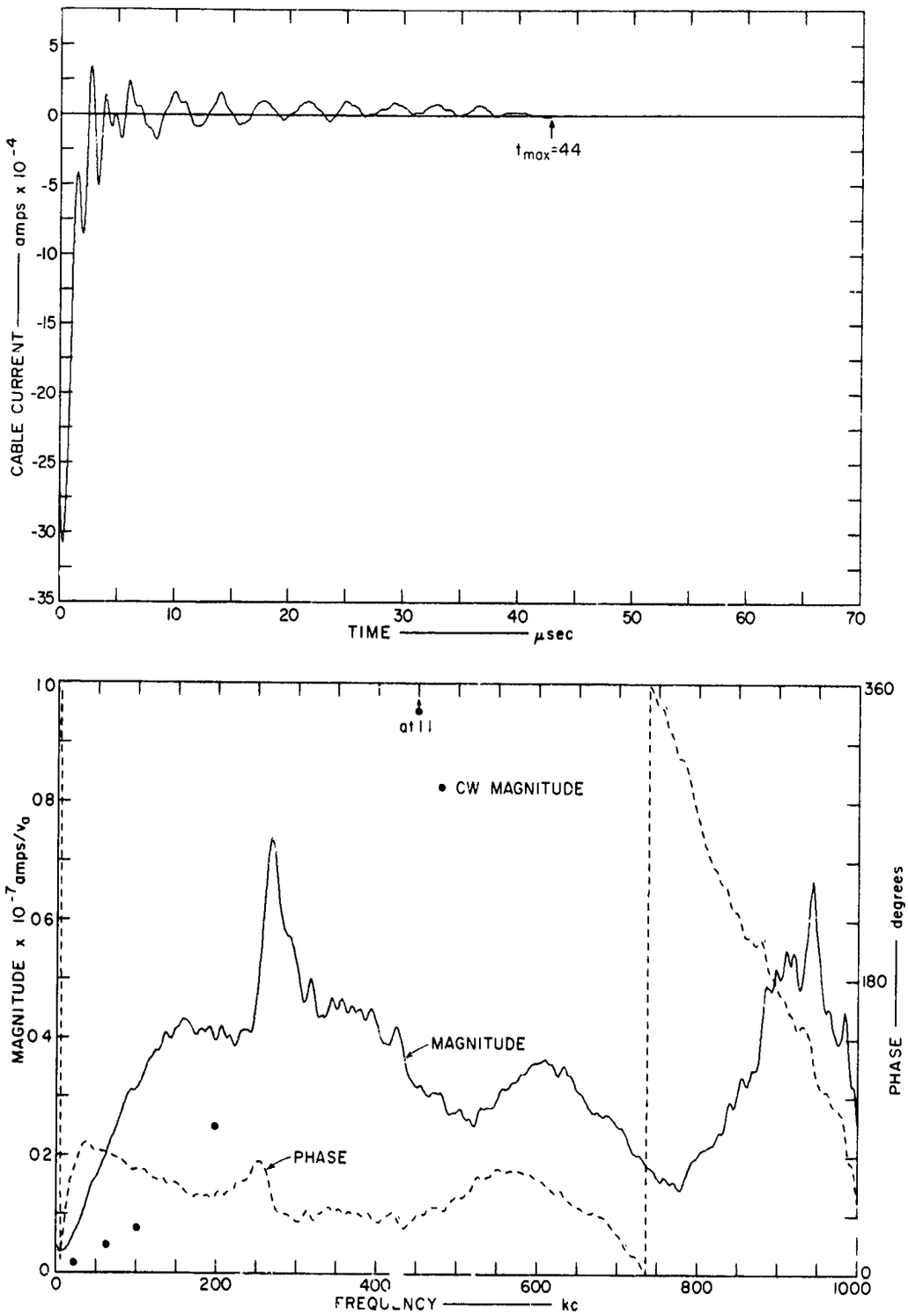

FIG. 105 PULSE CURRENT AT 3050 FEET IN CONDUCTING SHEATH CABLE

ly increasing with frequency) to indicate that the transfer function determined at a limited number of CW frequencies was adequate to define the function for all frequencies from 0.5 to 510 kc.

D. CURRENTS IN PIE-SHAPED LOOP

Pulse current measurements were made for both the shield and core currents of the pie-shaped loop shown in Fig. 2 and described in Sec. VII-F. These measurements were made on both the inner and outer arcs and in both radial legs of the loop. In clockwise rotation the location of cable current measurements are: (1) inner arc, (2) South radial (Bunker 523.09), (3) outer arc (Bunker 523.08), and (4) North radial (Bunker 523.07). The pulse data for the shield and core pulse currents in the cuter arc are shown in Figs. 106 and 107 respectively. The core current waveform (Fig. 107) looks like the shield current waveform (Fig. 106) if time equal to zero on Fig. 107 is set at about 7 microseconds in Fig. 106. The high-frequency leading pulse edge for the shield current is not present in the core current time waveform. The transfer function shown for the outer arc core current in Fig. 107 agrees with the shield current below 200 kc.

The shield and core currents in the two radials and the shield current in the inner arc all were similar in waveform and spectrum to the data shown in Figs. 106 and 107. All spectrums showed considerable frequency structure. The two magnitude maximums near 52 and 88 kc with a minimum near 66 kc was evident in all pie-shaped loop data. The CW data for the pie-shaped loop (See Sec. VII-F) was assumed to describe a smooth curve. The pulse data indicate considerable frequency dependance from 0 to 200 kc that was not defined by the CW measurements. The pie-shaped loop cable exhibited a time dependance shield-to-core resistance so that direct comparisons of data are not possible.

E. ELECTRIC AND MAGNETIC FIELDS

The major magnetic pulse fields (E_θ and H_ϕ) were measured over the bare 10-gauge copper wire at 1740 feet, at 1600 feet in an open area, and on top of Bunker 519.03 (see Fig. 2). The major electric (E_θ) and magnetic

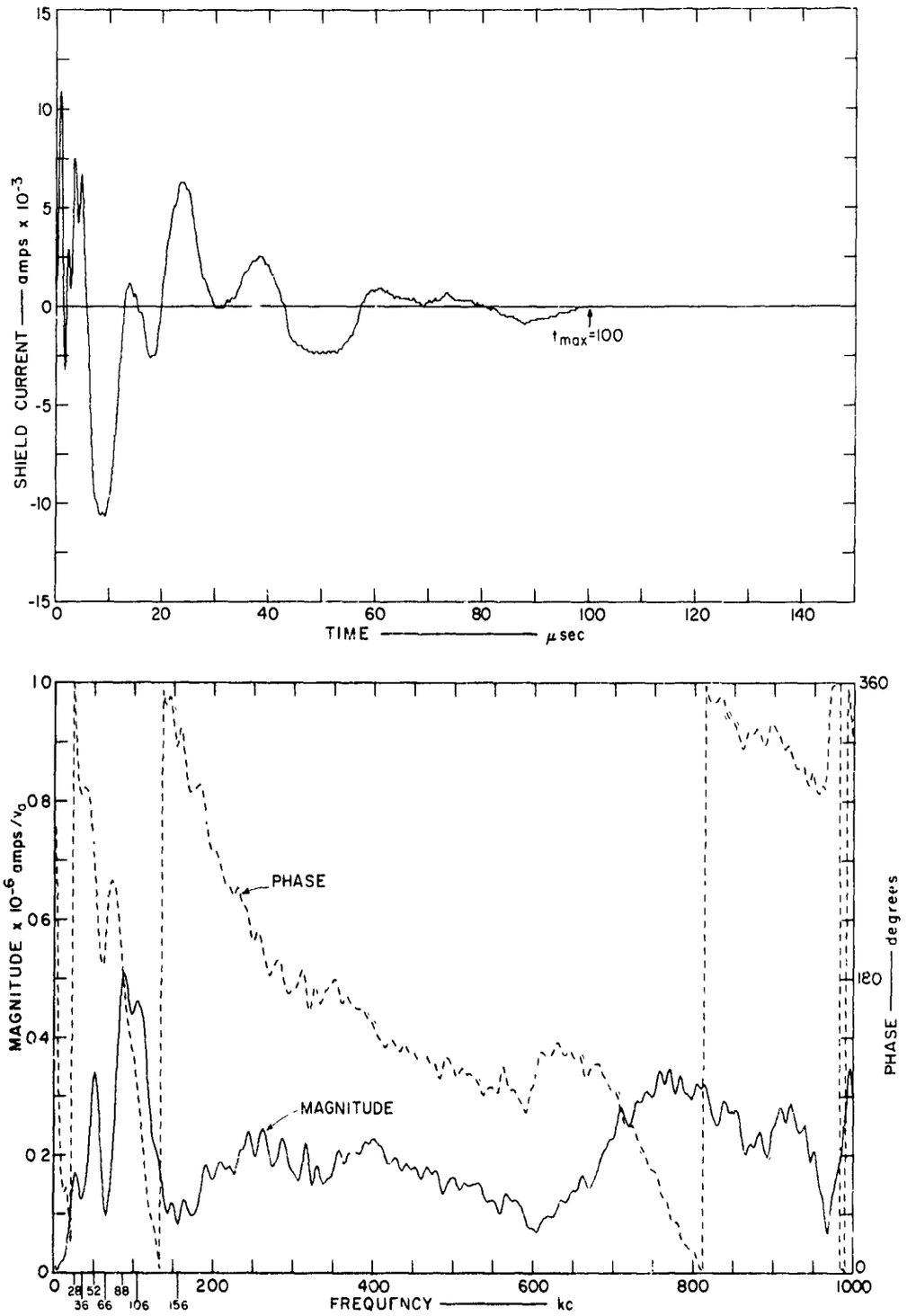

FIG. 106 PULSE SHEATH CURRENT IN OUTER ARC OF PIE-SHAPED LOOP (Bunker 523.08)

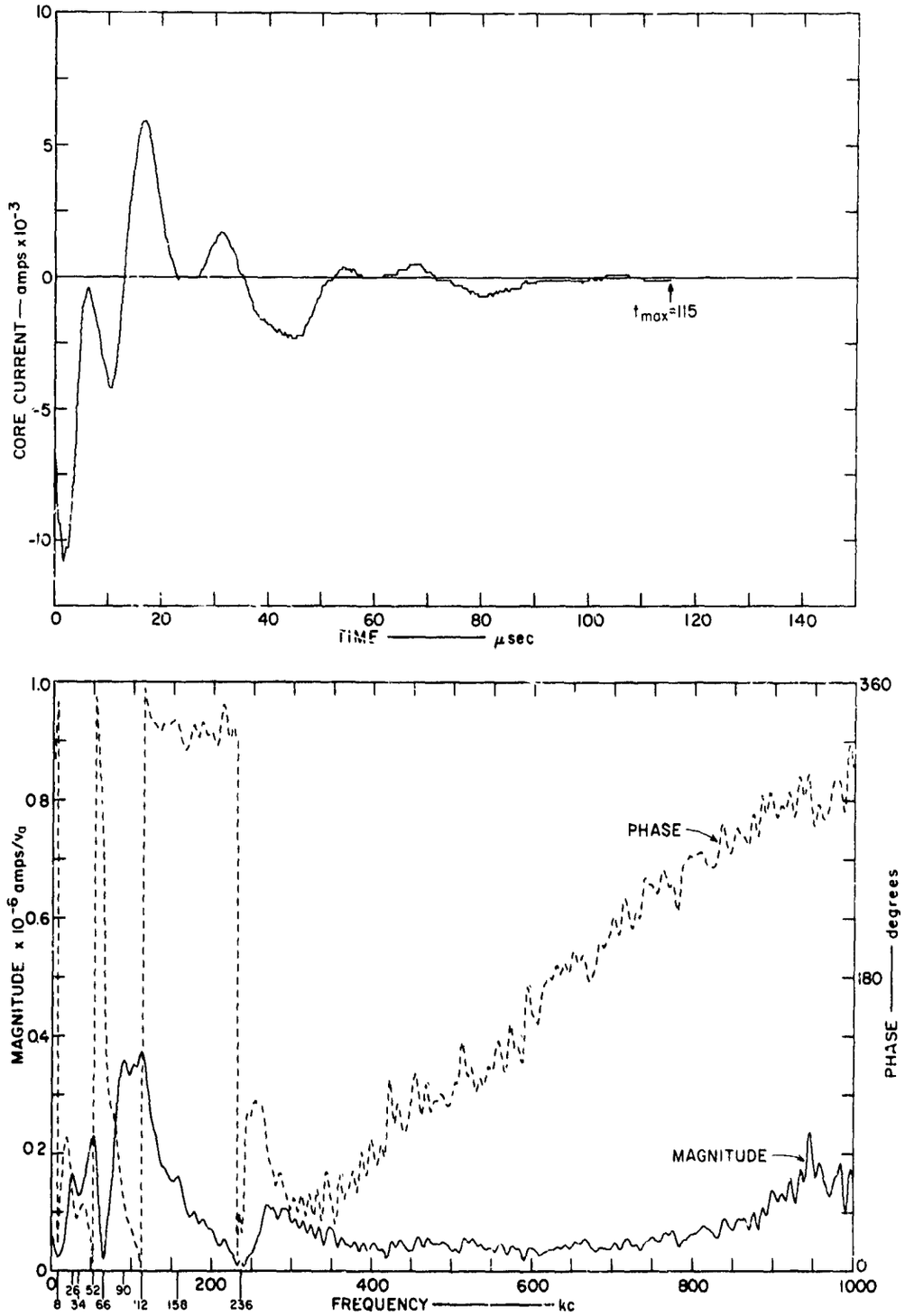

FIG. 107 PULSE CORE CURRENT IN OUTER ARC OF PIE-SHAPED LOOP
(Bunker 523.08)

(H_ϕ) pulse fields in the open area are shown in Figs. 108 and 109 along with their transmitter voltage-to-field transfer functions. Both the electric and magnetic fields show the 260-kc high-frequency portion of the transmitted spectrum. The electric field also has a low-frequency component. From Eq. (10) the transfer function magnitude for E_θ should be relatively flat for frequencies below 150 kc and increasing with frequency above 150 kc. From Eq. (11), the transfer function magnitude for H_ϕ should increase with frequency for all frequencies. (These theoretical values are shown in Figs. 108 and 109). The predicted behavior can be seen somewhat in Figs. 108 and 109 for the pulse data. Below 40 kc the electric field transfer function is relatively flat. The H_ϕ pulse data agrees well with theory (Fig. 109).*

The transmitted spectrum, shown in Fig. 97, contains considerable energy at 12 kc and a secondary peak in energy at 260 kc. Thus, using Eq. (10) for the E_θ transfer function, the received E_θ spectrum at 1600 feet will contain a peak near 12 kc due to the peak in the transmitted spectrum and the constant (near-field) transfer function at low frequencies, and a peak at about 260 kc due to the combined effects of the increasing magnitude of the transfer function in this frequency range (far-field) and the secondary peak in the transmitted spectrum at 260 kc. For H_ϕ, the resulting spectrum at 1600 feet using Eq. (11) will contain essentially one peak at about 260 kc caused by the increasing transfer function and the secondary peak in the transmitted spectrum at 260 kc. The peak in the transmitted spectrum at 12 kc is suppressed in the magnetic field spectrum by the very low values of the transfer function at low frequencies. The predicted time waveforms for E_θ and H_ϕ using the transmitted spectrum and theoretical transfer functions, are shown in Fig. 110. The predicted waveshapes agree well with the measured data. Measured magnitude of E_θ agrees with predictions; however, predicted and measured H_ϕ magnitude disagree, probably due either to system calibration error or to inaccurate transmitter spectrum, or to both. This ability to predict E_θ and H_ϕ indicates that the measured CW transforms and Fourier transforms can be used to give pulse data, providing the total system is linear.

*The 260-kc peak is due to scaling inaccuracies in the transmitted pulse.

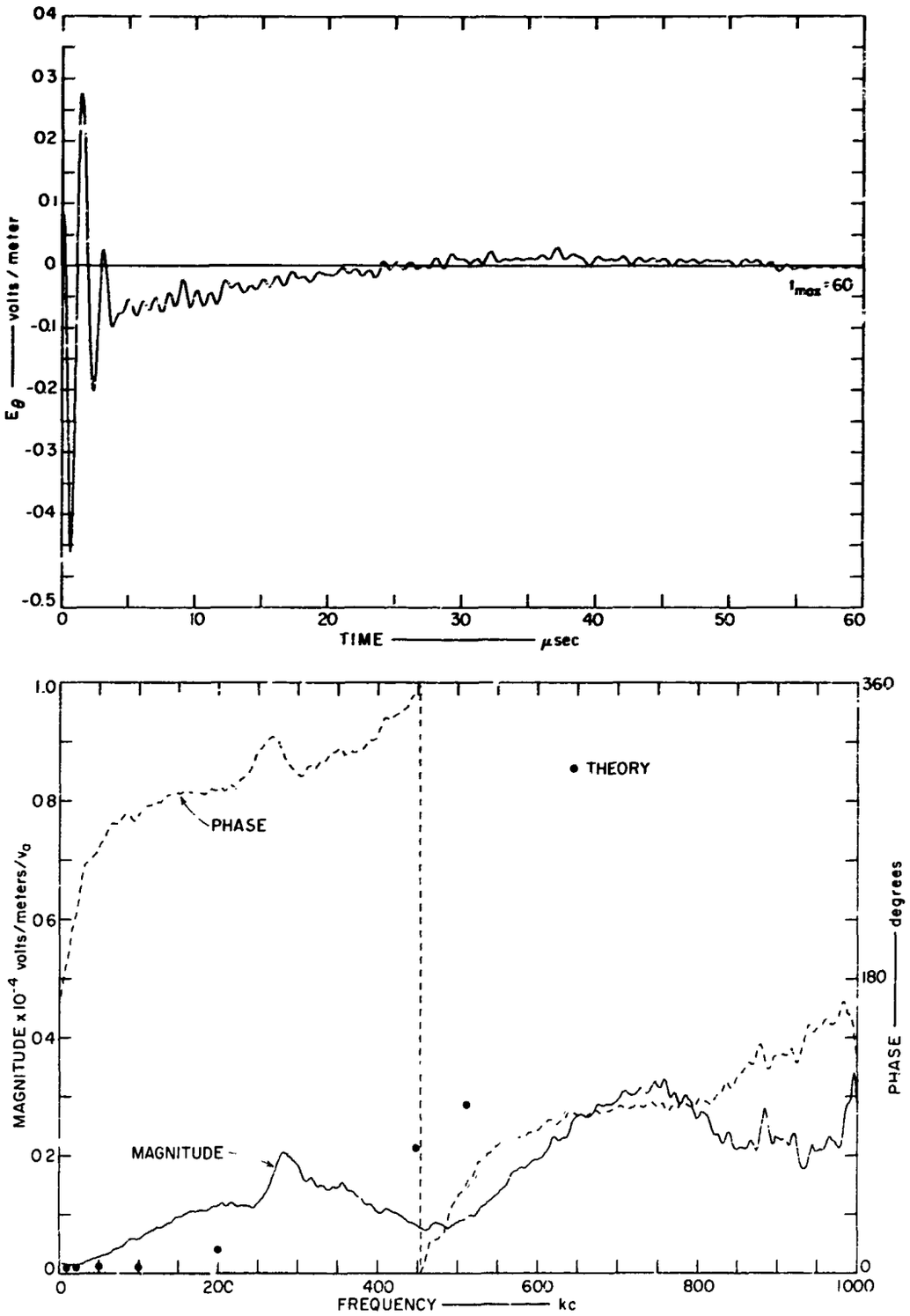

FIG. 108 E_θ AT 1600 FEET

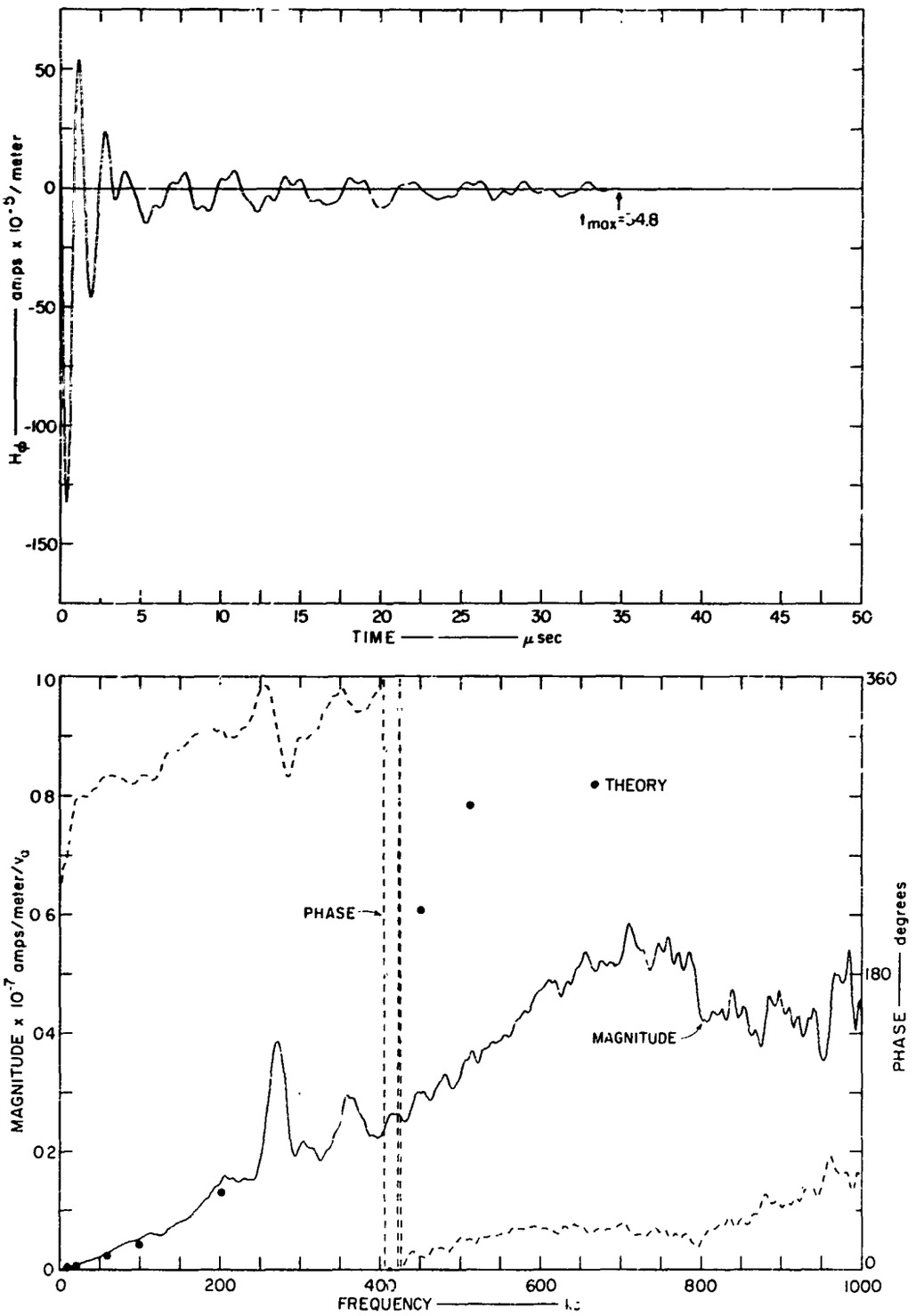

FIG. 109 H_ϕ AT 1600 FEET

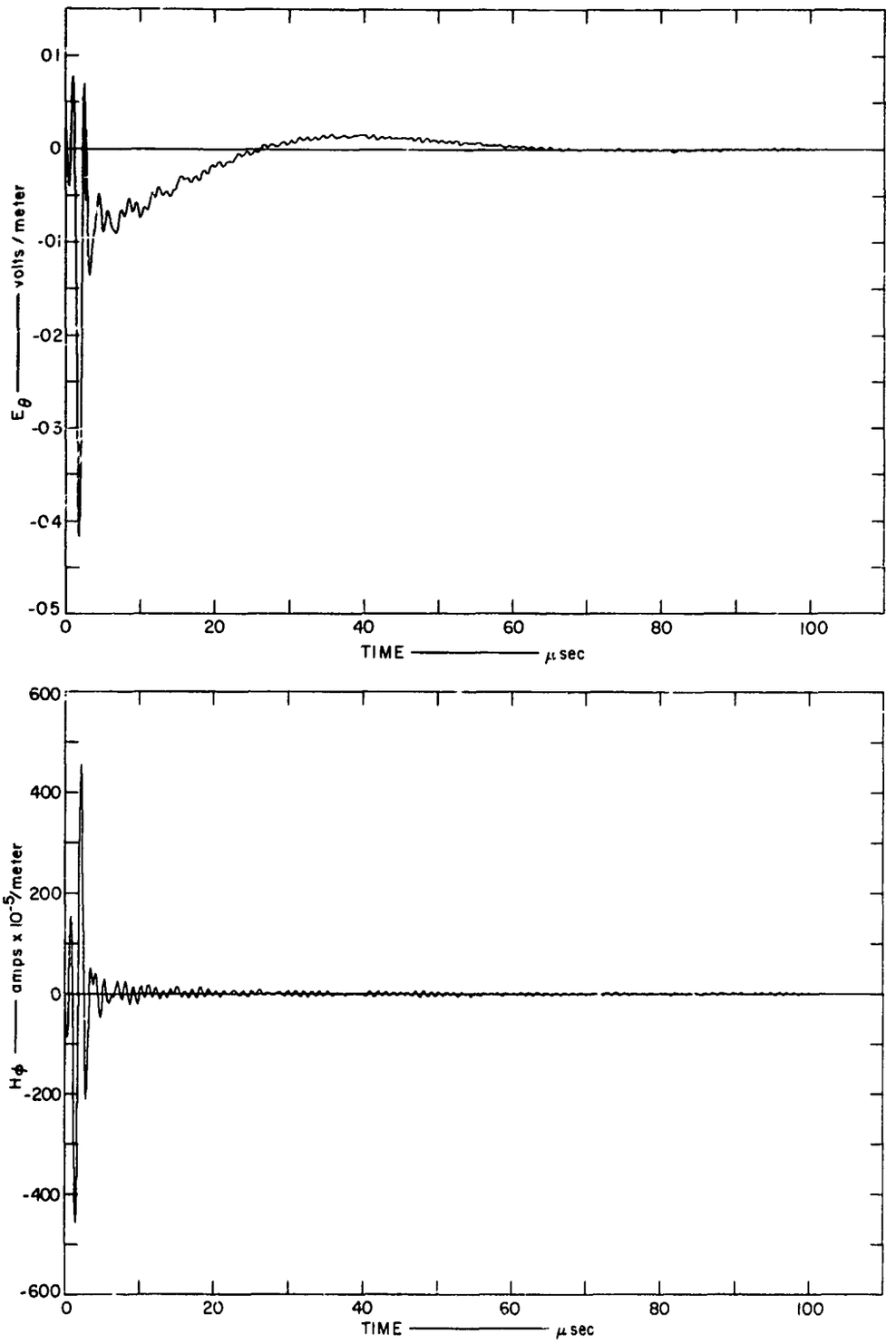

FIG. 110 PREDICTED E_θ AND H_ϕ AT 1600 FEET

The major electric E_θ and magnetic H_ϕ pulse fields over Bunker 519.03 are shown in Figs. 111 and 112. The time waveform data are very similar to the open area data. The transfer function magnitude for the magnetic field (Fig. 112) agrees with the open area data while the transfer function for the electric field (Fig. 111) is reduced. This reduction is compatible with the observed electric field distortion described in Sec. VIII-E, but is greater in magnitude than that recorded using the CW system.

The fields over the bare 10-gauge copper wire at 1740 feet are shown in Figs. 113 and 114. The electric field (Fig. 113) is larger in both peak amplitude and transfer function magnitude than the measurements at 1600 feet. The magnetic field agrees well with the other pulse measurements except for a slight enhancement at the low frequencies.

F. COMMENTS ON PULSE MEASUREMENTS

The pulse measurements presented here were made following a fairly complete CW measurements program at a limited number of frequencies. These data were adequate to describe the measured currents and fields in the 0.5-to-510-kc frequency range, providing that behavior between the measured CW data did not vary radically with frequency. In this section, examples have been given in which pulse data, being relatively continuous in frequency, were used to compute transfer functions throughout the frequency range of interest. The use of the pulse data for this purpose demonstrated the limitations inherent in pulse measurements. The pulse data did indicate, however, that all CW data, except possibly the pie-shaped loop data, were sufficient to define the transfer functions, and that by using the measured transfer functions, the transmitted waveform, and the Fourier transforms it is possible to predict the received pulse data. Such predictions naturally require that the entire system contain no saturation or hysteresis.

The transmitter-voltage-to-received-pulse transfer functions presented in this section showed considerable failings due to the limited film-reading accuracy and to the tendency of the transfer functions to accentuate the high-frequency end of the received spectrum. This reading accuracy and the wide transfer function variations with frequency will limit the accuracy of data obtained from any pulse system.

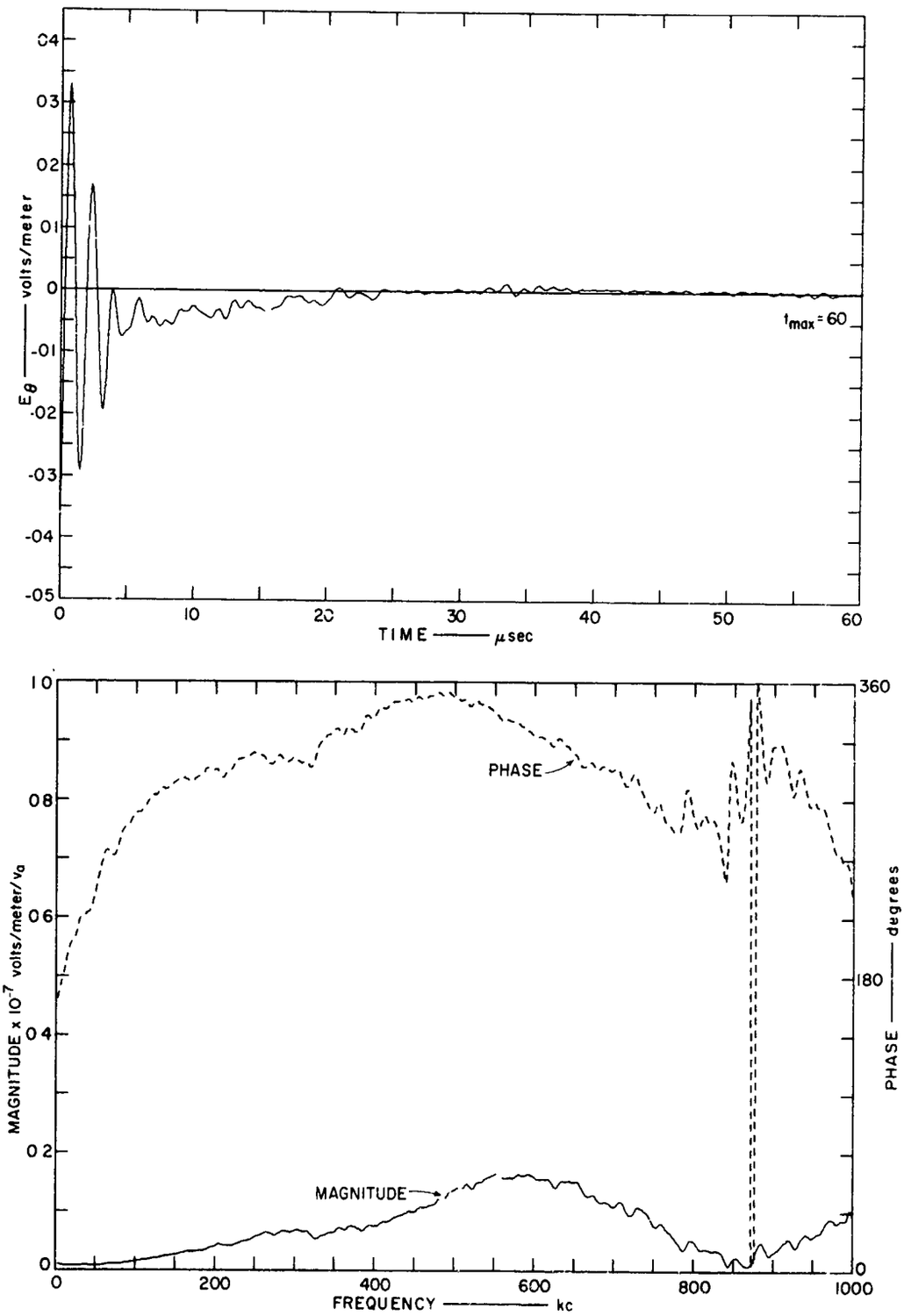

FIG. 111 E_θ OVER BUNKER 519.03

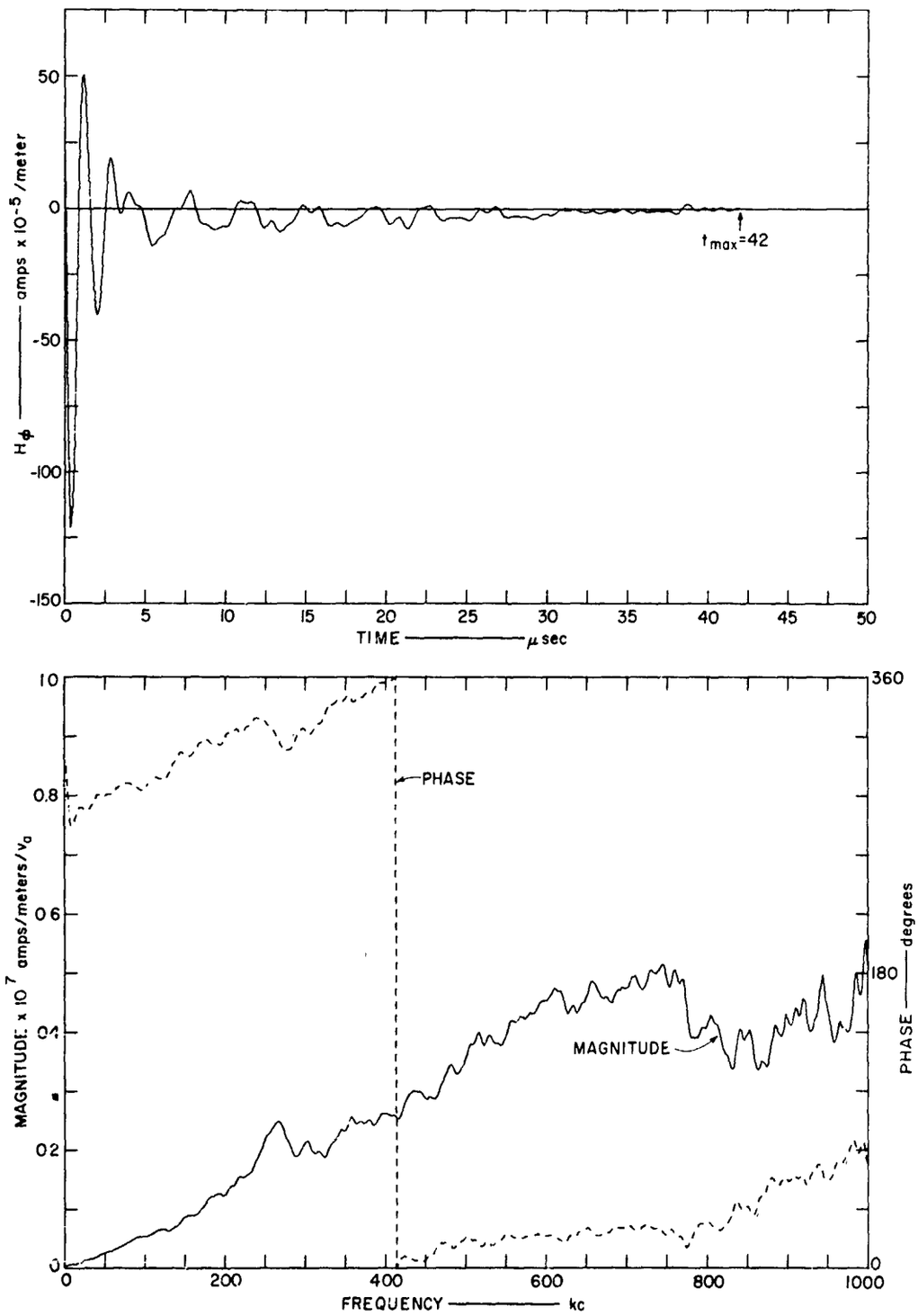

FIG. 112 H_ϕ OVER BUNKER 519.03

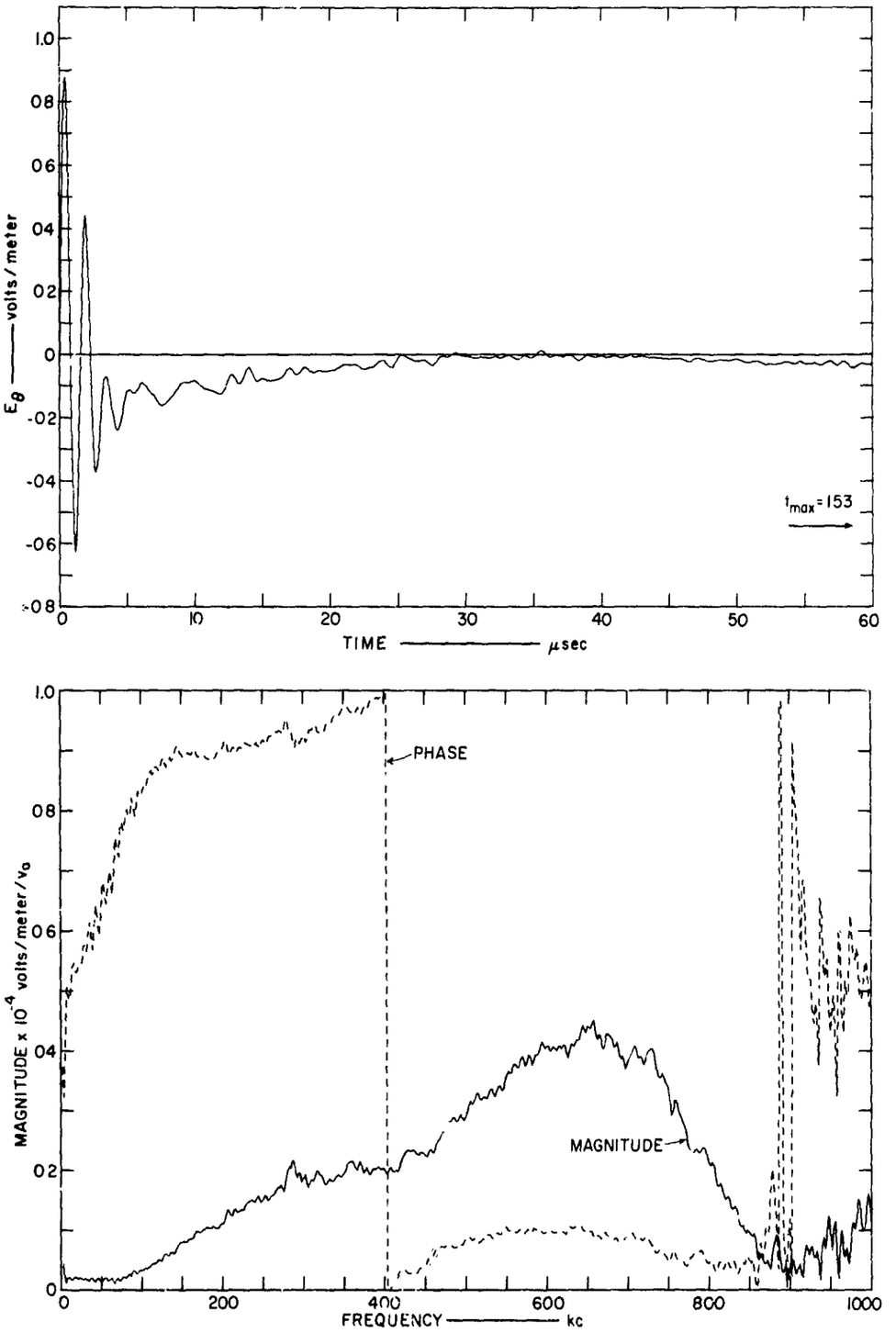

FIG. 113 E_θ OVER BARE 10-GAUGE COPPER WIRE AT 1740 FEET

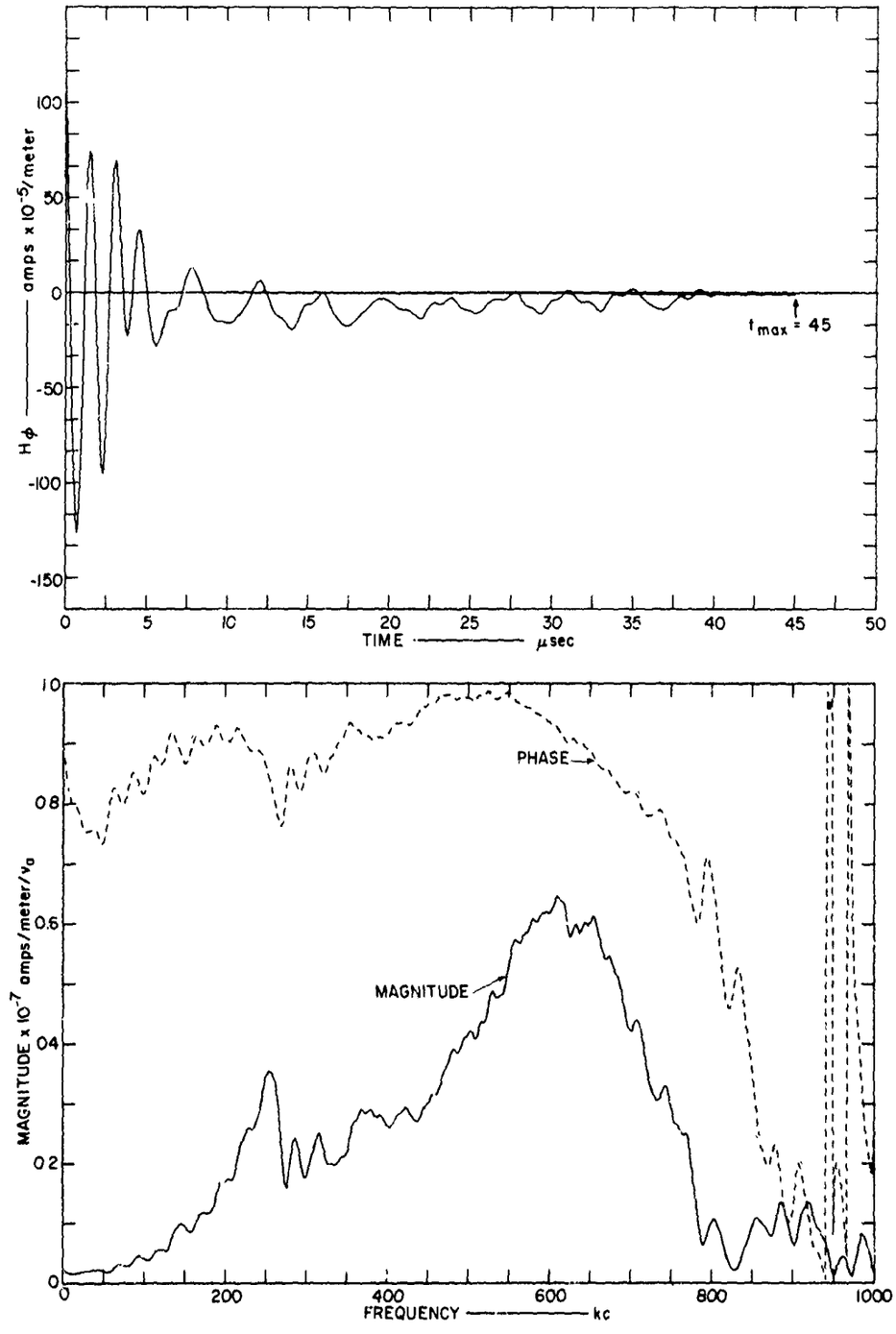

FIG. 114 H_ϕ OVER BARE 10-GAUGE COPPER WIRE AT 1740 FEET

This page intentionally left blank.

X SUMMARY AND CONCLUSIONS

An experimental and theoretical investigation was made to determine the electromagnetic effects of man-made inhomogeneities buried in the earth. These investigations determined currents in cable structures and distortions in electric and magnetic fields above the earth's surface.

Measurements were made using a low-power portable transmitter to transmit CW at 0.5, 1, 2, 5, 10, 20.6, 62, 100, 200, 450, and 510 kc and a 100-kv pulse whose spectrum was peaked at 12 kc.

A study of the cable current problem has led to the development of a relatively simple analytical theory based on a transmission line model for calculating the current induced in a conductor by electric fields tangential to the surface of the ground. In this transmission line theory it is assumed that the conductor is isolated or that other conductors, if present, are far enough away that they do not appreciably affect the tangential electric fields in the vicinity of the conductor. Currents measured in the cables studied in this report indicate that the transmission line theory is valid for isolated conductors, for arrays of bare conductors in contact with the soil when the conductors are spaced several skin depths (in the soil) apart, and for insulated conductors above or below the surface if the capacitive admittance per unit length of the insulation is small compared to the admittance per unit length contributed by the soil.

Measurements made on buried, bare radial conductors spaced less than a few skin depths apart indicate that the currents induced in these conductors are in general accordance with Wait's wave impedance theory. It is important to note that the wave impedance theory appears to apply only to conductor arrays that are tightly coupled to the electric fields in the ground (e.g. buried, bare conductors, or insulated conductors at frequencies high enough that the capacitive admittance per unit length of the isolation is large compared to the soil admittance per unit length.) Unless such tight coupling exists, the wave

impedance of the conductor array does not effectively shunt the wave impedance of the soil as is assumed in the derivation of the wave impedance theory.

Current measurements in cables oriented along a tangential arc about the transmitter indicate that such cables are effectively electric dipoles, with the dipole null oriented with the major electric field components. The currents in cable arcs are approximately two orders of magnitude below the current in a long radial conductor at a corresponding distance from the transmitter.

Current measurements on closed-loop structures have pointed out that two coupling mechanisms are generally active in inducing currents in closed loops. Coupling to the electric field in the ground occurs either through direct contact (on bare conductors) or through the capacitance of the insulation. Coupling to the magnetic field occurs if any magnetic flux passes through the loop (some magnetic coupling will exist even in a carefully designed loop). Magnetic coupling induces circulating currents in the loop, while electric coupling induces currents that flow in the same direction down the two sides of the loop. In the small (100-foot-diameter) insulated loops studied in this program, electric coupling predominated at frequencies above 62 kc, and magnetic coupling predominated at frequencies below 20 kc where the insulation admittance was too small to provide adequate electric coupling.

Studies of a closed loop (100-foot-diameter) provided with a guard ring consisting of a shorted turn of large insulated wire revealed information important to the design of circuit-protection systems. The shorted turn proved effective in reducing the circulating current induced in the protected loop by the magnetic field, but because it was insulated and did not short circuit the electric field in the ground, it was not very effective in reducing the current induced in the protected circuit by the electric field. To protect a buried circuit from currents induced by the electric field, the guard conductor should be bare so that it is more effective in short circuiting the electric field in the ground.

It is also concluded that CW measurements at selected frequencies are adequate to define a transfer function for use in analysis of the response of conductor currents to pulsed electromagnetic fields if the natural resonances of the conductor are suppressed due to (1) termination of the conductor in its

characteristic impedance, or (2) tight coupling between the conductor and the soil. If the conductor is insulated and is not terminated in its characteristic impedance, the conductor will resonate at frequencies at which its length is integer multiples of a half wavelength. CW measurements at many frequencies are required to accurately define the transfer function when such resonances occur.

CW measurements of electric and magnetic fields above the earth's surface, with no inhomogeneities in the earth, demonstrated the capability to measure the major electromagnetic fields (vertical electric and tangential magnetic) with a magnitude accuracy better than 5 percent, phase accuracy to 5 degrees, and spatial orientation accuracy to better than 1 degree. In addition, the normal forward electric field was observed whenever it exceeded 50 db below the vertical electric field (usually above 62 kc). For imperfect field sensors (with limited signal rejection in the direction of minimum response to a field) it has been shown that (1) the magnitude and phase can only be measured accurately on major fields, (2) the magnitudes of small orthogonal fields in the presence of large fields can only be crudely measured (their phase is essentially indeterminate), and (3) the spatial orientation of a resulting total field that contains more than one field component can be measured even for fields with complex polarization structures. All other variables in complex wave structures cannot be measured directly.

Measurements near buried cables showed magnetic fields above the surface caused by currents in the cable and surrounding ground due to the presence of the cable. These current-induced fields were generally detectable out to 100 feet. Electric and magnetic field measurements near buried bunkers showed distorted fields. For a large metal bunker flush with the earth's surface in good conducting earth, the magnetic field was observed to be distorted by the induced circulating current from the tangential field. The distortion resulted in a rejection of the normal field near the bunker. In addition, over this bunker the forward electric field was reduced (improved local ground conductivity), resulting in a change in total electric field spatial orientation.

Field distortions due to a small concrete bunker were not discernible. However, for the bunker used, there was a vertical wooden pole in the vicinity with a cable along this pole. This cable was observed to terminate the electric field in the vicinity, causing a conical spatial distortion of the electric field around the pole.

Field measurements and theory indicate that the measurement of electric and magnetic fields near buried bunkers can be misleading unless great care is taken to make the electromagnetic characteristics of the bunker compatible with the desired field measurements. (This includes care in the sensor design to minimize field distortions.) Small electromagnetic field components (orthogonal to large fields) can be only crudely measured by proper orientation of the sensor pattern null to minimize (not eliminate) the large field. For such measurements, orientation is critical to a part of 1 degree. Antennas mounted in fixed orientations to observe orthogonal fields are generally not oriented this accurately to the resulting fields. Measurements generally can be made on orthogonal field components that are large (not over one order of magnitude below the largest field component present).

The measurement of complex electromagnetic coupling phenomena can be made using the fixed-frequency CW system described in this report, providing the coupling is a fairly smooth function of frequency. Pulse measurements contain continuous frequency spectra and can consequently show the presence of peaks and nulls under complex coupling conditions. However, accuracy at all frequencies is difficult to obtain, indicating that a slow-sweeping CW measurement is desirable to obtain accurate electromagnetic coupling data in a broad frequency band.

APPENDIX A

SOLUTION TO THE CABLE-CURRENT EQUATION

This page intentionally left blank.

APPENDIX A

SOLUTION TO THE CABLE-CURRENT EQUATION

The differential equation for the current induced in a radial wire in or near the surface of the ground was shown to be of the form

$$\frac{d^2I}{dx^2} - \gamma^2 I = YE \tag{A-1}$$

where

γ^2 = ZY, the propagation factor squared

Z = R + $j\omega L$, the wire impedance per unit length

Y = G + $j\omega C$, the wire admittance per unit length

and

$$E = (1-j)\sqrt{\frac{\pi f \mu}{\sigma}}\,\frac{\omega h C_a V_a}{4\pi}\left[\frac{jk}{x+a} + \frac{1}{(x+a)^2}\right] e^{-jk(x+a)} \tag{A-2}$$

is the driving field, the radial field at the air/earth interface.* The differential equation to be solved is thus

$$\frac{d^2I}{dx^2} - \gamma^2 I = A\left[\frac{jk}{x+a} + \frac{1}{(x+a)^2}\right] e^{-jk(x+a)} \tag{A-3}$$

---

*It has been pointed out by W. R. Graham and D. Marston at AFWL that the above expression for the radial electric field will be in error very close to the base of the antenna (i.e., within one skin depth of the antenna base). Very near the antenna base, the current density in the soil will be approximately spherically distributed in the ground instead of parallel to the surface and exponentially decaying with depth as assumed in deriving Eq. (A-2).

where

$$A = (1-j)\ Y\sqrt{\frac{\pi f \mu}{\sigma}}\ \frac{\omega h C_a V_a}{4\pi} \quad . \tag{A-4}$$

The solution of this equation is[15]

$$I(x) = K_1 e^{\gamma x} + K_2 e^{-\gamma x} + \frac{A}{2\gamma}\left\{ e^{\gamma x}\int e^{-\gamma x}\left[\frac{jk}{x+a} + \frac{1}{(x+a)^2}\right] e^{-jk(x+a)}dx \right.$$
$$\left. - e^{-\gamma x}\int e^{\gamma x}\left[\frac{jk}{x+a} + \frac{1}{(x+a)^2}\right] e^{-jk(x+a)}dx \right\} \quad . \tag{A-5}$$

Because of the similarity of the two integrals, it will be necessary to solve only one of them; the second integral can then be evaluated by replacing γ by $-\gamma$ in the solution for the first. Hence, letting

$$\mathcal{I}_1 = \int e^{-\gamma x}\left[\frac{jk}{x+a} + \frac{1}{(x+a)^2}\right] e^{-jk(x+a)}dx$$
$$= e^{-jka}\left[jk\int\frac{e^{-(jk+\gamma)x}}{x+a}\,dx + \int\frac{e^{-(jk+\gamma)x}}{(x+a)^2}\,dx\right] \tag{A-6}$$

we can make use of the integral formulas[16]

$$\int\frac{e^{qx}}{x+a}\,dx = e^{-qa}\left\{\log(x+a) + \sum_{n=1}^{\infty}\frac{[q(x+a)]^n}{n\cdot n!}\right\} \tag{A-7}$$

and

$$\int\frac{e^{qx}}{(x+a)^2}\,dx = -\frac{e^{qx}}{x+a} + qe^{-qa}\left\{\log(x+a) + \sum_{n=1}^{\infty}\frac{[q(x+a)]^n}{n\cdot n!}\right\} \tag{A-8}$$

so that

$$\mathcal{I}_1 = e^{-jka}\left\{jk\int\frac{e^{-(jk+\gamma)x}}{x+a}\,dx - \frac{e^{-(jk+\gamma)x}}{x+a} - (jk+\gamma)\int\frac{e^{-(jk+\gamma)x}}{x+a}dx\right\}.$$

After rearranging,

$$\mathcal{I}_1 = e^{\gamma a}\left\{-\frac{e^{-(\gamma+jk)(x+a)}}{x+a} - \gamma\int\frac{e^{-(jk+\gamma)(x+a)}}{x+a}\,dx\right\}. \qquad \text{(A-9)}$$

Thus

$$F(x) = \frac{A}{2\gamma}\left\{e^{\gamma x}\mathcal{I}_1 - e^{-\gamma x}\mathcal{I}_2\right\}$$

$$= -\frac{A}{2}\left\{e^{\gamma(x+a)}\int\frac{e^{-(jk+\gamma)(x+a)}}{x+a}\,dx + e^{-\gamma(x+a)}\int\frac{e^{-(jk-\gamma)(x+a)}}{x+a}\,dx\right\}.$$

After performing the integrations and rearranging,

$$F(x) = -A\left\{\cosh\gamma(x+a)\log(x+a)\right.$$

$$\left. + \frac{e^{\gamma(x+a)}}{2}\sum_{n=1}^{\infty}\frac{\left[-(jk+\gamma)(x+a)\right]^n}{n\cdot n!} + \frac{e^{-\gamma(x+a)}}{2}\sum_{n=1}^{\infty}\frac{\left[-(jk-\gamma)(x+a)\right]^n}{n\cdot n!}\right\}. \qquad \text{(A-10)}$$

The wire current is then

$$I(x) = K_1 e^{\gamma x} + K_2\, e^{-\gamma x} + F(x) \qquad \text{(A-11)}$$

where K_1 and K_2 are arbitrary constants determined by the terminations at the end of the wire.

For large values of $(jk\pm\gamma)(x+a)$, the series is difficult to evaluate because the terms become very large before the series begins to converge. For large

arguments, therefore, the asymtotic expression for the exponential integral may be used.[17] Thus,

$$\int_{q(x+a)}^{\infty} \frac{e^{-u}}{u}\, du = -\gamma_e - \log q(x+a) - \sum_{n=1}^{\infty} \frac{\left[-q(x+a)\right]^n}{n \cdot n!}$$

$$\approx \frac{e^{-q(x+a)}}{q(x+a)} \sum_{n=0}^{N} \frac{n!}{\left[-q(x+a)\right]^n} \tag{A-12}$$

from which

$$\sum_{n=1}^{\infty} \frac{\left[-q(x+a)\right]^n}{n \cdot n!} = -\gamma_e - \log q(x+a) - \frac{e^{-q(x+a)}}{q(x+a)} \sum_{n=0}^{N} \frac{n!}{\left[-q(x+a)\right]^n} \tag{A-13}$$

where $\gamma_e = 0.577\,2157\ldots$, and N is chosen by considering the accuracy desired and the magnitude of the argument $-q(x+a)$.

To obtain the potential of the wire relative to the undisturbed ground potential, we note that

$$\frac{dI}{dx} = -YV(x) \quad . \tag{A-14}$$

Thus the wire voltage $V(x)$ can be written

$$V(x) = -Z_o \left[K_1 e^{\gamma x} - K_2 e^{-\gamma x}\right] - \frac{1}{Y} \frac{dF(x)}{dx} \tag{A-15}$$

where $Z_o = \gamma/Y = \sqrt{Z/Y}$ is the characteristic impedance of the line.

Letting

$$\frac{1}{Y}\frac{dF(x)}{dx} = Z_o F_v(x) \quad , \tag{A-16}$$

we have

$$V(x) = -Z_o \left[K_1 e^{\gamma x} - K_2 e^{-\gamma x} + F_v(x) \right] \tag{A-17}$$

where

$$F_v(x) = -A \left\{ \sinh \gamma(x+a) \log (x+a) + \frac{e^{-jk(x+a)}}{\gamma(x+a)} \right.$$

$$+ \frac{e^{\gamma(x+a)}}{2} \sum_{n=1}^{\infty} \frac{\left[-jk+ \ )(x+a)\right]^n}{n \cdot n!} \tag{A-18}$$

$$\left. - \frac{e^{-\gamma(x+a)}}{2} \sum_{n=1}^{\infty} \frac{\left[-(jk-\gamma)(x+a)\right]^n}{n \cdot n!} \right\} .$$

At $x = 0$ the wire is terminated in an impedance Z_1 , so that

$$-Z_1 \ I(0) = V(0) \tag{A-19}$$

or,

$$-Z_1 \left[K_1 + K_2 + F(0) \right] = -Z_o \left[K_1 - K_2 + F_v(0) \right] . \tag{A-20}$$

Similarly, at $x = d$, the wire is terminated in an impedance Z_2, so that $Z_2 I(d) = V(d)$ and

$$Z_2 \left[K_1 e^{\gamma d} + K_2 e^{-\gamma d} + F(d) \right] = -Z_o \left[K_1 e^{\gamma d} - K_2 e^{-\gamma d} + F_v(d) \right] . \tag{A-21}$$

Solving Eqs. (A-20) and (A-21) for K_1 and K_2, we get

$$K_1 = \frac{e^{-\gamma d}\left(1 - \frac{Z_0}{Z_2}\right)\left[\frac{Z_0}{Z_1} F_v(0) - F(0)\right] + \left(1 + \frac{Z_0}{Z_1}\right)\left[\frac{Z_0}{Z_2} F_v(d) + F(d)\right]}{\left(1 - \frac{Z_0}{Z_1}\right)\left(1 - \frac{Z_0}{Z_2}\right)e^{-\gamma d} - \left(1 + \frac{Z_0}{Z_1}\right)\left(1 + \frac{Z_0}{Z_2}\right)e^{\gamma d}}$$

$$K_2 = \frac{-e^{\gamma d}\left(1 + \frac{Z_0}{Z_2}\right)\left[\left(\frac{Z_0}{Z_1}\right)F_v(0) - F(0)\right] - \left(1 - \frac{Z_0}{Z_1}\right)\left[\frac{Z_0}{Z_2} F_v(d) + F(d)\right]}{\left(1 - \frac{Z_0}{Z_1}\right)\left(1 - \frac{Z_0}{Z_2}\right)e^{-\gamma d} - \left(1 + \frac{Z_0}{Z_1}\right)\left(1 + \frac{Z_0}{Z_2}\right)e^{\gamma d}} . \tag{A-22}$$

The general solution is thus obtained when the values of K_1 and K_2 from Eq. (A-22) are substituted in Eq. (A-11). Four special cases of interest will now be considered.

Case I -- The line is terminated with the same impedance at both ends $(Z_2 = Z_1)$. Equations (A-22) then reduce to

$$K_1 = \frac{e^{-\gamma d}\left(1 - \frac{Z_0}{Z_1}\right)\left[\frac{Z_0}{Z_1} F_v(0) - F(0)\right] + \left(1 + \frac{Z_0}{Z_i}\right)\left[\frac{Z_0}{Z_1} F_v(d) + F(d)\right]}{\left(1 - \frac{Z_0}{Z_1}\right)^2 e^{-\gamma d} - \left(1 + \frac{Z_0}{Z_1}\right)^2 e^{\gamma d}}$$

$$K_2 = \frac{-e^{\gamma d}\left(1 + \frac{Z_0}{Z_1}\right)\left[\frac{Z_0}{Z_1} F_v(0) - F(0)\right] - \left(1 - \frac{Z_0}{Z_1}\right)\left[\frac{Z_0}{Z_1} F_v(d) + F(d)\right]}{\left(1 - \frac{Z_0}{Z_1}\right)^2 e^{-\gamma d} - \left(1 + \frac{Z_0}{Z_1}\right)^2 e^{\gamma d}} . \tag{A-23}$$

Case II -- The line is open-circuited at both ends $(Z_1 = Z_2 = \infty)$. Equations (A-22) then reduce to

$$K_1 = \frac{F(0)\, e^{-\gamma d} - F(d)}{2 \sinh \gamma d}$$

$$K_2 = \frac{F(d) - e^{\gamma d} F(0)}{2 \sinh \gamma d} \tag{A-24}$$

and Eq. (A-11) becomes

$$I(x) = \frac{F(0) \sinh \gamma(x-d) - F(d) \sinh \gamma x}{\sinh \gamma d} + F(x) . \tag{A-25}$$

Case III -- The line is terminated in its characteristic impedance $(Z_1 = Z_2 = Z_0)$. Equations (A-22) reduce to

$$K_1 = -\frac{1}{2}\left[F_v(d) + F(d)\right] e^{-\gamma d}$$

$$K_2 = \frac{1}{2}\left[F_v(0) - F(0)\right] \tag{A-26}$$

and Eq. (A-11) becomes

$$I(x) = F(x) - \frac{1}{2}\left[F_v(d) + F(d)\right] e^{\gamma(x-d)} + \frac{1}{2}\left[F_v(0) - F(0)\right] e^{-\gamma x} . \tag{A-27}$$

Case III is applicable to buried bare conductors except within about a skin depth of the ends.

Case IV -- The line is terminated in an impedance $1/Y$. Equations (A-22) then become

$$K_1 = \frac{e^{-\gamma d}(1-\gamma)\left[\gamma F_v(0) - F(0)\right] + (1+\gamma)\left[\gamma F_v(d) + F(d)\right]}{(1-\gamma)^2 e^{-\gamma d} - (1+\gamma)^2 e^{\gamma d}}$$

$$K_2 = \frac{-e^{\gamma d}(1+\gamma)\left[\gamma F_v(0) - F(0)\right] - (1-\gamma)\left[\gamma F_v(d) + F(d)\right]}{(1-\gamma)^2 e^{-\gamma d} - (1+\gamma)^2 e^{\gamma d}} . \tag{A-28}$$

Case IV is applicable to the buried bare conductor to within a few meters of the ends.

When $(\gamma \pm jk)(x+a)$ is large so that the approximation of Eq. (A-13) applies and when γd is so large that the denominator of Eqs. (A-28) can be replaced by $-(1+\gamma)^2 \exp(\gamma d)$, Eqs. (A-28) approach

$$K_1 = \frac{\gamma F_v(d) + F(d)}{(1+\gamma) e^{\gamma d}}$$

$$K_2 = \frac{\gamma F_v(o) - F(o)}{1+\gamma} + \frac{1-\gamma}{(1+\gamma)^2} \frac{\gamma F_v(d) + F(d)}{e^{\gamma d}} . \tag{A-29}$$

Substituting Eq. (A-13) in Eqs. (A-10) and (A-18),

$$\gamma F_v(d) \pm F(d) = -\frac{A}{2}\left\{e^{\gamma(d+a)} B(\gamma)(\gamma \pm 1) - e^{-\gamma(d+a)} B(-\gamma)(\gamma \mp 1) - \frac{e^{-jk(d+a)}}{d+a}\left[\frac{\gamma \pm 1}{jk+\gamma} S(\gamma, d) - \frac{\gamma \mp 1}{jk-\gamma} S(-\gamma, d) - 1\right]\right\} \tag{A-30}$$

and

$$F(x) = -\frac{A}{2}\left\{e^{\gamma(x+a)} B(\gamma) + e^{-\gamma(x+a)} B(-\gamma) - \frac{e^{-jk(x+a)}}{x+a}\left[\frac{S(\gamma, x)}{jk+\gamma} + \frac{S(-\gamma, x)}{jk-\gamma}\right]\right\} \tag{A-31}$$

where

$$B(\gamma) = \log \frac{1}{jk+\gamma} - 0.577\,2157 \tag{A-32}$$

and

$$S(\gamma, x) = \sum_{n=o}^{N} \frac{n!}{\left[-(jk+\gamma)(x+a)\right]^n} . \tag{A-33}$$

Using these values in Eqs. (A-29) and noting that

$$I(x) = K_1 e^{\gamma x} + K_2 e^{-\gamma x} + F(x)$$

we obtain

$$I(x) \approx \frac{A}{2}\left\{\frac{e^{-jk(x+a)}}{x+a}\left[\frac{S(\gamma,x)}{jk+\gamma} + \frac{S(-\gamma,x)}{jk-\gamma}\right]\right.$$

$$+ e^{-\gamma x}\,\frac{e^{-jka}}{a}\left[\frac{\gamma-1}{\gamma+1}\,\frac{S(\gamma,o)}{jk+\gamma} - \frac{S(-\gamma,o)}{jk-\gamma} - 1\right] \qquad \text{(A-34)}$$

$$\left. - e^{-\gamma(d-x)}\,\frac{e^{-jk(d+a)}}{d+a}\left[\frac{S(\gamma,d)}{jk+\gamma} - \frac{\gamma-1}{\gamma+1}\,\frac{S(-\gamma,d)}{jk-\gamma} - 1\right]\right\}$$

where terms involving $\exp\left[-\gamma(x+d)\right]$ and $\exp\left[-\gamma(2d+a-x)\right]$ have been neglected. Far from the ends of the wire, $\exp\left[-\gamma(d-x)\right]$ and $\exp(-\gamma x)$ are both small if the real part of the argument is large. Furthermore, when $\gamma(x+a) \gg 1$, the value of $S(\gamma,x)$ is closely approximated by the first term. Assuming also that $\gamma \gg k$,

$$I(x) \approx -\frac{A}{2}\,\frac{e^{-jk(x+a)}}{x+a}\,\frac{2jk}{\gamma^2} \qquad \text{(A-35)}$$

far from either end of the wire. This approximation is useful for computing the current induced in buried bare conductors over a few hundred meters from the transmitting antenna. If the other two terms of Eq. (A-34) are included, the current can also be computed near the ends of the wire.

APPENDIX B

EQUIPMENT SCHEMATICS

This page intentionally left blank.

APPENDIX B

EQUIPMENT SCHEMATICS

This appendix contains the schematics of all equipment described in Secs. IV and V. Figures B-1 through B-5 are for the CW transmitter. Figures B-6 through B-14 are for the CW receiving systems. Figure B-15 is the pulse transmitter. Figures B-16 through B-19 are the pulse receivers. Schematic symbols are generally self explanatory. Resistors are 1/4 watt unless indicated. Resistor values are unmarked for ohms, and marked k for 10^3 ohms, and M for 10^6 ohms. Capacitors are marked $\mu\mu$f for micro-microfarads and either μf or unmarked for microfarads. Capacitors showing polarity signs and/or voltage are electrolytic.

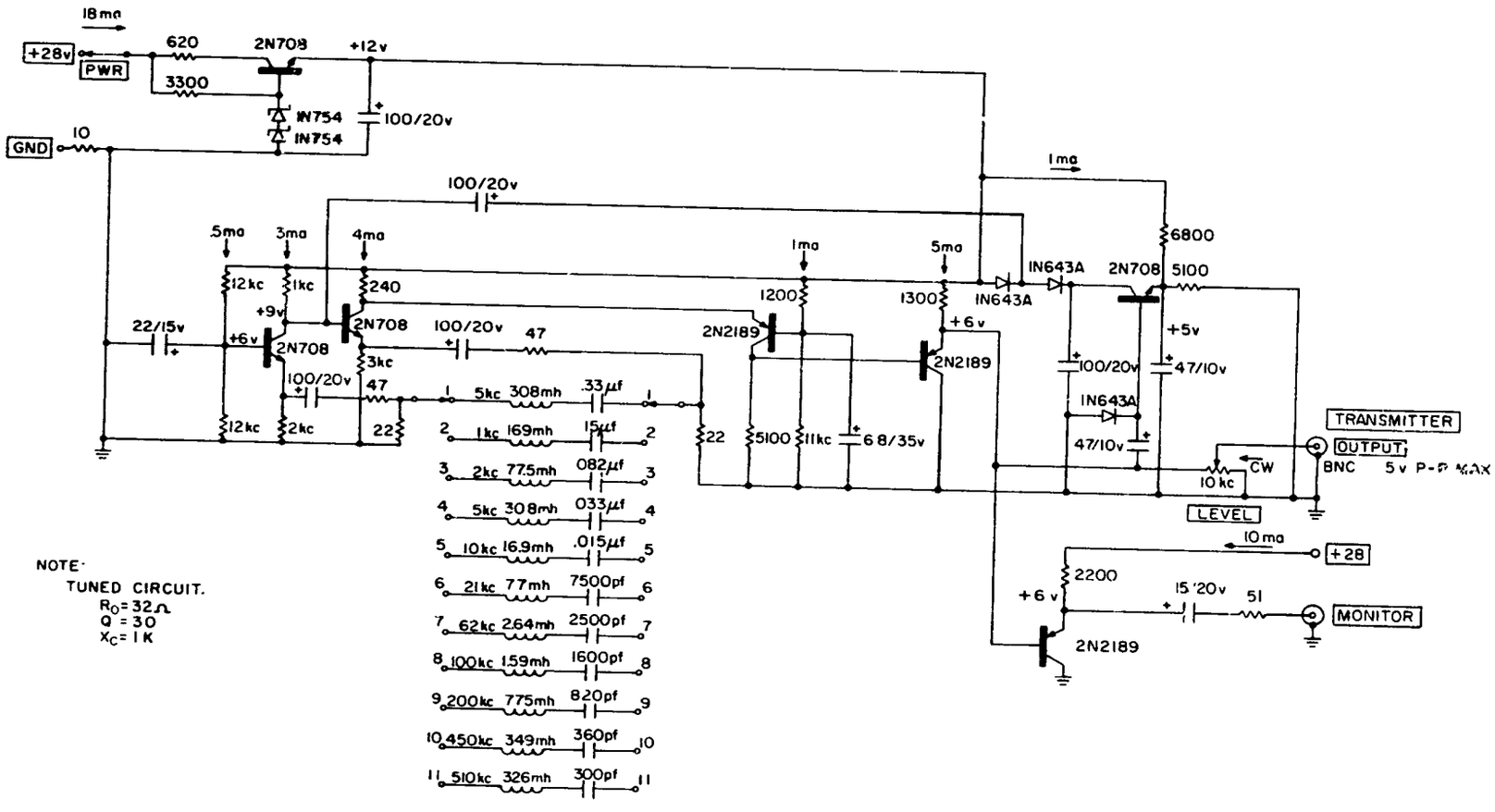

FIG. B-1 SWITCHABLE FREQUENCY OSCILLATOR SCHEMATIC

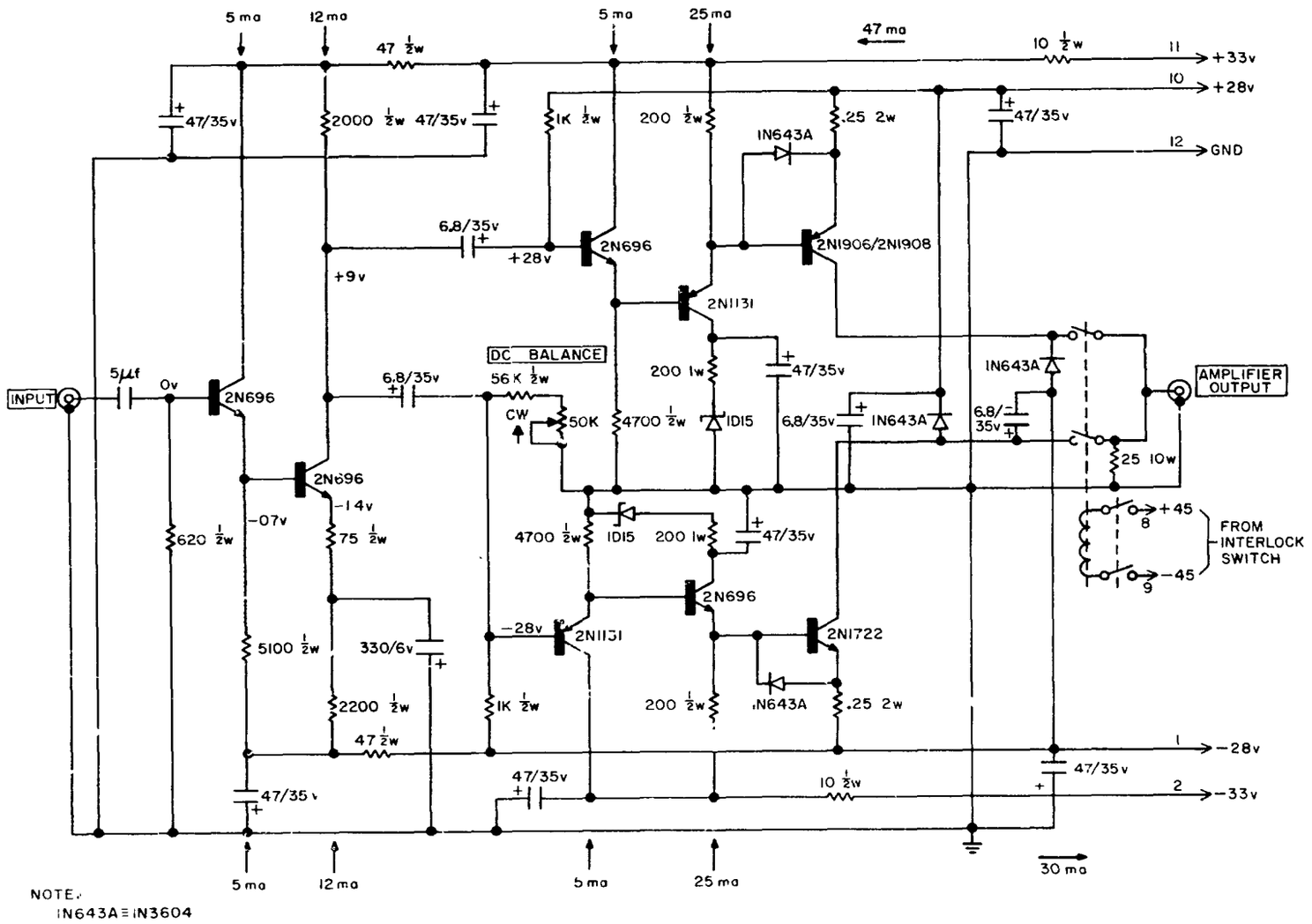

FIG. B-2 CW TRANSMITTER POWER AMPLIFIER SCHEMATIC

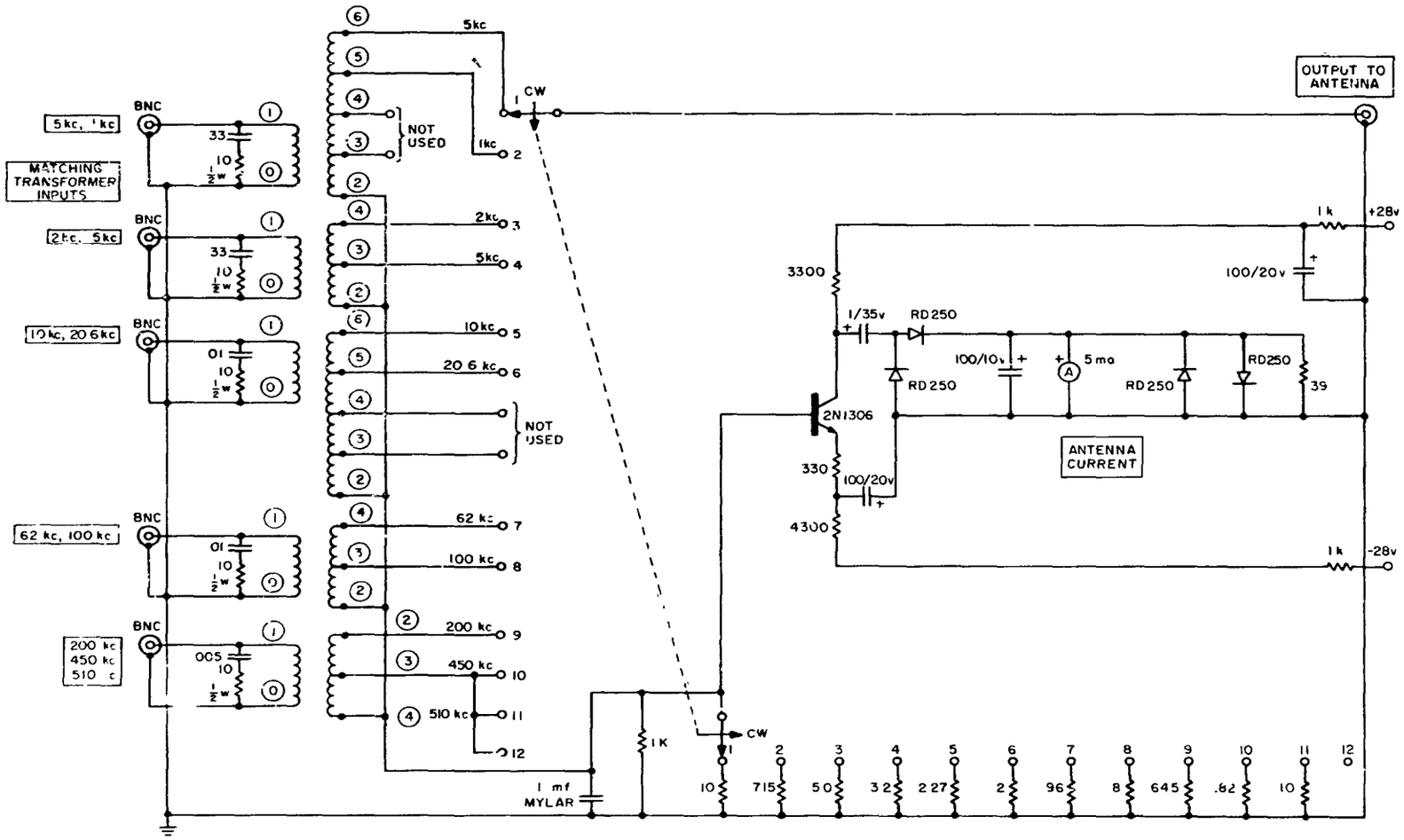

FIG. B-3 MATCHING TRANSFORMERS AND ANTENNA CURRENT MONITOR SCHEMATIC

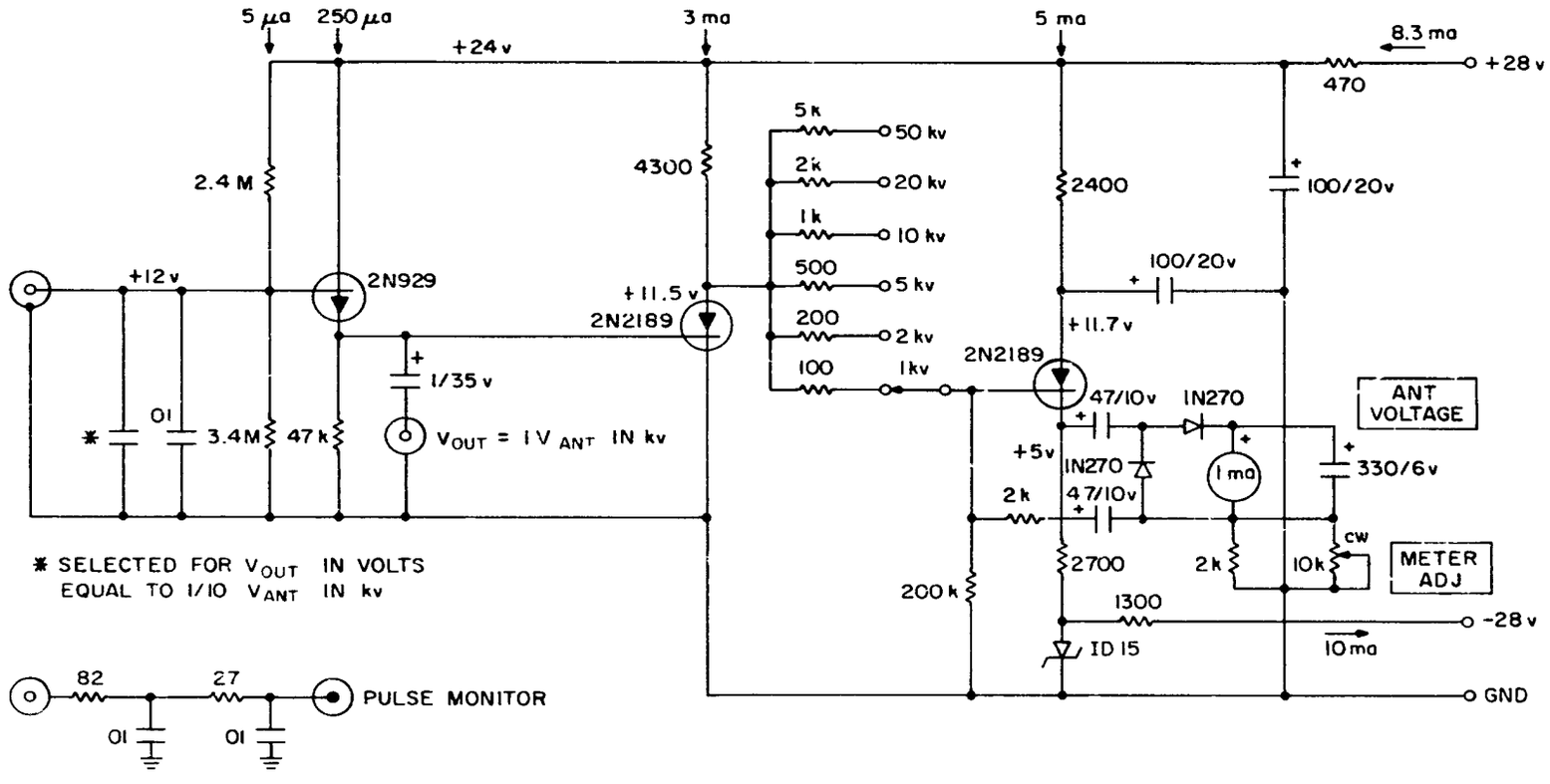

FIG. B-4 ANTENNA VOLTAGE MONITOR SCHEMATIC

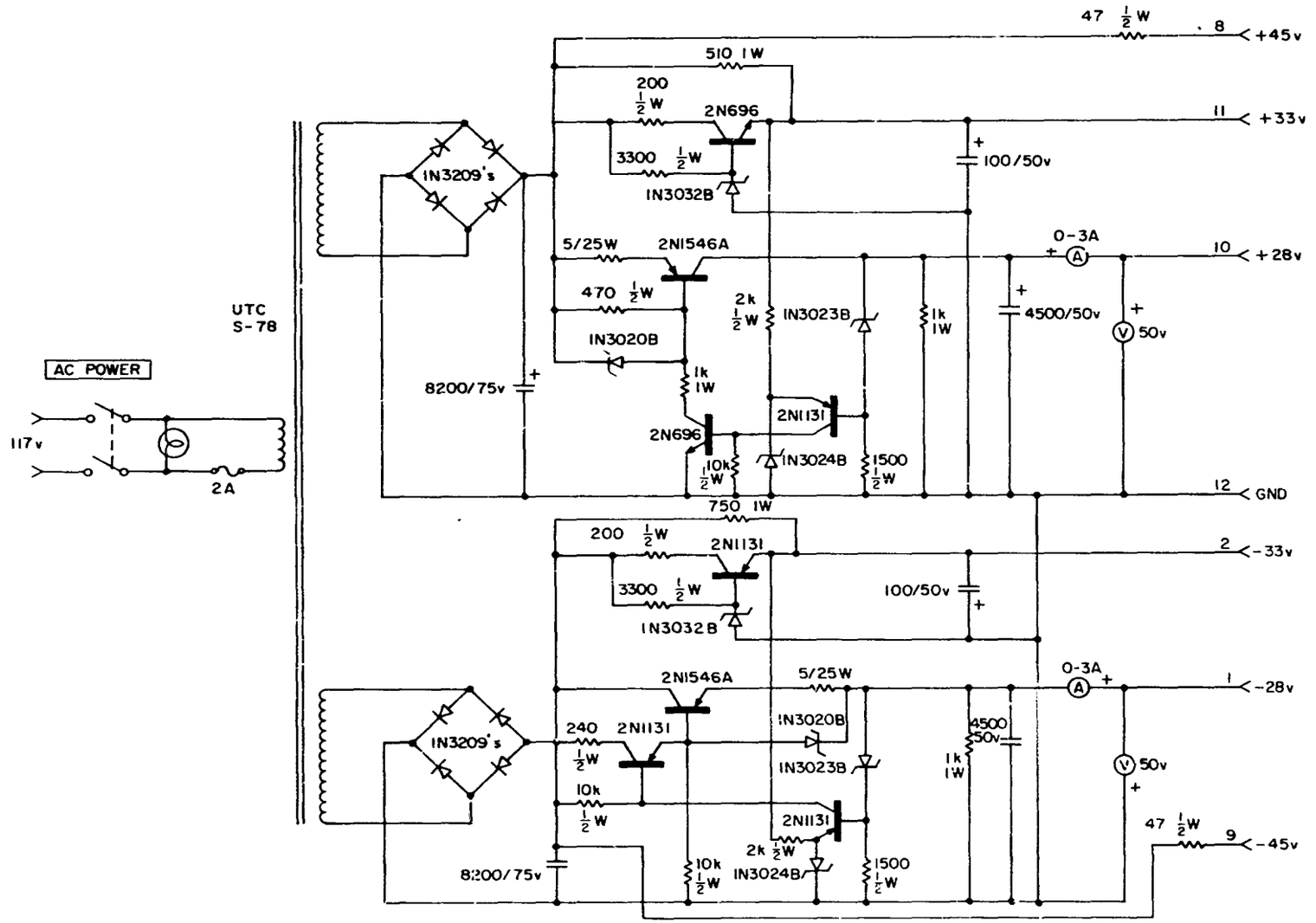

FIG. B-5 CW TRANSMITTER POWER SUPPLY SCHEMATIC

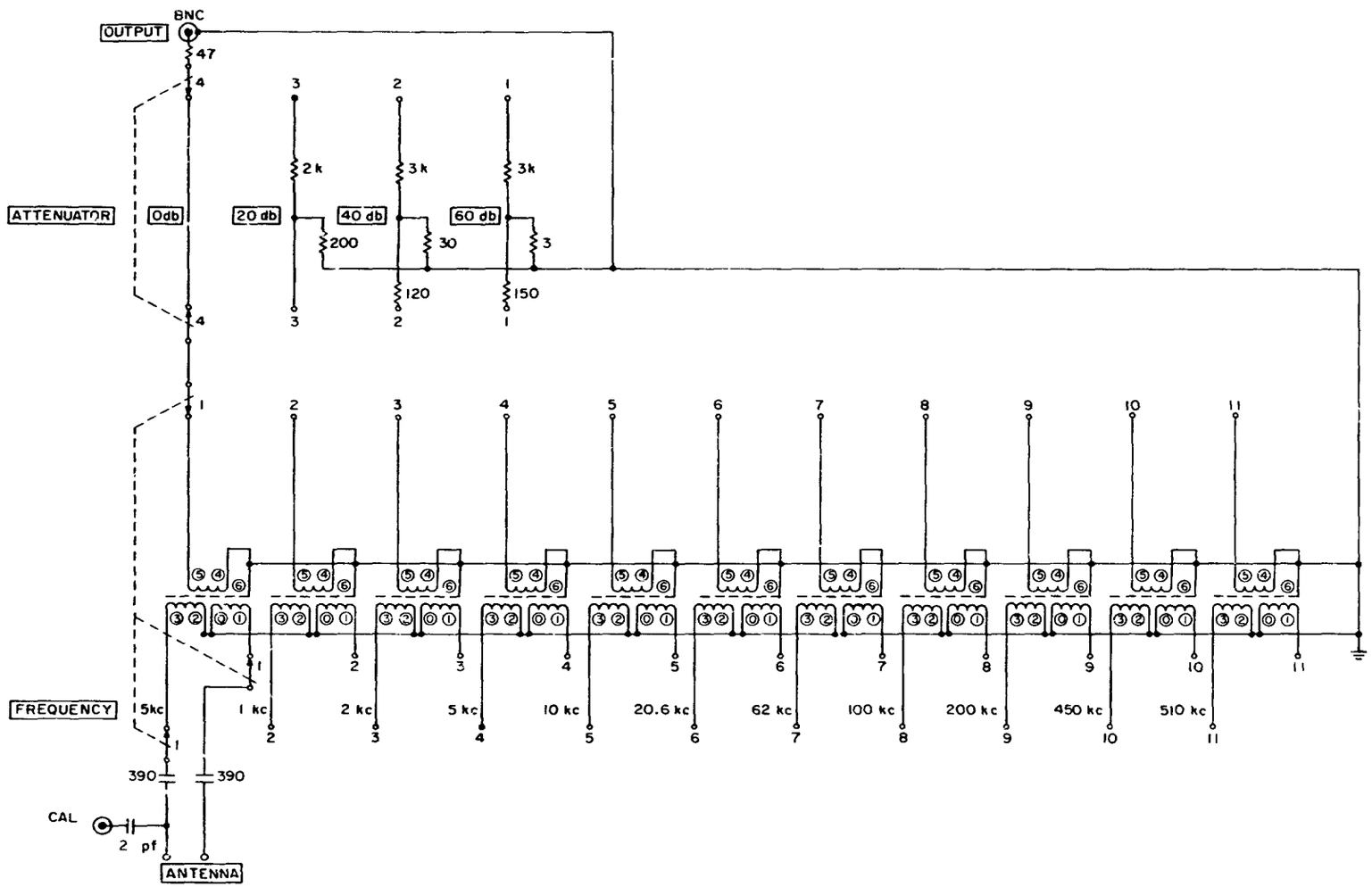

FIG. B-6 PLATE MATCHING NETWORK SCHEMATIC

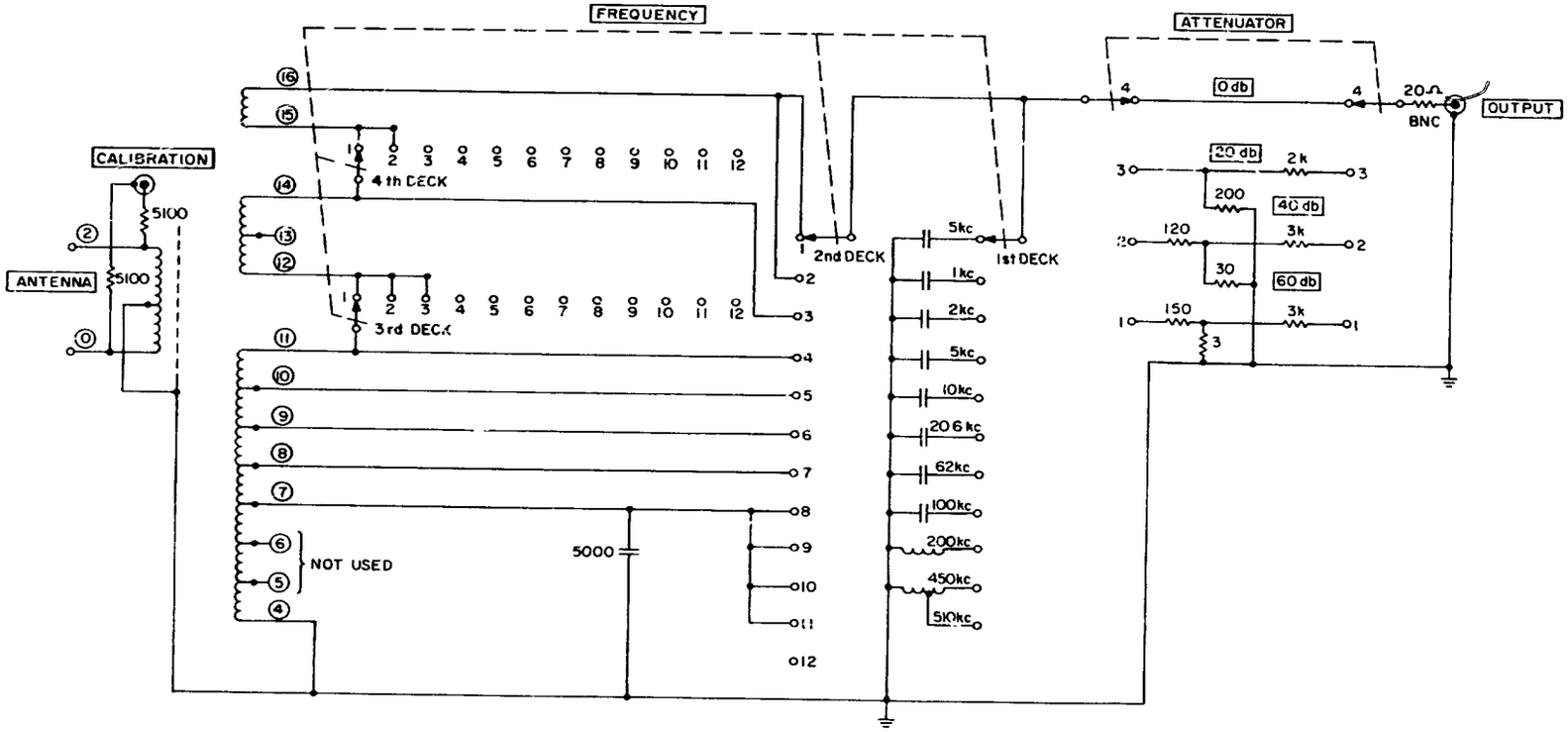

FIG. B-7 LOOP MATCHING NETWORK SCHEMATIC

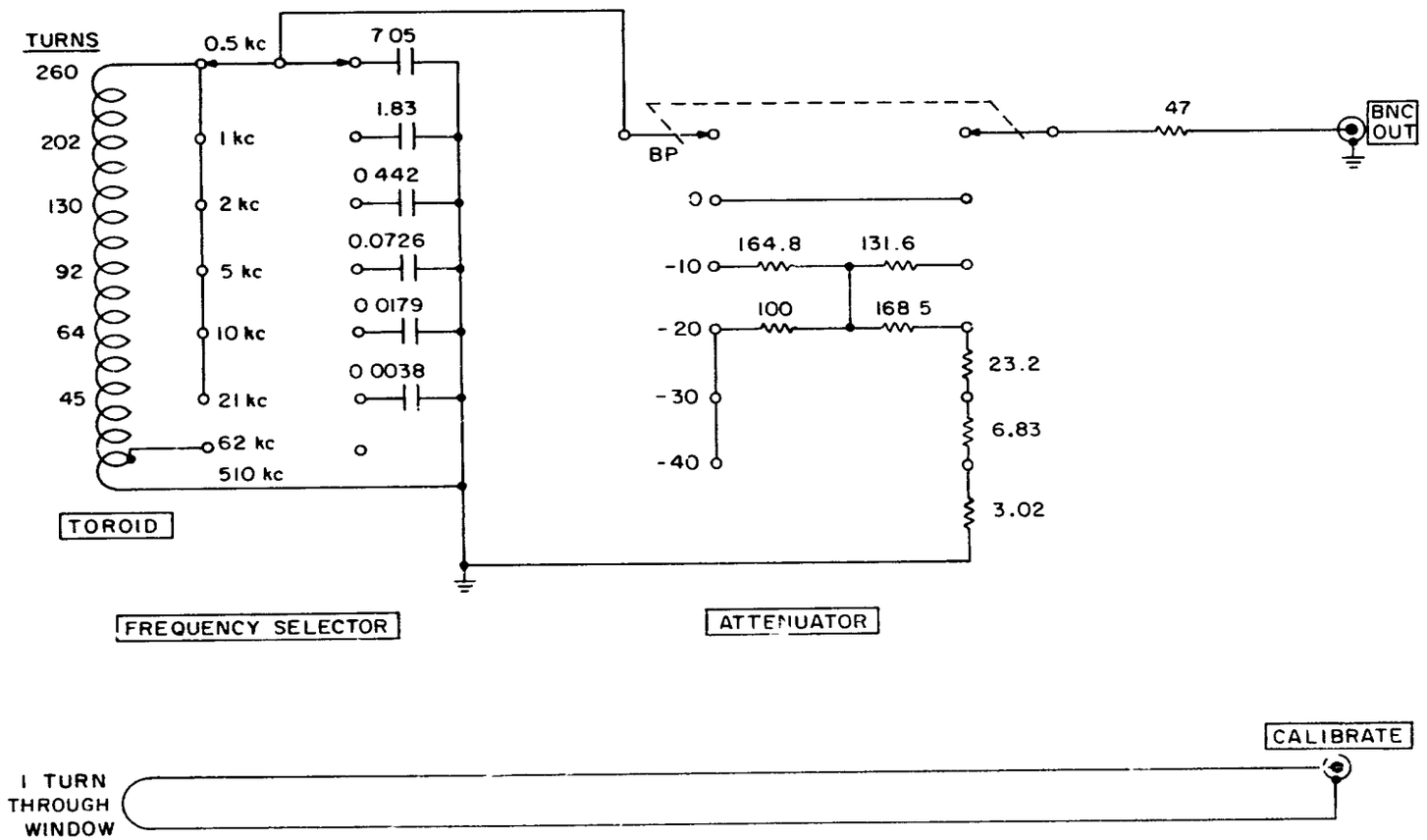

FIG. B-8 MO-PERMALLOY CURRENT SENSOR SCHEMATIC

THIS
PAGE
IS
MISSING
IN
ORIGINAL
DOCUMENT

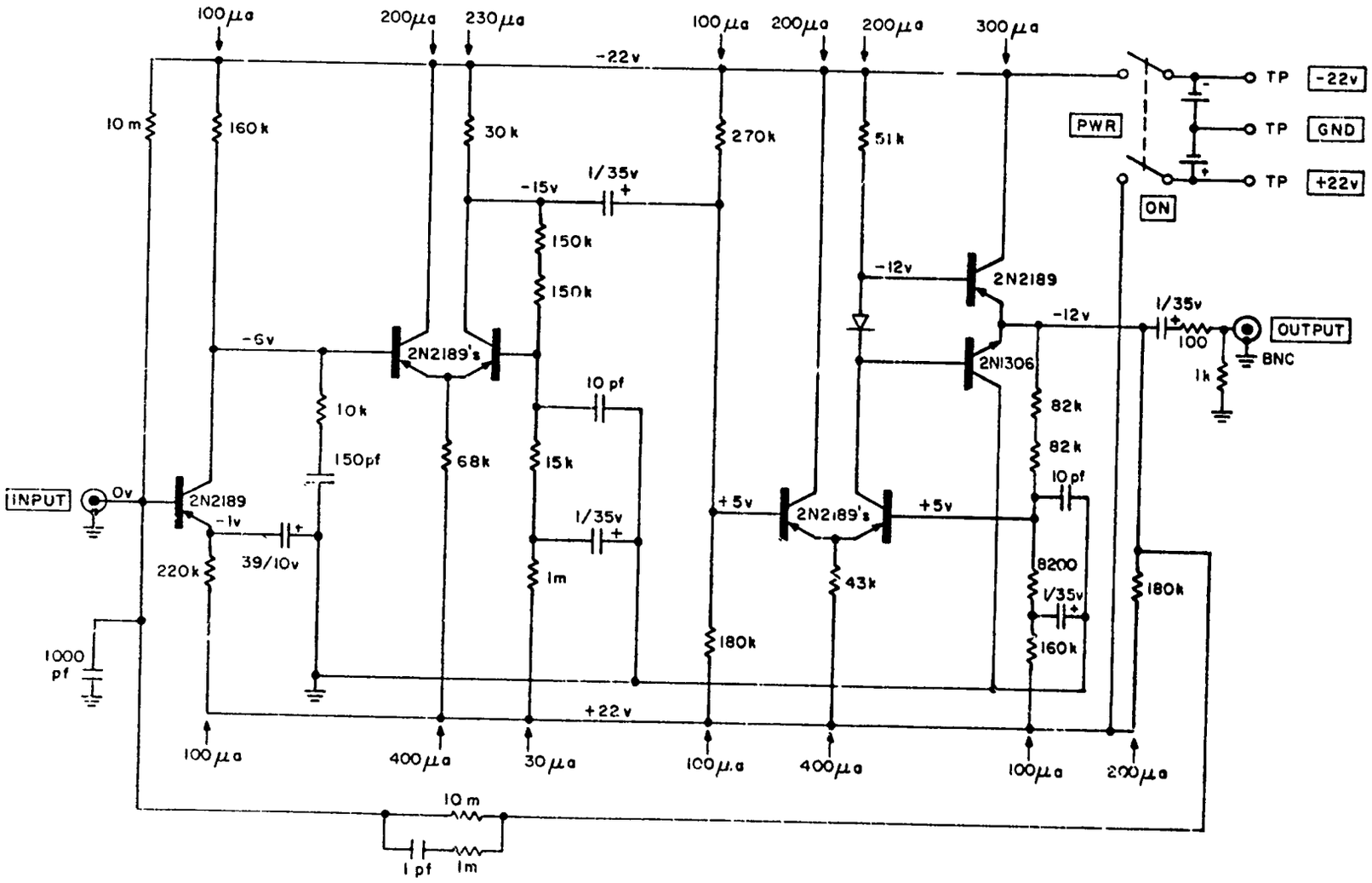

FIG. B-10 WIDE-BAND PREAMPLIFIER SCHEMATIC

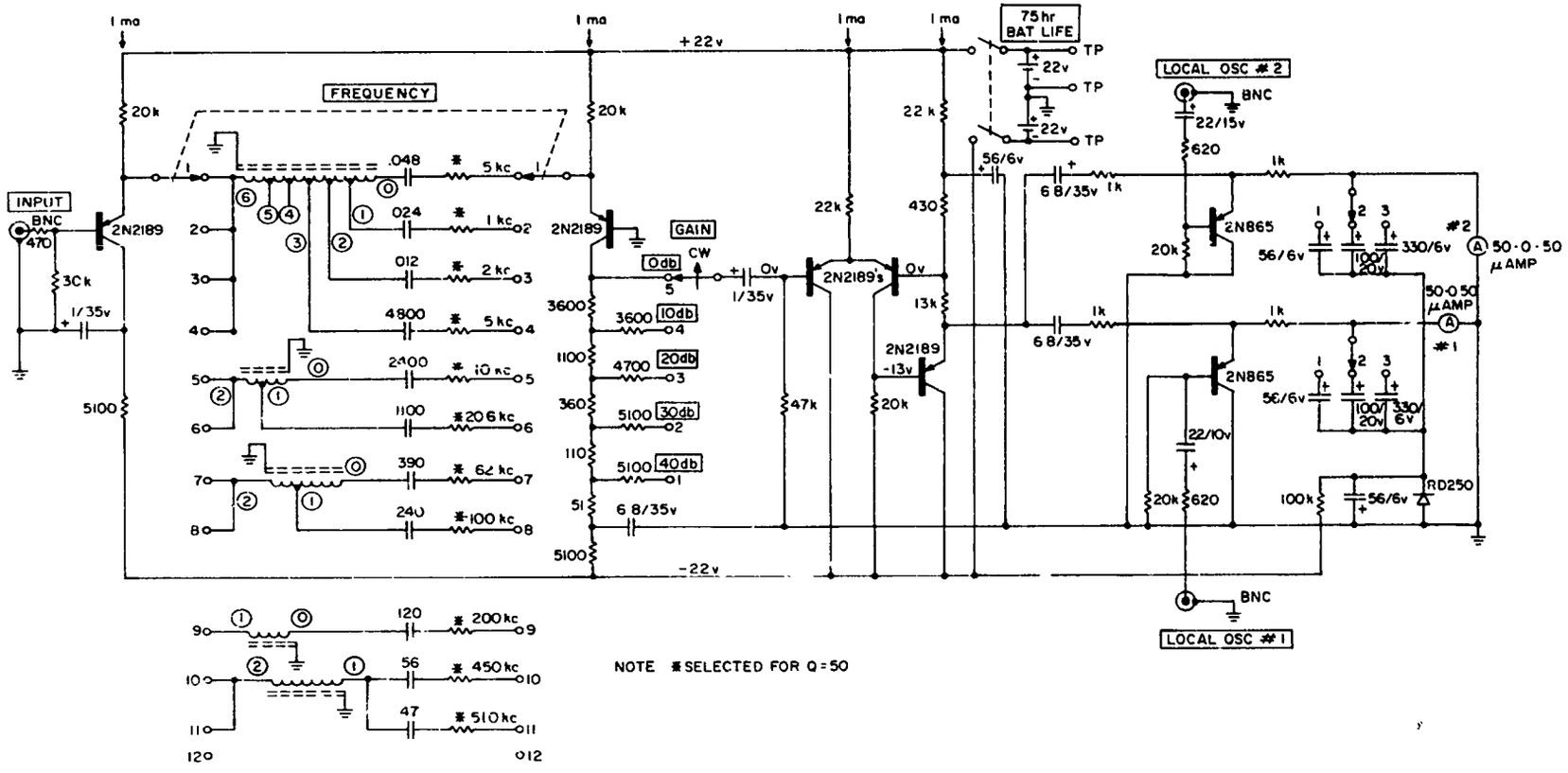

FIG. B-11 SWITCHABLE FREQUENCY RECEIVER SCHEMATIC

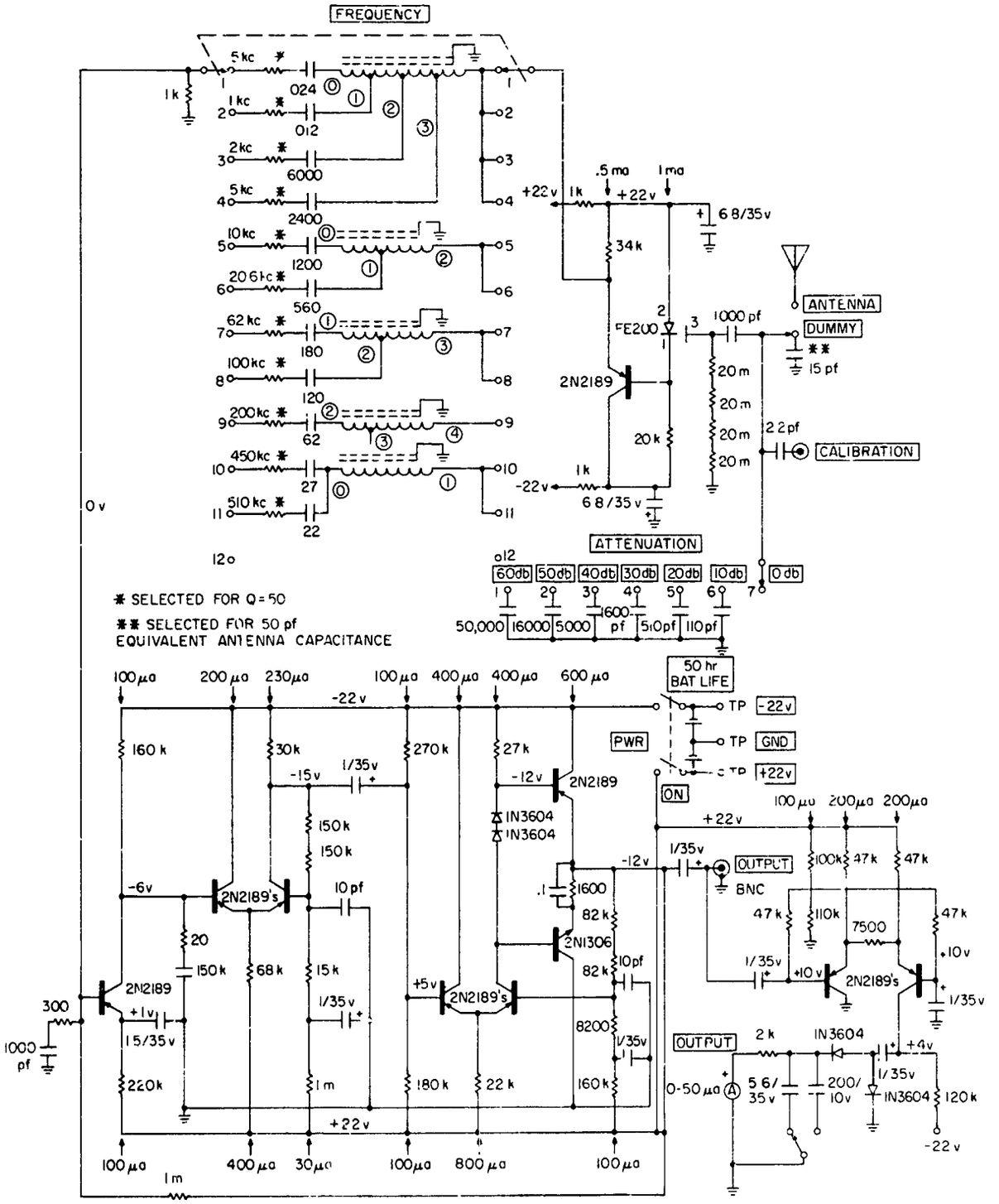

FIG. B-12 PHASE REFERENCE RECEIVER SCHEMATIC

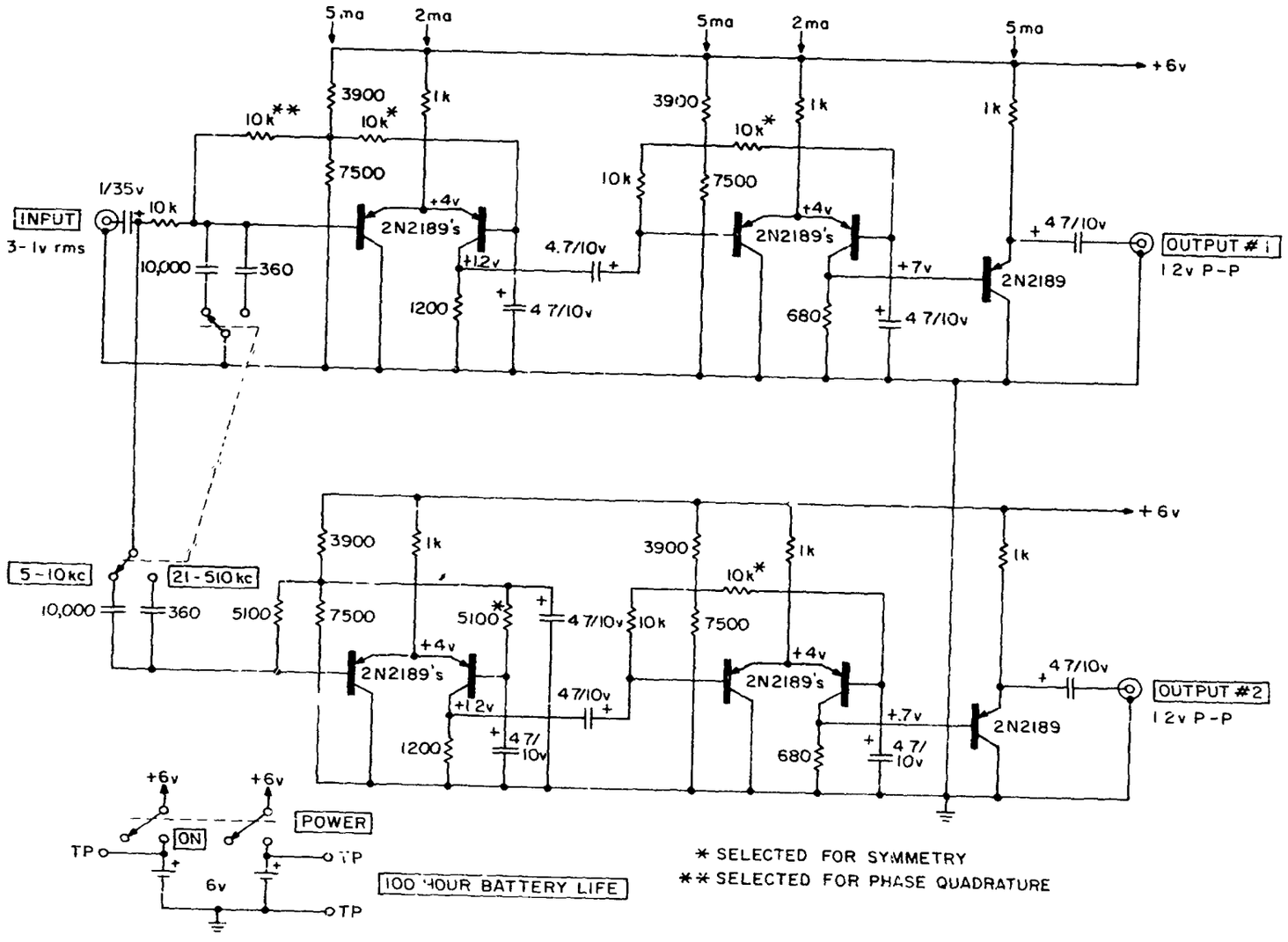

FIG B-13 QUADRATURE SIGNAL GENERATOR SCHEMATIC

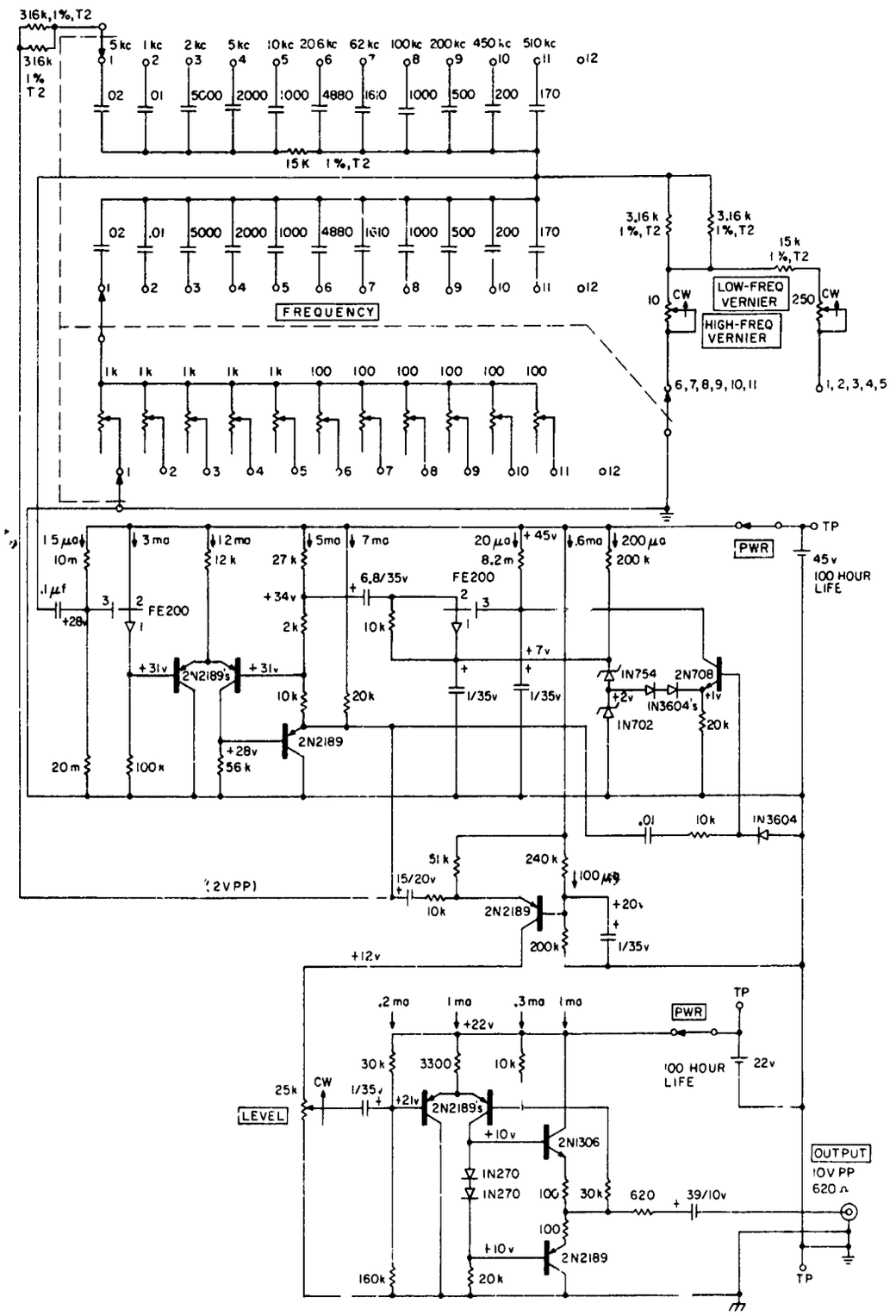

FIG. B-14 CALIBRATION OSCILLATOR SCHEMATIC

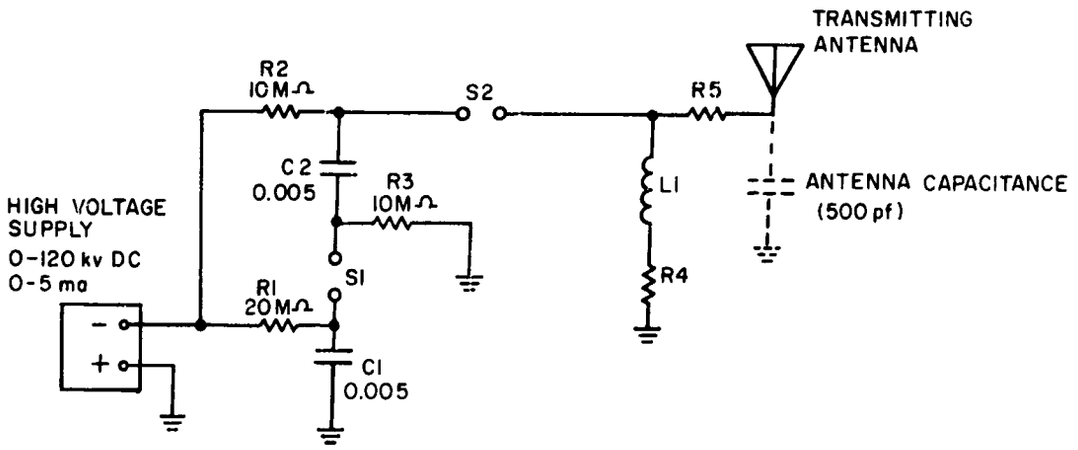

NOTE:

C1, C2	FOUR OF 600-502N 60 kv 0.005 mf CAPACITORS COMBINED TO GIVE 0.005 mf AT 120 kv (PLASTIC CAPACITORS, INC.)
R1, R2, R3	DZZ-1 125 kv (RESISTANCE PRODUCTS CO.)
R4	3.5 kΩ 200 kv WIRE WOUND (SR1)
R5	500Ω CARBON FILM (SR1)
L1	36 mh 200 kv OIL FILLED (SR1)
S1	SPARK GAP BETWEEN 4.5" DIAMETER SPHERES (SET TO 1.5")
S2	SPARK GAP BETWEEN 4.5" DIAMETER SPHERES (SET TO 2.5")

FIG. B-15 PULSE TRANSMITTER SCHEMATIC

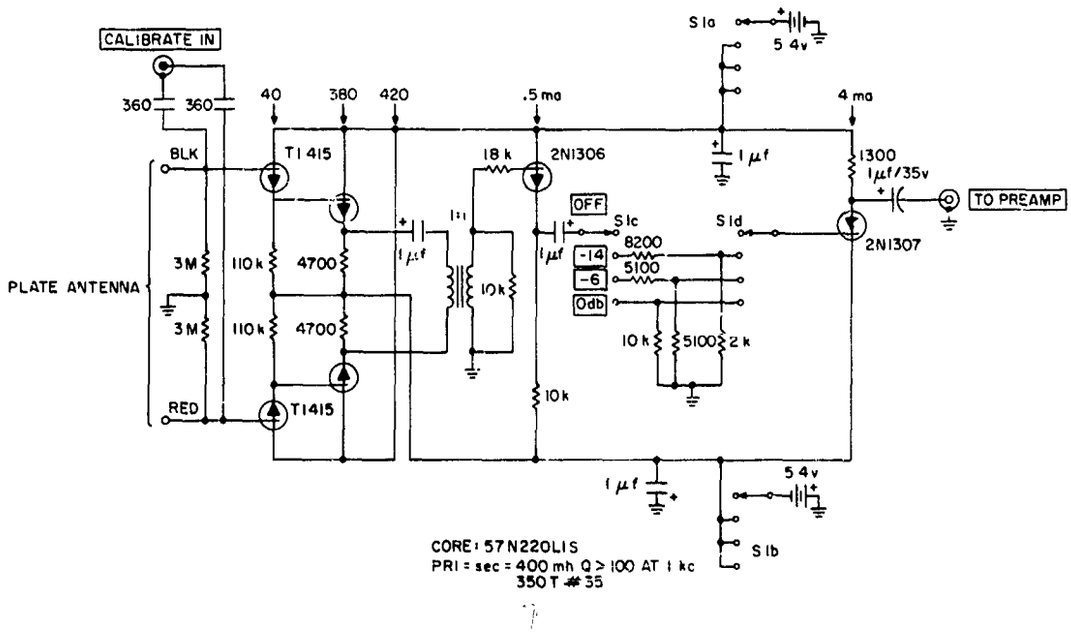

FIG. B-16 PLATE MATCHING UNIT (Pulse) SCHEMATIC

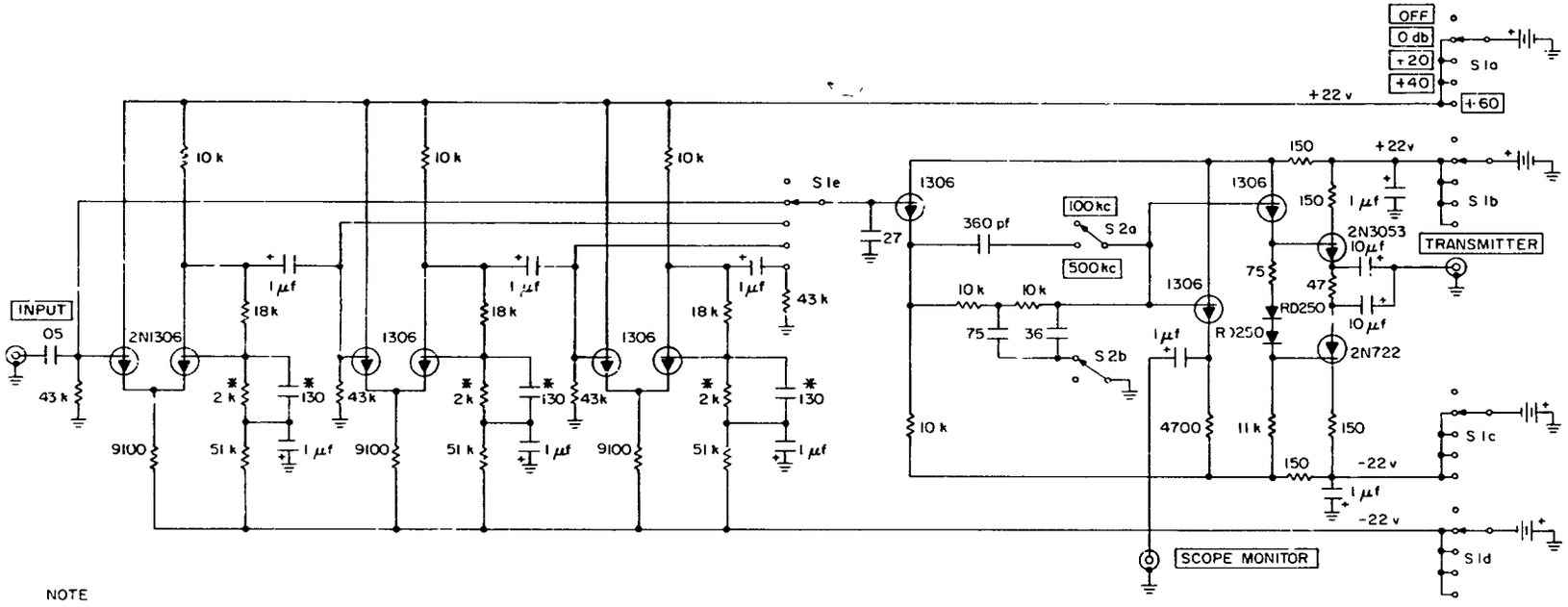

FIG. B-17 PLATE AMPLIFIER (Pulse) SCHEMATIC

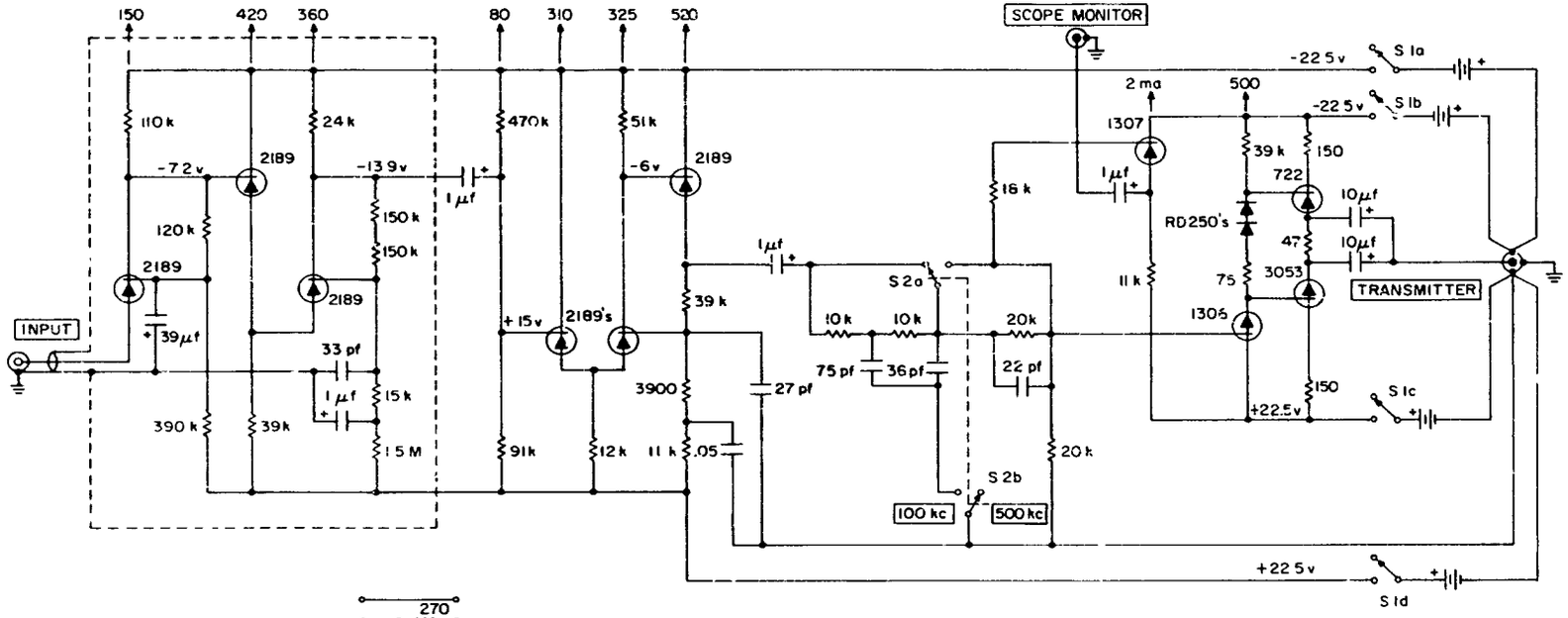

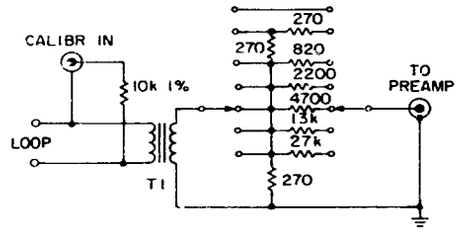

LOOP MATCHING TRANSFORMER AND ATTENUATOR

POSITIONS		
	0 db	-26 db
	-6 db	-34 db
	-14 db	-40 db
	-20 db	

LOOP MATCHING TRANSFORMER T1

CORE 61N280LIS
$A_L \simeq 6300$

PRIMARY 24 μh
2T #14 FLAT (3 WINDINGS IN PARALLEL)

SECONDARY: 320 mh
225 T #30 Q=93 AT 1 kc

NOTE OUTPUT LIMITED BY SECOND STAGE AT 500 kc
KEEP OUTPUT BELOW 3.0 v p-p

LOOP ANTENNA PREAMP 3-500 kc

FIG. B-18 LOOP RECEIVER (Pulse) SCHEMATIC

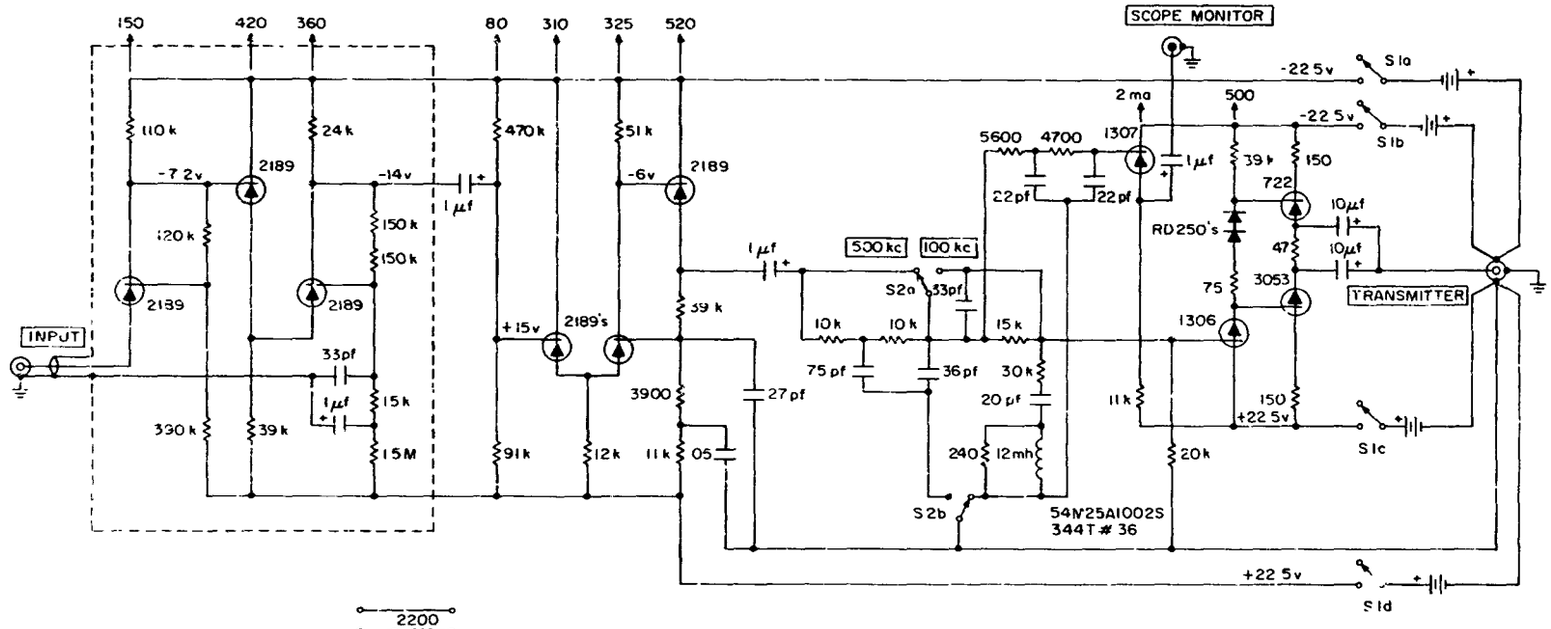

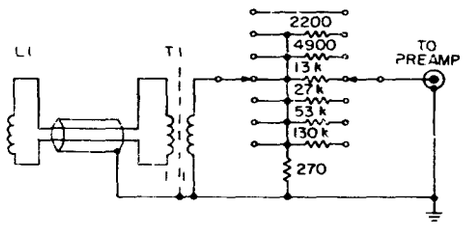

PICKUP, MATCHING TRANSFORMER AND ATTENUATOR

POSITIONS		
	0 db	-40 db
	-20 db	-46 db
	-26 db	-54 db
	-34 db	

L1 - 160T #30 INSULATED ON C-CORE
88 mh Q = 55 AT 1 kc (BEFORE SHIELDING)

T1 - 57N220L3S A_L = 3200
PRIMARY : 230T # 32
SPLIT ON OUTER SECTIONS
160 mh
SECONDARY 230T # 36
ALL ON CENTER SECTION
SHIELDED

NOTE KEEP OUTPUT LEVEL BELOW 3.0 v p-p

FIG. B-19 CURRENT RECEIVER (Pulse) SCHEMATIC

APPENDIX C

TABULATED CW DATA

This page intentionally left blank.

APPENDIX C

TABULATED CW DATA

The tables in this Appendix contain the CW wire current data presented in the body of this report. Magnitude is tabulated in decibels relative to 1.0 microampere normalized to 1.0 kilovolt applied to the transmitting antenna. The phase is tabulated in degrees, and in all cases the phase is measured with respect to the local vertical electric field (E_θ). Distance from transmitter (r) is in feet, and frequency is in kc. For convenience in relating the tabulated data to the data plotted in the figures in the body of the report, the figure in which the data is plotted is indicated in each table. The format of the various tables is selected to be compatible with the form of presentation used in each figure.

Table C-1

INDUCED CURRENT IN 10-GAUGE INSULATED WIRE*

Frequency (kc)	2		10		62		200		510	
Distance From Transmitter (r)	Magnitude (db)	Phase (deg)	Magnitude (db)	Phase (deg)	Magnitude (db)	Phase (deg)	Magnitude (db)	Phase (deg)	Magnitude (db)	Phase (deg)
300	-68.03		-17.87		11.68		23.86		37.28	
400					14.18	-43	40.15	-37	58.79	-160
500	-36.35	87	-13.28	59	17.37	-46	44.04	-59	59.81	174
600					21.25	-70	45.64	-90	61.11	157
700					24.15	-80	47.23	-128	61.13	127
750	-33.89	88	-7.68	56						
800					28.04	-91	47.75	-153	61.03	112
900					29.75	-97	48.93	-176	64.52	77
1000	-33.29	84	-5.81	57	31.65	-105	49.12	170	63.27	65
1100					33.35	-111	49.87	159	60.35	71
1200					34.50	-115	51.01	154	60.16	65
1300					34.91	-120	50.83	149	57.57	40
1400					36.01	-134	50.46	152	55.17	23
1500	-33.45	83	-4.56	54	36.68	-138	50.38	148	55.27	16
1600					37.10	-140	49.91	144	53.14	-4
1700					37.62	-157	49.41	142	50.97	-26
1800					38.99	-150	47.71	141	46.79	-85
1900					39.77	-156	47.20	123	49.10	-126
2000	-34.79	79	-5.11	51	39.73	-157	46.54	109	50.74	-168
2100					39.57	-156	47.07	99	50.96	-177
2200					40.92	-150	48.48	88	51.85	159
2300					39.97	-150	47.79	78	52.76	123
2400					39.19	-150	48.21	71	54.39	114
2500	-36.69	80	-7.25	49	39.09	-146	48.11	66	54.32	115
2600					39.67	-141	47.31	69	54.51	104
2700					39.85	-138	45.77	65	52.18	88
2800					39.35	-130	43.47	65	52.18	69
2900					38.72	-126	39.11	73	52.63	62
3000	-39.69	75	-9.78	48	39.18	-125	34.96	25	52.50	57
3100					37.59	-123	37.26	-23	49.92	70
3200					37.08	-119	41.25	135	43.72	64
3300					36.27	-118	42.99	-55	39.67	-18
3400					35.63	-117	44.32	-55	42.98	-18
3500	-44.57	75	-14.53	46	34.94	-115	46.16	-58	45.27	16
3600					32.57	-110	45.20	-62	42.68	85
3700					30.06	-107	43.49	-64	45.74	151
3800					25.72	-108	39.90	-54	47.68	-169
3900					18.55	-109	33.41	-51	44.14	-142
4000	-91.28		-66.98		-8.63		-9.86		11.59	

*Data on this table are plotted on Figs. 21 and 22.

Table C-2

INDUCED CURRENT AT 62 KC IN
RESONANT-LENGTH 10-GAUGE INSULATED WIRE*

Distance From Transmitter (r) \ Length of Wire (ft)	3250		2500	
	Magnitude (db)	Phase (deg)	Magnitude (db)	Phase (deg)
300	-6.38		-9.55	
500	32.84	-49	32.84	24
750	40.29	-64		
1000	44.03	-70	39.97	17
1300			41.33	10
1500	46.95	-89	42.49	1
1700	47.89	-101	41.13	-7
1900	47.97	-104		
2000			39.39	-32
2100	48.05	-108		
2300	47.07	-98		
2500			32.29	-67
2800	43.83	-98	-22.80	
3200	38.94	-112		
3400	32.38	-111		
3550	-25.22			

*Ref. Fig. 24.

Table C-3

INDUCED CURRENT IN 100-FOOT-DIAMETER LOOP*

Frequency (kc) \ Measurement Location†	West		East		South		North	
	Magnitude (db)	Phase (deg)	Magnitude (db)	Phase (deg)	Magnitude (db)	Phase (deg)	Magnitude (db)	Phase (deg)
2	-20.10	-116	-21.63	13	-21.15	-117	-20.92	-117
10	-15.51	-164	-16.46	0	-15.44	-170	-16.09	-172
62	-15.44	84	-5.82	14	-12.43	169	-10.93	150
200	30.42	-51	26.13	11	11.95	-87	12.39	-126
510	49.91	148	42.87	-2	22.31	41	27.19	31

*Ref. Fig. 28.

†See Fig. 2.

Table C-4

INDUCED CURRENT IN BARE 10-GAUGE COPPER WIRE (CABLE Z)*

Distance From Transmitter r (ft) / Frequency (kc)	725		1000		1750		2380		3000	
	Magnitude (db)	Phase (deg)	Magnitude (db)	Phase (deg)	Magnitude (db)	Phase (deg)	Magnitude (db)	Phase (deg)	Magnitude (db)	Phase (deg)
0.5	-42.57	153	-20.19	155	-33.16	160	-46.17	180		
	-42.08	154	-28.07	152			-44.92	169		
1	-30.60	149	-17.27	157						
2	-19.82	143	-6.68	139	-11.00	134	-22.68	157		
5					6.36	149	-7.14	142		
10			19.59	129	10.93	133			-45.74	85
			19.48	128	11.08	141				
20.6	12.20	121							-37.12	70
	13.05	123								
	13.66	115								
62	22.25	108	25.91	58	18.56	42	13.98	26	-21.29	45
	22.03	112	26.70	56	19.24	43	14.70	28		
			25.73	55	20.21	47	16.04	25		
100	27.38	96	29.94	39	22.42	2	18.69	-28	-13.07	34
	29.33	98	31.08	40	23.21	4	19.73	-22		
	29.36	90								
200	38.53	59	38.09	9	32.24	-28	29.38	-45	-0.51	38
	37.24	57					29.71	-39	2.70	20
	37.41	60								
450	51.09	28	45.74	-46	43.19	-46	41.64	-43	21.18	27
510	53.76	28	48.44	-39	45.57	-45	43.80	-45	23.93	24

*Data in this table are plotted on Figs. 29 and 30.

Table C-5

INDUCED CURRENT IN INSULATED CABLE N*

Frequency (kc) \ Distance From Transmitter r (ft)	550		1050		1550		2050		2550		3050	
	Magnitude (db)	Phase (deg)	Magnitude (db)	Phase (deg)	Magnitude (db)	Phase (deg)	Magnitude (db)	Phase (deg)	Magnitude (db)	Phase (deg)	Magnitude (db)	Phase (deg)
0.5	-70.31	198	-64.24	211	-57.85	218	-58.58	207	-61.87	227	-71.62	215
1					-38.64	210						
2			-27.16	184			-27.23	206	-27.82	208	-40.00	212
5	-11.66	214	-6.00	215	-4.91	214	-6.38	218	-6.85	215	-19.12	215
10	3.46	212	10.86	210	12.63	209	12.05	210	9.01	208	-0.50	204
			11.73	213					8.31	208		
62	36.22	164	38.47	61	37.30	162	36.59	19	29.59	13	33.93	39
	38.31	161										
	38.79	160	39.42	64	37.52	160	37.21	3	30.65	11	33.16	47
			40.14	72	37.33	162			31.82	2		
			40.63	58								
100	43.96	120	41.84	-28	40.52	76	38.42	-81	37.04	53	35.76	-89
	42.92	118	42.18	-28	42.51	68	40.67	-73	36.86	50	37.28	-85
	45.50	115	43.69	-19	42.45	68			37.06	44		
200	53.98	62	47.98	22	41.39	19	31.14	33	28.68	-33	33.15	-36
	53.94	63	47.51	20	40.28	16	32.89	31	30.33	-24	33.97	-58
			46.77	21	41.06	20	32.54	26	30.44	-23	34.20	-28
450	60.43	-46	53.02	-45	48.24	-45	41.82	-44	42.07	-24	38.15	-34
	61.06	-43			47.56	-44			43.99	-43	38.84	-27
510	61.72	-62	52.86	-45	48.91	-51	44.25	-46	44.03	-55	43.80	-39
			51.59	-41	48.93	-47	43.76	-44	44.59	-46	43.09	-31
			51.66	-56								

*Data in this table are plotted on Figs. 35 and 36.

Table C-6

INDUCED CURRENT IN CONDUCTING SHEATH CABLE L*

Frequency (kc) \ Distance From Transmitter r (ft)	550		1050		1550		2050		2550		3050	
	Magnitude (db)	Phase (deg)	Magnitude (db)	Phase (deg)	Magnitude (db)	Phase (deg)	Magnitude (db)	Phase (deg)	Magnitude (db)	Phase (deg)	Magnitude (db)	Phase (deg)
0.5					-0.47	56	-7.85	36	-13.24	51	-15.57	59
1											-11.47	58
2			15.77	43	3.41	45	-1.13	39	-4.66	44	-6.93	53
5	27.34	78	16.90	41								
10	31.78 31.48	62 61	18.22 17.45	42 49	8.69	45	3.97	44	1.52	43	-1.95	47
20.6			21.10	52	12.89	48			3.19	37	2.93	44
62	39.53	55	27.42 29.53	46 47	19.42 20.41	40 41	14.35 16.54	41 47	9.62 8.87	27 23	12.96	31
100	42.48	50	30.20 32.93	25 28	22.74 24.59	3 3	20.08 22.48	-14 -5	15.58 17.35	-25 -25	17.57	-31
200	50.03 49.74	25 34	36.91 39.14	-36 -21	31.25 32.62	-47 -32	29.08 31.14	-40 -28	25.69 27.63	-40 -29	27.21 28.70	-44 -33
450	57.96	-22	48.55	-49	42.53	-40	42.21	-36	40.79	-38	40.98 40.74	-46 -40
510	59.30	-26	49.93	-51	45.56	-42	43.61	-37	42.79	-38	43.16 42.80	-40 -47

*Data in this table are plotted on Figs. 40 and 41.

Table C-7

INDUCED CURRENT IN LEAD SHEATH CABLE A*

Distance From Transmitter r (ft) / Frequency (kc)	500		1000		1500		2000		4000	
	Magnitude (db)	Phase (deg)	Magnitude (db)	Phase (deg)	Magnitude (db)	Phase (deg)	Magnitude (db)	Phase (deg)	Magnitude (db)	Phase (deg)
0.5			9.70	46	-3.41	20	-11.23	54		
							-8.75	39		
1	18.93	56								
2	22.39	44	14.53	52			-1.87	41	-9.07	45
5					5.71	38			-4.81	53
10			18.66	48	8.27	48	3.10	39	-1.42	45
							4.61	39		
62	38.94	50	29.74	48	19.14	30	15.74	43	15.91	7
	38.88	57	31.98	49			16.53	40	14.81	16
							16.69	44		
							15.22	41		
100	41.16	49	33.09	34	44.56	0	21.22	-7		
			34.80	35			21.06	-8		
							21.42	-8		
200	45.31	8	41.69	-14			30.01	-25	32.33	-32
	45.53	18					30.37	-24		
							30.76	-24		
450	54.53	-32	49.97	-49			41.73	-37	43.89	-47
							42.82	-88		
510	56.21	-38	51.43	-53			44.78	-43	45.75	-52
							44.68	-40		

*Data in this table are plotted on Figs. 42 and 43.

Table C-8

INDUCED SHIELD CURRENT IN PIE-SHAPED LOOP*

Location / Frequency (kc)	On 340-ft arc		Bunker 523.07		Bunker 523.08		Bunker 523.09	
	Magnitude (db)	Phase (deg)	Magnitude (db)	Phase (deg)	Magnitude (db)	Phase (deg)	Magnitude (db)	Phase (deg)
0.5			-10.44	263				
2	-10.95	232	3.22	265	-18.22	268	-14.34	217
5			7.72	255				
10					-6.44	226	10.05	205
							11.36	209
62			32.90	54	12.26	93		
100	35.85	116	35.80	24	20.67	31	43.52	12
200	44.24	60	44.08	-16	25.34	-41	52.42	-14
450	55.86	-31	53.02	-243	36.40	-151		
510	56.86	-59	54.20	-245	37.90	-180		

*See Fig. 2. Data in this table are plotted on Figs. 48 and 49.

Table C-9

INDUCED CORE CURRENT IN PIE-SHAPED LOOP*

Location	Bunker 523.07				Bunker 523.08				Bunker 523.09	
Core-to-Shield Resistence	500 kilohms		50 kilohoms		500 kilohms		50 kilohms		500 kilohms	
Frequency (kc)	Magnitude (db)	Phase (deg)	Magnitude (db)	Phase (deg)	Magnitude (db)	Phase (deg)	Magnitude (db)	Phase (deg)	Magnitude (db)	Phase (deg)
0.5	-35.38	161	-17.90	237	-35.92	146	-18.59	241	-35.38	164
2			-2.48	249						
10			9.42	212			8.13	210		
100	13.62	147			9.97	114			13.62	144
200	18.69	94			19.64	85			18.69	104

*See Fig. 2. Data in this table are plotted on Figs. 50 and 51.

Table C-10

INDUCED CURRENT IN 12-GAUGE 100-FOOT-DIAMETER LOOP*

Location / Frequency (kc)	Bunker 528.02		Inner Hole		South Hole		North Hole	
	Magnitude (db)	Phase (deg)	Magnitude (db)	Phase (deg)	Magnitude (db)	Phase (deg)	Magnitude (db)	Phase (deg)
2	-24.30	194	-24.45	191	-25.36	191	-24.14	194
10	-19.14	240	-18.83	239	-19.75	240	-18.52	240
62	-7.76	34	-7.20	192				
	-7.09	10	-4.89	198				
	-7.08	22	-5.39	214				
100	0.01	-36	-1.01	143	11.44	4	8.76	232
	-1.52	-38	0.98	147			7.40	220
	0.17	-15	0.83	151				
200	7.91	-205	7.53	114	30.26	-12	29.31	167
					28.84	-12	30.30	173
450			24.78	-60	61.04	-118	61.60	88
510	26.75	-263	25.82	-168	63.93	-170	64.24	21

*See Fig. 2. Data in this table are plotted on Figs. 52 and 53.

Table C-11

INDUCED CURRENT IN GUARDED 100-FOOT-DIAMETER LOOPS*

Location / Loop Wire / Frequency (kc)	Bunker 523.05						Inner Hole			
	4/0 Gauge		12 Gauge		Both		4/0 Gauge		12 Gauge	
	Magnitude (db)	Phase (deg)	Magnitude (db)	Phase (deg)	Magnitude (db)	Phase (deg)	Magnitude (db)	Phase (deg)	Magnitude (db)	Phase (deg)
2	-20.82	186	-34.10	196	-18.64	182	21.51	172	-32.77	197
62							-3.20	192	-14.58	108
100			-11.55	-46						
	0.24	-25	-13.40	-38	1.11	-27	3.64	225	8.18	125
			-12.17	-32	-1.07	-44				
200	9.10	-90					11.35	164	4.92	13
450			17.64	-221	30.51	-201			22.97	-44
510			16.02	-203	31.13	-207			20.61	-50

Location / Loop Wire / Frequency (kc)	South Hole						North Hole			
	4/0 Gauge		12 Gauge		Both		4/0 Gauge		12 Gauge	
	Magnitude (db)	Phase (deg)	Magnitude (db)	Phase (deg)	Magnitude (db)	Phase (deg)	Magnitude (db)	Phase (deg)	Magnitude (db)	Phase (deg)
0.5					-22.21	140				
2					-19.65	184	-20.98	179		
5			-33.06	293						
10			-31.06	276	-13.92	270			-31.77	277
20.6			-24.95	282			-10.93	266		
62										
100			27.55	8	17.78	28	15.89	234	7.87	224
									8.10	208
200	32.60	-12	28.72	-22	35.77	-16	36.16	161	28.00	156
					39.04	-13			26.84	162
450			51.28	-182	60.80	-192			51.75	-5
510			51.52	-204	61.13	-204			51.95	-18

*See Fig 2. Data in this table are plotted on Figs. 54 through 59.

Table C-12

INDUCED CURRENT IN ARC OF ALUMINUM SHEATH CABLE*

Distance From Transmitter r (ft)	500						2000					
Location	South Hole		Middle Hole		North Hole		South Hole		Middle Hole		North Hole	
Frequency (kc)	Magnitude (db)	Phase (deg)	Magnitude (db)	Phase (deg)	Magnitude (db)	Phase (deg)	Magnitude (db)	Phase (deg)	Magnitude (db)	Phase (deg)	Magnitude (db)	Phase (deg)
10	35.53	151	-34.45	161	-33.64	160						
62	-1.01	181	2.62	191			-14.05	84	-15.70	94	-14.51	4
							-14.12	83	-13.26	92	-16.01	-14
									-16.54	74	-10.37	8
											-10.63	6
100	9.75	183	12.75	185	11.77	181	0.16	235	-13.50	154	0.01	235
	12.83	182	15.05	187	14.10	178	0.16	237	-16.15	138	0.25	238
							0.30	237	-13.50	155	-0.26	236
									-13.26	154	-0.51	233
200	30.21	52	30.26	46	28.46	43	-6.66	85	4.48	152	-0.47	116
	27.50	48	32.06	50	31.00	46	-6.13	63	3.68	153	-0.16	117
							-6.32	80	7.31	162	-0.96	112
									7.71	161	3.92	132
											3.40	133
450	35.98	-53	34.93	-31	34.87	-35	18.17	-16	20.59	8	20.66	32
									21.14	13	18.99	32
510	32.06	-31	33.50	-69	35.28	-46	17.15	-54	19.89	-12	20.91	1
									19.95	-9	19.65	-2

*See Fig. 2. Data in this table are plotted on Figs. 60 through 63.

This page intentionally left blank.

APPENDIX D

FOURIER TRANSFORM

This page intentionally left blank.

APPENDIX D

FOURIER TRANSFORM

The pulse analysis presented in Sec. IX uses the Fourier integral pair

$$F(\omega) = \frac{1}{\sqrt{2\pi}} \int_{-\infty}^{+\infty} f(t) e^{-j\omega t} dt \tag{D-1}$$

$$f(t) = \frac{1}{\sqrt{2\pi}} \int_{-\infty}^{+\infty} F(\omega) e^{j\omega t} d\omega \tag{D-2}$$

to transform time functions to frequency functions and vice-versa. A time function $v(t)$ for $t > o$ and $v(o) = 0$ is transformed (by numerical integration) to obtain

$$V(\omega_i) = \frac{1}{\sqrt{2\pi}} \sum_{k=1}^{N} \left(t_k - t_{k-1}\right) \left[\frac{v\left(t_k\right) + v\left(t_{k-1}\right)}{2}\right] e^{-j\omega_i \left(\frac{t_k + t_{k-1}}{2}\right)} \tag{D-3}$$

where t_k are the positive time values where $v(t)$ is defined and ω_i are the angular frequency values to be determined. If $\Delta t_k = t_k - t_{k-1}$ is constant, the phase of the exponential term in Eq. (D-3) increases in increments of $-\omega_i \Delta t_k$. Hence for faithful integration,

$$\omega_i \Delta t_k \ll 2\pi \tag{D-4}$$

or

$$\Delta t_k \ll \frac{1}{f_1}.$$

The inverse transform, Eq. (D-2), is then (again using numerical integration),

$$v(t_k) = \frac{2}{\sqrt{2\pi}} \mathrm{Re} \left\{ \sum_{i=1}^{M} \left(\omega_i - \omega_{i-1}\right) \left[\frac{V\left(\omega_i\right) - V\left(\omega_{i-1}\right)}{2} \right] e^{jt_k \left(\frac{\omega_i + \omega_{i-1}}{2} \right)} \right\} \quad \text{(D-5)}$$

where advantage has been taken of the fact that

$$\int_{-\infty}^{\infty} F(\omega) e^{j\omega t} d\omega = 2 \mathrm{Re} \left\{ \int_{0}^{\infty} F(\omega) e^{j\omega t} d\omega \right\} \quad \text{(D-6)}$$

if the magnitude of $F(\omega)$ is an even function of ω and the phase of $F(\omega)$ is an odd function of ω. If $\Delta\omega_i = \omega_i - \omega_{i-1}$ is constant, the phase of the exponential term increases in increments of $\Delta\omega_i t_k$ and faithful integration requires that

$$\Delta\omega_i t_k \ll 2\pi \quad \text{(D-7)}$$

or

$$\Delta f_i \ll \frac{1}{t_k}.$$

Using a $\Delta t_k = 0.2$ microseconds and a maximum frequency of 500 kc, the inequality in Eq. (D-4) is 10 and the numerical integration in Eq. (D-3) is a good integration. At a maximum frequency of 1000 kc the inequality is 5 and the integration is still fairly good. The theoretical limit for the inequality from sampling theory is 2.

Using a $\Delta f_i = 2$ kc and a maximum time duration of 100 microseconds, the inequality in Eq. (D-7) is 10 giving good integration in Eq. (D-5). For a maximum of 200 microseconds the inequality is 5 giving fairly good integration.

This page intentionally left blank.

REFERENCES

1. J. R. Scott, "Electrical Resistivity of Earth Sediments near Dipole Antenna Site...," Technical Letters: Special Projects-10, United States Department of the Interior, Geological Survey, Denver, Colorado (January 1964).

2. R. D. Carroll and D. R. Cunningham, "Ground Conductivity Changes...," Technical Letter: Special Projects-14, United States Department of the Interior, Geological Survey, Denver, Colorado (June 1964).

3. S. Ramo and J. R. Whinnery, Fields and Waves in Modern Radio, 2nd ed., pp. 497-98 (John Wiley & Sons, New York, N.Y., 1953).

4. S. Schelkunoff, and H. T. Friis, "Antennas: Theory and Practice," Sec. 10.5 (John Wiley & Sons, New York, N.Y., 1952).

5. J. D. Kraus, Antennas, p. 230 ff. (McGraw-Hill Book Co., Inc., New York, N.Y., 1950).

6. S. Schelkunoff, op. cit., Sec. 10.3, Eq. (11).

7. Y. T. Lo, "A Note on the Cylindrical Antenna of Noncircular Cross Section," J. Appl. Phys., Vol. 24, Part 2, No. 10, pp. 1338-39 (1953).

8. J. D. Kraus, op. cit., pp. 464-484.

9. J. R. Wait, Proc. IRE (Letters) 46, pp. 1539-1541 (August 1958).

10. S. Ramo and J. R. Whinnery, op. cit., p. 253.

11. Ibid., p. 246.

12. E. D. Sunde, Earth Conduction Effects in Transmission Systems, p. 148 (D. Van Nostrand Company, Inc., New York, N.Y., 1949).

13. D. R. Marston and W. R. Graham, "Currents Induced in Cables in the Earth by a CW Electromagnetic Field," TR 65-94, Air Force Weapons Lab., Albuquerque, New Mexico (to be published).

14. J. Van Bladel, Electromagnetic Fields, p. 274 (McGraw-Hill Book Co., Inc., New York, N.Y., 1964).

15. L. A. Pipes, Applied Mathematics for Engineers and Physicists, 1st ed., p. 112 (McGraw-Hill Book Co., Inc., New York, N.Y., 1946).

16. R. S. Burington, Handbook of Mathematical Tables and Formulas, Formulas 307 and 308, 3rd ed. (Handbook Publishers, Inc., Sandusky, Ohio, 1949).

17. Tables of the Exponential Integral of Complex Arguments, National Bureau of Standards Applied Mathematics Series 51, U. S. Government Printing Office, Washington, D.C. (May 1958).

DISTRIBUTION

No. cys

HEADQUARTERS USAF

1 Hq USAF (AFORQ), Wash, DC 20330

1 Hq USAF (AFTAC), Wash, DC 20330

1 USAF Dep, The Inspector General (AFIDI), Norton AFB, Calif 92409

1 USAF Directorate of Nuclear Safety (AFINS), Kirtland AFB, NM 87117

MAJOR AIR COMMANDS

1 AFSC (SCT), Andrews AFB, Wash, DC 20331

1 SAC (DICC), Offutt AFB, Nebr 68113

1 ADC (ADOAC), Ent AFB, Colo 80912

1 AUL, Maxwell AFB, Ala 36112

1 USAFIT, Wright-Patterson AFB, Ohio 45433

1 USAFA, Colo 80840

AFSC ORGANIZATIONS

1 AFSC Scientific and Technical Liaison Office, Research and Technology Division, AFUPO, Los Angeles, Calif 90045

1 AF Materials Laboratory, Wright-Patterson AFB, Ohio 45433

1 ASD (SEPIR), Wright-Patterson AFB, Ohio 45433

1 RTD (RTS), Bolling AFB, Wash, DC 20332

1 AF Msl Dev Cen (RRRT), Holloman AFB, NM 88330

1 AFMTC (MU-135, Tech Library), Patrick AFB, Fla 32925

BSD, Norton AFB, Calif 92409

1 (BST)

1 (BSQ)

1 (BSR)

1 ESD (ESTI), L.C. Hanscom Fld, Bedford, Mass 01731

1 RADC (EMLAL-1), Griffiss AFB, NY 13442

DISTRIBUTION (cont'd)

No. cys	
	KIRTLAND AFB ORGANIZATIONS
1	AFSWC (SWEH), Kirtland AFB, NM 87117
1	ADC (ADSWO), Special Weapons Office, Kirtland AFB, NM 87117
	AFWL, Kirtland AFB, NM 87117
10	(WLIL)
3	(WLAV/Lt W. Druen)
1	(WLDE)
1	(WLRE)
5	(WLRP/Lt D.R. Marston)
1	(WLX)
1	SAC Res Rep (SACLO), AFSWC, Kirtland AFB, NM 87117
	OTHER AIR FORCE AGENCIES
2	Director, USAF Project RAND (RAND Physics Div/Dr. W.R. Graham), via: Air Force Liaison Office, The RAND Corporation, 1700 Main Street, Santa Monica, Calif 90406
1	USAF Engineering Liaison Office, APO 125, New York, NY
1	AFCRL, L. G Hanscom Fld, Bedford, Mass 01731
	ARMY ACTIVITIES
1	Chief of Research and Development, Department of the Army (Special Weapons and Air Defense Division), Wash, DC 20310
1	US Army Materiel Command, Harry Diamond Laboratories (ORDTL 06.33, Technical Library), Wash, DC 20438
1	ARGMA Liaison Office, Bell Telephone Laboratories, Whippany, NJ
1	Director, Ballistic Research Laboratories (Library), Aberdeen Proving Ground, Md 21005
1	Commanding Officer (AMSELRAXS), US Army Electronics Research and Development Laboratory, Ft Monmouth, NJ 07703
1	Army Ordnance Liaison Officer, P.O. Box 5100, Sandia Base, NM 87115
1	US Army Research Office, ATTN: Lt Gregory D. Atmore, Box CM, Duke Station, Durham, NC
1	Chief of Engineers (ENGMC-EM), Department of the Army, Wash, DC 20315

DISTRIBUTION (cont'd)

No. cys	
	Director, US Army Engineer Research and Development Laboratories, Ft Belvoir, Va 20260
2	(STINFO Branch)
2	(Mr. D. Dinger)
1	Commanding General, White Sands Missile Range (Technical Library), White Sands, NM 88002
	NAVY ACTIVITIES
1	Chief of Naval Research, Department of the Navy, Wash, DC 20390
1	Chief, Bureau of Naval Weapons (RRNU), Department of the Navy, Wash, DC 20360
1	Commanding Officer, Naval Research Laboratory, Wash, DC 20390
1	Commanding Officer and Director, Navy Electronics Laboratory (Code 4223), San Diego, Calif 92152
1	Commanding Officer and Director, Naval Applied Science Laboratory, Brooklyn, NY
1	Commander, US Naval Air Missile Test Center (Code 3022), Point Mugu, Calif
1	Commander, Naval Ordnance Laboratory, ATTN: Dr. Rudlin, White Oak, Silver Spring, Md 20910
1	Office of Naval Research, Wash, DC 20360
1	Director of Naval Warfare Analyses, Institute of Naval Studies, Office of the Chief of Navy Ops, 545 Technology Square, Cambridge 39, Mass
1	Commanding Officer, US Naval Weapons Evaluation Facility (NWEF, Code 404), Kirtland AFB, NM 87117
	OTHER DOD ACTIVITIES
2	Director, Defense Atomic Support Agency (Document Library Branch), Wash, DC 20301
1	Commander, Field Command, Defense Atomic Support Agency (FCAG3, Special Weapons Publication Distribution), Sandia Base, NM 87115
1	Director, Weapon Systems Evaluation Group, Room 1D-847, The Pentagon, Wash, DC 20330
1	Office of Director of Defense Research and Engineering, ATTN: John E. Jackson, Office of Atomic Programs, Room 3E 1071, The Pentagon, Wash, DC 20330
20	DDC (TIAAS), Cameron Station, Alexandria, Va 22314

DISTRIBUTION (cont'd)

No. cys	
	AEC ACTIVITIES
1	Sandia Corporation (Information Distribution Division), Box 5800, Sandia Base, NM 87115
1	Sandia Corporation (Technical Library), P.O. Box 969, Livermore, Calif 94551
1	University of California Lawrence Radiation Laboratory, ATTN: Director's Office, Technical Information Division, P.O. Box 808, Livermore, Calif 94551
1	Director, Los Alamos Scientific Laboratory (Helen Redman, Report Library), P.O. Box 1663, Los Alamos, NM 87554
	OTHER
1	Office of Assistant Secretary of Defense (Civil Defense), Wash, DC 20301
1	National Bureau of Standards, Radiological Equipment Section, Wash, DC
1	Director, National Bureau of Standards, Central Radio Propagation Laboratory, Boulder, Colo
1	Arms Control and Disarmament Agency, Chief, Reference Research Bureau, Wash 25, DC
1	Institute for Defense Analysis, Room 2B257, The Pentagon, Wash, DC 20330 THRU: ARPA
2	Massachusetts Institute of Technology, Lincoln Laboratory (Document Library), P.O. Box 73, Lexington, Mass 02173
1	Aerospace Corporation, ATTN: Mr. Ivan Weeks, Ballistic Missile Division, San Bernardino, Calif
1	Allied Research Associates, Inc., ATTN: Mr. D.C. Knodel, Virginia Road, Concord, Mass 01742
1	AVCO Corporation, Research and Advanced Development Division, ATTN: Chief Librarian, 201 Lowell Street, Wilmington, Mass
1	The Dikewood Corporation, 4805 Menaul Bldvd NE, Albuquerque, NM
1	General Electric Company, MSD, ATTN: Dr. F.A. Lucy, Room M9505, P.O. Box 8555, Philadelphia 1, Pa
1	University of Michigan, University Research Security Office, Lobby 1, East Engineering Bldg, Ann Arbor, Mich
1	Space Technology Laboratories, Inc., AF Contr Mgt Office, c/o STLTD, Bldg S/1930, One Space Park, Redondo Beach, Calif 90278
80	Stanford Research Institute, ATTN: G-037, External Reports, Menlo Park, Calif 94025
2	Bell Telephone Laboratories, ATTN: Mr. Ian Duran, Whippany, NJ
1	Official Record Copy (Lt D.R. Marston, WLRP)

UNCLASSIFIED
Security Classification

DOCUMENT CONTROL DATA - R&D

(Security classification of title, body of abstract and indexing annotation must be entered when the overall report is classified)

1 ORIGINATING ACTIVITY *(Corporate author)* Stanford Research Institute Menlo Park, California	2a REPORT SECURITY CLASSIFICATION Unclassified 2b GROUP

3 REPORT TITLE

Electromagnetic Field Distortions and Currents In and Near Buried Cables and Bunkers

4 DESCRIPTIVE NOTES *(Type of report and inclusive dates)*

18 March 1963 to 28 February 1965

5 AUTHOR(S) *(Last name, first name, initial)*

Whitson, Arthur L.
Vance, Edward F.

6 REPORT DATE September 1965	7a TOTAL NO. OF PAGES 292	7b NO OF REFS 17
8a CONTRACT OR GRANT NO. AF 29(601)-5904 b. PROJECT NO. 5710 c Program Element 7.60.06.01.5 d.	9a ORIGINATOR'S REPORT NUMBER(S) AFWL-TR-65-39 9b OTHER REPORT NO(S) *(Any other numbers that may be assigned this report)*	

10. AVAILABILITY/LIMITATION NOTICES

Qualified users may obtain copies of this report from DDC.
Distribution is limited because of the technology discussed in the report.

11. SUPPLEMENTARY NOTES	12. SPONSORING MILITARY ACTIVITY Air Force Weapons Laboratory Kirtland Air Force Base, New Mexico

13 ABSTRACT

The first purpose of this report is to establish the electromagnetic properties of a land area containing numerous buried wires, cables, and other subterranean structures by measuring the deviations produced by these structures in the electric and magnetic fields from an electric monopole antenna of known characteristics. The second purpose of this report is to determine the currents induced in the buried conductors and to establish a practical method of predicting these currents for conductors near the surface of the earth. The portable system utilized in the experimental work is designed to perform the necessary field mapping (both CW and impulse) in the 0.5- to 510-kc frequency range. This system is described and evaluated. Field mapping accuracy is demonstrated to be 5 percent for magnitude, 5 degrees for phase relative to local vertical electric field, and 1 degree for the spatial orientation of the fields. A cable current theory based on a transmission line model is developed for isolated or widely separated cables. This theory and Wait's wave impedance theory for currents induced in closely spaced cables are experimentally confirmed by measurements of currents induced in conductors on or near the surface of the earth. For pulse field and current calculations, the transfer functions from the transmitter to the receiving location are obtained using a computer program for Fourier transforms.

DD FORM 1 JAN 64 1473

UNCLASSIFIED
Security Classification

UNCLASSIFIED
Security Classification

14 KEY WORDS	LINK A ROLE	LINK A WT	LINK B ROLE	LINK B WT	LINK C ROLE	LINK C WT
Electromagnetic properties						
Electric currents						
Electric cables						
Underground structures						

INSTRUCTIONS

1. ORIGINATING ACTIVITY: Enter the name and address of the contractor, subcontractor, grantee, Department of Defense activity or other organization *(corporate author)* issuing the report.

2a. REPORT SECURITY CLASSIFICATION: Enter the overall security classification of the report. Indicate whether "Restricted Data" is included. Marking is to be in accordance with appropriate security regulations.

2b. GROUP: Automatic downgrading is specified in DoD Directive 5200.10 and Armed Forces Industrial Manual. Enter the group number. Also, when applicable, show that optional markings have been used for Group 3 and Group 4 as authorized.

3. REPORT TITLE: Enter the complete report title in all capital letters. Titles in all cases should be unclassified. If a meaningful title cannot be selected without classification, show title classification in all capitals in parenthesis immediately following the title.

4. DESCRIPTIVE NOTES: If appropriate, enter the type of report, e.g., interim, progress, summary, annual, or final. Give the inclusive dates when a specific reporting period is covered.

5. AUTHOR(S): Enter the name(s) of author(s) as shown on or in the report. Enter last name, first name, middle initial. If military, show rank and branch of service. The name of the principal author is an absolute minimum requirement.

6. REPORT DATE: Enter the date of the report as day, month, year; or month, year. If more than one date appears on the report, use date of publication.

7a. TOTAL NUMBER OF PAGES: The total page count should follow normal pagination procedures, i.e., enter the number of pages containing information.

7b. NUMBER OF REFERENCES: Enter the total number of references cited in the report.

8a. CONTRACT OR GRANT NUMBER: If appropriate, enter the applicable number of the contract or grant under which the report was written.

8b, 8c, & 8d. PROJECT NUMBER: Enter the appropriate military department identification, such as project number, subproject number, system numbers, task number, etc.

9a. ORIGINATOR'S REPORT NUMBER(S): Enter the official report number by which the document will be identified and controlled by the originating activity. This number must be unique to this report.

9b. OTHER REPORT NUMBER(S): If the report has been assigned any other report numbers *(either by the originator or by the sponsor)*, also enter this number(s).

10. AVAILABILITY/LIMITATION NOTICES: Enter any limitations on further dissemination of the report, other than those imposed by security classification, using standard statements such as:

(1) "Qualified requesters may obtain copies of this report from DDC."

(2) "Foreign announcement and dissemination of this report by DDC is not authorized."

(3) "U. S. Government agencies may obtain copies of this report directly from DDC. Other qualified DDC users shall request through _____."

(4) "U. S. military agencies may obtain copies of this report directly from DDC. Other qualified users shall request through _____."

(5) "All distribution of this report is controlled. Qualified DDC users shall request through _____."

If the report has been furnished to the Office of Technical Services, Department of Commerce, for sale to the public, indicate this fact and enter the price, if known.

11. SUPPLEMENTARY NOTES: Use for additional explanatory notes.

12. SPONSORING MILITARY ACTIVITY: Enter the name of the departmental project office or laboratory sponsoring *(paying for)* the research and development. Include address.

13. ABSTRACT: Enter an abstract giving a brief and factual summary of the document indicative of the report, even though it may also appear elsewhere in the body of the technical report. If additional space is required, a continuation sheet shall be attached.

It is highly desirable that the abstract of classified reports be unclassified. Each paragraph of the abstract shall end with an indication of the military security classification of the information in the paragraph, represented as *(TS)*, *(S)*, *(C)*, or *(U)*.

There is no limitation on the length of the abstract. However, the suggested length is from 150 to 225 words.

14. KEY WORDS: Key words are technically meaningful terms or short phrases that characterize a report and may be used as index entries for cataloging the report. Key words must be selected so that no security classification is required. Identifiers, such as equipment model designation, trade name, military project code name, geographic location, may be used as key words but will be followed by an indication of technical context. The assignment of links, rules, and weights is optional.